

AD-A241 848



2



Method of Moments Analysis of Scattering by Chiral Media

M.S. Kluskens and E.H. Newman



The Ohio State University
ElectroScience Laboratory

Department of Electrical Engineering
Columbus, Ohio 43212

Technical Report 721566-2
Grant No. N00014-89-J-1007
July 1991

Department of the Navy
Office of Naval Research
800 N. Quincy St.
Arlington, Virginia 22217-5000

91-13664

NOTICES

When Government drawings, specifications, or other data are used for any purpose other than in connection with a definitely related Government procurement operation, the United States Government thereby incurs no responsibility nor any obligation whatsoever, and the fact that the Government may have formulated, furnished, or in any way supplied the said drawings, specifications, or other data, is not to be regarded by implication or otherwise as in any manner licensing the holder or any other person or corporation, or conveying any rights or permission to manufacture, use, or sell any patented invention that may in any way be related thereto.

REPORT DOCUMENTATION PAGE	1. REPORT NO.	2.	3. Recipient's Accession No.
4. Title and Subtitle Method of Moments Analysis of Scattering by Chiral Media			5. Report Date July 1991
7. Author(s) M.S. Kluskens and E.H. Newman			6.
9. Performing Organization Name and Address The Ohio State University ElectroScience Laboratory 1320 Kinnear Road Columbus, OH 43212			8. Performing Org. Rept. No. 721566-2
12. Sponsoring Organization Name and Address Dept. of the Navy, Office of Naval Research 800 N. Quincy St. Arlington, Virginia 22217-5000			10. Project/Task/Work Unit No.
15. Supplementary Notes			11. Contract(C) or Grant(G) No. (C) (G) N00014-89-J-1007
16. Abstract (Limit: 200 words) In this report, the interaction of electromagnetic fields with objects composed of chiral media is analyzed using eigenfunction and method of moments techniques. The historical basis for the constitutive relationships of chiral media is presented in the first chapter. The wave equation, volume equivalence theorem, and image theory for chiral media are presented in the second chapter. An eigenfunction solution for scattering by a multilayer circular chiral cylinder with a center cylinder described by an impedance surface is developed in the third chapter. A pulse-basis point-matching method of moments solution for scattering by an inhomogeneous object composed of chiral media in free-space or in the presence of a perfectly conducting half-plane is presented in the fourth chapter. A spectral-domain Galerkin method of moments solution for a microstrip transmission line on a chiral substrate is developed in the fifth chapter. Numerical data in each case demonstrated that the chirality of the objects causes a significant asymmetry in the electromagnetic fields, which is not present for achiral objects.			13. Report Type/Period Covered Technical Report
17. Document Analysis a. Descriptors CHIRAL MEDIA HALF-PLANE MOMENT METHOD b. Identifiers/Open-Ended Terms c. COSATI Field/Group			14.
18. Availability Statement A. Approved for public release; Distribution is unlimited.		19. Security Class (This Report) Unclassified	21. No. of Pages 187
		20. Security Class (This Page) Unclassified	22. Price

Contents

List of Figures	vi
List of Symbols	x
1 Introduction	1
1.1 What is Chiral Media	1
1.2 Overview	4
1.3 History of Constitutive Relationships for Optical Activity	5
1.4 Microwave Models for Optical Activity	8
1.5 Electromagnetic Scattering and Optical Activity	8
1.6 History of Chiral Media	9
2 Theory	12
2.1 Constitutive Relationships	12
2.2 Chiral Wave Equation	13
2.3 Circular Vector Potentials	16
2.4 Chiral Volume Equivalence Theorem	17
2.5 Image Theory for Chiral Media	18
3 Scattering by a Multilayer Cylinder	23
3.1 The Eigenfunction Expansion	25
3.2 Determining the Coefficients	28
3.2.1 Perfectly Conducting Center Cylinder	30
3.2.2 Surface Impedance Center Cylinder	31
3.2.3 Material Center Cylinder	33
3.2.4 Exterior Region	33
3.3 Numerical Results	35
3.3.1 TM_z Incident Plane Wave	36
3.3.2 TE_z Incident Plane Wave	40
3.3.3 Chirality Versus Scattering	46
3.4 Summary	54

4	Scattering by an Arbitrary Cylinder	56
4.1	Derivation of General Integral Equations	57
4.2	Integral Equations for a Two-Dimensional Body	59
4.3	Method of Moments Solution	60
4.3.1	The Impedance Matrix $[Z]$	62
4.3.2	The Impedance Matrix $[\Delta Z]$	64
4.3.3	The Current Vector I	65
4.3.4	The Voltage Vector V	65
4.3.5	Scattered and Internal Fields	66
4.4	Free-Space Numerical Results	66
4.5	Half-Plane Numerical Results	81
4.6	Summary	89
5	A Microstrip Line on a Chiral Substrate	90
5.1	Microstrip Field Expansions	91
5.1.1	Field Expansions in the Free Space Region	91
5.1.2	Field Expansions in the Chiral Slab	93
5.2	Coefficients of the Field Expansions	95
5.3	Electric Fields at the Interface	97
5.4	Method of Moments Solution	98
5.5	Evaluating the Microstrip Integral Equations	102
5.6	Numerical Results	106
5.7	Summary	110
6	Conclusions	116
Appendices		
A	Scattering by a Chiral Coated Perfectly Conducting Cylinder	119
B	Evaluating the Half-Plane Green's Function Integrals	124
C	Chiral Slab and Normal Incident Plane Wave	133
D	Fields of Circular Vector Potentials	135
E	Spectral Domain Fields in a Half Space	138
F	Fourier Transforms for Microstrip Problems	140
G	Numerical Integration for the Self-Impedance of the Dominant Microstrip Current	142
H	Generalized Sine and Cosine Integrals	144

I	Evaluation of the Microstrip Impedance Elements in the Spatial Domain	147
J	Two-Dimensional Traveling Wave Electric Currents	151
K	Spherical Wave Spectrum of a Cylindrical Traveling Wave	155
L	Small Argument Approximations for Integrals of Hankel Functions	157
M	Limitations of the Reciprocity Theorem in Two-Dimensions	159

Accession For	
NTIS CRA&I	↓
DTIC TAB	□
Unannounced	□
Justification	
By	
Distribution	
Availability Codes	
Dist	Avail and/or Special
A-1	

RECEIVED

List of Figures

1.1	Examples of (a) a chiral medium composed of a three-dimensional array of randomly orientated helices and (b) an artificial dielectric composed of a three-dimensional array of spheres.	2
1.2	Constitutive relationships for the major subdivisions of media.	3
1.3	Overview of geometries studied in this report.	6
2.1	Image theory for a chiral body over a perfect electric conductor derived using the chiral volume equivalence theorem and conventional image theory for currents.	20
2.2	Image theory for a chiral body over a perfect magnetic conductor.	21
3.1	Geometry of a general multilayer circular chiral cylinder with a surface impedance center cylinder.	24
3.2	The co-polarized and cross-polarized bistatic echo width of a two-layer chiral cylinder with a perfect electric conducting center cylinder for a TM_z incident plane wave.	37
3.3	The co-polarized and cross-polarized bistatic echo width of a two-layer chiral cylinder for a TM_z incident plane wave.	38
3.4	The bistatic echo width of the two layer chiral and achiral cylinders shown in Figure 3.3 for a TM_z incident plane wave.	39
3.5	The co-polarized and cross-polarized bistatic echo width of a two layer chiral cylinder with a perfect electric conducting center cylinder for a TE_z incident plane wave.	41
3.6	The co-polarized and cross-polarized bistatic echo width of a two layer chiral cylinder for a TE_z incident plane wave.	42
3.7	Internal fields along $x = 0$ for the chiral cylinder shown in Figure 3.5.	43
3.8	Internal fields along $x = 0$ for the achiral cylinder of Figure 3.5.	44
3.9	Internal H_ϕ and H_z fields at the surface of the conducting cylinder for the geometry shown in Figure 3.5.	45
3.10	Internal fields along $y = 0$ for the chiral cylinder shown in Figure 3.5.	47
3.11	Backscatter echo width versus the magnitude of the chirality admittance for TM_z incident plane wave.	48

3.12	Backscatter echo width versus the magnitude of the chirality admittance for TE_Z incident plane wave.	49
3.13	Bistatic echo width versus the magnitude of the chirality admittance for TE_Z incident plane wave.	50
3.14	Backscatter echo width versus the magnitude of the chirality admittance for TM_Z incident plane wave.	52
3.15	Backscatter echo width versus the magnitude of the chirality admittance for TE_Z incident plane wave.	53
4.1	Volume Equivalence Theorem (a) Original problem: impressed currents, half-plane, and chiral scatterer. (b) Equivalent problem: scatterer replaced by free space and the equivalent currents.	57
4.2	A trapezoidal cross section cylinder split into N smaller trapezoidal cells.	60
4.3	A TM_Z plane wave normally incident upon a tapered chiral slab.	66
4.4	The magnitude and phase of the E_z and E_x fields along the y -axis for the tapered chiral slab shown in Figure 4.3.	68
4.5	The magnitude and phase of the H_z and H_x fields along the y -axis for the tapered chiral slab shown in Figure 4.3.	69
4.6	The co-polarized and cross-polarized bistatic echo width of a circular chiral cylinder for a TM_Z incident plane wave.	70
4.7	The co-polarized and cross-polarized bistatic echo width of a circular chiral cylinder for a TE_Z incident plane wave.	71
4.8	Internal fields along $y = 0$ for the chiral cylinder shown in Figure 4.7.	73
4.9	The co-polarized and cross-polarized bistatic echo width of a 0.1 m x 2.0 m homogeneous chiral slab for a TM_Z plane wave incident at 30° off the x -axis.	75
4.10	Internal fields along $y = 0$ for the homogeneous chiral slab shown in Figure 4.9.	76
4.11	The co-polarized and cross-polarized bistatic echo width of a 0.1 m x 2.0 m homogeneous chiral slab for a TE_Z plane wave incident at 30° off the x -axis.	77
4.12	Internal fields along $y = 0$ for the homogeneous chiral slab shown in Figure 4.11.	78
4.13	The co-polarized and cross-polarized bistatic echo width of a 0.1 m x 2.0 m inhomogeneous chiral slab for a TM_Z plane wave incident at 30° off the x -axis.	79
4.14	Internal fields along $y = 0$ for the inhomogeneous chiral slab shown in Figure 4.13.	80
4.15	The co-polarized and cross-polarized bistatic echo width of a 0.1 m x 2.0 m inhomogeneous chiral slab for a TM_E plane wave incident at 30° off the x -axis.	82

4.16	The co-polarized and cross-polarized backscatter echo width of a 0.1 m x 2.0 m homogeneous chiral slab for a TM_Z plane wave incident at 30° off the x-axis.	83
4.17	The co-polarized and cross-polarized backscatter echo width of a 0.1 m x 2.0 m homogeneous chiral slab for a TE_Z plane wave incident at 30° off the x-axis.	84
4.18	The co-polarized and cross-polarized backscatter ($\phi = \phi^i$) echo width of a lossless chiral slab at the tip of a perfectly conducting half-plane.	85
4.19	Internal fields along $y = 0.1$ meters for the chiral slab and half-plane geometry shown in Figure 4.18 with a TM_Z incident wave from 60°	87
4.20	The co-polarized and cross-polarized bistatic echo width of a perfectly conducting half-plane with a chiral double-wedge at the tip.	88
5.1	Microstrip line on a grounded chiral slab.	91
5.2	First four basis functions for the longitudinal and transverse current components.	100
5.3	Integration contour to avoid surface wave poles.	104
5.4	Integrand of the self-impedance of a Maxwellian current distribution ($Z_{zz(0,0)}$) for a normalized guide wavelength of 0.6 ($k_z=349.3$) and a range of chirality admittances.	105
5.5	E_z and E_x fields at $y = T$ for identical chiral and achiral microstrip lines, solved using the two lowest order expansion functions.	108
5.6	Fields and currents at $y = T$ for a chiral microstrip solved using ten J_z modes and ten J_x modes.	109
5.7	Fields and currents at $y = T$ for a chiral microstrip at 5 GHz solved using ten J_z modes and ten J_x modes.	112
5.8	Normalized guide wavelength (λ_g/λ_0) versus frequency for the fundamental mode of chiral and achiral microstrip lines, for a range of chiral parameters.	113
5.9	Normalized guide wavelength (λ_g/λ_0) versus substrate thickness for the fundamental mode of chiral and achiral microstrip lines at two frequencies.	114
5.10	Normalized guide wavelength (λ_g/λ_0) versus microstrip line width for the fundamental mode of chiral and achiral microstrip lines at two frequencies.	115
A.1	Geometry of a chiral coated perfectly conducting cylinder.	120
B.1	The real and imaginary parts of the integrand of the half-plane integral for $i = 1$ and $\beta = 1$	125
B.2	Regions for each method of evaluating the S_i integrals in the half-plane Green's function for a \hat{z} polarized line source.	126
B.3	Integration contour in the complex u plane.	127

C.1	Geometry for an infinite chiral slab	134
I.1	Equivalent geometry for self-impedance of J_z microstrip current mode.	148
M.1	Sources a and b in a region enclosed by the surface Σ	161

LIST OF SYMBOLS

- A Magnetic vector potential.
- \mathcal{B} Magnetic flux density (time-varying).
- B Magnetic flux density (time-harmonic).
- c Velocity of light in free space.
- \bar{d} Dyadic quantities are indicated by a bar over a bold symbol.
- \mathcal{D} Electric flux density (time-varying).
- D Electric flux density (time-harmonic).
- \mathcal{E} Electric field density (time-varying).
- E Electric field density (time-harmonic).
- E' Incident electric field.
- E_L Electric field of a left circularly polarized wave.
- E_R Electric field of a right circularly polarized wave.
- E^S Scattered electric field.
- F Electric vector potential.
- $H_n^{(1)}$ Hankel function of the first kind of order n .
- $H_n^{(2)}$ Hankel function of the second kind of order n .
- \mathcal{H} Magnetic field intensity (time-varying).
- H Magnetic field intensity (time-harmonic).
- H' Incident magnetic field.
- H^S Scattered magnetic field.
- J_n Bessel function of the first kind of order n .
- J Electric volume current density.

- \mathbf{J}' Impressed electric current.
 k_0 Wave number of free space.
 k_L Wave number of a left circularly polarized wave.
 k_R Wave number of a right circularly polarized wave.
 \mathbf{M}_n Vector wave function.
 \mathbf{M} Magnetic volume current density.
 \mathbf{M}' Impressed magnetic current.
 \mathbf{N}_n Vector wave function.
 Y_n Bessel function of the second kind of order n (also called Weber's or Neumann's function).
 $Z_n^{(p)}$ Bessel function of type p .
 Z_{TE} TE surface impedance
 Z_{TM} TM surface impedance.
 ϵ Permittivity.
 ϵ_0 Permittivity of free space.
 ϵ_c Effective permittivity of a chiral medium.
 ϵ_r Relative permittivity.
 η_0 Wave impedance of free space
 η_c Wave impedance of chiral media.
 λ Wavelength.
 μ Permeability.
 μ_0 Permeability of free space.
 μ_r Relative permeability.
 ξ_c Chirality admittance.
 ρ Electric charge density.
 ω Angular frequency.

Chapter 1

Introduction

In this report, the interaction of electromagnetic fields with objects composed of chiral media is analyzed using eigenfunction and method of moments techniques. The term *chiral media* was first used by Jaggard, Mickelson, and Papas in 1979 [1], who defined chiral media as *consisting of macroscopic chiral objects randomly embedded in a dielectric*. The word chiral describes something that is handed, i.e., an object whose mirror image can not be produced solely by rotating and translating the original object. An example of chiral media is shown in Figure 1.1(a). For comparison, an artificial dielectric is shown in Figure 1.1(b).

1.1 What is Chiral Media

Chiral media are a class of artificial dielectrics that exhibit optical activity, a property of many biological and chemical substances which occurs naturally almost exclusively at optical frequencies [2]. Optical activity is a reciprocal property characterized by differing wave numbers for right and left circularly polarized waves. One effect is to cause a linearly or elliptically polarized wave to rotate its axis of polarization as it propagates through the optically active medium; this is known as optical rotation, circular birefringence, or circular double refraction [3]. The other effect, circular dichroism, is the difference in the attenuation rates for the right and left circularly polarized waves, thereby causing a linearly polarized wave to degenerate into an

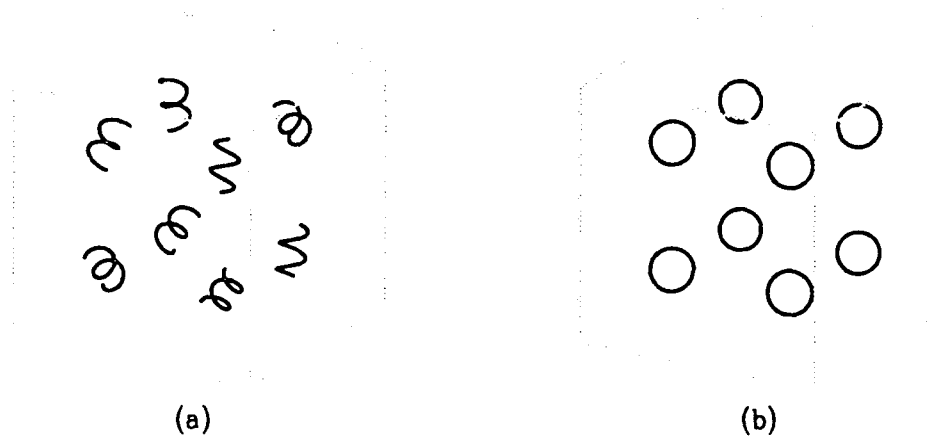


Figure 1.1: Examples of (a) a chiral medium composed of a three-dimensional array of randomly orientated helices and (b) an artificial dielectric composed of a three-dimensional array of spheres.

elliptically polarized wave. The Faraday effect is similar to optical activity, except the latter is reciprocal and can occur in isotropic as well as anisotropic media, while the former is nonreciprocal and occurs only in anisotropic media.

To put chiral media in perspective with respect to other media, consider the constitutive relationships for the major subdivisions of media shown in Figure 1.2. The constitutive relationships for bianisotropic media, the most general media, are shown at the top of the figure, where the explicit dependence of the constitutive parameters on space, time, etc., has not been shown for clarity [4, 5]. Research on bianisotropic media can be applied to chiral media since chiral media is a scalar version of bianisotropic media [6]—[18]. The first set of equations shown for bianisotropic media can be written as

$$\begin{bmatrix} c\mathbf{D} \\ \mathbf{H} \end{bmatrix} = \begin{bmatrix} \bar{\mathbf{P}} & \bar{\mathbf{L}} \\ \bar{\mathbf{M}} & \bar{\mathbf{Q}} \end{bmatrix} \begin{bmatrix} \mathbf{E} \\ c\mathbf{B} \end{bmatrix} \quad (1.1)$$

where $c\mathbf{D}$ and \mathbf{H} have the same units (A/m), \mathbf{E} and $c\mathbf{B}$ have the same units (V/m), and in combination they each form six-dimensional vectors (tensors of rank one).

BIANISOTROPIC	
$c\mathbf{D} = \bar{\mathbf{P}} \cdot \mathbf{E} + \bar{\mathbf{L}} \cdot c\mathbf{B}$	$\mathbf{D} = \bar{\epsilon} \cdot \mathbf{E} + \bar{\xi} \cdot \mathbf{H}$
	or
$\mathbf{H} = \bar{\mathbf{M}} \cdot \mathbf{E} + \bar{\mathbf{Q}} \cdot c\mathbf{B}$	$\mathbf{B} = \bar{\zeta} \cdot \mathbf{E} + \bar{\mu} \cdot \mathbf{H}$
ANISOTROPIC	BIISOTROPIC
$\mathbf{D} = \bar{\epsilon} \cdot \mathbf{E}$	$\mathbf{D} = \epsilon \mathbf{E} + \xi \mathbf{H}$
$\mathbf{B} = \bar{\mu} \cdot \mathbf{H}$	$\mathbf{B} = \zeta \mathbf{E} + \mu \mathbf{H}$
ISOTROPIC	CHIRAL
$\mathbf{D} = \epsilon \mathbf{E}$	$\mathbf{D} = \epsilon \mathbf{E} - j \xi_c \mathbf{B}$
$\mathbf{B} = \mu \mathbf{H}$	$\mathbf{H} = \frac{1}{\mu} \mathbf{B} - j \xi_c \mathbf{E}$

Figure 1.2: Constitutive relationships for the major subdivisions of media.

Of particular importance is that all of the constitutive parameters have the same units and together form a six-dimensional tensor of rank two. That the constitutive parameters $\bar{\mathbf{P}}$ and $\bar{\mathbf{Q}}$ individually are three-dimensional tensors of rank two is well documented in the literature on bianisotropic media; however, that the constitutive parameters $\bar{\mathbf{L}}$ and $\bar{\mathbf{M}}$ individually are pseudotensors of rank two is often neglected. This characteristic is important because pseudotensors are not invariant with respect to improper coordinate transformations. A coordinate transformation is improper if the determinant of its Jacobian is negative; one example is the transformation to create the image of an object [6, sec. 2.6, 6.2], [19, pg. 813]. This translates into a minus sign as was shown in 1971 by Kong when developing image theory for bianisotropic media [11]. A similar result is developed in Section 2.5 for chiral media using the volume equivalence theorem of Section 2.4. The same result can also be obtained by using the fact that ξ_c is a pseudoscalar (pseudotensor of rank zero).

1.2 Overview

The remainder of this chapter presents historical background on the constitutive relationships for chiral and optically active media, as well as an outline of the work on chiral media. Chapter 2 presents background electromagnetic theory for chiral media. The geometries studied in this report are shown in Figure 1.3. Figure 1.3(a) shows the cylindrical geometry for which Bohren [20] developed an eigenfunction solution for scattering by a normally incident plane wave. This solution was used as the base for developing the solution for scattering by the multilayer circular chiral cylinder presented in Chapter 3 and shown in Figure 1.3(b). The eigenfunction solution by Bohren was also used as the reference solution when developing the pulse-basis point-matching method of moments solution for scattering by an inhomogeneous object composed of chiral media in free-space presented in Chapter 4 and shown in Figure 1.3(c). Chapter 4 also presents a pulse-basis point-matching method of moments solution for scattering by an inhomogeneous object composed of chiral media

in the presence of a perfectly conducting half-plane as shown in Figure 1.3(d). This solution could be generalized for scattering in a half-space and verified using the image theory for chiral media developed in Chapter 2 and shown in Figure 1.3(e). Chapter 5 presents a spectral-domain Galerkin method of moments solution for a microstrip transmission line on a chiral substrate as shown in Figure 1.3(f).

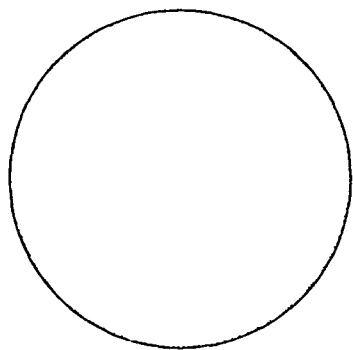
1.3 History of Constitutive Relationships for Optical Activity

This section presents a brief history of the constitutive relationships for optically active media. In the fields of biology, chemistry, and physics, optical activity has been studied since early in the nineteenth century [2]. However, it was not until nearly a century later that researchers began to develop theories for natural optical activity in terms of electromagnetic wave theory. The early theories were based on classical mechanics [21, pg. 616–635]; later, quantum mechanical theories were developed [21, pg. 703–723]. In these theories, optical activity is the result of a second-order term in the dispersion formula. This causes a time-harmonic electric field to create not only an electric dipole but also a linked magnetic dipole. The reverse is true for a time-harmonic magnetic field. In 1937, Condon [3, 22] summarized the quantum mechanical theories for natural isotropic optical activity and presented constitutive relationships of the form

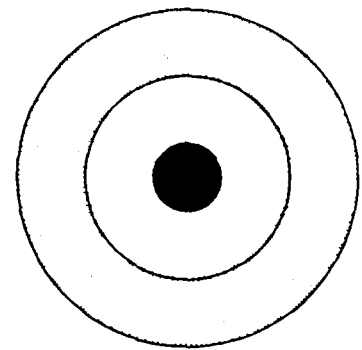
$$\mathcal{D} = \epsilon \mathcal{E} + f \mathcal{H} - g \frac{\partial \mathcal{H}}{\partial t} \quad (1.2a)$$

$$\mathcal{B} = \mu_0 \mathcal{H} + f \mathcal{E} + g \frac{\partial \mathcal{E}}{\partial t} \quad (1.2b)$$

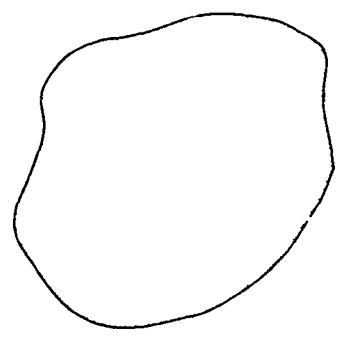
where g is the rotatory parameter and f is small with only a second order effect on the phase velocity and no effect on optical rotation.



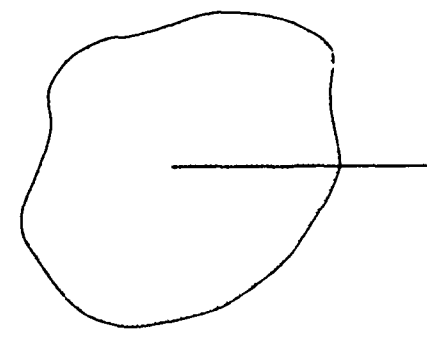
(a) Eigenfunction



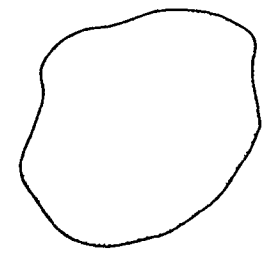
(b) Multilayer



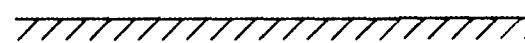
(c) Method of Moments



(d) Half-plane



(e) Image Theory



(f) Microstrip

Figure 1.3: Overview of geometries studied in this report.

In 1959, Moffitt and Moscovitz extended this work with constitutive relationships of the form

$$\mathbf{D}(\omega, t) = \epsilon(\omega) \mathbf{E}(\omega, t) + f(\omega) \mathbf{H}(\omega, t) - g(\omega) \frac{\partial}{\partial t} \mathbf{H}(\omega, t) \quad (1.3a)$$

$$\mathbf{B}(\omega, t) = \mu(\omega) \mathbf{H}(\omega, t) + f(\omega) \mathbf{E}(\omega, t) + g(\omega) \frac{\partial}{\partial t} \mathbf{E}(\omega, t) \quad (1.3b)$$

where the time-dependence was not dropped [23, pg. 652]. They showed that the real and imaginary components of the constitutive parameters $\epsilon(\omega)$, $\mu(\omega)$, $f(\omega)$, and $g(\omega)$ are related by the Kramers-Kronig relations [5, 6]

$$\zeta'(\omega) = \frac{2}{\pi} \int \frac{s \zeta''(s)}{s^2 - \omega^2} ds \quad (1.4a)$$

$$\zeta''(\omega) = -\frac{2}{\pi} \int \frac{\omega \zeta'(s)}{s^2 - \omega^2} ds \quad (1.4b)$$

where $\zeta(\omega) = \zeta'(\omega) - j\zeta''(\omega)$ and $\zeta = \epsilon, \mu, f, g$. Moffitt and Moscovitz showed that the optical rotation is proportional to g' and the circular dichroism is proportional to g'' ; therefore, these two measured quantities are related by Kramers-Kronig relations. This is true because f is small and affects only the average phase velocity with a second order effect. This can be seen by examining the wave numbers for right (k_R) and left (k_L) circularly polarized waves propagating in an optically active media described by Equation (1.3):

$$k_R = \omega \sqrt{\mu\epsilon - \frac{f^2}{c^2}} + \frac{\omega^2 g}{c} \quad (1.5a)$$

$$k_L = \omega \sqrt{\mu\epsilon - \frac{f^2}{c^2}} - \frac{\omega^2 g}{c} \quad (1.5b)$$

The factor $k_R - k_L$ contains only g , and it is this factor that is responsible for optical rotation and circular dichroism. Additional information on optical activity and how the constitutive equations are derived can be found in the previously mentioned references and [24]—[36].

1.4 Microwave Models for Optical Activity

The optical activity of helical molecules led researchers to consider large-scale models at microwave frequencies. Some of the earliest experimental work on this topic was done in 1920 and 1922 by Lindman [37, 38], who measured the rotation of microwaves propagating through randomly oriented copper helices. In 1956, Winkler [39] repeated Lindman's work and obtained slightly different results. Similar measurements were done in 1957 by Tinoco and Freeman [40] for oriented arrays of helices. They showed that the array of helices rotated the polarization of incident plane waves over a wide frequency range. The strongest optical rotation and circular dichroism corresponded to the case of $\lambda = 2L/k$, where $k = 1, 2, 3, \dots$ and L is the length of the wire in the helix. However, these researchers were interested in how their results matched models for optical activity, not in the electromagnetic properties of arrays of wire helices.

1.5 Electromagnetic Scattering and Optical Activity

One of the first researchers to study scattering by optically active bodies using electromagnetic wave theory was Bohren; a previous researcher used the approximate Mie scattering technique [41]. Bohren used constitutive relationships of the form [42, 43]

$$\mathbf{D} = \epsilon \mathbf{E} + \alpha \epsilon \nabla \times \mathbf{E} \quad (1.6a)$$

$$\mathbf{B} = \mu \mathbf{H} + \beta \mu \nabla \times \mathbf{H} \quad (1.6b)$$

where α and β are the parameters which account for the optical activity. The parameters α and β are equal in the absence of an externally applied magnetic field. His work on scattering by electromagnetic waves was limited to eigenfunction solutions for homogeneous spheres [42], spherical shells [44], and cylinders [20]. He also

presented an approximate solution for arbitrarily shaped inhomogeneous bodies using the Rayleigh-Debye approximation, which is valid only for small bodies with low density [45]. However, his interest in optically active bodies was based on modeling the measurement of biological particles such as viruses [46].

1.6 History of Chiral Media

The history of chiral media starts in 1979 with the introductory paper by Jaggard, Mickelson, and Papas [1]. They examined the approximate scattering by a single perfectly conducting short wire helix and concluded that a randomly oriented collection of such objects would behave macroscopically as a medium with constitutive relationships of the form

$$\mathbf{D} = \epsilon \mathbf{E} - j\xi_c \mathbf{B} \quad (1.7a)$$

$$\mathbf{H} = \frac{1}{\mu} \mathbf{B} - j\xi_c \mathbf{E} \quad (1.7b)$$

where ξ_c is the chirality admittance and the $e^{j\omega t}$ time convention is used. The next paper on chiral media was not published until 1982 and considered the transition radiation generated by a charged particle passing through a plate composed of chiral media [47]. Later research has extended this work to Čerenkov radiation in infinite chiral media [48, 49].

Chiral Interfaces and Slabs

Silverman, in 1985, examined scattering by an achiral/chiral interface, where the chiral medium was described by either the Condon (Equation (1.2) with $f = 0$) or the Born (Equation (1.6) with $\beta = 0$) forms of the constitutive relationships [50]. Additional research has been done on scattering by achiral/chiral interfaces [51]—[57], chiral/chiral interfaces [58], the interface of mirror-conjugated chiral media [59], and periodic achiral/chiral interfaces [60]. Researchers have also studied scattering by chiral slabs [54, 61] and chiral slabs backed by perfect conductors [62]—[64].

Related research has studied wave propagation along a chiral slab [65]. Creation of an anisotropic chiral slab using slabs of uniaxial media has also been studied [66].

Scattering by Chiral Bodies

Research on scattering by objects composed of chiral media has expanded since the early work by Bohren [20], [42]—[45]. In 1985, Lakhtakia, V. K. Varadan, and V. V. Varadan presented results for scattering by spheroidal objects using the T-matrix method [67]. Later work by Uslenghi extended the spherical problem to a single chiral layer on a sphere with an impedance surface [68]. Related work has been done on the eigenmodes of a perfectly conducting sphere filled with chiral media [69]. Research by the author, presented in Chapter 3, extended the homogeneous circular cylinder studied by Bohren [20] to a multilayer circular chiral cylinder with the center cylinder described by an impedance surface [70]. Additional work by the author, presented in Chapter 4, extended scattering to objects of arbitrary cross-section using the volume equivalence theorem [71, 72]. Numerical results were presented for two-dimensional objects in free space [71, 72] and in the presence of a perfectly conducting half-plane [73]. An alternative approach requiring fewer unknowns has been developed by Rojas [74].

Basic Research

The majority of the early research concentrated on the electromagnetic properties of infinite chiral media [75]—[87] and the Dyadic Green's functions for one, two, and three dimensions [88]—[90]. There is the possibility that this research may be applied to modeling vegetation layers for remote sensing [88]. This research has been applied to antennas radiating in infinite chiral media [91, 92] and in the presence of a chiral sphere [93]. Related research has been done on a point dipole radiating inside a chiral sphere [94]. Surface integral equations have been developed for scattering by perfect electrically conducting bodies in an infinite chiral medium [95].

Construction of Chiral Media

Research into the construction of microwave chiral media has been limited to theoretical studies of scattering by beaded helices [96, 97] and measurements of chiral media constructed with wire helices embedded in a dielectric [61, 98, 99]. Related research has studied the mixing of small chiral bodies in an infinite chiral media [100, 101].

Applied Research

In 1988, an excellent introductory article on chiral media was published by Engheta and Jaggard [102]. Since then, research has expanded into parallel plate waveguides [103], circular waveguides [104]—[109], periodic structures [110], lenses [111], and microstrip antennas on chiral substrates [112, 113].

Chapter 2

Theory

This chapter presents electromagnetics theory for the analysis of the interaction of electromagnetic fields with objects composed of chiral media. Section 2.1 presents the constitutive relationships and basic notation for chiral media. Section 2.2 presents a technique for transforming the coupled wave equations of chiral media into a set of uncoupled wave equations in terms of right and left circularly polarized waves. Section 2.3 presents circular vector potentials which have properties similar to those of the usual magnetic and electric vector potentials, except that they result in circular rather than linearly polarized fields. This property makes them useful for field expansions in chiral media. Section 2.4 presents the volume equivalence theorem for chiral media, which is used in Chapter 4 for a method of moments calculation of scattering by arbitrarily shaped bodies. The volume equivalence theorem is also used in Section 2.5 to develop image theory for a chiral body over a perfectly conducting electric or magnetic ground plane.

2.1 Constitutive Relationships

This section presents the constitutive relationships and notation used in this report. All fields and currents are considered to be time harmonic with the $e^{j\omega t}$ time dependence suppressed. The constitutive relationships for a chiral or an isotropic optically

active medium [6, sec. 8.3] can be written as

$$\mathbf{D} = \epsilon \mathbf{E} - j\xi_c \mathbf{B} \quad (2.1a)$$

$$\mathbf{H} = \frac{1}{\mu} \mathbf{B} - j\xi_c \mathbf{E} \quad (2.1b)$$

where μ is the permeability, ϵ is the permittivity, and the pseudoscalar ξ_c is the chirality admittance of the medium. The medium is lossy if μ , ϵ , or ξ_c are complex. If $\xi_c = 0$, then Equation (2.1) reduces to the constitutive relationships for an isotropic achiral medium. To simplify the following developments, Equation (2.1) can be written as

$$\mathbf{D} = \epsilon_c \mathbf{E} - j\mu\xi_c \mathbf{H} \quad (2.2a)$$

$$\mathbf{B} = \mu \mathbf{H} + j\mu\xi_c \mathbf{E} \quad (2.2b)$$

where the effective permittivity, ϵ_c , of the chiral medium is defined as

$$\epsilon_c = \epsilon + \mu\xi_c^2. \quad (2.3)$$

2.2 Chiral Wave Equation

This section presents the wave equations for chiral media and a technique for transforming the coupled \mathbf{E} and \mathbf{H} wave equations into uncoupled wave equations in terms of right and left circularly polarized waves, which can be solved by the classical approach.

Regardless of the medium, the fields (\mathbf{E} , \mathbf{B} , \mathbf{D} , \mathbf{H}), produced by the impressed electric and magnetic currents (\mathbf{J}^i , \mathbf{M}^i), are related by Maxwell's equations [114],

$$-\nabla \times \mathbf{E} = j\omega \mathbf{B} + \mathbf{M}^i \quad (2.4a)$$

$$\nabla \times \mathbf{H} = j\omega \mathbf{D} + \mathbf{J}^i \quad (2.4b)$$

$$\nabla \cdot \mathbf{D} = \rho \quad (2.4c)$$

$$\nabla \cdot \mathbf{B} = 0 \quad (2.4d)$$

where ρ is the electric charge density given by $\rho = j\nabla \cdot \mathbf{J}/\omega$.

Now consider a chiral medium with constitutive parameters (μ, ϵ, ξ_c) . The fields (\mathbf{E}, \mathbf{H}) produced by $(\mathbf{J}', \mathbf{M}')$ in the chiral medium are obtained by substituting Equation (2.2) into Maxwell's equations resulting in

$$-\nabla \times \mathbf{E} = j\omega\mu\mathbf{H} - \omega\mu\xi_c\mathbf{E} + \mathbf{M}' \quad (2.5a)$$

$$\nabla \times \mathbf{H} = j\omega\epsilon_c\mathbf{E} + \omega\mu\xi_c\mathbf{H} + \mathbf{J}' \quad (2.5b)$$

$$\nabla \cdot \mathbf{E} = \rho/\epsilon \quad (2.5c)$$

$$\nabla \cdot \mathbf{H} = -j\xi_c\rho/\epsilon. \quad (2.5d)$$

Equation (2.5) can be written in matrix form as

$$\nabla \times \begin{pmatrix} \mathbf{E} \\ \mathbf{H} \end{pmatrix} = [K] \begin{pmatrix} \mathbf{E} \\ \mathbf{H} \end{pmatrix} + \begin{pmatrix} -\mathbf{M}' \\ \mathbf{J}' \end{pmatrix} \quad (2.6a)$$

$$\nabla \cdot \begin{pmatrix} \mathbf{E} \\ \mathbf{H} \end{pmatrix} = \frac{\rho}{\epsilon} \begin{pmatrix} 1 \\ -j\xi_c \end{pmatrix} \quad (2.6b)$$

where

$$[K] = \begin{bmatrix} \omega\mu\xi_c & -j\omega\mu \\ j\omega\epsilon_c & \omega\mu\xi_c \end{bmatrix}. \quad (2.7)$$

Using Equation (2.6), the source-free wave equation is

$$\nabla^2 \begin{pmatrix} \mathbf{E} \\ \mathbf{H} \end{pmatrix} + [K]^2 \begin{pmatrix} \mathbf{E} \\ \mathbf{H} \end{pmatrix} = 0. \quad (2.8)$$

Following the work of Bohren [42, 43], although for constitutive relationships different than those used here, the coupling caused by $[K]$ in the wave equation can be removed by diagonalizing $[K]$ such that

$$[K] = [A] \begin{bmatrix} k_R & 0 \\ 0 & -k_L \end{bmatrix} [A]^{-1}. \quad (2.9)$$

Using linear algebra techniques, $[A]$ is found to be

$$[A] = \begin{bmatrix} 1 & 1 \\ j/\eta_c & -j/\eta_c \end{bmatrix} \quad (2.10)$$

with the chiral wave impedance given by

$$\eta_c = \sqrt{\frac{\mu}{\epsilon_c}} \quad (2.11)$$

and the chiral wave numbers given by

$$\left. \begin{array}{l} k_R \\ k_L \end{array} \right\} = \omega \sqrt{\mu \epsilon_c} \pm \omega \mu \xi_c. \quad (2.12)$$

Substituting Equation (2.9) into Equation (2.8) and multiplying through from the left by $[A]^{-1}$ results in

$$[A]^{-1} \nabla^2 \begin{pmatrix} \mathbf{E} \\ \mathbf{H} \end{pmatrix} + \begin{bmatrix} k_R & 0 \\ 0 & -k_L \end{bmatrix}^2 [A]^{-1} \begin{pmatrix} \mathbf{E} \\ \mathbf{H} \end{pmatrix} = 0. \quad (2.13)$$

To simplify Equation (2.13) define

$$[A]^{-1} \begin{pmatrix} \mathbf{E} \\ \mathbf{H} \end{pmatrix} = \begin{pmatrix} \mathbf{E}_R \\ \mathbf{E}_L \end{pmatrix} \quad (2.14)$$

where \mathbf{E}_R and \mathbf{E}_L can be shown to be the electric fields of right and left circularly polarized waves with wave numbers k_R and k_L , respectively [43]. Then, the uncoupled source-free wave equation in chiral media is

$$\nabla^2 \begin{pmatrix} \mathbf{E}_R \\ \mathbf{E}_L \end{pmatrix} + \begin{pmatrix} k_R^2 \mathbf{E}_R \\ k_L^2 \mathbf{E}_L \end{pmatrix} = 0. \quad (2.15)$$

Multiplying Equation (2.14) through from the left by $[A]$ gives

$$\begin{pmatrix} \mathbf{E} \\ \mathbf{H} \end{pmatrix} = \begin{bmatrix} 1 & 1 \\ j/\eta_c & -j/\eta_c \end{bmatrix} \begin{pmatrix} \mathbf{E}_R \\ \mathbf{E}_L \end{pmatrix}. \quad (2.16)$$

Substituting Equation (2.16) into Equation (2.6) results in the uncoupled Maxwell's equations for chiral media

$$\nabla \times \begin{pmatrix} \mathbf{E}_R \\ \mathbf{E}_L \end{pmatrix} = \begin{pmatrix} k_R \mathbf{E}_R \\ -k_L \mathbf{E}_L \end{pmatrix} - \frac{1}{2} \begin{bmatrix} 1 & j\eta_c \\ 1 & -j\eta_c \end{bmatrix} \begin{pmatrix} \mathbf{M} \\ \mathbf{J} \end{pmatrix} \quad (2.17a)$$

$$\nabla \cdot \begin{pmatrix} \mathbf{E}_R \\ \mathbf{E}_L \end{pmatrix} = \frac{\rho}{2\epsilon} \begin{pmatrix} 1 - \eta_c \xi_c \\ 1 + \eta_c \xi_c \end{pmatrix}. \quad (2.17b)$$

From Equation (2.16), the magnetic fields are given by

$$\begin{pmatrix} \mathbf{H}_R \\ \mathbf{H}_L \end{pmatrix} = \frac{j}{\eta_c} \begin{pmatrix} \mathbf{E}_R \\ -\mathbf{E}_L \end{pmatrix}. \quad (2.18)$$

The total electric or magnetic field is the sum of the right and left circularly polarized electric or magnetic fields

$$\mathbf{E} = \mathbf{E}_R + \mathbf{E}_L \quad (2.19a)$$

$$\mathbf{H} = \mathbf{H}_R + \mathbf{H}_L. \quad (2.19b)$$

2.3 Circular Vector Potentials

This section develops the right and left circular vector potentials, which simplify the field expansions for chiral media. These potentials are analogous to the magnetic (\mathbf{A}) and electric (\mathbf{F}) vector potentials. In an homogeneous source-free achiral region the magnetic vector potential \mathbf{A} is obtained by solving the wave equation

$$\nabla^2 \mathbf{A} + k^2 \mathbf{A} = 0 \quad (2.20)$$

where $\nabla \times \mathbf{A} = \mathbf{B}$, $\nabla \cdot \mathbf{A} = -j\omega\mu\epsilon\Phi$, and Φ is the electric scalar potential [115]. However, in an homogeneous source-free chiral region, the corresponding wave equation is

$$\nabla^2 \mathbf{A} + 2\omega\mu\xi_c \nabla \times \mathbf{A} + k^2 \mathbf{A} = 0 \quad (2.21)$$

using the same definitions as used for Equation (2.20) and the constitutive relationships for chiral media. Solutions for equations of this form are known [78, 88]; however, an alternate solution is presented below based on the same method that was used in the previous section to uncouple the wave equation for chiral media.

Following the techniques used for vector wave functions [114, sec. 7.1] the right (\mathbf{R}) and left (\mathbf{L}) circular vector potentials are defined as

$$\mathbf{R} = \hat{\mathbf{a}}\psi(k_R) \quad (2.22a)$$

$$\mathbf{L} = \hat{\mathbf{a}}\psi(k_L) \quad (2.22b)$$

where $\hat{\mathbf{a}}$ is an arbitrary constant unit vector and $\psi(\mathbf{k})$ is a solution of the scalar wave equation

$$\nabla^2\psi(\mathbf{k}) + k^2\psi(\mathbf{k}) = 0. \quad (2.23)$$

From these vector potentials the right and left circularly polarized electric fields are formed using

$$\mathbf{E}_R = \nabla \times \left(\mathbf{R} + \frac{1}{k_R} \nabla \times \mathbf{R} \right) \quad (2.24a)$$

$$\mathbf{E}_L = \nabla \times \left(\mathbf{L} - \frac{1}{k_L} \nabla \times \mathbf{L} \right). \quad (2.24b)$$

The right (or left) circular vector potential component R_y (or L_y) produces a right (or left) circular to y field RC_y (or LC_y), just as the magnetic vector potential component A_y produces a transverse magnetic to y field TM_y .

2.4 Chiral Volume Equivalence Theorem

This section develops the volume equivalence theorem for chiral media [114, sec. 1.6], [115, sec. 3-11], [116], [117], [118, p. 327]. The volume equivalence theorem allows a chiral scatterer to be replaced by free space and equivalent electric and magnetic volume polarization currents (\mathbf{J} , \mathbf{M}). From Maxwell's equations the incident or free space fields, denoted (\mathbf{E}^i , \mathbf{H}^i), of the impressed electric and magnetic currents (\mathbf{J}^i , \mathbf{M}^i) are related by

$$-\nabla \times \mathbf{E}^i = j\omega\mu_0\mathbf{H}^i + \mathbf{M}^i \quad (2.25a)$$

$$\nabla \times \mathbf{H}^i = j\omega\epsilon_0\mathbf{E}^i + \mathbf{J}^i \quad (2.25b)$$

where (μ_0, ϵ_0) are the constitutive parameters of free space.

Now consider an inhomogeneous chiral medium with constitutive parameters (μ, ϵ, ξ_c) . The total fields, denoted (\mathbf{E} , \mathbf{H}), produced by (\mathbf{J}^i , \mathbf{M}^i) in the inhomogeneous chiral medium are given by Equation (2.5) and can be written as

$$-\nabla \times \mathbf{E} = j\omega\mu_0\mathbf{H} + j\omega(\mu - \mu_0)\mathbf{H} - \omega\mu\xi_c\mathbf{E} + \mathbf{M}^i \quad (2.26a)$$

$$\nabla \times \mathbf{H} = j\omega\epsilon_0\mathbf{E} + j\omega(\epsilon_c - \epsilon_0)\mathbf{E} + \omega\mu\xi_c\mathbf{H} + \mathbf{J}^i \quad (2.26b)$$

where $j\omega\mu_0\mathbf{H}$ and $j\omega\epsilon_0\mathbf{E}$ have been added and subtracted from the right hand sides of Equations (2.26a) and (2.26b), respectively, to simplify the next step.

By definition the scattered fields, denoted $(\mathbf{E}^S, \mathbf{H}^S)$, are the difference between the total fields and the incident fields,

$$\mathbf{E}^S = \mathbf{E} - \mathbf{E}^i \quad (2.27a)$$

$$\mathbf{H}^S = \mathbf{H} - \mathbf{H}^i. \quad (2.27b)$$

Subtracting Equation (2.25a) from (2.26a), Equation (2.25b) from (2.26b), and making use of Equation (2.27) yields

$$-\nabla \times \mathbf{F}^S = j\omega\mu_0\mathbf{H}^S + [j\omega(\mu - \mu_0)\mathbf{H} - \omega\mu\xi_c\mathbf{E}]. \quad (2.28a)$$

$$\nabla \times \mathbf{H}^S = j\omega\epsilon_0\mathbf{E}^S + [j\omega(\epsilon_c - \epsilon_0)\mathbf{E} + \omega\mu\xi_c\mathbf{H}] \quad (2.28b)$$

By comparing Equation (2.28a) to (2.25a) and Equation (2.28b) to (2.25b), it can be seen that the scattered fields appear to be produced by the equivalent electric and magnetic volume polarization currents

$$\mathbf{J} = j\omega(\epsilon_c - \epsilon_0)\mathbf{E} + \omega\mu\xi_c\mathbf{H} \quad (2.29a)$$

$$\mathbf{M} = j\omega(\mu - \mu_0)\mathbf{H} - \omega\mu\xi_c\mathbf{E} \quad (2.29b)$$

radiating in free space. Note that (\mathbf{J}, \mathbf{M}) are nonzero only where the parameters of the inhomogeneous chiral medium differ from those of free space.

2.5 Image Theory for Chiral Media

This section develops image theory for a chiral body over an infinite perfectly conducting electric or magnetic ground plane [119]. Image theory defines an equivalent problem for currents and material bodies over an infinite ground plane, in which the ground plane is removed and replaced by the image of the currents and material bodies.

A chiral medium was originally defined as *consisting of macroscopic chiral objects randomly embedded in a dielectric* [1]. From this definition, the image of a material body consisting of chiral media does not have the same material parameters as the original body, since the image body consists of macroscopic chiral objects of the opposite handedness.

The chiral volume equivalence theorem, developed in Section 2.4, is used to replace the chiral body by free space and equivalent electric and magnetic currents. Next, conventional image theory is used to replace the ground plane by conventional image currents. Finally, the chiral volume equivalence theorem is used to replace the image currents by the image of the original chiral body.

Figure 2.1(a) shows the original problem consisting of the impressed currents $(\mathbf{J}^i, \mathbf{M}^i)$ producing the total fields (\mathbf{E}, \mathbf{H}) in the presence of a chiral body with material parameters (μ, ϵ, ξ_c) over an infinite perfectly conducting electric ground plane at $y = 0$. For simplicity, the ambient medium is considered to be free space with material parameters (μ_0, ϵ_0) . In Figure 2.1(b), the chiral volume equivalence theorem is used to replace the chiral body by free space and the equivalent electric and magnetic volume polarization currents given by Equation (2.29).

In Figure 2.1(d), conventional image theory for currents is used to replace the ground plane by $(\mathbf{J}^{\prime\prime}, \mathbf{M}^{\prime\prime})$, the image of the impressed currents, and $(\mathbf{J}^{\prime}, \mathbf{M}^{\prime})$, the image of the equivalent currents, which are related to the total fields (\mathbf{E}, \mathbf{H}) in the upper half space by

$$J'_{H,V}(\mathbf{x}, -y, z) = \mp j\omega(\epsilon_c - \epsilon_0)E_{H,V}(\mathbf{x}, y, z) \mp \omega\mu\xi_c H_{H,V}(\mathbf{x}, y, z) \quad (2.30a)$$

$$M'_{H,V}(\mathbf{x}, -y, z) = \pm j\omega(\mu - \mu_0)H_{H,V}(\mathbf{x}, y, z) \mp \omega\mu\xi_c E_{H,V}(\mathbf{x}, y, z) \quad (2.30b)$$

where the subscripts H and V refer to the horizontal (\hat{x}, \hat{z}) and vertical (\hat{y}) vector components, respectively. The image fields below $y = 0$ are given by

$$E'_{H,V}(\mathbf{x}, -y, z) = \mp E_{H,V}(\mathbf{x}, y, z) \quad (2.31a)$$

$$H'_{H,V}(\mathbf{x}, -y, z) = \pm H_{H,V}(\mathbf{x}, y, z) \quad (2.31b)$$

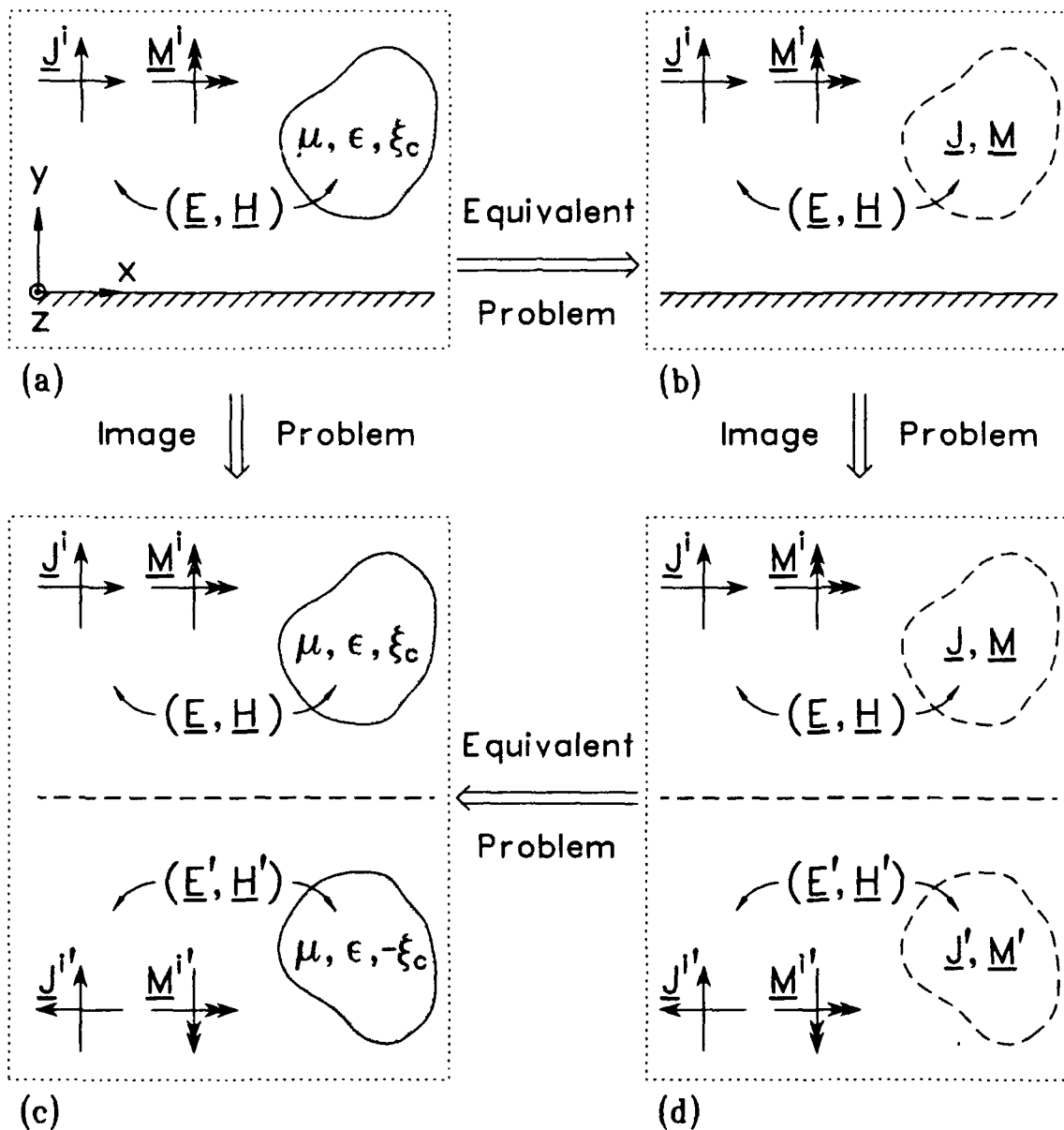


Figure 2.1: Image theory for a chiral body over a perfect electric conductor derived using the chiral volume equivalence theorem and conventional image theory for currents.

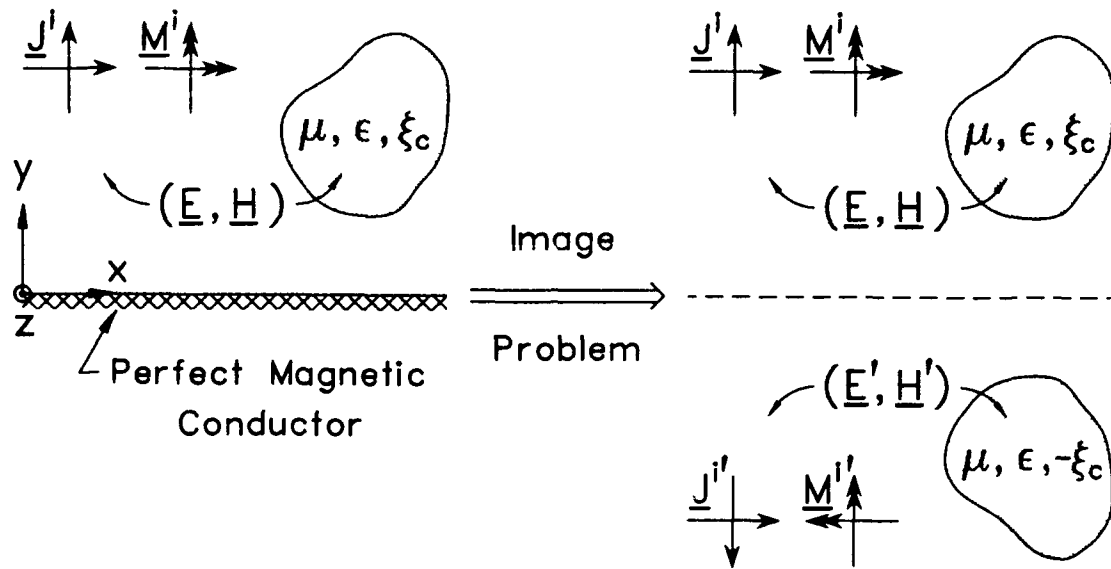


Figure 2.2: Image theory for a chiral body over a perfect magnetic conductor.

Combining Equation (2.30) and Equation (2.31), $(\mathbf{J}', \mathbf{M}')$ are related to $(\mathbf{E}', \mathbf{H}')$ in the lower half space by

$$\mathbf{J}'(x, -y, z) = j\omega(\epsilon_c - \epsilon_0)\mathbf{E}'(x, -y, z) - \omega\mu\xi_c\mathbf{H}'(x, -y, z) \quad (2.32a)$$

$$\mathbf{M}'(x, -y, z) = j\omega(\mu - \mu_0)\mathbf{H}'(x, -y, z) + \omega\mu\xi_c\mathbf{E}'(x, -y, z). \quad (2.32b)$$

Finally, comparing Equation (2.29) with Equation (2.32) shows that the image of the chiral body has material parameters of $(\mu, \epsilon, -\xi_c)$, as shown in Figure 2.1(c). Similarly, as illustrated in Figure 2.2, the image of a chiral body over a perfectly conducting magnetic ground plane also has material parameters of $(\mu, \epsilon, -\xi_c)$.

This section has developed image theory for a chiral body over an infinite perfectly conducting electric or magnetic ground plane. In both cases it was shown that the image of a chiral body has the same material parameters as the original body, except that the chirality admittance of the image is the negative of the original. In essence the mirror image of a chiral object is that object, such as a helix, with the opposite handedness.

Alternatively, the same results can be obtained using tensor analysis and the fact that ξ_c is a pseudoscalar (pseudotensor of rank zero). Pseudoscalars, unlike scalars (tensors of rank zero), are not invariant with respect to coordinate transformations. The image of the chiral body is obtained by spatial inversion, an improper coordinate transformation, which introduces the sign change [6, sec. 2.6, 6.2, 8.3], [19, pg. 813].

Chapter 3

Scattering by a Multilayer Cylinder

This chapter presents an efficient recursive eigenfunction solution for scattering by a multilayer circular chiral cylinder, with or without a surface impedance center cylinder, for transverse magnetic (TM) and transverse electric (TE) normal incidence plane waves, as shown in Figure 3.1. The special cases of zero or infinite surface impedance correspond to a perfect electric or magnetic conducting center cylinder, respectively.

The solution for scattering by an M layer chiral cylinder requires finding an eigenfunction expansion in each layer, then matching continuity of tangential electric and magnetic fields at the M interfaces. The $M = 1$ or homogeneous cylinder has been analyzed by Bohren [20]. In that case, solving directly for the four unknown coefficients is manageable. However, if even one more layer is added the coefficients in the eigenfunction expansion are algebraically complex and unwieldy to find. This can be seen in Appendix A, which presents an eigenfunction solution for scattering by a perfectly conducting cylinder coated by a single homogeneous layer of chiral media. An alternate technique is to set up and numerically solve a $4M \times 4M$ matrix equation which enforces boundary conditions at the M interfaces. To avoid the computer CPU time and storage associated with large matrix equations, here we generalize Richmond's method [120, 121] to apply to multilayer circular chiral

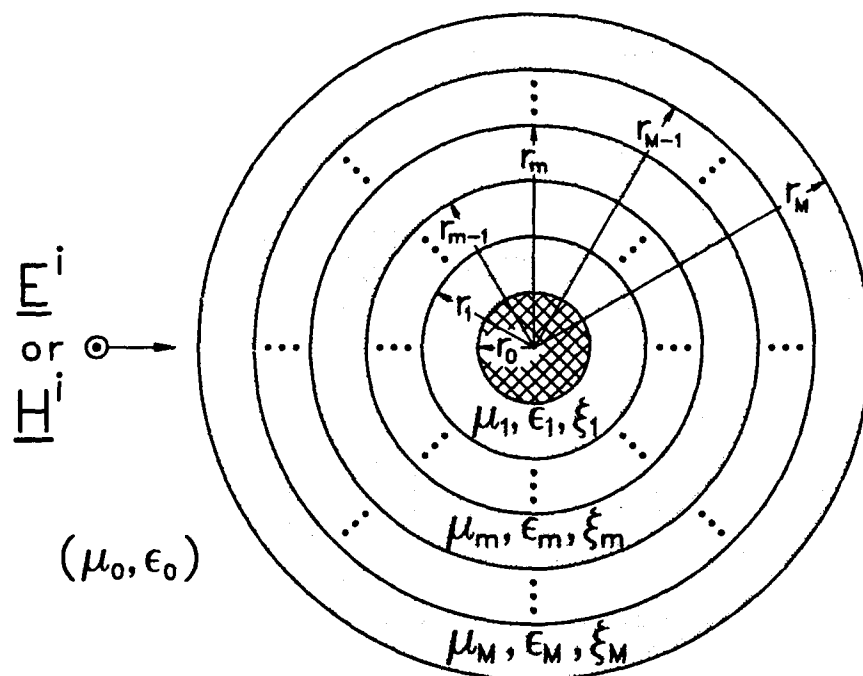


Figure 3.1: Geometry of a general multilayer circular chiral cylinder with a surface impedance center cylinder.

cylinders. The present technique requires the multiplication of M 4×4 matrices to determine the coefficients in the eigenfunction expansion. The difference between the solutions for TM and TE incident plane waves is extremely simple, differing by only a plus/minus sign at one step in the solution. Further, the addition of a surface impedance center cylinder involves only one additional matrix multiplication.

3.1 The Eigenfunction Expansion

In this section, the eigenfunction expansion for a general multilayer circular chiral cylinder, with or without a surface impedance center cylinder, is presented by expanding the electric and magnetic fields in terms of right and left circularly polarized waves using the notation presented in Section 2.2. The geometry of the cylinder is shown in Figure 3.1, where the constitutive parameters and the outer radius of layer m are $(\mu_m, \epsilon_m, \xi_m)$ and r_m , where $m = 1, 2, \dots, M$. The right and left wave numbers of the m th layer, k_R^m and k_L^m , and the wave impedance, η_m , are defined by Equations (2.12) and (2.11). Note that $m = 1$ is the innermost material layer and $m = M$ is the outermost material layer. The outer radius of the impenetrable surface impedance center cylinder, when included, is denoted r_0 . The external medium is free space, with parameters (μ_0, ϵ_0) , wave number $k_0 = \omega\sqrt{\mu_0\epsilon_0}$, and characteristic impedance $\eta_0 = \sqrt{\mu_0/\epsilon_0}$.

First, consider the fields external to the cylinder. These fields may be expanded as an infinite sum of vector wave functions, \mathbf{M}_n and \mathbf{N}_n , which are related by [114, sec. 7.1]:

$$\nabla \times \mathbf{N}_n = k\mathbf{M}_n \quad (3.1a)$$

$$\nabla \times \mathbf{M}_n = k\mathbf{N}_n. \quad (3.1b)$$

These vector wave functions are solutions to $\nabla \times \nabla \times \mathbf{C} - k^2\mathbf{C} = 0$ and $\nabla \cdot \mathbf{C} = 0$, where $\mathbf{C} = \mathbf{M}_n$ or \mathbf{N}_n . In cylindrical coordinates, they may be written as

$$\mathbf{N}_n^{(p)}(\mathbf{k}) = \hat{\mathbf{z}}e^{jn\phi}Z_n^{(p)}(k\rho) \quad (3.2a)$$

$$\mathbf{M}_n^{(p)}(\mathbf{k}) = \hat{\rho} \frac{j^n}{k\rho} e^{jn\phi} Z_n^{(p)}(k\rho) - \hat{\phi} e^{jn\phi} Z_n^{(p)'}(k\rho) \quad (3.2b)$$

where $Z_n^{(p)}$ is a Bessel function of type p ($Z_n^{(1)} = J_n$, $Z_n^{(2)} = Y_n$, $Z_n^{(3)} = H_n^{(1)}$, $Z_n^{(4)} = H_n^{(2)}$) and the prime indicates the derivative with respect to the argument.

In the case of a TM_Z plane wave normally incident from $\phi = 180^\circ$, the incident fields may be written as [115, sec. 5-8]

$$\mathbf{E}^i = \hat{z} e^{-jk_0 x} = \sum_{n=-\infty}^{\infty} j^{-n} \mathbf{N}_n^{(1)}(k_0) \quad (3.3a)$$

$$\mathbf{H}^i = -\hat{y} \frac{1}{\eta_0} e^{-jk_0 x} = \frac{j}{\eta_0} \sum_{n=-\infty}^{\infty} j^{-n} \mathbf{M}_n^{(1)}(k_0) \quad (3.3b)$$

where Equation (3.3b) is obtained from Equation (3.3a) using $\mathbf{H} = \frac{j}{\omega\mu} \nabla \times \mathbf{E}$ and $\nabla \times \mathbf{N}_n = \frac{\omega\mu}{\eta} \mathbf{M}_n$. For the TE_Z case, to maintain the symmetry of the solution, the incident fields are

$$\mathbf{E}^i = \hat{y} j e^{-jk_0 x} = \sum_{n=-\infty}^{\infty} j^{-n} \mathbf{M}_n^{(1)}(k_0) \quad (3.4a)$$

$$\mathbf{H}^i = \hat{z} \frac{j}{\eta_0} e^{-jk_0 x} = \frac{j}{\eta_0} \sum_{n=-\infty}^{\infty} j^{-n} \mathbf{N}_n^{(1)}(k_0). \quad (3.4b)$$

Due to the chiral cylinder the scattered fields will have TM_Z and TE_Z components; therefore, the scattered fields are expanded as

$$\mathbf{E}^S = \sum_{n=-\infty}^{\infty} j^{-n} [a_n \mathbf{N}_n^{(1)}(k_0) + b_n \mathbf{M}_n^{(1)}(k_0)] \quad (3.5a)$$

$$\mathbf{H}^S = \frac{j}{\eta_0} \sum_{n=-\infty}^{\infty} j^{-n} [a_n \mathbf{M}_n^{(1)}(k_0) + b_n \mathbf{N}_n^{(1)}(k_0)]. \quad (3.5b)$$

In the chiral cylinder, the eigenfunction expansion must account for the rotation of polarization inherent to chiral media. In a z -independent problem, this results in a coupling between the TM_Z and TE_Z fields, which prevents the eigenfunction expansion from being written as a simple superposition of TM_Z and TE_Z fields, as was done in Equation (3.5) for the scattered fields in the free space region. However, the eigenfunction expansion can be written as a superposition of right and left

circularly polarized fields. This is done by combining the vector wave functions, \mathbf{M}_n and \mathbf{N}_n , to form right and left circularly polarized vector wave functions [20]

$$\mathbf{E}_{R,n}^{(p)} = \mathbf{M}_n^{(p)}(\mathbf{k}_R) + \mathbf{N}_n^{(p)}(\mathbf{k}_R) \quad (3.6a)$$

$$\mathbf{E}_{L,n}^{(p)} = \mathbf{M}_n^{(p)}(\mathbf{k}_L) - \mathbf{N}_n^{(p)}(\mathbf{k}_L) \quad (3.6b)$$

which satisfy the vector wave equation (2.15) and Maxwell's equations (2.17a) and (2.17b) in a source-free chiral region. Then, the fields in layer m of the chiral cylinder may be represented as

$$\mathbf{E}^m = \sum_{n=-\infty}^{\infty} j^{-n} \left[c_n^m \mathbf{E}_{R,n}^{(1)} + d_n^m \mathbf{E}_{L,n}^{(1)} + f_n^m \mathbf{E}_{R,n}^{(4)} + g_n^m \mathbf{E}_{L,n}^{(4)} \right] \quad (3.7a)$$

$$\mathbf{H}^m = \frac{j}{\eta_m} \sum_{n=-\infty}^{\infty} j^{-n} \left[c_n^m \mathbf{E}_{R,n}^{(1)} - d_n^m \mathbf{E}_{L,n}^{(1)} + f_n^m \mathbf{E}_{R,n}^{(4)} - g_n^m \mathbf{E}_{L,n}^{(4)} \right] \quad (3.7b)$$

where the c_n^m , d_n^m , f_n^m , and g_n^m are unknown coefficients and Equation (3.7b) is obtained from Equation (3.7a) using Equation (2.18) of Section 2.2. Note that the fields in each layer of the chiral cylinder are expanded in terms of inward $\mathbf{E}^{(1)}$ and outward $\mathbf{E}^{(4)}$ propagating right \mathbf{E}_R and left \mathbf{E}_L circularly polarized waves, thus requiring four coefficients per layer.

Expanding Equation (3.7) to get an explicit representation for the field components in each layer produces:

$$E_z^m = \sum_{n=-\infty}^{\infty} j^{-n} \left[c_n^m J_n(k_R^m \rho) - d_n^m J_n(k_L^m \rho) + f_n^m H_n^{(2)}(k_R^m \rho) - g_n^m H_n^{(2)}(k_L^m \rho) \right] e^{jn\phi} \quad (3.8a)$$

$$H_z^m = \frac{j}{\eta_m} \sum_{n=-\infty}^{\infty} j^{-n} \left[c_n^m J_n(k_R^m \rho) + d_n^m J_n(k_L^m \rho) + f_n^m H_n^{(2)}(k_R^m \rho) + g_n^m H_n^{(2)}(k_L^m \rho) \right] e^{jn\phi} \quad (3.8b)$$

$$E_\phi^m = - \sum_{n=-\infty}^{\infty} j^{-n} \left[c_n^m J_n'(k_R^m \rho) + d_n^m J_n'(k_L^m \rho) + f_n^m H_n^{(2)'}(k_R^m \rho) + g_n^m H_n^{(2)'}(k_L^m \rho) \right] e^{jn\phi} \quad (3.8c)$$

$$H_\phi^m = \frac{-j}{\eta_m} \sum_{n=-\infty}^{\infty} j^{-n} \left[c_n^m J_n'(k_R^m \rho) - d_n^m J_n'(k_L^m \rho) \right] e^{jn\phi}$$

$$+ f_n^m H_n^{(2)'}(k_R^m \rho) - g_n^m H_n^{(2)'}(k_L^m \rho) \Big] e^{jn\phi} \quad (3.8d)$$

$$E_\rho^m = \frac{j}{\rho} \sum_{n=-\infty}^{\infty} j^{-n} \left[\frac{c_n^m}{k_R^m} J_n(k_R^m \rho) + \frac{d_n^m}{k_L^m} J_n(k_L^m \rho) \right. \\ \left. + \frac{f_n^m}{k_R^m} H_n^{(2)}(k_R^m \rho) + \frac{g_n^m}{k_L^m} H_n^{(2)}(k_L^m \rho) \right] n e^{jn\phi} \quad (3.8e)$$

$$H_\rho^m = \frac{-1}{\eta_m \rho} \sum_{n=-\infty}^{\infty} j^{-n} \left[\frac{c_n^m}{k_R^m} J_n(k_R^m \rho) - \frac{d_n^m}{k_L^m} J_n(k_L^m \rho) \right. \\ \left. + \frac{f_n^m}{k_R^m} H_n^{(2)}(k_R^m \rho) - \frac{g_n^m}{k_L^m} H_n^{(2)}(k_L^m \rho) \right] n e^{jn\phi}. \quad (3.8f)$$

3.2 Determining the Coefficients

This section presents a recursive technique for determining the coefficients of the eigenfunction expansions presented in the previous section. These unknowns include c_n^m , d_n^m , f_n^m , and g_n^m in each of the M layers as well as the a_n and b_n from Equation (3.5). This technique is a generalization of that developed by Richmond for achiral multilayer circular dielectric/ferrite cylinders [120, 121]. The unknown coefficients are determined by applying the boundary conditions of continuous tangential electric and magnetic fields at the boundary of each layer, which can be written as

$$E_z^{m+1} = E_z^m \quad (3.9a)$$

$$E_\phi^{m+1} = E_\phi^m \quad (3.9b)$$

$$H_z^{m+1} = H_z^m \quad (3.9c)$$

$$H_\phi^{m+1} = H_\phi^m. \quad (3.9d)$$

Using Equation (3.8), the boundary conditions can be expressed as

$$[Z^{m+1}] \begin{bmatrix} c_n^{m+1} \\ d_n^{m+1} \\ f_n^{m+1} \\ g_n^{m+1} \end{bmatrix} = [Z^m] \begin{bmatrix} c_n^m \\ d_n^m \\ f_n^m \\ g_n^m \end{bmatrix} \quad (3.10)$$

where

$$[Z^m] = \begin{bmatrix} J_n(k_R^m \rho) & -J_n(k_L^m \rho) & H_n^{(2)}(k_R^m \rho) & -H_n^{(2)}(k_L^m \rho) \\ J_n'(k_R^m \rho) & J_n'(k_L^m \rho) & H_n^{(2)'}(k_R^m \rho) & H_n^{(2)'}(k_L^m \rho) \\ \frac{1}{\eta_m} J_n(k_R^m \rho) & \frac{1}{\eta_m} J_n(k_L^m \rho) & \frac{1}{\eta_m} H_n^{(2)}(k_R^m \rho) & \frac{1}{\eta_m} H_n^{(2)}(k_L^m \rho) \\ \frac{1}{\eta_m} J_n'(k_R^m \rho) & -\frac{1}{\eta_m} J_n'(k_L^m \rho) & \frac{1}{\eta_m} H_n^{(2)'}(k_R^m \rho) & -\frac{1}{\eta_m} H_n^{(2)'}(k_L^m \rho) \end{bmatrix}. \quad (3.11)$$

The resulting relationship between the coefficients for layers m and $m+1$ can be represented in matrix form by

$$\begin{bmatrix} c_n^{m+1} \\ d_n^{m+1} \\ f_n^{m+1} \\ g_n^{m+1} \end{bmatrix} = [Y^m] \begin{bmatrix} c_n^m \\ d_n^m \\ f_n^m \\ g_n^m \end{bmatrix} \quad (3.12)$$

where

$$[Y^m] = [Z^{m+1}]^{-1} [Z^m]. \quad (3.13)$$

After simplification¹ the matrix $[Y^m]$ is given by

$$[Y^m] = \begin{bmatrix} U_n^{(1,4)}(R) & X_n^{(1,4)}(L, R) & U_n^{(4,4)}(R) & X_n^{(4,4)}(L, R) \\ X_n^{(1,4)}(R, L) & U_n^{(1,4)}(L) & X_n^{(4,4)}(R, L) & U_n^{(4,4)}(L) \\ -U_n^{(1,1)}(R) & -X_n^{(1,1)}(L, R) & -U_n^{(4,1)}(R) & -X_n^{(4,1)}(L, R) \\ -X_n^{(1,1)}(R, L) & -U_n^{(1,1)}(L) & -X_n^{(4,1)}(R, L) & -U_n^{(4,1)}(L) \end{bmatrix} \quad (3.14)$$

¹The symbolic algebra program MACSYMATM supplied by Symbolics, Inc. of Cambridge, Mass. greatly aided in this simplification.

where

$$U_n^{(p,q)}(S) = j \frac{\pi k_S^{m+1} r_m}{4} \left[\frac{\eta_{m+1}}{\eta_m} + 1 \right] \cdot \left[Z_n^{(p)}(k_S^m r_m) Z_n^{(q)'}(k_S^{m+1} r_m) - Z_n^{(p)'}(k_S^m r_m) Z_n^{(q)}(k_S^{m+1} r_m) \right] \quad (3.15a)$$

$$X_n^{(p,q)}(S, T) = j \frac{\pi k_T^{m+1} r_m}{4} \left[\frac{\eta_{m+1}}{\eta_m} - 1 \right] \cdot \left[Z_n^{(p)}(k_S^m r_m) Z_n^{(q)'}(k_T^{m+1} r_m) + Z_n^{(p)'}(k_S^m r_m) Z_n^{(q)}(k_T^{m+1} r_m) \right] \quad (3.15b)$$

and S, T are L or R .

3.2.1 Perfectly Conducting Center Cylinder

If the innermost cylinder is a perfect electrical conductor, the boundary condition of zero tangential electric fields at $\rho = r_0$ can be written in matrix form as

$$\begin{aligned} \begin{bmatrix} H_n^{(2)}(k_R^1 r_0) & -H_n^{(2)}(k_L^1 r_0) \\ H_n^{(2)'}(k_R^1 r_0) & H_n^{(2)'}(k_L^1 r_0) \end{bmatrix} \begin{bmatrix} f_n^1 \\ g_n^1 \end{bmatrix} \\ = \begin{bmatrix} -J_n(k_R^1 r_0) & J_n(k_L^1 r_0) \\ -J_n'(k_R^1 r_0) & -J_n'(k_L^1 r_0) \end{bmatrix} \begin{bmatrix} c_n^1 \\ d_n^1 \end{bmatrix} \end{aligned} \quad (3.16)$$

using Equations (3.8a) and (3.8c).

Solving Equation (3.16) for f_n^1 and g_n^1 in terms of c_n^1 and d_n^1 produces

$$\begin{bmatrix} f_n^1 \\ g_n^1 \end{bmatrix} = \begin{bmatrix} Y_{31}^0 & Y_{32}^0 \\ Y_{41}^0 & Y_{42}^0 \end{bmatrix} \begin{bmatrix} c_n^1 \\ d_n^1 \end{bmatrix} \quad (3.17)$$

where

$$Y_{31}^0 = -\frac{1}{\Delta_n} \left[J_n(k_R^1 r_0) H_n^{(2)'}(k_L^1 r_0) + J_n'(k_R^1 r_0) H_n^{(2)}(k_L^1 r_0) \right] \quad (3.18a)$$

$$Y_{32}^0 = \frac{-2j}{\pi k_L^1 r_0 \Delta_n} \quad (3.18b)$$

$$Y_{41}^0 = \frac{-2j}{\pi k_R^1 r_0 \Delta_n} \quad (3.18c)$$

$$Y_{42}^0 = -\frac{1}{\Delta_n} \left[J_n(k_L^1 r_0) H_n^{(2)'}(k_R^1 r_0) + J_n'(k_L^1 r_0) H_n^{(2)}(k_R^1 r_0) \right] \quad (3.18d)$$

and

$$\Delta_n = H_n^{(2)}(k_R^1 r_0) H_n^{(2)'}(k_L^1 r_0) + H_n^{(2)'}(k_R^1 r_0) H_n^{(2)}(k_L^1 r_0). \quad (3.19)$$

To define a $[Y^0]$ that can be used with Equation (3.12), Equation (3.17) can be written as

$$\begin{bmatrix} c_n^1 \\ d_n^1 \\ f_n^1 \\ g_n^1 \end{bmatrix} = [Y^0] \begin{bmatrix} c_n^1 \\ d_n^1 \\ 0 \\ 0 \end{bmatrix} \quad (3.20)$$

where

$$[Y^0] = \begin{bmatrix} 1 & 0 & 0 & 0 \\ 0 & 1 & 0 & 0 \\ Y_{31}^0 & Y_{32}^0 & 0 & 0 \\ Y_{41}^0 & Y_{42}^0 & 0 & 0 \end{bmatrix}. \quad (3.21)$$

3.2.2 Surface Impedance Center Cylinder

If the innermost cylinder is described by TM and TE surface impedances the boundary conditions at $\rho = r_0$ are given by [122]

$$Z_{TE} = -\frac{E_\phi^1}{H_z^1} \quad (3.22a)$$

$$Z_{TM} = \frac{E_z^1}{H_\phi^1} \quad (3.22b)$$

where the perfect electric conductor in Section 3.2.1 is the special case of $Z_{TE} = 0$ and $Z_{TM} = 0$.

Using Equation (3.8) these boundary conditions can be expressed as

$$Z_{TE} \frac{j}{\eta_1} \left[c_n^1 J_n(k_R^1 r_0) + d_n^1 J_n(k_L^1 r_0) + f_n^1 H_n^{(2)}(k_R^1 r_0) + g_n^1 H_n^{(2)}(k_L^1 r_0) \right] = \left[c_n^1 J_n'(k_R^1 r_0) + d_n^1 J_n'(k_L^1 r_0) + f_n^1 H_n^{(2)'}(k_R^1 r_0) + g_n^1 H_n^{(2)'}(k_L^1 r_0) \right] \quad (3.23a)$$

$$-Z_{TM} \frac{j}{\eta_1} \left[c_n^1 J_n'(k_R^1 r_0) - d_n^1 J_n'(k_L^1 r_0) + f_n^1 H_n^{(2)'}(k_R^1 r_0) - g_n^1 H_n^{(2)'}(k_L^1 r_0) \right] = \left[c_n^1 J_n(k_R^1 r_0) - d_n^1 J_n(k_L^1 r_0) + f_n^1 H_n^{(2)}(k_R^1 r_0) - g_n^1 H_n^{(2)}(k_L^1 r_0) \right]. \quad (3.23b)$$

As in Equation (3.16), the relationship between the inward and outward propagating waves in region 1 can be obtained by relating f_n^1 and g_n^1 to c_n^1 and d_n^1 by writing Equation (3.23) in matrix form as

$$\begin{aligned} & \begin{bmatrix} Z_{TE} \frac{j}{\eta_1} H_n^{(2)}(k_R^1 r_0) - H_n^{(2)'}(k_R^1 r_0) & Z_{TE} \frac{j}{\eta_1} H_n^{(2)}(k_L^1 r_0) - H_n^{(2)'}(k_L^1 r_0) \\ -Z_{TM} \frac{j}{\eta_1} H_n^{(2)'}(k_R^1 r_0) - H_n^{(2)}(k_R^1 r_0) & Z_{TM} \frac{j}{\eta_1} H_n^{(2)'}(k_L^1 r_0) + H_n^{(2)}(k_L^1 r_0) \end{bmatrix} \begin{bmatrix} f_n^1 \\ g_n^1 \end{bmatrix} \\ &= \begin{bmatrix} J_n'(k_R^1 r_0) - Z_{TE} \frac{j}{\eta_1} J_n(k_R^1 r_0) & J_n'(k_L^1 r_0) - Z_{TE} \frac{j}{\eta_1} J_n(k_L^1 r_0) \\ J_n(k_R^1 r_0) + Z_{TM} \frac{j}{\eta_1} J_n'(k_R^1 r_0) & -J_n(k_L^1 r_0) - Z_{TM} \frac{j}{\eta_1} J_n'(k_L^1 r_0) \end{bmatrix} \begin{bmatrix} c_n^1 \\ d_n^1 \end{bmatrix}. \end{aligned} \quad (3.24)$$

Solving Equation (3.24) for f_n^1 and g_n^1 , as was done for Equation (3.16), results in $[Y^0]$ matrix elements given by

$$\begin{aligned} Y_{31}^0 &= -\frac{J_n(k_R^1 r_0) H_n^{(2)'}(k_L^1 r_0) + J_n'(k_R^1 r_0) H_n^{(2)}(k_L^1 r_0)}{\Delta_n} \left(1 + \frac{Z_{TE} Z_{TM}}{\eta_1^2} \right) \\ &\quad + \frac{2j}{\eta_1 \Delta_n} \left[Z_{TE} J_n(k_R^1 r_0) H_n^{(2)}(k_L^1 r_0) - Z_{TM} J_n'(k_R^1 r_0) H_n^{(2)'}(k_L^1 r_0) \right] \end{aligned} \quad (3.25a)$$

$$Y_{32}^0 = -\left(1 - \frac{Z_{TE} Z_{TM}}{\eta_1^2} \right) \frac{2j}{\pi k_L^1 r_0 \Delta_n} \quad (3.25b)$$

$$Y_{41}^0 = -\left(1 - \frac{Z_{TE} Z_{TM}}{\eta_1^2} \right) \frac{2j}{\pi k_R^1 r_0 \Delta_n} \quad (3.25c)$$

$$\begin{aligned} Y_{42}^0 &= -\frac{J_n(k_L^1 r_0) H_n^{(2)'}(k_R^1 r_0) + J_n'(k_L^1 r_0) H_n^{(2)}(k_R^1 r_0)}{\Delta_n} \left(1 + \frac{Z_{TE} Z_{TM}}{\eta_1^2} \right) \\ &\quad + \frac{2j}{\eta_1 \Delta_n} \left[Z_{TE} J_n(k_L^1 r_0) H_n^{(2)}(k_R^1 r_0) - Z_{TM} J_n'(k_L^1 r_0) H_n^{(2)'}(k_R^1 r_0) \right] \end{aligned} \quad (3.25d)$$

where

$$\begin{aligned} \Delta_n &= \left[H_n^{(2)}(k_R^1 r_0) H_n^{(2)'}(k_L^1 r_0) + H_n^{(2)'}(k_R^1 r_0) H_n^{(2)}(k_L^1 r_0) \right] \left(1 + \frac{Z_{TE} Z_{TM}}{\eta_1^2} \right) \\ &\quad - \frac{2j}{\eta_1} \left[Z_{TE} H_n^{(2)}(k_R^1 r_0) H_n^{(2)}(k_L^1 r_0) - Z_{TM} H_n^{(2)'}(k_R^1 r_0) H_n^{(2)'}(k_L^1 r_0) \right]. \end{aligned} \quad (3.26)$$

A perfect magnetic conducting center cylinder is the special case of the surface impedance boundary condition where $Z_{TE} = Z_{TM} \rightarrow \infty$.

3.2.3 Material Center Cylinder

If there is no center impenetrable cylinder, i.e., region 1 extends to the origin, then the requirement of finite fields at the origin forces $f_n^1 = g_n^1 = 0$, i.e., no outward propagating waves in region 1. To use the same formulation as in Equation (3.20), define $[Y^0]$ by

$$[Y^0] = \begin{bmatrix} 1 & 0 & 0 & 0 \\ 0 & 1 & 0 & 0 \\ 0 & 0 & 0 & 0 \\ 0 & 0 & 0 & 0 \end{bmatrix}. \quad (3.27)$$

3.2.4 Exterior Region

By defining the exterior region to be layer $M + 1$, the relationship between the coefficients for layers 1 and $M + 1$ is given by

$$\begin{bmatrix} c_n^{M+1} \\ d_n^{M+1} \\ f_n^{M+1} \\ g_n^{M+1} \end{bmatrix} = \begin{bmatrix} X_{11} & X_{12} & X_{13} & X_{14} \\ X_{21} & X_{22} & X_{23} & X_{24} \\ X_{31} & X_{32} & X_{33} & X_{34} \\ X_{41} & X_{42} & X_{43} & X_{44} \end{bmatrix} \begin{bmatrix} c_n^1 \\ d_n^1 \\ 0 \\ 0 \end{bmatrix} \quad (3.28)$$

where the matrix $[X]$ is given by

$$[X] = [Y^M] [Y^{M-1}] \dots [Y^2] [Y^1] [Y^0]. \quad (3.29)$$

Note that Equation (3.28) applies for chiral cylinders with or without a surface impedance center cylinder by the proper choice of $[Y^0]$. Requiring the different representations for fields in the exterior region to be equal, i.e., $\mathbf{E}^i + \mathbf{E}^S = \mathbf{E}^{M+1}$ and $\mathbf{H}^i + \mathbf{H}^S = \mathbf{H}^{M+1}$, results in the following relationships between (a_n, b_n) and $(c_n^{M+1}, d_n^{M+1}, f_n^{M+1}, g_n^{M+1})$:

$$\begin{aligned} \overbrace{J_n(k_0\rho)}^{TM} + a_n H_n^{(2)}(k_0\rho) &= (c_n^{M+1} - d_n^{M+1}) J_n(k_0\rho) \\ &\quad + (f_n^{M+1} - g_n^{M+1}) H_n^{(2)}(k_0\rho) \end{aligned} \quad (3.30a)$$

$$\overbrace{J'_n(k_0\rho)}^{TE} + b_n H_n^{(2)'}(k_0\rho) = (c_n^{M+1} + d_n^{M+1}) J'_n(k_0\rho) + (f_n^{M+1} + g_n^{M+1}) H_n^{(2)'}(k_0\rho) \quad (3.30b)$$

$$\overbrace{J_n(k_0\rho)}^{TE} + b_n H_n^{(2)}(k_0\rho) = (c_n^{M+1} + d_n^{M+1}) J_n(k_0\rho) + (f_n^{M+1} + g_n^{M+1}) H_n^{(2)}(k_0\rho) \quad (3.30c)$$

$$\overbrace{J'_n(k_0\rho)}^{TM} + a_n H_n^{(2)'}(k_0\rho) = (c_n^{M+1} - d_n^{M+1}) J'_n(k_0\rho) + (f_n^{M+1} - g_n^{M+1}) H_n^{(2)'}(k_0\rho) \quad (3.30d)$$

where the $\overbrace{\quad}^{TM}$ and $\overbrace{\quad}^{TE}$ indicate terms that are nonzero for TM_Z and TE_Z incident fields, respectively. From Equation (3.30) the coefficients c_n^{M+1} and d_n^{M+1} are given by

$$c_n^{M+1} = \frac{1}{2} \quad (3.31a)$$

$$-d_n^{M+1} = \pm \frac{1}{2} \quad (3.31b)$$

where the plus and minus signs of \pm are used for TM_Z and TE_Z incident fields, respectively.

Using Equations (3.28) and (3.31) the solution for the coefficients c_n^1 and d_n^1 in layer 1 is

$$c_n^1 = \frac{X_{22} \pm X_{12}}{2(X_{11}X_{22} - X_{21}X_{12})} \quad (3.32a)$$

$$d_n^1 = -\frac{X_{21} \pm X_{11}}{2(X_{11}X_{22} - X_{21}X_{12})} \quad (3.32b)$$

where the plus and minus signs of \pm are used for TM_Z and TE_Z incident fields, respectively. From Equation (3.30) the coefficients for the scattered fields are

$$a_n = f_n^{M+1} - g_n^{M+1} \quad (3.33a)$$

$$b_n = f_n^{M+1} + g_n^{M+1}. \quad (3.33b)$$

These coefficients have the following properties:

$$a_{-n} = a_n \quad (3.34a)$$

$$b_{-n} = b_n \quad (3.34b)$$

$$a_n(TE_Z) = b_n(TM_Z). \quad (3.34c)$$

As a result of Equation (3.34c), the cross-polarized echo widths of circular cylinders for TM_Z and TE_Z incident plane waves are identical.

In summary, Equation (3.33) provides the unknown coefficients in the eigenfunction expansions for the scattered fields given by Equation (3.5), which can be written in the far field as

$$E_z = \sqrt{\frac{2j}{\pi k_0}} \frac{e^{-jk_0\rho}}{\sqrt{\rho}} \sum_{n=-\infty}^{\infty} a_n e^{jn\phi} \quad (3.35a)$$

$$E_\phi = j \sqrt{\frac{2j}{\pi k_0}} \frac{e^{-jk_0\rho}}{\sqrt{\rho}} \sum_{n=-\infty}^{\infty} b_n e^{jn\phi} \quad (3.35b)$$

using the large argument approximation for the Hankel function. In addition, the internal fields are found using Equation (3.7), where the coefficients are found using

$$\begin{bmatrix} c_n^m \\ d_n^m \\ f_n^m \\ g_n^m \end{bmatrix} = [Y^{m-1}] [Y^{m-2}] \dots [Y^2] [Y^1] [Y^0] \begin{bmatrix} c_n^1 \\ d_n^1 \\ 0 \\ 0 \end{bmatrix}. \quad (3.36)$$

3.3 Numerical Results

This section presents numerical results for TM_Z and TE_Z scattering by several different multilayer circular chiral cylinders in free space. Comparison is made with similar multilayer achiral cylinders in each case. For convenience, all data is at a frequency of 300 MHz. The chiral parameters used in this section obey the limit set in [102] of $|\xi_c| < \sqrt{\epsilon/\mu}$.

3.3.1 TM_z Incident Plane Wave

This section presents the bistatic scattering patterns for a low-loss two-layer chiral cylinder with and without a perfectly conducting center cylinder for a TM_z incident plane wave with comparison to equivalent achiral cylinders. Figure 3.2 shows the co-polarized and cross-polarized bistatic echo widths for a TM_z plane wave ($E_z^i = e^{-jk_0x}$) incident upon the chiral cylinder with a perfect electric conducting center cylinder. The outer radius is 1.25 free space wavelengths. The curve marked 'Achiral ($\xi_c = 0$)' is the bistatic echo width for an identical multilayer cylinder with the chirality admittance set to zero in both layers. The chirality of the material clearly caused a significant change in the co-polarized scattered fields while generating a low level cross-polarized scattered field. The chirality admittance in the inner and outer layers is 65% and 33%, respectively, of the theoretical maximum of $|\xi_c| < \sqrt{\epsilon/\mu}$ set in [102].

Figure 3.3 shows the co-polarized and cross-polarized bistatic echo widths for chiral and achiral cylinders with the same geometry as those in Figure 3.2 except that the conducting center cylinder has been replaced by the same material as the inner layer. Note that the co-polarized and cross-polarized fields are of comparable magnitudes, indicating that the chirality of the cylinder has caused a significant rotation in the polarization of the scattered fields. In addition, the bistatic pattern of the achiral cylinder has more lobes than that of the chiral cylinder. This is unusual because the chiral cylinder is larger electrically, since one of the two wavelengths in chiral media is always smaller than that of the corresponding achiral media; therefore, its pattern should have more lobes. Figure 3.4 shows this point more clearly using a polar plot where, because of symmetry, the upper half shows the co- and cross-polarized bistatic echo width for the chiral cylinder and the lower half shows the echo width for the achiral cylinder.

Chiral Cylinder with PEC Frequency = 300 MHz

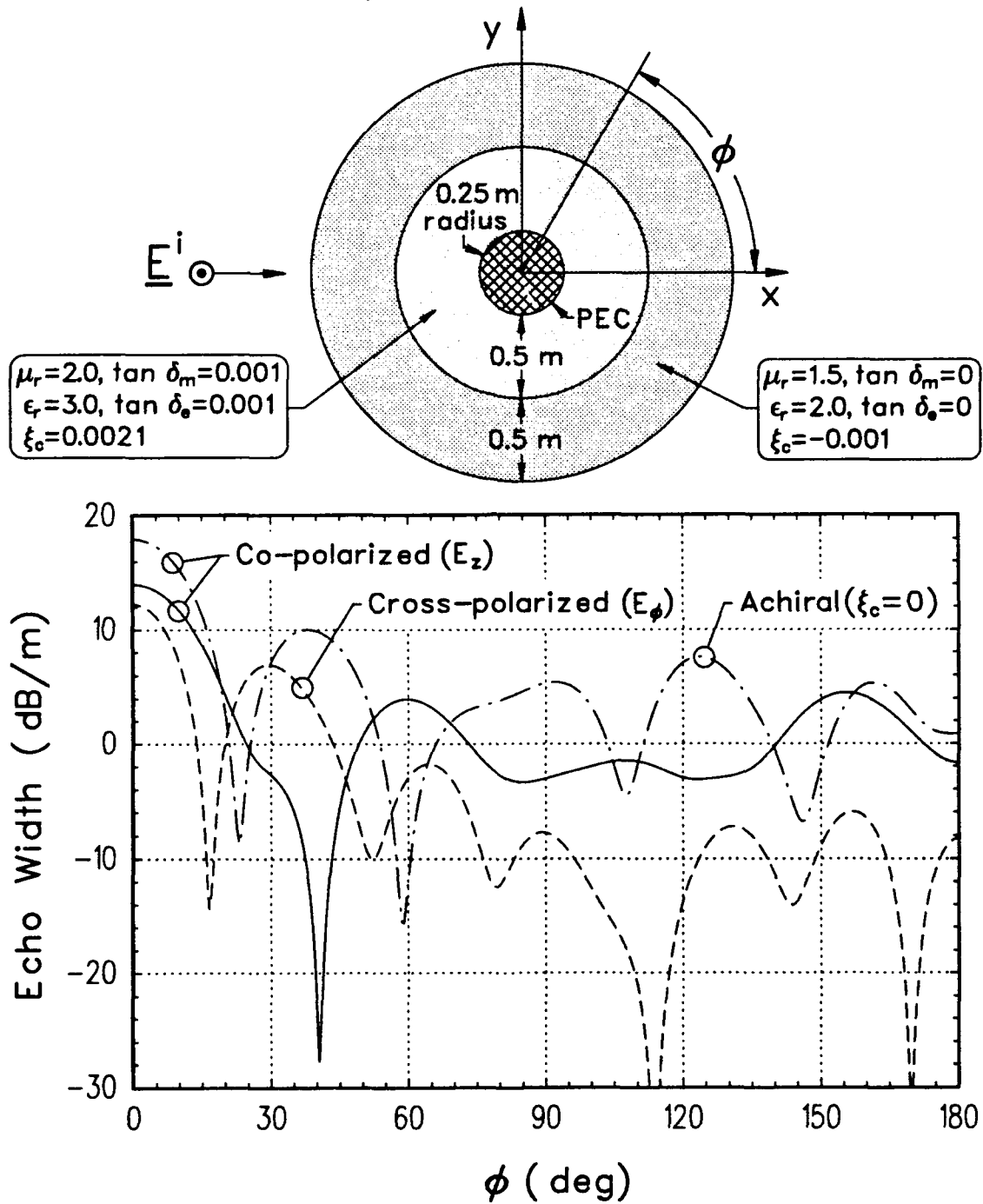


Figure 3.2: The co-polarized and cross-polarized bistatic echo width of a two-layer chiral cylinder with a perfect electric conducting center cylinder for a TM_z incident plane wave.

Two-layer Chiral Cylinder Frequency = 300 MHz

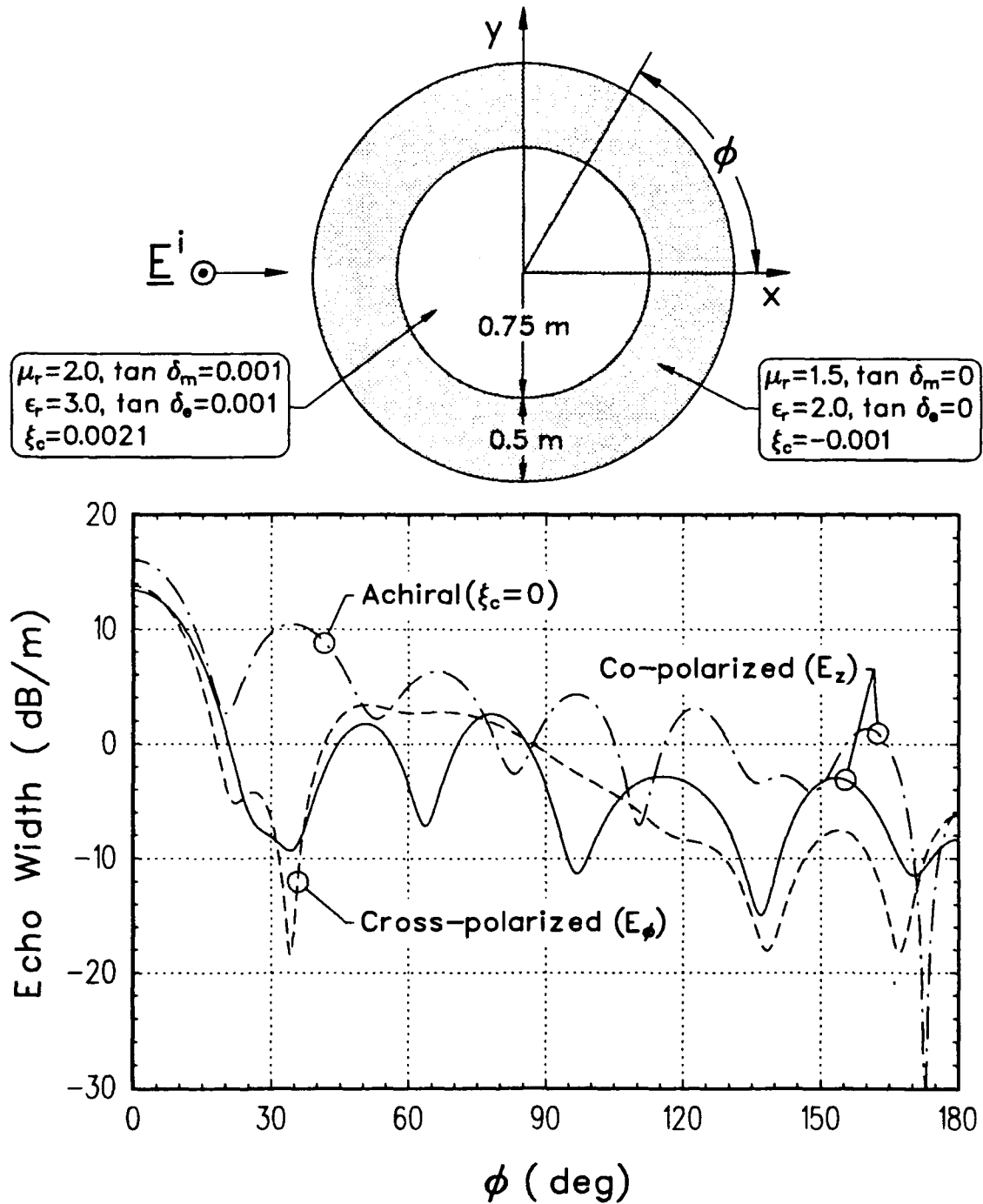


Figure 3.3: The co-polarized and cross-polarized bistatic echo width of a two-layer chiral cylinder for a TM_z incident plane wave.

Two-layer Chiral Cylinder Bistatic Scattering Pattern

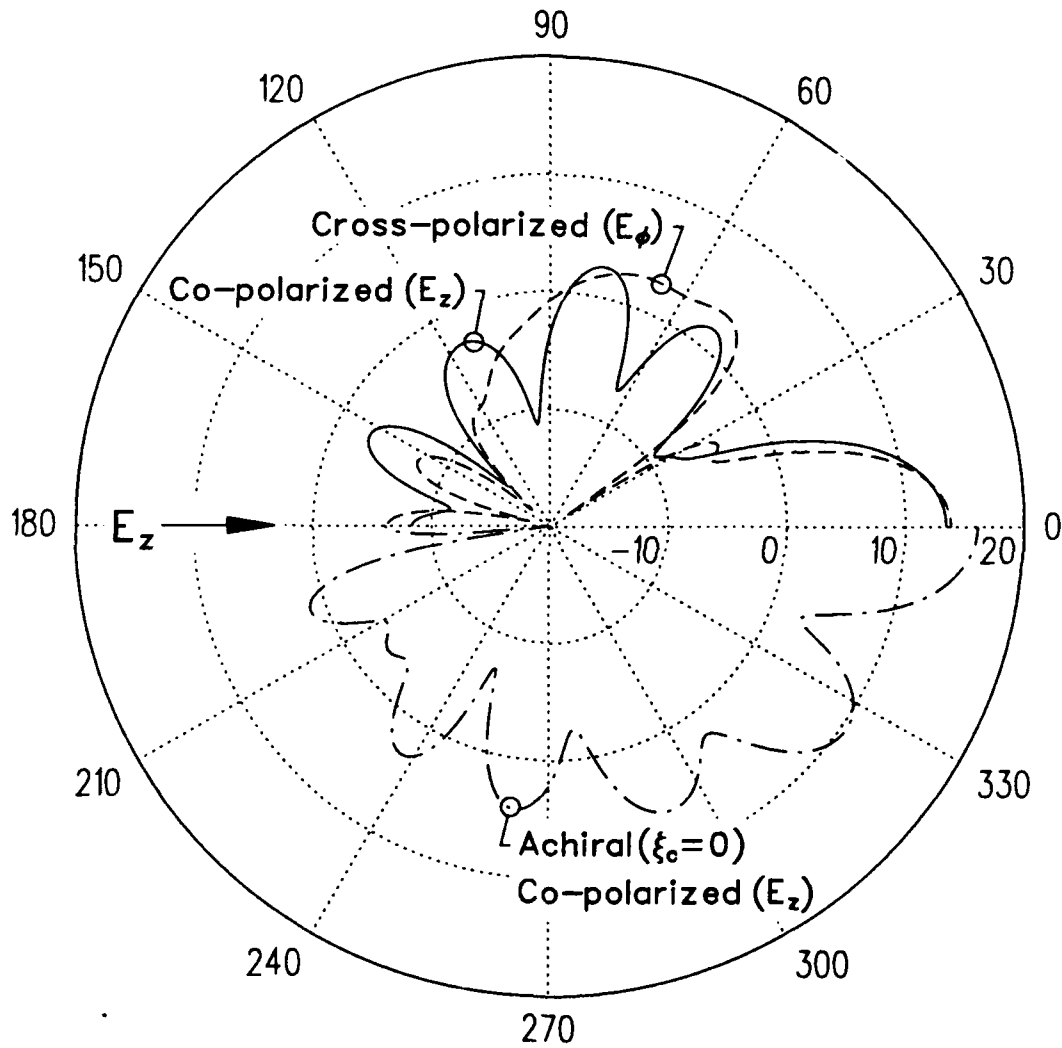


Figure 3.4: The bistatic echo width of the two layer chiral and achiral cylinders shown in Figure 3.3 for a TM_z incident plane wave.

3.3.2 TE_Z Incident Plane Wave

This section presents the bistatic scattering patterns for a high-loss two-layer chiral cylinder with and without a perfectly conducting center cylinder for a TE_Z incident plane wave. Internal fields and approximate surface currents on the center cylinder are presented for the chiral cylinder with the perfectly conducting center cylinder.

Figures 3.5 and 3.6 are similar to Figures 3.2 and 3.3, except that they are for the TE_Z polarization and for higher loss chiral media. In these figures the cross-polarized fields are greater than the co-polarized fields for angles between 20 and 70 degrees, indicating that the chirality of the cylinder has caused a significant rotation in the polarization of the scattered fields. The chirality admittance in the inner and outer layers is 23% and 80%, respectively, of the theoretical maximum of $|\xi_c| < \sqrt{\epsilon/\mu}$ set in [102].

Figures 3.7 and 3.8 show the near zone electric and magnetic fields along the positive y axis for the chiral and achiral cylinders of Figure 3.5 with the perfect electric conducting center cylinder. At the two material boundaries, $y = 0.75$ and $y = 1.25$ meters, E_y and H_y are discontinuous as required. At the boundary between free space and the outer material layer, the E_x and H_z fields of the achiral cylinder exhibit a much smaller slope discontinuity than the fields of the chiral cylinder. Interestingly, these same fields at the inner material boundary, $y = 0.75$ meters, exhibit almost no slope discontinuity in both cylinders. However, the related E_z and H_x fields exhibit sharp slope discontinuities at both boundaries of the chiral cylinder. In Figure 3.7, the magnitude of H_x at the surface of the conducting cylinder is greater than that of H_z . This means that at the point ($x = 0, y = 0.25m$), the J_z surface current on the conducting cylinder is greater than the J_x , i.e., the J_ϕ surface current. For a conducting cylinder coated with an achiral material only the J_ϕ surface current will be nonzero for a TE_Z incident plane wave as shown in Figure 3.8.

Figure 3.9 shows the tangential magnetic fields at the surface of the conducting center cylinder for the chiral and achiral cylinders shown in Figure 3.5. The J_z

Chiral Cylinder with PEC Frequency = 300 MHz

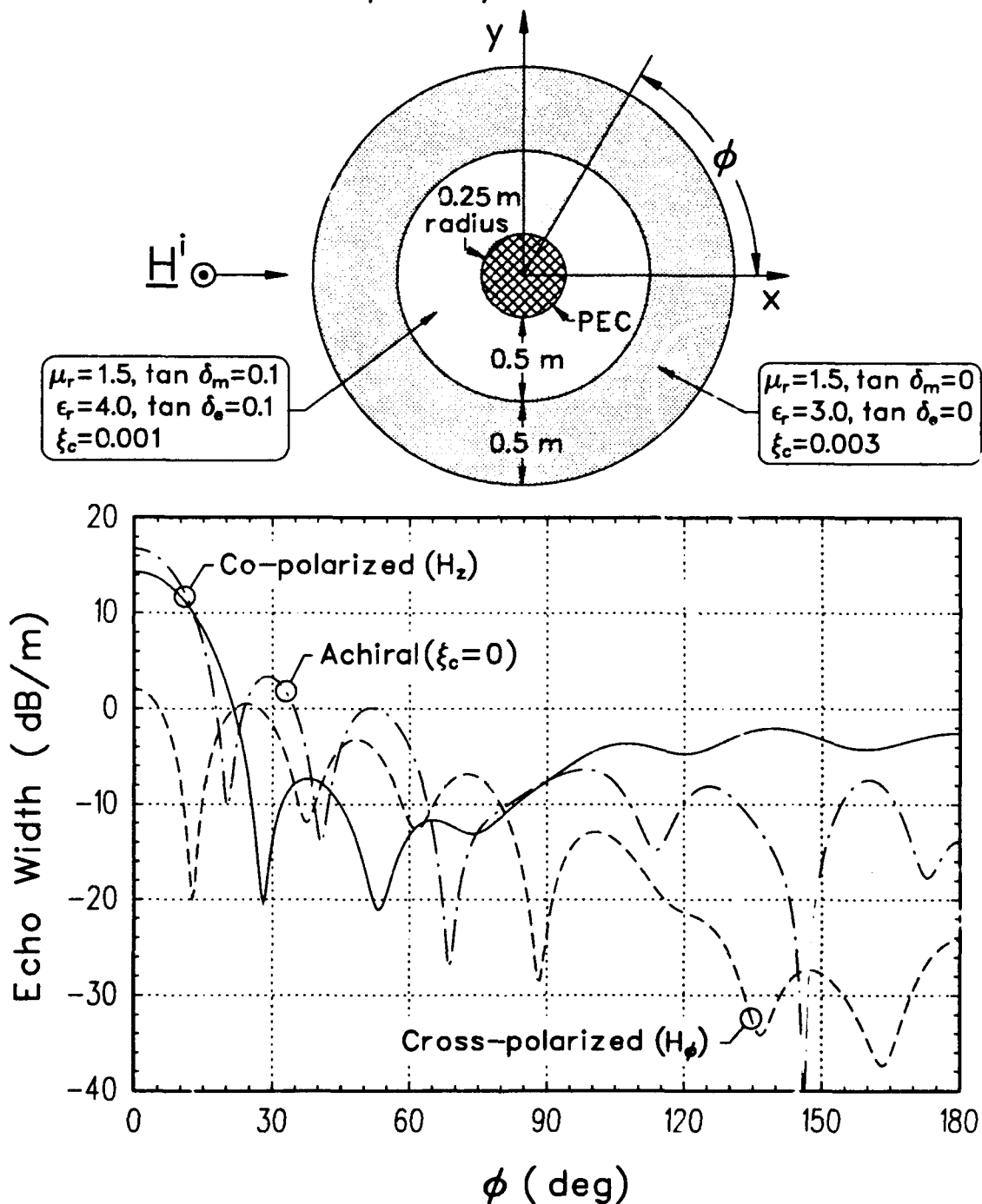


Figure 3.5: The co-polarized and cross-polarized bistatic echo width of a two layer chiral cylinder with a perfect electric conducting center cylinder for a TE_z incident plane wave.

Two-layer Chiral Cylinder Frequency = 300 MHz

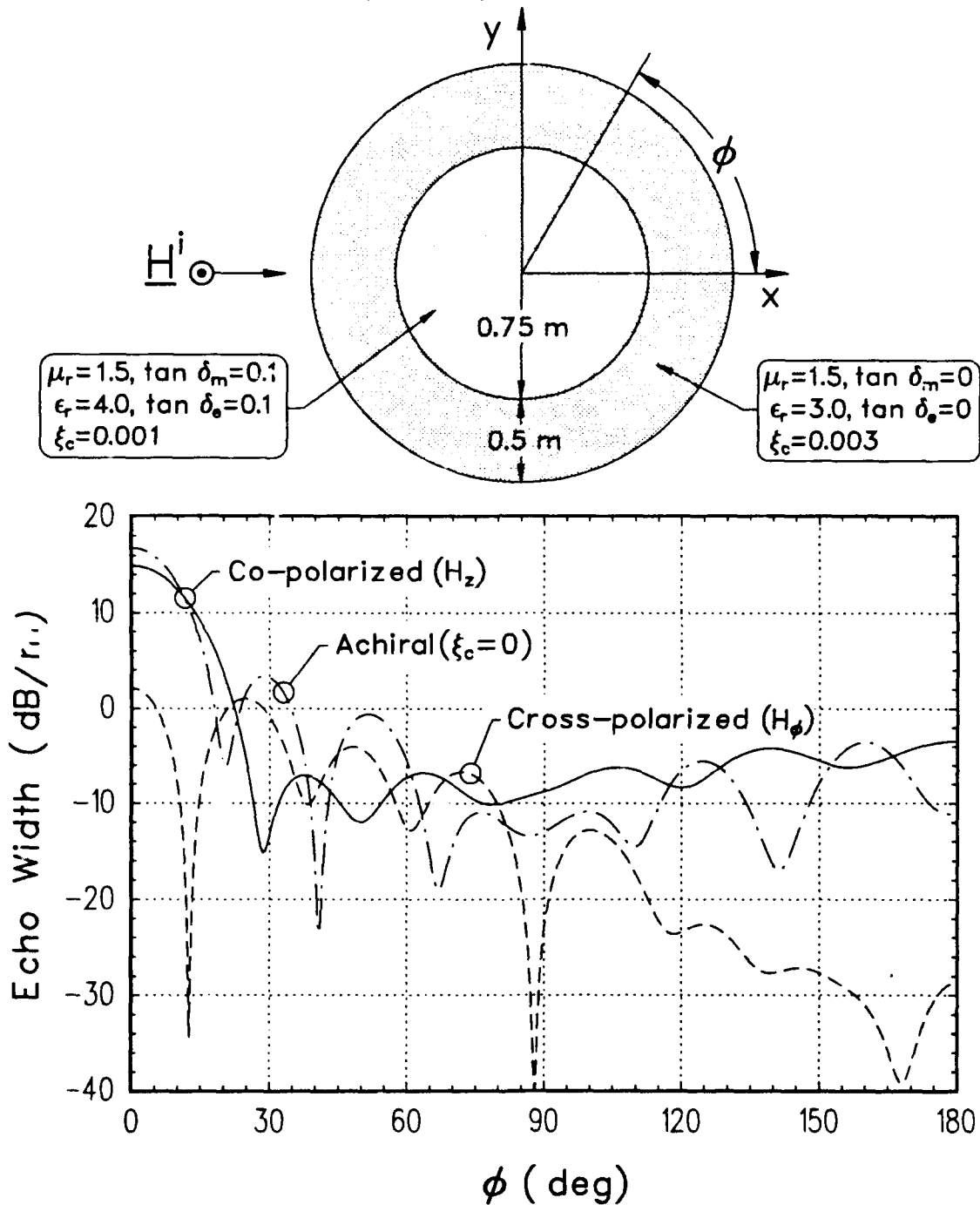


Figure 3.6: The co-polarized and cross-polarized bistatic echo width of a two layer chiral cylinder for a TE_z incident plane wave.

Chiral Cylinder with PEC

Frequency = 300 MHz

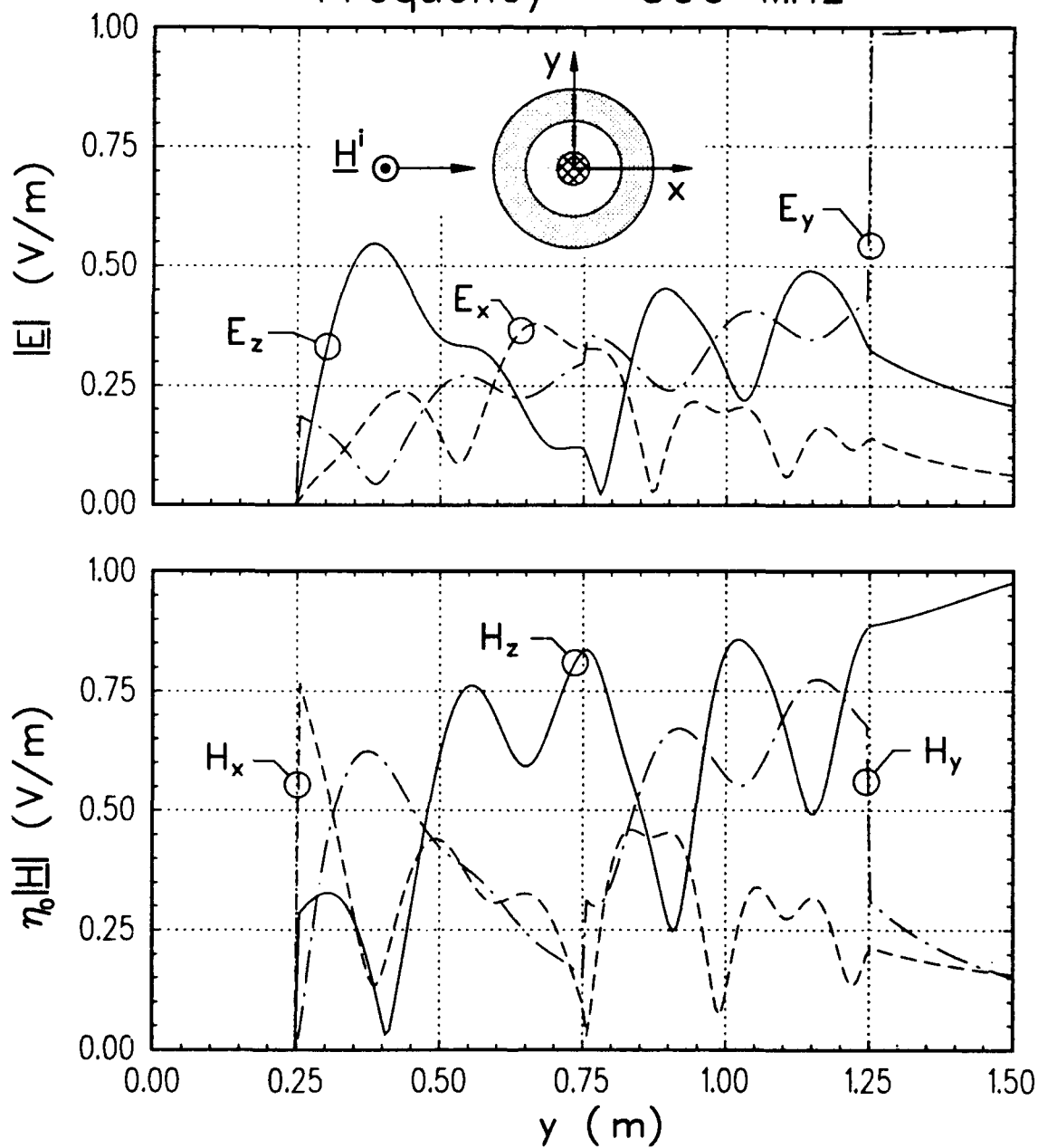


Figure 3.7: Internal fields along $x = 0$ for the chiral cylinder shown in Figure 3.5.

Achiral Cylinder with PEC

Frequency = 300 MHz

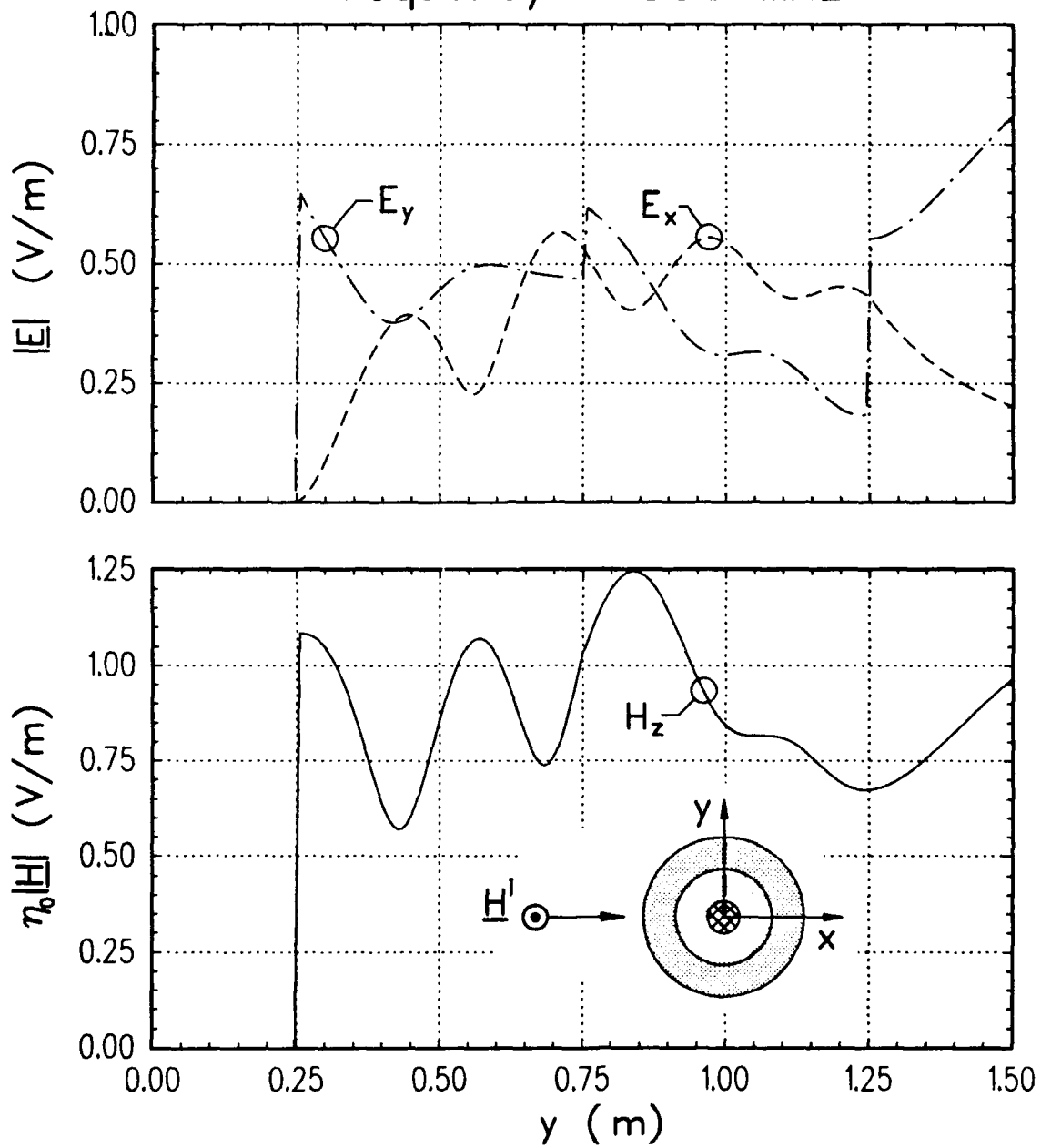


Figure 3.8: Internal fields along $x = 0$ for the achiral cylinder of Figure 3.5.

Chiral Cylinder with PEC

PEC Surface Currents

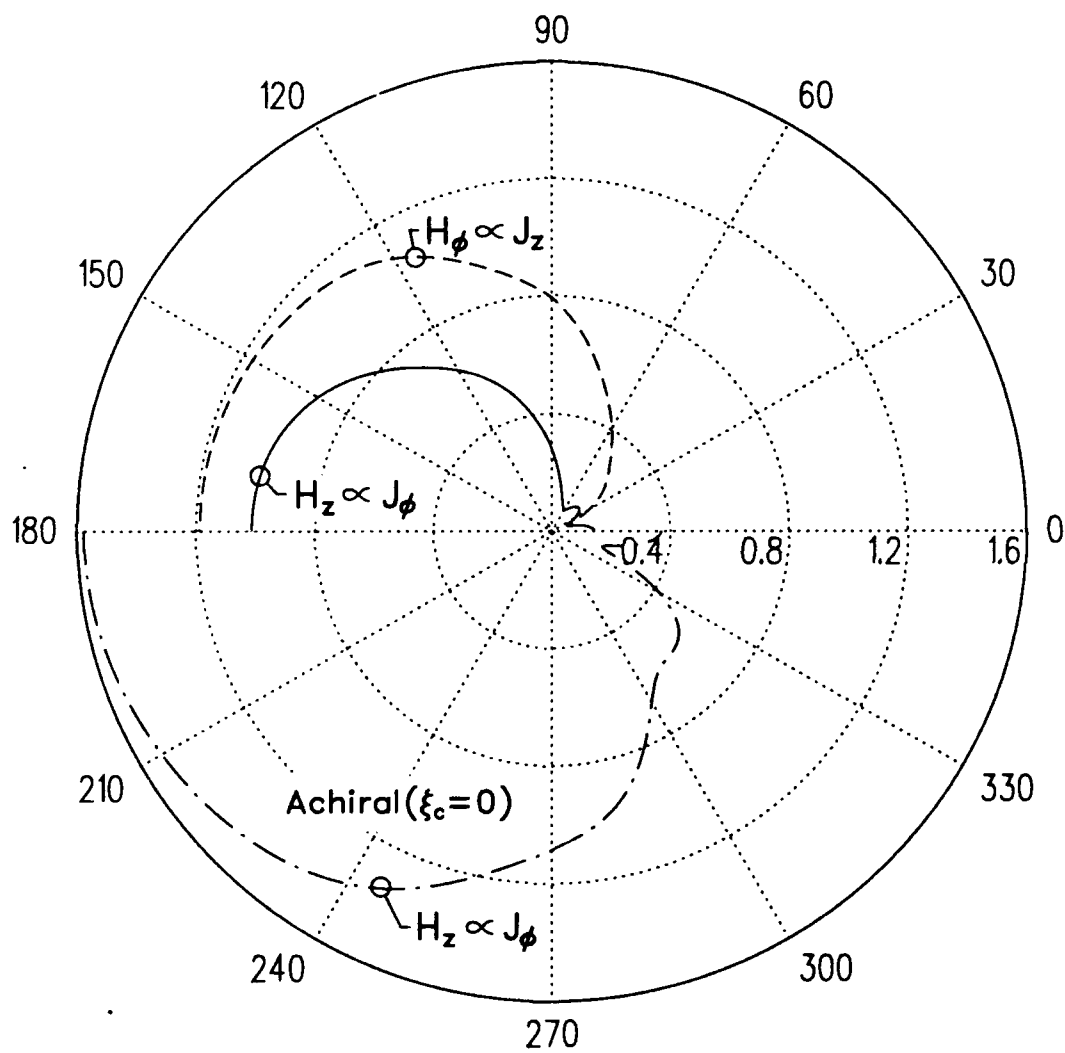


Figure 3.9: Internal H_ϕ and H_z fields at the surface of the conducting cylinder for the geometry shown in Figure 3.5.

current is greater than the J_ϕ current over the entire surface of the conducting cylinder in the center of the two-layer chiral cylinder, even though the J_z current is zero on the surface of a conducting cylinder at the center of an identical achiral cylinder.

Figure 3.10 shows the near zone electric and magnetic fields along the x axis, for the geometry shown at the top of Figure 3.5 with the perfect electric conducting center cylinder.

3.3.3 Chirality Versus Scattering

This section examines the effect of the chirality admittance on the backscatter and bistatic scattering patterns. First, a homogeneous chiral cylinder with $\mu_r = 2$, $\epsilon_r = 3$, and a radius of 0.15 meters is examined over the range of $\xi_c = 0$ (achiral) to the theoretical maximum of $|\xi_c| < \sqrt{\epsilon/\mu} = 0.00325$ [102], for lossless and lossy media. Figure 3.11 and 3.12 present the co- and cross-polarized backscatter echo width versus the magnitude of the chirality admittance for TM_z and TE_z incident plane waves. In all four cases, the cross-polarized echo width increases rapidly as ξ_c increases and equals the co-polarized echo width when ξ_c is approximately 18% of the theoretical maximum. The most interesting case of the four is the TE_z plane wave incident on the lossy chiral cylinder. In this problem the backscattered field is entirely cross-polarized for a small range of the chirality admittance. Figure 3.13 shows the co-polarized bistatic scattering pattern of this cylinder for a TE_z incident plane wave for the full range of ξ_c . Even through the achiral ($\xi_c = 0$) bistatic scattering pattern has no deep nulls, this figure shows that deep nulls will occur for certain ranges of ξ_c . Interestingly, nothing significant happens at the theoretical maximum of $|\xi_c| < \sqrt{\epsilon/\mu}$ set in [102].

Next, a homogeneous chiral cylinder with $\mu_r = 2$, $\epsilon_r = 3$, a radius of 0.15 meters, and a perfectly conducting center cylinder of radius 0.05 meters is examined over the range of ξ_c . Figures 3.14 and 3.15 present the co- and cross-polarized backscatter

Chiral Cylinder with PEC

Frequency = 300 MHz

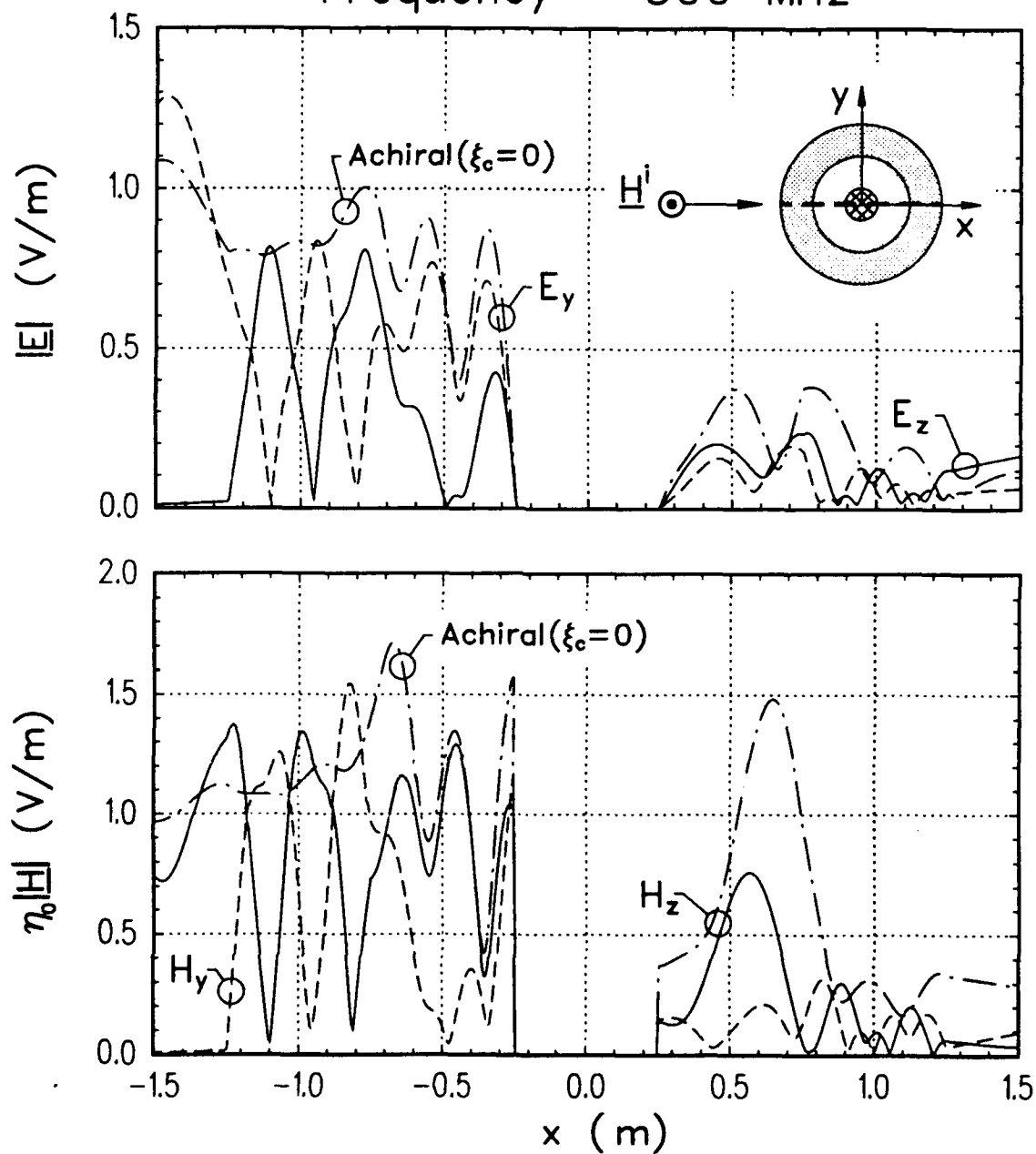


Figure 3.10: Internal fields along $y = 0$ for the chiral cylinder shown in Figure 3.5.

Backscatter versus Chirality

$\epsilon_r = 3, \mu_r = 2, \text{ radius} = 0.15 \text{ m}$

Frequency = 300 MHz

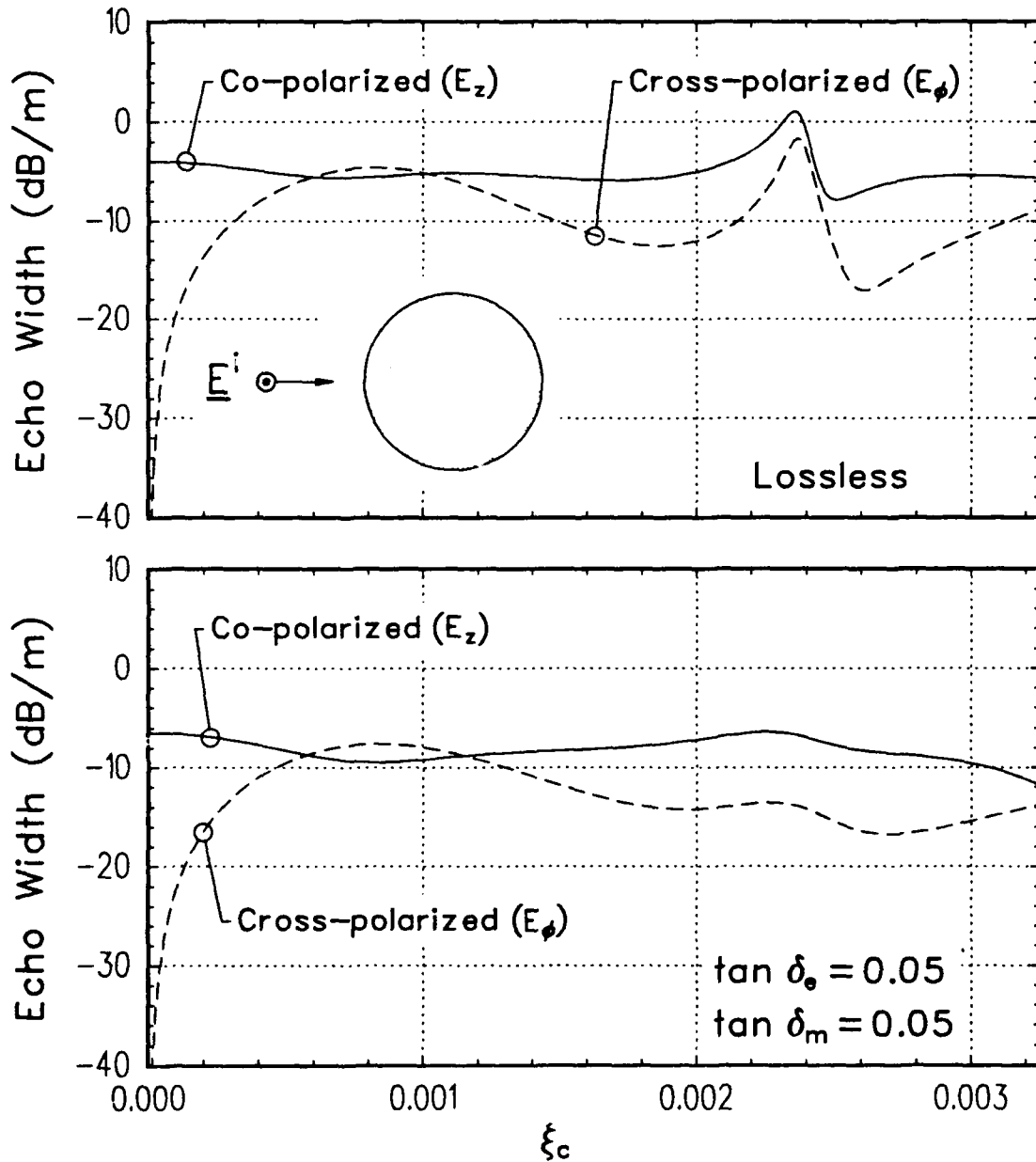


Figure 3.11: Backscatter echo width versus the magnitude of the chirality admittance for TM_z incident plane wave.

Backscatter versus Chirality

$$\epsilon_r = 3, \mu_r = 2, \text{ radius} = 0.15 \text{ m}$$

$$\text{Frequency} = 300 \text{ MHz}$$

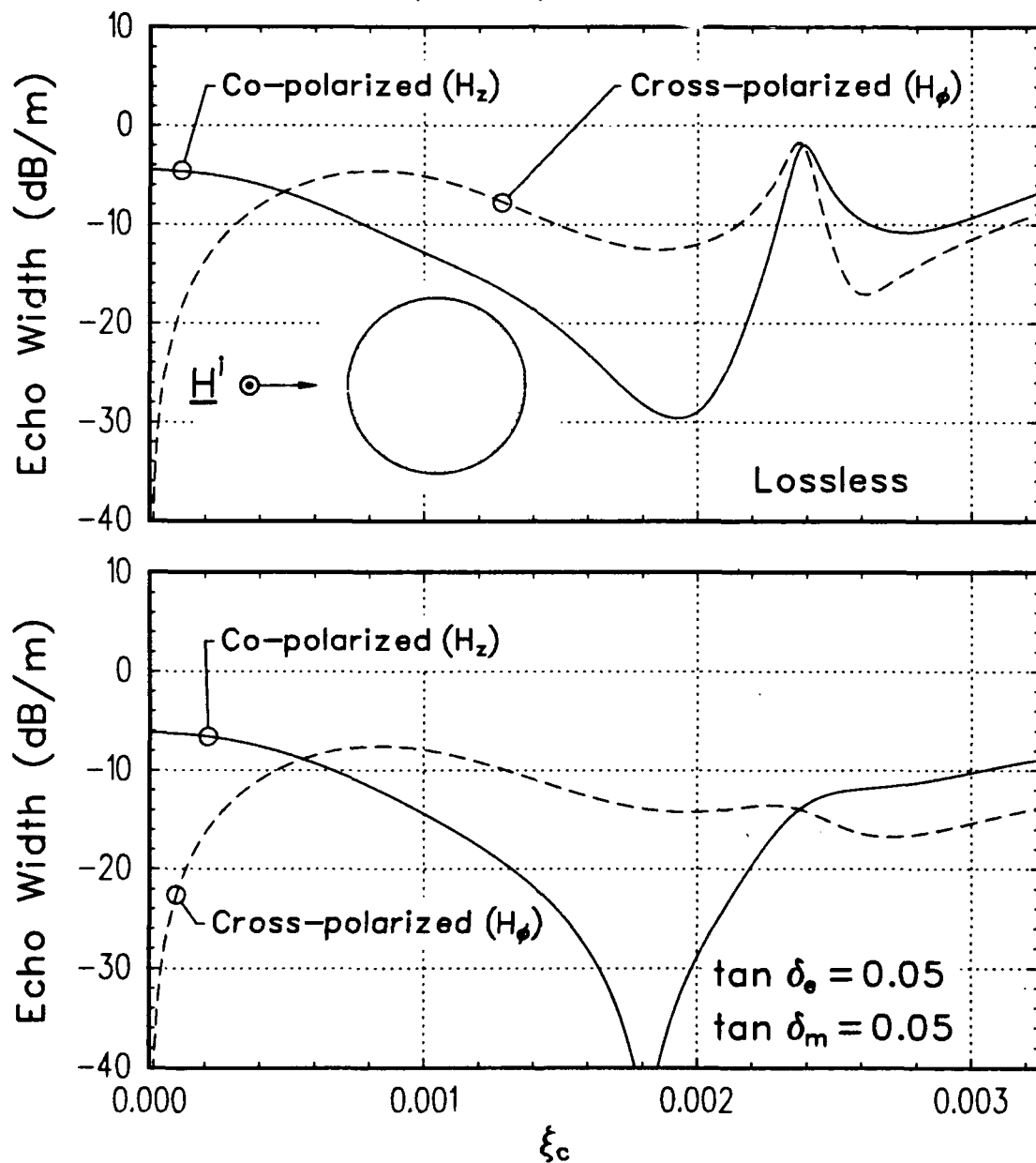


Figure 3.12: Backscatter echo width versus the magnitude of the chirality admittance for TE_z incident plane wave.

Bistatic Scattering versus Chirality

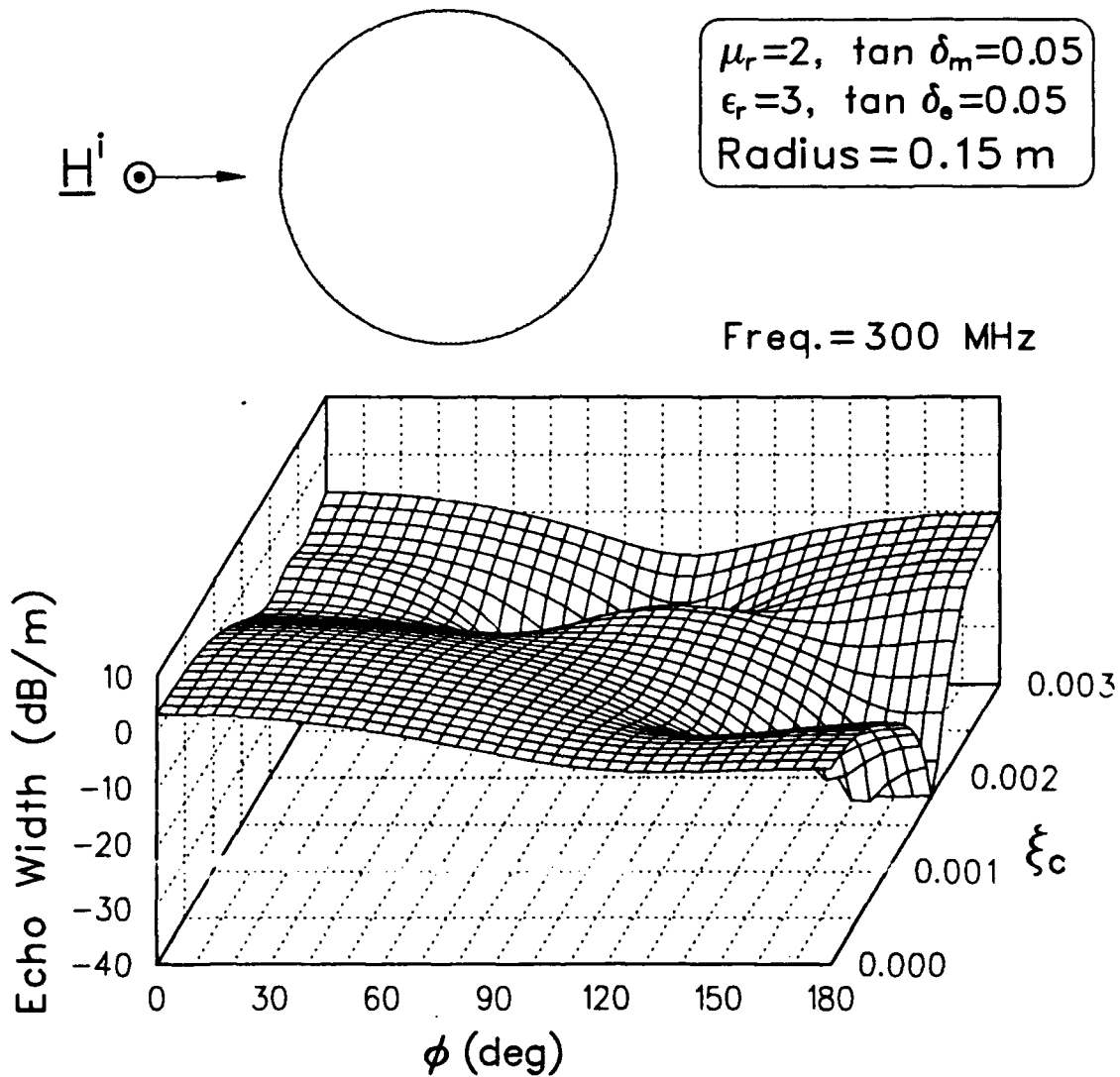


Figure 3.13: Bistatic echo width versus the magnitude of the chirality admittance for TE_z incident plane wave.

echo width versus the magnitude of the chirality admittance for TM_z and TE_z incident plane waves. In all four cases, the cross-polarized echo width increases rapidly as ξ_c increases and equals the co-polarized echo width when ξ_c is approximately 40% of the theoretical maximum. As the radius of the conducting cylinder is increased, the thickness of the coating is reduced and less material interacts with the incident field, thereby producing less cross-polarized scattered fields. This relationship is easily seen when comparing Figures 3.11 and 3.12 with Figures 3.14 and 3.15.

Backscatter versus Chirality

$\epsilon_r = 3, \mu_r = 2, \text{ radius} = 0.15 \text{ m}$

Frequency = 300 MHz

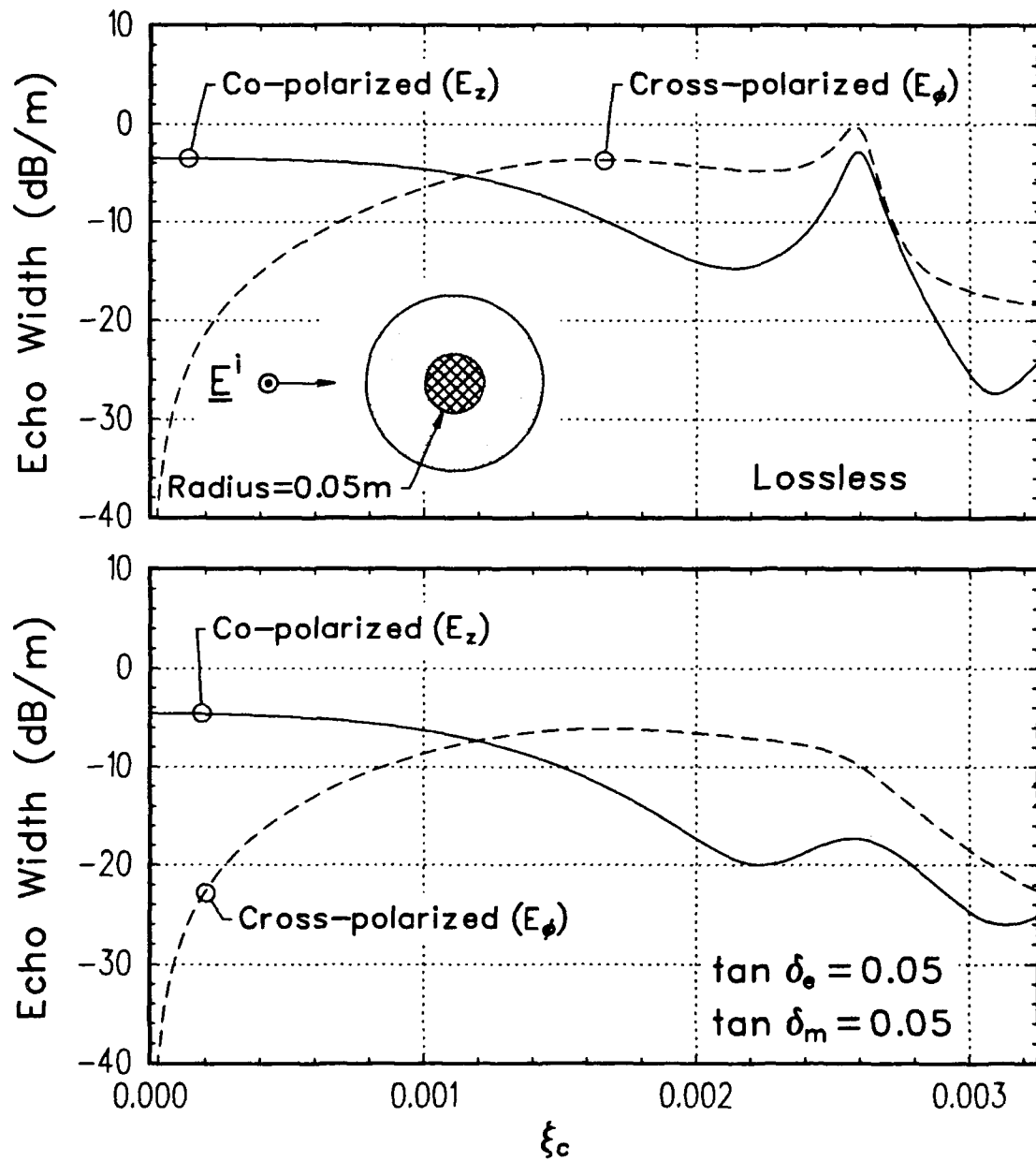


Figure 3.14: Backscatter echo width versus the magnitude of the chirality admittance for TM_z incident plane wave.

Backscatter versus Chirality

$$\epsilon_r = 3, \mu_r = 2, \text{ radius} = 0.15 \text{ m}$$

$$\text{Frequency} = 300 \text{ MHz}$$

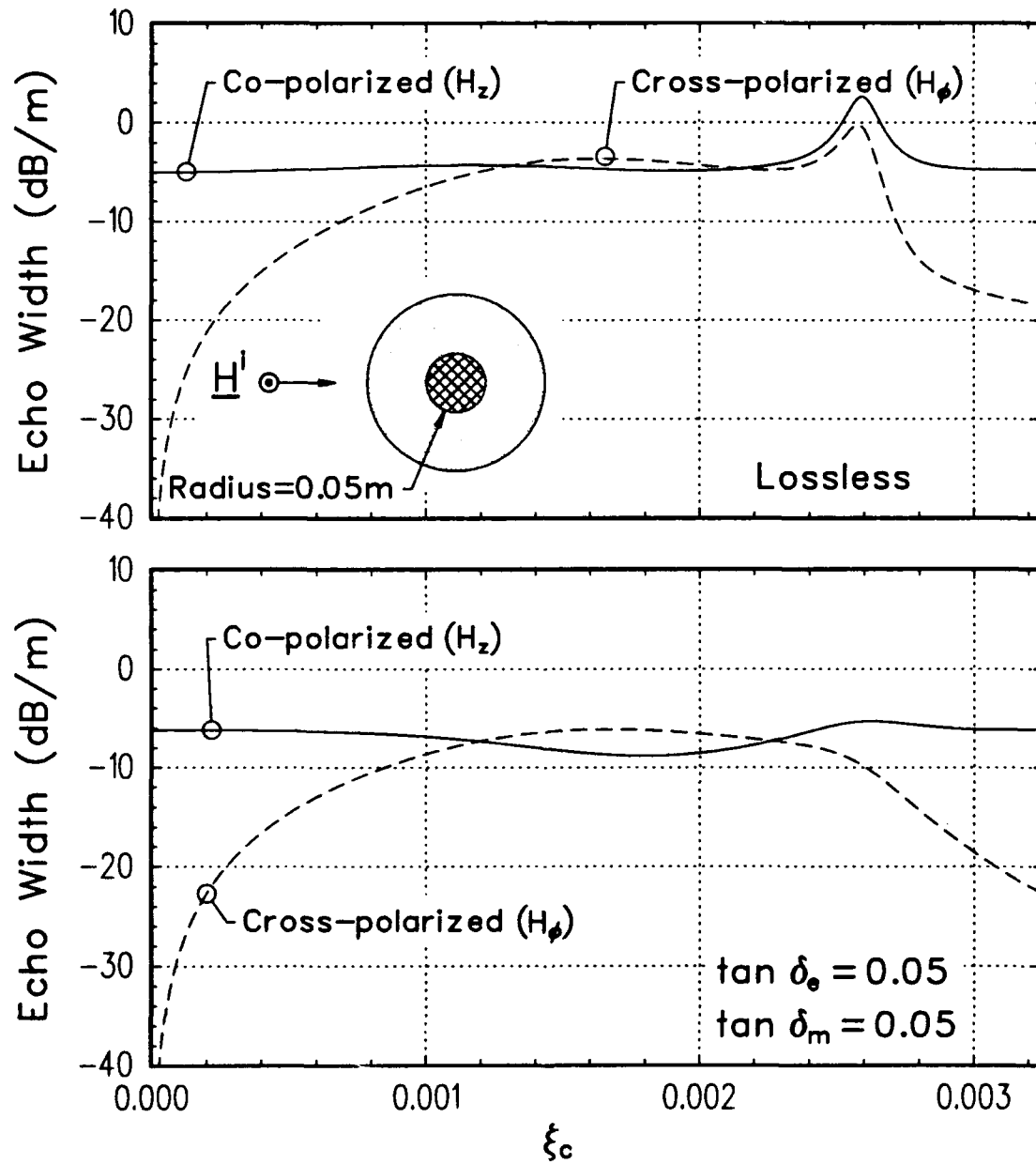


Figure 3.15: Backscatter echo width versus the magnitude of the chirality admittance for TE_z incident plane wave.

3.4 Summary

This chapter has presented an efficient recursive eigenfunction solution for scattering by a general multilayer circular chiral cylinder, with or without a surface impedance center cylinder, for a TM_z or TE_z normal incidence plane wave. The internal fields were expanded as inward and outward propagating right and left circularly polarized waves, using circularly polarized vector wave functions, resulting in four unknown coefficients in each layer. The resulting solution requires the multiplication of M 4×4 matrices for an M layer cylinder. The TE_z solution differs from the TM_z solution by only a plus/minus sign at one step. Including a surface impedance center cylinder requires only one additional matrix multiplication. An examination of coefficients responsible for the scattered fields showed that the cross-polarized bistatic echo width of circular cylinders is identical for TM_z and TE_z incident plane waves.

TM_z and TE_z bistatic scattering patterns for two-layer chiral cylinders with and without a perfectly conducting center cylinder were presented as reference solutions. These patterns demonstrated that the chirality of these cylinders caused a significant rotation in the polarization of the scattered fields. More significant was the effect of the chirality on the internal fields. In one case, more J_z than J_ϕ current was induced on the perfectly conducting cylinder coated by two layers of chiral media for a TE_z incident plane wave, even though the achiral problem would have induced no J_z current on the conducting center cylinder. The chirality admittance in these cases was greater than 50% of the theoretical maximum of $|\xi_c| < \sqrt{\epsilon/\mu}$ set in [102].

To examine the relationship between the magnitude of the chirality admittance and scattered fields, backscatter and bistatic scattering patterns were presented for the full range of ξ_c . Even though the achiral bistatic scattering pattern may have no deep nulls, the co-polarized bistatic pattern for a chiral cylinder can have deep nulls for certain ranges of ξ_c . In one case the backscattered field was entirely cross-polarized for a small range of the chirality admittance. The cross-polarized backscattered fields increased in similar fashion for all of the geometries examined as ξ_c was

increased. The rate of increase was dependent on the amount of chiral material, since chirality is a bulk effect.

Chapter 4

Scattering by an Arbitrary Cylinder

This chapter presents a pulse-basis point-matching method of moments solution [123, 124] to the two-dimensional problem of scattering by an isotropic inhomogeneous chiral cylinder of arbitrary cross section in free space or in the presence of a perfectly conducting half-plane. The method of moments solution for scattering by a chiral cylinder is obtained using the volume equivalence theorem developed in Section 2.4 to replace the chiral scatterer by free space and equivalent electric and magnetic volume polarization currents (\mathbf{J} , \mathbf{M}), as shown in Figure 4.1. By enforcing the volume equivalence theorem in the chiral scatterer, a pair of coupled vector integral equations for the currents (\mathbf{J} , \mathbf{M}) are obtained. These coupled vector integral equations are equivalent to six coupled scalar integral equations for (J_x, J_y, J_z) and (M_x, M_y, M_z) , which are solved using a pulse-basis point-matching method of moments solution. This problem could be formulated in terms of surface currents on the chiral cylinder [74, 80, 95]. The main advantage of the volume formulation is that it can more easily treat inhomogeneous media.

The electric surface currents on the half-plane are not explicitly included as unknowns in the method of moments solution. Instead, their effects are exactly accounted for by including the half-plane Green's function in the kernel of the integral equation [125, sec. 8.3]. Efficient techniques for accurately evaluating the integrals

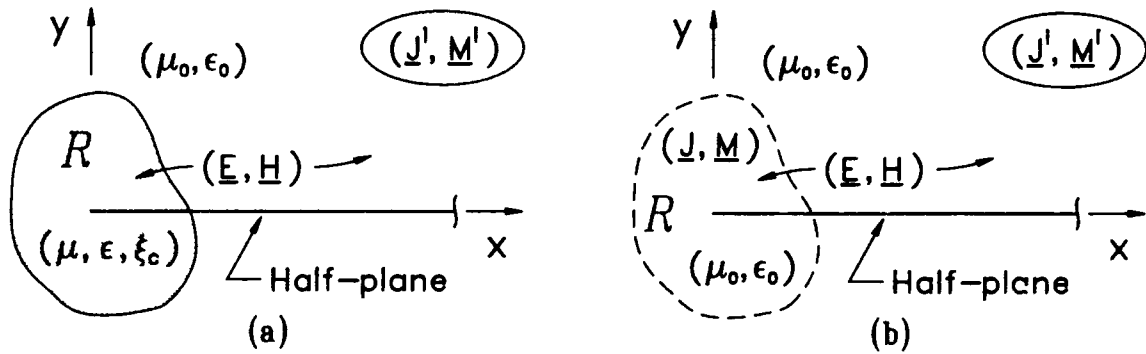


Figure 4.1: Volume Equivalence Theorem (a) Original problem: impressed currents, half-plane, and chiral scatterer. (b) Equivalent problem: scatterer replaced by free space and the equivalent currents.

in this Green's function are presented in Appendix B. In the free space problem the half-plane Green's function is replaced by the free space Green's function.

4.1 Derivation of General Integral Equations

This section develops a set of coupled integral equations for the equivalent electric and magnetic currents representing a chiral scatterer in free space or in the presence of a perfectly conducting half-plane. In the original problem of Figure 4.1(a), the impressed currents $(\mathbf{J}^i, \mathbf{M}^i)$ radiate the total fields (\mathbf{E}, \mathbf{H}) in a medium which is free space except for the perfectly conducting half-plane and a chiral scatterer with constitutive parameters (μ, ϵ, ξ_c) confined to the region R . The scatterer may be lossy and inhomogeneous. As shown in Figure 4.1(b), the volume equivalence theorem developed in Section 2.4 is used to replace the chiral scatterer by free space and the equivalent electric and magnetic volume polarization currents

$$\mathbf{J} = j\omega(\epsilon_c - \epsilon_0)\mathbf{E} + \omega\mu\xi_c\mathbf{H} \quad (4.1a)$$

$$\mathbf{M} = j\omega(\mu - \mu_0)\mathbf{H} - \omega\mu\xi_c\mathbf{E} \quad (4.1b)$$

confined to the region R .

In the equivalent problem of Figure 4.1(b), the total fields (\mathbf{E} , \mathbf{H}) at any point in space are given by

$$\mathbf{E} = \mathbf{E}^i + \mathbf{E}^J + \mathbf{E}^M \quad (4.2a)$$

$$\mathbf{H} = \mathbf{H}^i + \mathbf{H}^J + \mathbf{H}^M \quad (4.2b)$$

where $(\mathbf{E}^i, \mathbf{H}^i)$, $(\mathbf{E}^J, \mathbf{H}^J)$, and $(\mathbf{E}^M, \mathbf{H}^M)$ are the fields radiated by $(\mathbf{J}^i, \mathbf{M}^i)$, \mathbf{J} , and \mathbf{M} , respectively, in free space or in the presence of the half-plane. Then, substituting Equation (4.2) into Equation (4.1) yields

$$-\mathbf{E}^J - \mathbf{E}^M - c_E [\mathbf{H}^J + \mathbf{H}^M] + a_E \mathbf{J} = \mathbf{E}^i + c_E \mathbf{H}^i \quad (4.3a)$$

$$-\mathbf{H}^J - \mathbf{H}^M - c_M [\mathbf{E}^J + \mathbf{E}^M] + a_M \mathbf{M} = \mathbf{H}^i + c_M \mathbf{E}^i \quad (4.3b)$$

in region R , where c_E , c_M , a_E , and a_M are defined by

$$c_E = \frac{\omega \mu \xi_c}{j\omega(\epsilon_c - \epsilon_0)} \quad (4.4a)$$

$$c_M = -\frac{\omega \mu \xi_c}{j\omega(\mu - \mu_0)} \quad (4.4b)$$

$$a_E = \frac{1}{j\omega(\epsilon_c - \epsilon_0)} \quad (4.4c)$$

$$a_M = \frac{1}{j\omega(\mu - \mu_0)} \quad (4.4d)$$

Equation (4.3) can be considered to be a coupled integral equation for (\mathbf{J}, \mathbf{M}) since the fields $(\mathbf{E}^J, \mathbf{H}^J)$ or $(\mathbf{E}^M, \mathbf{H}^M)$ can be written as integrals, over the region R containing the chiral scatter, of \mathbf{J} or \mathbf{M} , respectively, dotted into the appropriate dyadic Green's function [126]. For example, \mathbf{E}^M could be written as

$$\mathbf{E}^M(\mathbf{r}) = \int_R \mathbf{M}(\mathbf{r}') \cdot \overline{\mathbf{G}}(\mathbf{r}, \mathbf{r}') dv, \quad (4.5)$$

where \mathbf{r}' is the source point, \mathbf{r} is the field point, and $\overline{\mathbf{G}}$ is the electric field dyadic Green's function for the magnetic source radiating in free space or in the presence of a perfectly conducting half-plane.

4.2 Integral Equations for a Two-Dimensional Body

In this section, the general integral equation of the previous section, Equation (4.3), is simplified for the case of normal incidence scattering by chiral cylinders of arbitrary cross section. Since this is now a two-dimensional problem, there are some simplifications from the general three-dimensional case. In particular, the TM currents (J_z, M_x, M_y) generate only the (E_z, H_x, H_y) fields and the TE currents (M_z, J_x, J_y) generate only the (H_z, E_x, E_y) fields. In this case, Equation (4.3) reduces to the following six scalar equations valid in R :

$$-E_z^{J_z} - E_z^{M_x} - E_z^{M_y} - c_E(H_z^{M_z} + H_z^{J_x} + H_z^{J_y}) + a_E J_z = E_z^i + c_E H_z^i \quad (4.6a)$$

$$-H_x^{J_z} - H_x^{M_x} - H_x^{M_y} - c_M(E_x^{M_z} + E_x^{J_x} + E_x^{J_y}) + a_M M_x = H_x^i + c_M E_x^i \quad (4.6b)$$

$$-H_y^{J_z} - H_y^{M_x} - H_y^{M_y} - c_M(E_y^{M_z} + E_y^{J_x} + E_y^{J_y}) + a_M M_y = H_y^i + c_M E_y^i \quad (4.6c)$$

$$-c_M(E_z^{J_z} + E_z^{M_x} + E_z^{M_y}) - H_z^{M_z} - H_z^{J_x} - H_z^{J_y} + a_M M_z = H_z^i + c_M E_z^i \quad (4.6d)$$

$$-c_E(H_x^{J_z} + H_x^{M_x} + H_x^{M_y}) - E_x^{M_z} - E_x^{J_x} - E_x^{J_y} + a_E J_x = E_x^i + c_E H_x^i \quad (4.6e)$$

$$-c_E(H_y^{J_z} + H_y^{M_x} + H_y^{M_y}) - E_y^{M_z} - E_y^{J_x} - E_y^{J_y} + a_E J_y = E_y^i + c_E H_y^i \quad (4.6f)$$

In Equation (4.6), the superscript indicates the source and the subscript the field component. For example, $H_y^{J_z}$ is the \hat{y} component of the magnetic field of J_z and E_x^i is the \hat{x} component of the electric field of $(\mathbf{J}^i, \mathbf{M}^i)$ in free space or in the presence of a half-plane. For normal incidence scattering by achiral cylinders, the TM and TE currents are uncoupled and can be determined separately [127]–[129]. However, Equation (4.6) shows that the TM and TE currents are coupled for chiral cylinders, and it is therefore necessary to solve for all currents simultaneously.

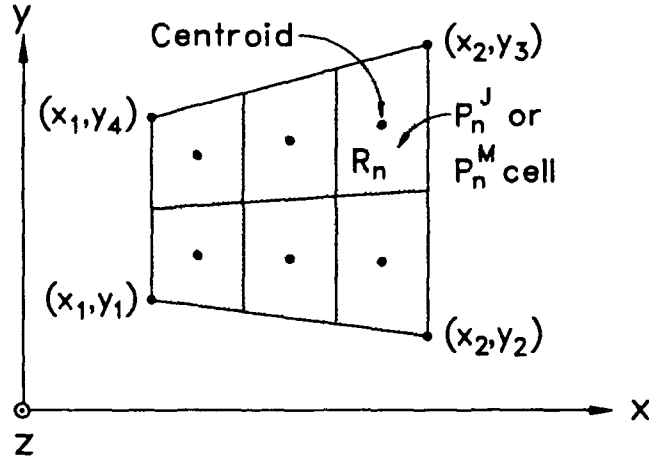


Figure 4.2: A trapezoidal cross section cylinder split into N smaller trapezoidal cells.

4.3 Method of Moments Solution

The pulse-basis point-matching method of moments solution of Equation (4.6) is presented in this section. For convenience, the chiral cylinder is restricted to be composed of one or more blocks of trapezoidal cross section. Without loss of generality, consider a single trapezoidal cross section cylinder as shown in Figure 4.2. The trapezoid is split into N smaller trapezoidal cells by dividing the opposite sides of the trapezoid into equal segments. These cells must be sufficiently small so that the electromagnetic fields and the constitutive parameters of the chiral cylinder can be considered as essentially constant within each cell. For a pulse-basis point-matching method of moments solution of scattering by achiral cylinders, the maximum dimension of the cells is typically less than one-tenth of the wavelength in the material. The region occupied by the n th cell is denoted by R_n , and has cross-sectional area A_n . Now define the volume electric and magnetic current pulse expansion functions for $n = 1, 2, \dots, N$ as

$$P_n^J = \begin{cases} 1/A_n & \text{A/m}^2, & \text{within } R_n \\ 0, & \text{otherwise} \end{cases} \quad (4.7a)$$

$$P_n^M = \begin{cases} 1/A_n \text{ V/m}^2, & \text{within } R_n \\ 0, & \text{otherwise.} \end{cases} \quad (4.7b)$$

The equivalent electric and magnetic currents can then be expanded as

$$\begin{aligned} \mathbf{J} &= \hat{\mathbf{x}}J_x + \hat{\mathbf{y}}J_y + \hat{\mathbf{z}}J_z \\ &= \hat{\mathbf{x}} \sum_{n=1}^N C_{xn} P_n^J + \hat{\mathbf{y}} \sum_{n=1}^N C_{yn} P_n^J + \hat{\mathbf{z}} \sum_{n=1}^N C_{zn} P_n^J \end{aligned} \quad (4.8a)$$

$$\begin{aligned} \mathbf{M} &= \hat{\mathbf{x}}M_x + \hat{\mathbf{y}}M_y + \hat{\mathbf{z}}M_z \\ &= \hat{\mathbf{x}} \sum_{n=1}^N K_{xn} P_n^M + \hat{\mathbf{y}} \sum_{n=1}^N K_{yn} P_n^M + \hat{\mathbf{z}} \sum_{n=1}^N K_{zn} P_n^M. \end{aligned} \quad (4.8b)$$

Note that for N cells there are $6N$ unknown coefficients: C_{xn} , C_{yn} , C_{zn} , K_{xn} , K_{yn} , and K_{zn} ($n = 1, 2, \dots, N$).

The pulse-basis point-matching method of moments solution is obtained by substituting Equation (4.8) into Equation (4.6) and requiring the resulting six equations to be exactly satisfied at the centroid of each of the N cells. This transforms Equation (4.6) into a $6N \times 6N$ system of simultaneous linear equations which can be compactly written in matrix form as

$$[Z + \Delta Z] I = V. \quad (4.9)$$

This equation can be symbolically decomposed into submatrices representing the relationships between the TM_z and TE_z fields and currents

$$\begin{bmatrix} TM/TM & TM/TE \\ TE/TM & TE/TE \end{bmatrix} \begin{bmatrix} TM \\ TE \end{bmatrix} = \begin{bmatrix} TM \\ TE \end{bmatrix}. \quad (4.10)$$

4.3.1 The Impedance Matrix $[Z]$

For an inhomogeneous chiral cylinder, the impedance matrix $[Z]$ can be written as a 6×6 block matrix

$$[Z] = \begin{bmatrix} Z_{11} & Z_{12} & Z_{13} & C_E Z_{44} & C_E Z_{45} & C_E Z_{46} \\ Z_{21} & Z_{22} & Z_{23} & C_M Z_{54} & C_M Z_{55} & C_M Z_{56} \\ Z_{31} & Z_{32} & Z_{33} & C_M Z_{64} & C_M Z_{65} & C_M Z_{66} \\ \hline C_M Z_{11} & C_M Z_{12} & C_M Z_{13} & Z_{44} & Z_{45} & Z_{46} \\ C_E Z_{21} & C_E Z_{22} & C_E Z_{23} & Z_{54} & Z_{55} & Z_{56} \\ C_E Z_{31} & C_E Z_{32} & C_E Z_{33} & Z_{64} & Z_{65} & Z_{66} \end{bmatrix} \quad (4.11)$$

where each of the Z_{ij} is an $N \times N$ matrix, where the m, n element is the negative F_i field of the $\mathbf{P}_{j(n)}$ current expansion function evaluated at the centroid of the cell m , i.e.,

$$Z_{ij(m,n)} = -F_i(\mathbf{P}_{j(n)}) \Big|_m \quad (4.12)$$

where

$$F_i = \begin{cases} E_z, & i = 1 \\ H_x, & i = 2 \\ H_y, & i = 3 \\ H_z, & i = 4 \\ E_x, & i = 5 \\ E_y, & i = 6 \end{cases} \quad (4.13)$$

and

$$\mathbf{P}_{j(n)} = \begin{cases} \hat{\mathbf{z}} P_n^J, & j = 1 \\ \hat{\mathbf{x}} P_n^M, & j = 2 \\ \hat{\mathbf{y}} P_n^M, & j = 3 \\ \hat{\mathbf{z}} P_n^M, & j = 4 \\ \hat{\mathbf{x}} P_n^J, & j = 5 \\ \hat{\mathbf{y}} P_n^J, & j = 6 \end{cases} \quad (4.14)$$

for $m, n = 1, 2, \dots, N$. For example, the m, n element of Z_{23} is $-H_x(\hat{\mathbf{y}} P_n^M)$ evaluated at the centroid of cell m .

The C_E and C_M are $N \times N$ diagonal matrices given by

$$C_E = \begin{bmatrix} c_E|_1 & & 0 \\ & \ddots & \\ 0 & & c_E|_N \end{bmatrix} \quad (4.15a)$$

$$C_M = \begin{bmatrix} c_M|_1 & & 0 \\ & \ddots & \\ 0 & & c_M|_N \end{bmatrix} \quad (4.15b)$$

where $c_E|_m$ is c_E from Equation (4.4) evaluated at the centroid of cell m and similarly for $c_M|_m$.

The computational effort to obtain the free space impedance matrix $[Z]$ can be reduced by recognizing simple relationships between the $Z_{i,j}$ block matrices. Let $(\mathbf{E}^J, \mathbf{H}^J)$ and $(\mathbf{E}^M, \mathbf{H}^M)$ denote the free space fields of the arbitrary electric and magnetic currents \mathbf{J} and \mathbf{M} , respectively. Then, directly from Maxwell's equations, it can be shown that if \mathbf{J} is numerically equal to \mathbf{M} , then

$$\mathbf{E}^M \doteq -\mathbf{H}^J \quad (4.16a)$$

$$\mathbf{H}^M \doteq \mathbf{E}^J / \eta_0^2, \quad (4.16b)$$

where $\eta_0 = \sqrt{\mu_0/\epsilon_0}$ is the characteristic impedance of free space and \doteq should be read "numerically equal". Examining Equations (4.13) and (4.14), and noting that

$P_n^I \doteq P_n^{II}$, yields

$$\begin{bmatrix} Z_{44} & Z_{45} & Z_{46} \\ Z_{54} & Z_{55} & Z_{56} \\ Z_{64} & Z_{65} & Z_{66} \end{bmatrix} \doteq \begin{bmatrix} \frac{1}{\eta_0^2} Z_{11} & -Z_{12} & -Z_{13} \\ -Z_{21} & \eta_0^2 Z_{22} & \eta_0^2 Z_{23} \\ -Z_{31} & \eta_0^2 Z_{32} & \eta_0^2 Z_{33} \end{bmatrix}. \quad (4.17)$$

4.3.2 The Impedance Matrix $[\Delta Z]$

The impedance matrix $[\Delta Z]$ is a $6N \times 6N$ diagonal matrix given in block matrix form as

$$[\Delta Z] = \left[\begin{array}{ccc|ccc} \Delta Z_{11} & & 0 & & & \\ & \Delta Z_{22} & & & & 0 \\ 0 & & \Delta Z_{33} & & & \\ \hline & & & \Delta Z_{44} & & 0 \\ & 0 & & & \Delta Z_{55} & \\ & & & 0 & & \Delta Z_{66} \end{array} \right]. \quad (4.18)$$

Each of the ΔZ_{ii} 's is a $N \times N$ diagonal matrix given by

$$\Delta Z_{ii} = \begin{bmatrix} a_i|_1/A_1 & & 0 \\ & \ddots & \\ 0 & & a_i|_N/A_N \end{bmatrix} \quad (4.19)$$

where A_m is the cross-sectional area of cell m and $a_i|_m$ is given by

$$a_i|_m = \begin{cases} a_E|_m, & \text{for } i=1,5,6 \\ a_M|_m, & \text{for } i=2,3,4, \end{cases} \quad (4.20)$$

where $a_E|_m$ is a_E from Equation (4.4) evaluated at the centroid of cell m and similarly for $a_M|_m$.

4.3.3 The Current Vector I

The current vector I is defined as a 6 element block vector

$$I = \begin{bmatrix} C_z \\ K_x \\ K_y \\ K_z \\ C_x \\ C_y \end{bmatrix} \quad (4.21)$$

where the coefficients C_{xn} , C_{yn} , C_{zn} , K_{xn} , K_{yn} , and K_{zn} ($n = 1, 2, \dots, N$) of Equation (4.8) are contained in the length N column vectors C_x , C_y , C_z , K_x , K_y , and K_z , respectively.

4.3.4 The Voltage Vector V

The voltage vector V is also defined as a 6 element block vector

$$V = \begin{bmatrix} E_z^i + C_E H_z^i \\ H_x^i + C_M E_x^i \\ H_y^i + C_M E_y^i \\ H_z^i + C_M E_z^i \\ E_x^i + C_E H_x^i \\ E_y^i + C_E H_y^i \end{bmatrix} \quad (4.22)$$

where the terms $E_x^i, E_y^i, E_z^i, H_x^i, H_y^i, H_z^i$ are length N column vectors consisting of the fields of the impressed currents ($\mathbf{J}^i, \mathbf{M}^i$) evaluated at the centroid of cell $m = 1, \dots, N$. For example, the m th element of E_z^i is the \hat{z} component of the electric field generated by the currents ($\mathbf{J}^i, \mathbf{M}^i$), evaluated at the centroid of cell m . C_E and C_M are the $N \times N$ diagonal matrices defined in Equation (4.15).

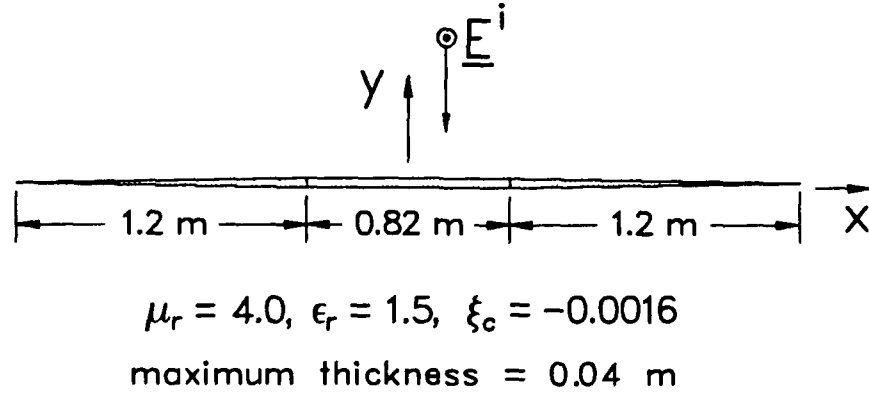


Figure 4.3: A TM_z plane wave normally incident upon a tapered chiral slab.

4.3.5 Scattered and Internal Fields

Equation (4.9) can be solved for the current vector I which, when substituted into Equation (4.8), provides an approximation to the equivalent electric and magnetic currents (\mathbf{J}, \mathbf{M}). The scattered fields are simply the fields of (\mathbf{J}, \mathbf{M}).

The total internal fields at the centroid of a cell are given by

$$\mathbf{E} = \frac{-j(\mu - \mu_0)\mathbf{J} + \mu\xi_c\mathbf{M}}{\omega [(\epsilon_c - \epsilon_0)(\mu - \mu_0) - \mu^2\xi_c^2]} \quad (4.23a)$$

$$\mathbf{H} = \frac{j(\epsilon_c - \epsilon_0)\mathbf{M} + \mu\xi_c\mathbf{J}}{\omega [(\epsilon_c - \epsilon_0)(\mu - \mu_0) - \mu^2\xi_c^2]} \quad (4.23b)$$

where (μ, ϵ_c, ξ_c) and (\mathbf{J}, \mathbf{M}) are evaluated at the centroid of the cell.

4.4 Free-Space Numerical Results

This section presents numerical results for TM and TE scattering by a variety of chiral cylinders in free space. All data is at a frequency of 300 MHz, and includes both echo width and internal fields.

Figure 4.3 shows a TM_z polarized plane wave normally incident upon a chiral slab ($E_z^i = e^{jk_0y}$, where k_0 is the free space wave number). The center section of the slab

is 0.82 meters wide and 0.04 meters thick. The tapered sections are each 1.2 meters long. The slab is lossless with parameters of $\epsilon_r = 1.5$, $\mu_r = 4.0$, and $\xi_c = -0.0016$ A/V. Near the origin the fields for the tapered slab should approximate that of an infinite slab of uniform thickness 0.04 m. Figures 4.4 and 4.5 show a comparison of the method of moments solution for the total fields of the tapered slab to the exact solution developed in Appendix C for the infinite uniform slab along the line $x = 0$. The phase of the fields has been normalized by dividing fields by $e^{jk_0 y}$, i.e., the phase of a plane wave propagating in free space in the $-\hat{y}$ direction. The incident electric field is a \hat{z} polarized plane wave. When this wave hits the uniform slab it produces a purely \hat{z} polarized reflected wave, resulting in a partial standing wave pattern to the right of the slab. As the wave enters the slab, the polarization begins to rotate, causing the \hat{x} component of the electric field to increase, and the \hat{z} component to decrease. Finally, as the wave exits the slab it is a linearly polarized wave, but with its polarization rotated from \hat{z} . The solution for the tapered slab has a small \hat{x} polarized back scattered field which is not present for an infinite slab.

Next the method of moments solution is compared to the exact eigenfunction solution [20] for the bistatic echo width of a 0.1 m radius circular chiral cylinder. The inset in Figure 4.6 shows a TM_Z plane wave ($E_z^i = e^{-jk_0 x}$) incident upon a circular cylinder approximated by a number of trapezoidal cells, corresponding to the method of moments expansion functions. Denoting d as the maximum dimension of the cells, Figure 4.6 shows the eigenfunction and method of moments solution for $d = 0.2\lambda_m$ (18 cells) and $d = 0.1\lambda_m$ (63 cells). λ_m denotes the minimum wavelength for left or right circularly polarized plane waves in the chiral media. For the material parameters in Figure 4.6, $\lambda_m \cong 0.301$ meters. Note that as the number of cells increases, the method of moments solution approaches the exact eigenfunction solution for both the co-polarized and cross-polarized scattered fields.

A comparison of the eigenfunction and method of moments solution for the bistatic echo width for a TE_Z plane wave ($H_z^i = e^{-jk_0 x}/\eta_0$) incident upon a 0.15

Tapered Chiral Slab
 $\mu_r = 4.0, \epsilon_r = 1.5, \xi_c = -0.0016$
 Freq. = 300 MHz

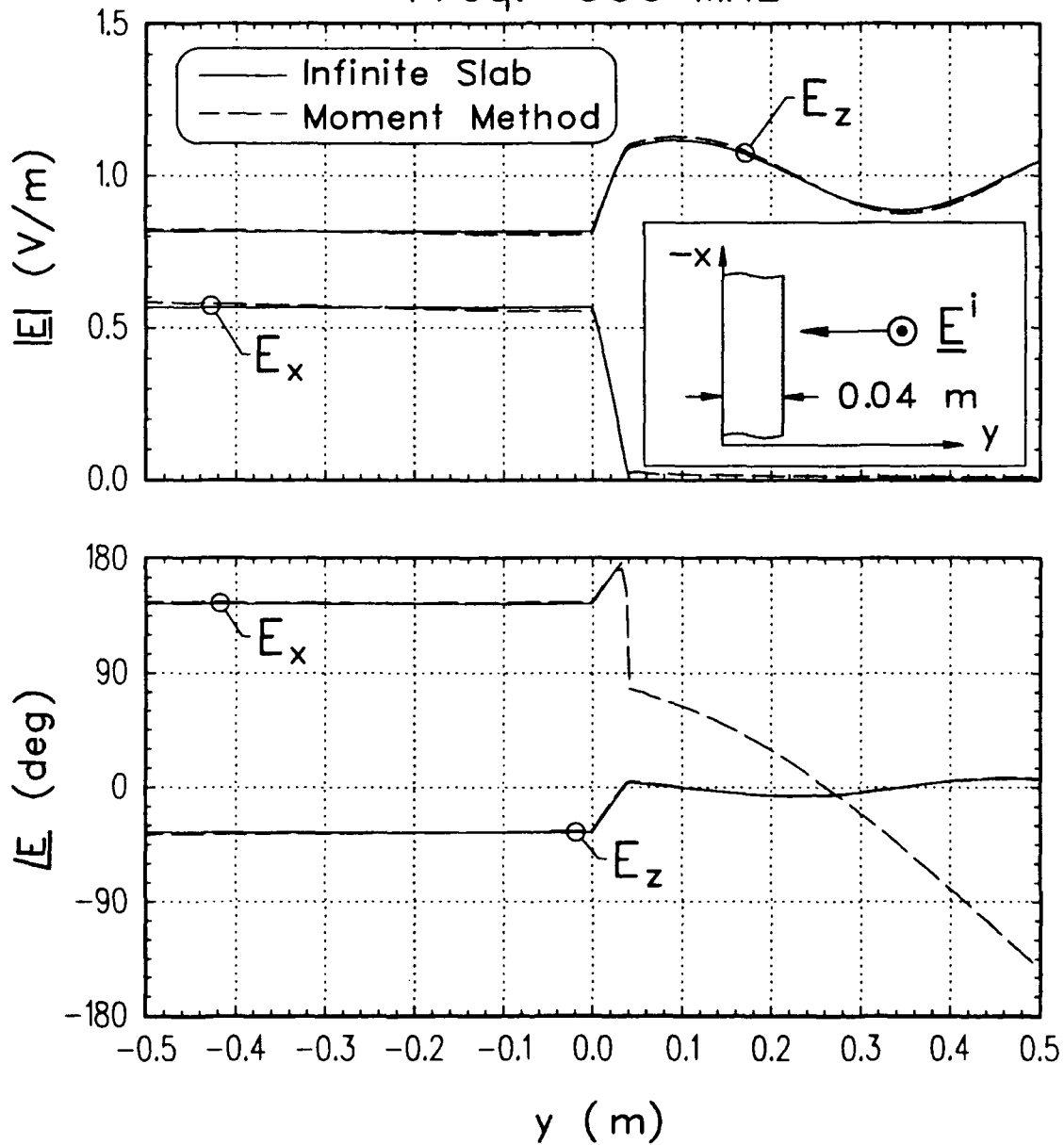


Figure 4.4: The magnitude and phase of the E_z and E_x fields along the y-axis for the tapered chiral slab shown in Figure 4.3.

Tapered Chiral Slab
 $\mu_r = 4.0, \epsilon_r = 1.5, \xi_c = -0.0016$
 Freq. = 300 MHz

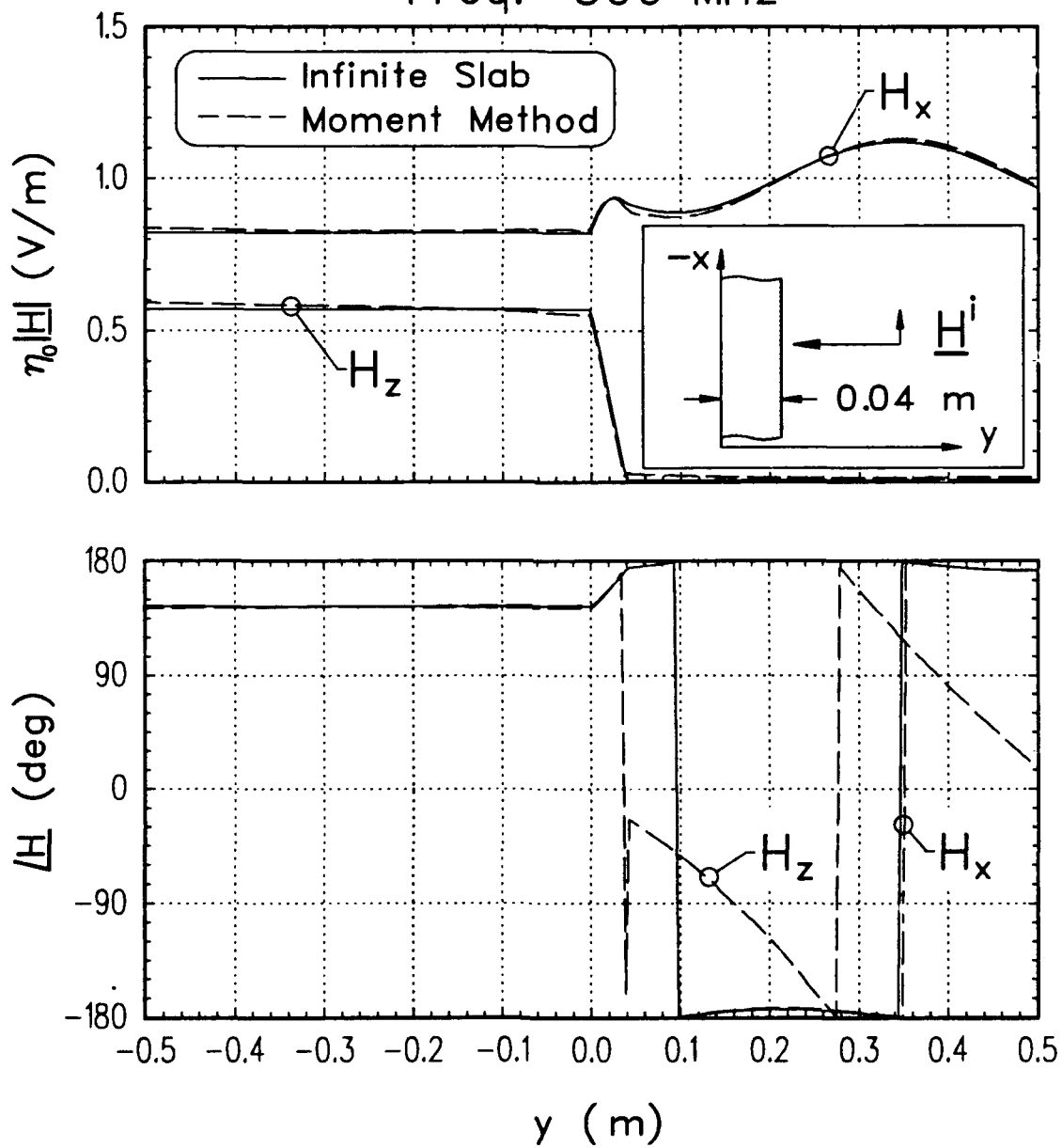


Figure 4.5: The magnitude and phase of the H_z and H_x fields along the y-axis for the tapered chiral slab shown in Figure 4.3.

Chiral Cylinder, Radius = 0.1 meters

$\mu_r = 4.0$, $\epsilon_r = 1.5$, $\xi_c = 0.0005$

Freq. = 300 MHz

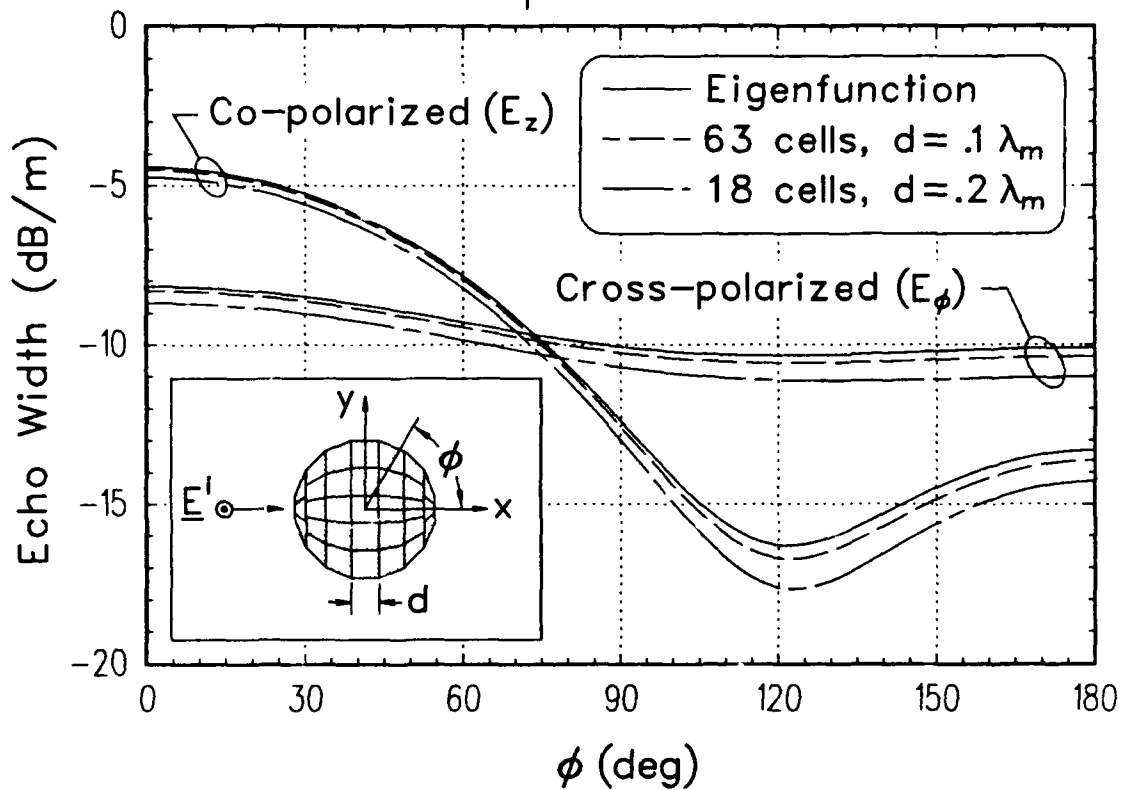


Figure 4.6: The co-polarized and cross-polarized bistatic echo width of a circular chiral cylinder for a TM_z incident plane wave.

Chiral Cylinder, radius = 0.15 meters

$\mu_r = 2$, $\tan \delta_m = .05$, Freq. = 300 MHz

$\epsilon_r = 3$, $\tan \delta_e = .05$, $\xi_c = .002$

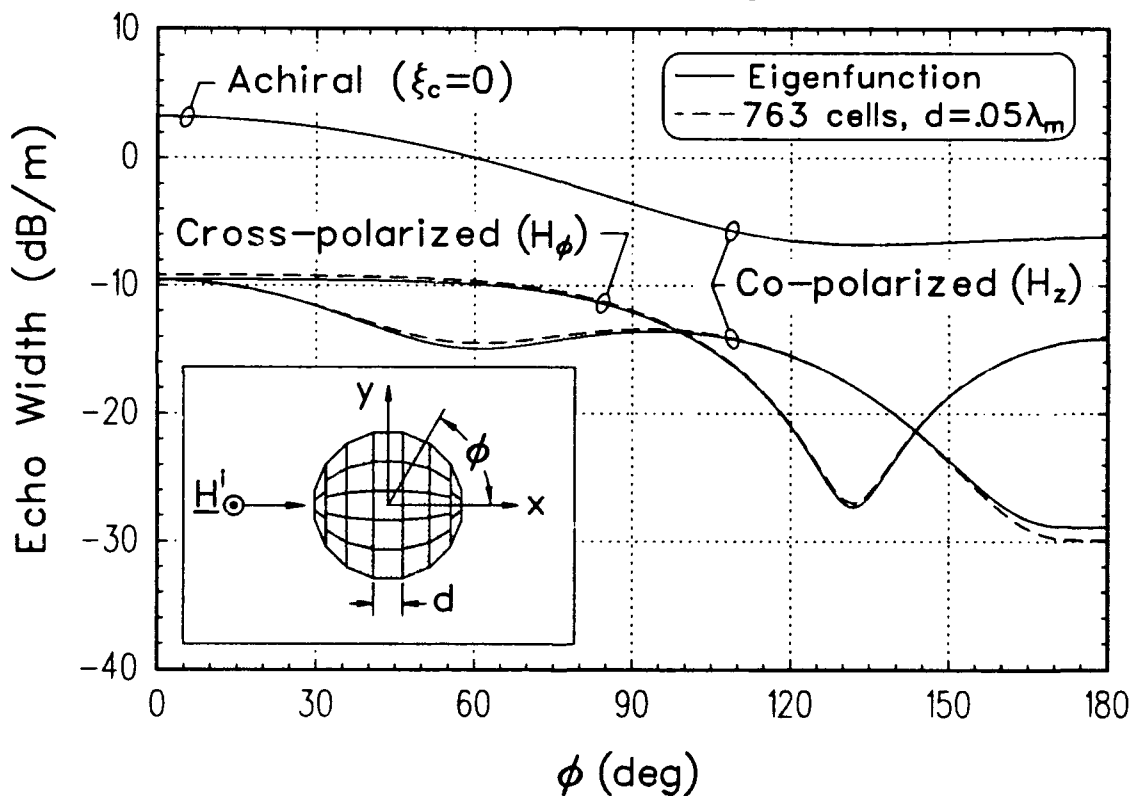


Figure 4.7: The co-polarized and cross-polarized bistatic echo width of a circular chiral cylinder for a TE_z incident plane wave.

m radius lossy circular chiral cylinder is shown in Figure 4.7. Note that the cross-polarized field is greater for most angles than the co-polarized field, indicating that the chirality of the cylinder has caused a significant rotation in the polarization of the scattered fields. For comparison, the echo width for an achiral cylinder, obtained by setting $\xi_c = 0$, is also shown. A segment size of $0.05 \lambda_m$ was required to obtain a well converged result, where $\lambda_m \cong 0.228$ meters for the material parameters shown. The backscatter ($\phi = 180^\circ$) echo width for this geometry was highly sensitive to the segment size and in Figure 4.7 the greatest error occurs at $\phi = 180^\circ$. The backscatter echo width of this cylinder was examined in Figure 3.12 of Chapter 3 for the full range of ξ_c and found to be highly sensitive to the value of ξ_c in the region of $\xi_c = 0.002$. The sensitivity of this cylinder to segment size may be related to the sensitivity in ξ_c in the same way the calculated scattering from a resonant body is sensitive to minor changes in its materials and geometry, as well as the method used to calculate the scattering.

The magnitude of the internal fields along the cylinder's centerline are shown in Figure 4.8. As the incident H_z field propagates through the cylinder, the H_z internal field decreases and the E_z field increases due to the chirality of the material. This is in addition to the effects due to the cylindrical geometry. The most significant effect of the chirality, besides generating cross-polarized fields, is to reduce the effective wavelength in the cylinder, as well as the actual wavelength in the medium. For the achiral cylinder, the actual material wavelength is 0.408 meters with a spacing of 0.12 to 0.15 between the peaks and valleys of the internal fields. The right and left wavelengths of the chiral medium are 0.228 and 0.730 meters, respectively. The spacing between peaks and valleys of the internal fields varied between 0.03 and 0.09 meters, with 0.05 meters being typical. Based on the achiral cylinder, the spacing should have been 0.067 to 0.084 meters. The chirality caused approximately a 25% reduction in the effective wavelength in the medium beyond that predicted based on the smallest chiral wavelength. This becomes very important when choosing the

Chiral Cylinder, radius = 0.15 meters

$\mu_r = 2$, $\tan \delta_m = .05$, Freq. = 300 MHz

$\epsilon_r = 3$, $\tan \delta_e = .05$, $\xi_c = .002$

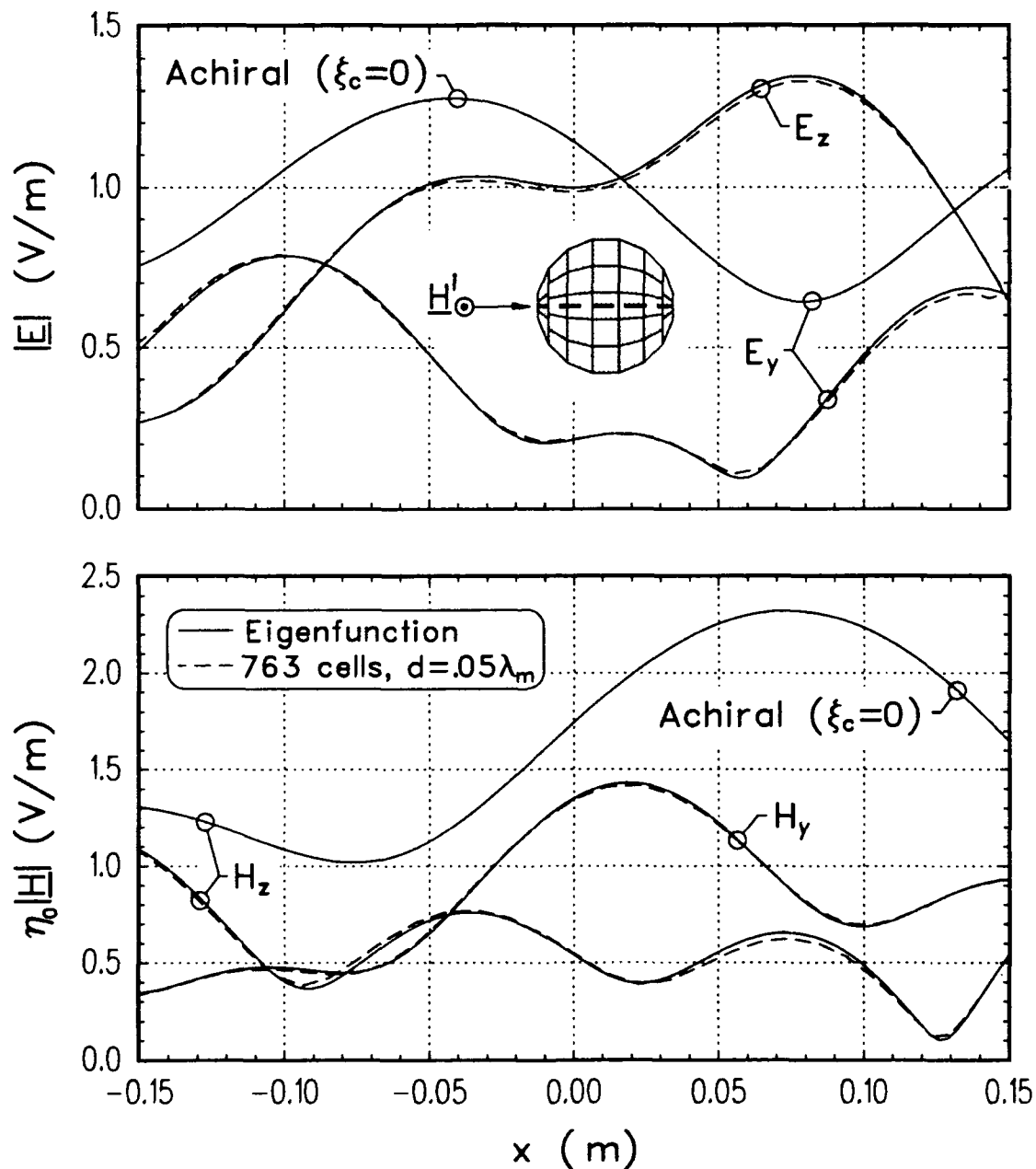


Figure 4.8: Internal fields along $y = 0$ for the chiral cylinder shown in Figure 4.7.

cell size to use for a method of moments solution. For the point-matching pulse-basis solution used here, the cell size for the achiral cylinder should have been 0.041 meters, using a ten cells per wavelength rule. Using the same rule, the cell size in the chiral cylinder should have been 0.023 meters. However, after adjusting for the observed reduction in the effective wavelength in the chiral cylinder, the cell size should be 0.017 meters. Overall, the chirality caused a factor of 5 increase in the number of cells needed for the method of moments solution.

Figure 4.9 shows the bistatic echo width for a $0.1 \text{ m} \times 2.0 \text{ m}$ chiral slab with a TM_z plane wave incident at 30° from the x -axis. The cell size of the basis functions is $0.057 \lambda_m$, where $\lambda_m \cong 0.35$ meters for the material parameters shown. As in the previous figures, the chirality has generated a substantial cross-polarized field. The magnitude of the internal fields along the x -axis of the slab are shown in Figure 4.10. As the E_z incident field propagates along the slab, a H_z internal field is generated by the chirality of the material. Figures 4.11 and 4.12 show the bistatic echo width and internal fields for the $0.1 \text{ m} \times 2.0 \text{ m}$ chiral slab shown in Figure 4.9 for a TE_z plane wave incident from 30° off the x -axis. The co-polarized bistatic pattern in Figure 4.11 is very similar to the co-polarized bistatic pattern in Figure 4.9. The cross-polarized bistatic patterns are almost identical. In Figure 4.12, the internal fields also show almost the same patterns as in Figure 4.10, except E and H are reversed. As the H_z incident field propagates along the slab, a E_z internal field is generated by the chirality of the material, just as in Figure 4.10.

Figure 4.13 shows an inhomogeneous chiral slab, identical to that shown in Figure 4.9 except that $\xi_c = 0.0005 \text{ A/V}$ for $x > 0$, and $\xi_c = -0.0005 \text{ A/V}$ for $x < 0$, with a TM_z incident plane wave from 30° off the x -axis. The most significant change from Figure 4.9 is that the field scattered back along the x -axis is 20 dB lower. The magnitude of the internal fields along the x -axis of the slab is shown in Figure 4.14, which is similar to Figure 4.10 except that the H_z field, which increased along the slab in Figure 4.10, decreases suddenly at the interface between the two

Chiral Slab

$$\mu_r=2, \epsilon_r=3, \xi_c=0.0005$$

Freq.=300 MHz

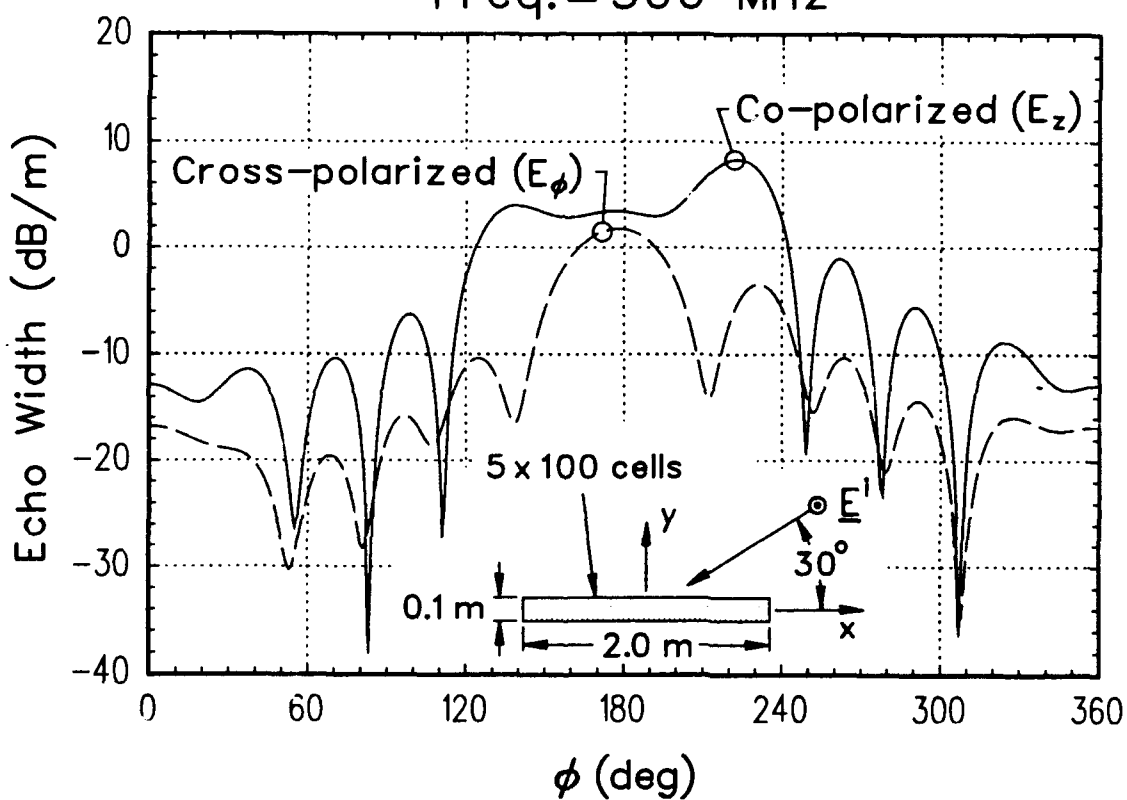


Figure 4.9: The co-polarized and cross-polarized bistatic echo width of a 0.1 m x 2.0 m homogeneous chiral slab for a TM_z plane wave incident at 30° off the x-axis.

Chiral Slab
 $\mu_r=2, \epsilon_r=3, \xi_c=0.0005$
 Freq.=300 MHz

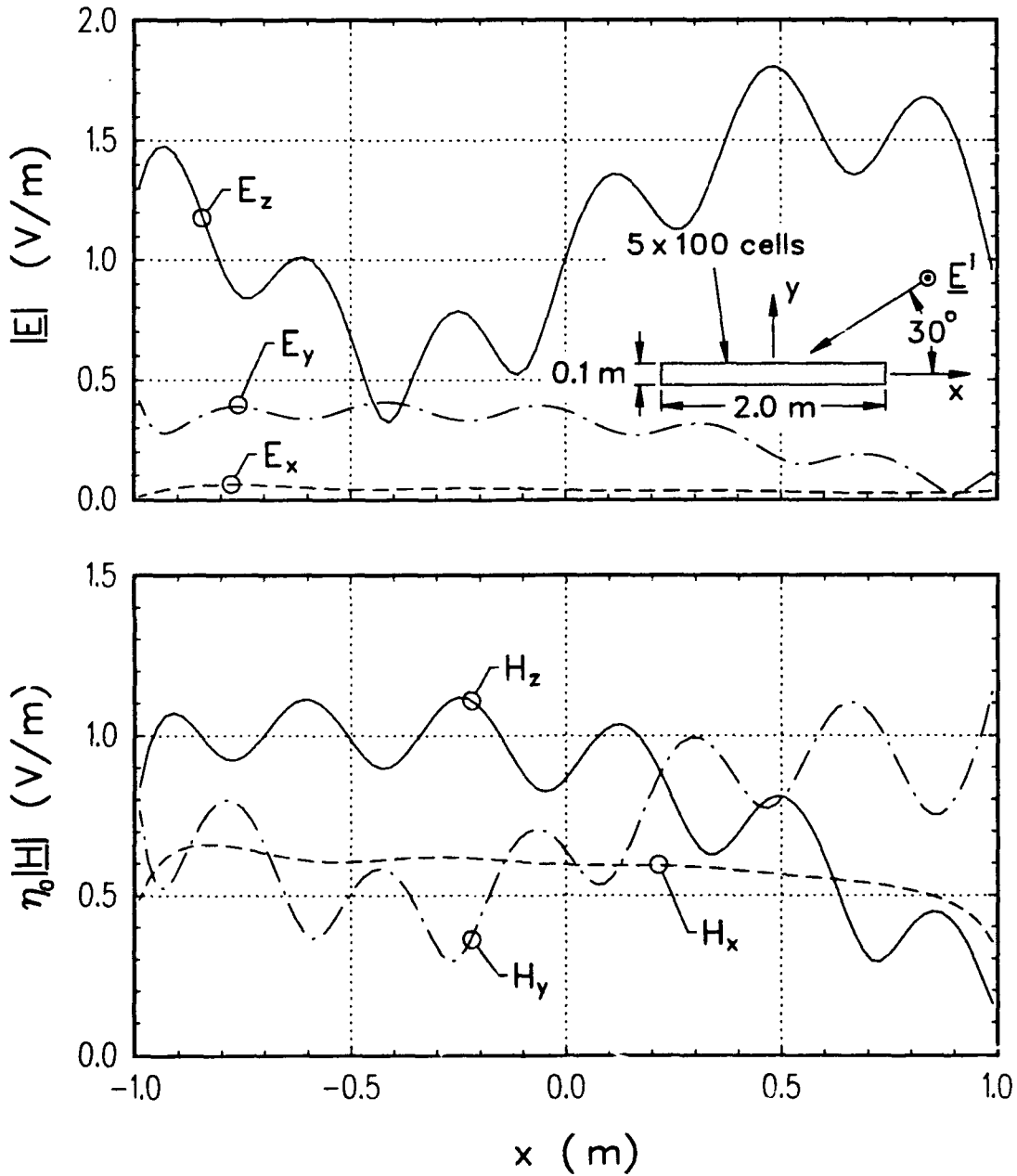


Figure 4.10: Internal fields along $y = 0$ for the homogeneous chiral slab shown in Figure 4.9.

Chiral Slab

$$\mu_r=2, \epsilon_r=3, \xi_c=0.0005$$

Freq.= 300 MHz

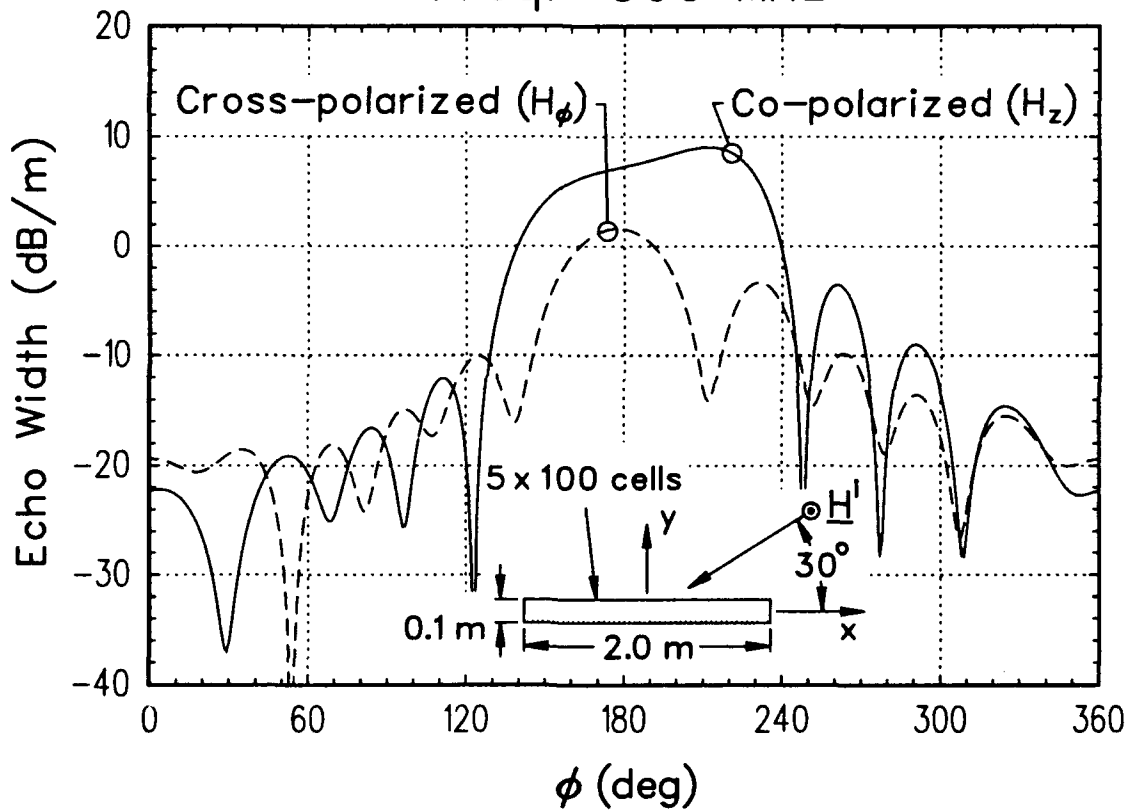


Figure 4.11: The co-polarized and cross-polarized bistatic echo width of a 0.1 m x 2.0 m homogeneous chiral slab for a TE_z plane wave incident at 30° off the x-axis.

Chiral Slab
 $\mu_r=2, \epsilon_r=3, \xi_c=0.0005$
 Freq. = 300 MHz

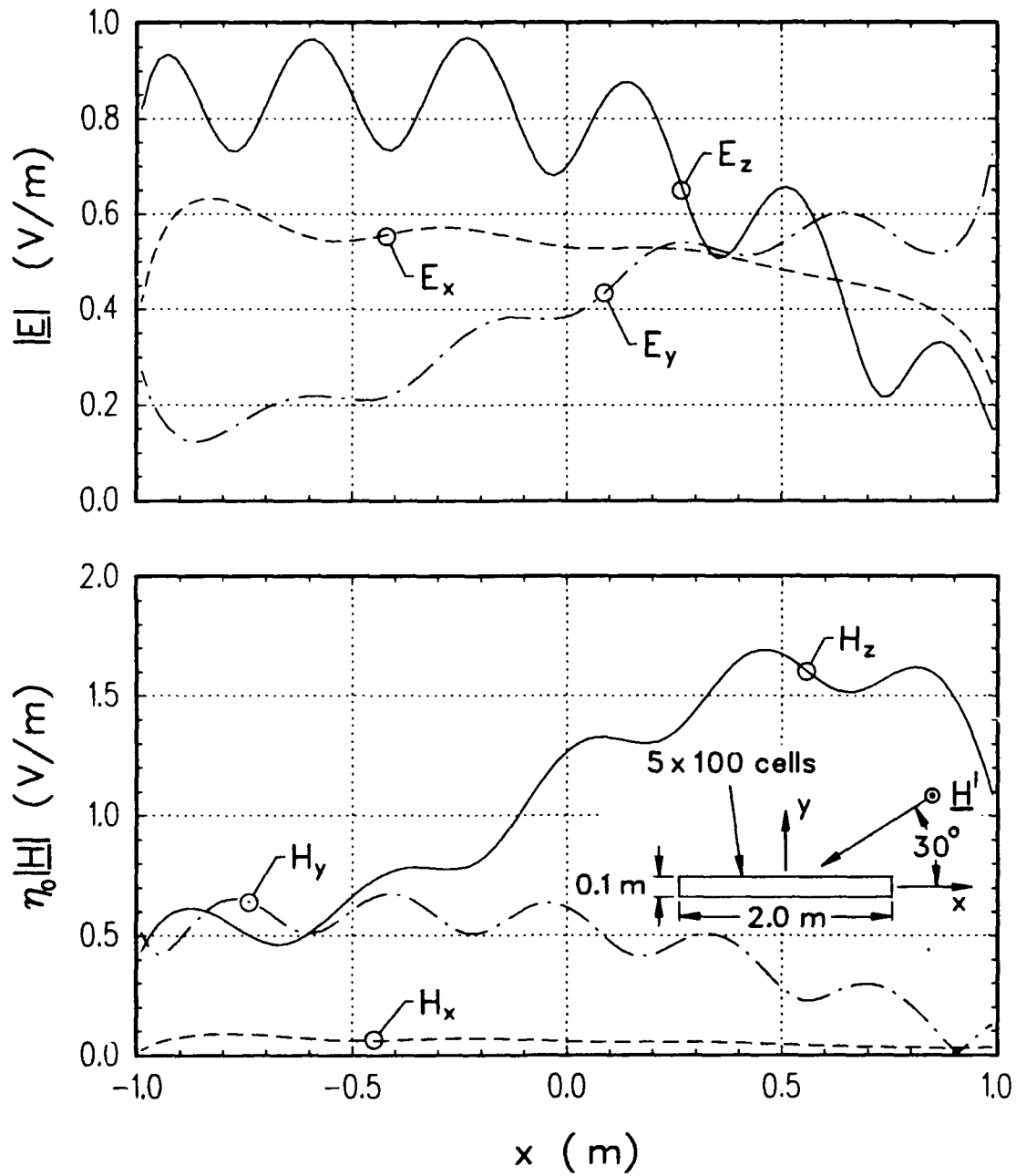


Figure 4.12: Internal fields along $y = 0$ for the homogeneous chiral slab shown in Figure 4.11.

Chiral Slab

$$\mu_r = 2, \quad \epsilon_r = 3$$

Freq. = 300 MHz

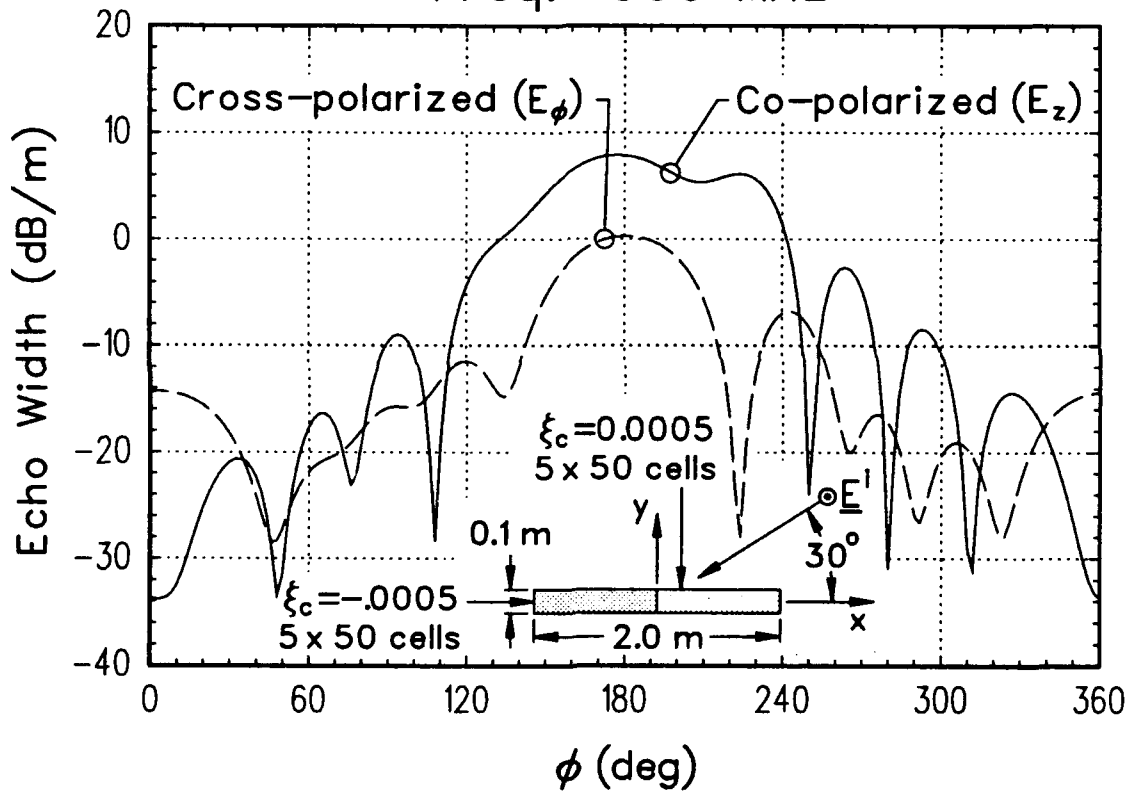


Figure 4.13: The co-polarized and cross-polarized bistatic echo width of a 0.1 m x 2.0 m inhomogeneous chiral slab for a TM_z plane wave incident at 30° off the x-axis.

Chiral Slab
 $\mu_r=2, \epsilon_r=3$
 Freq. = 300 MHz

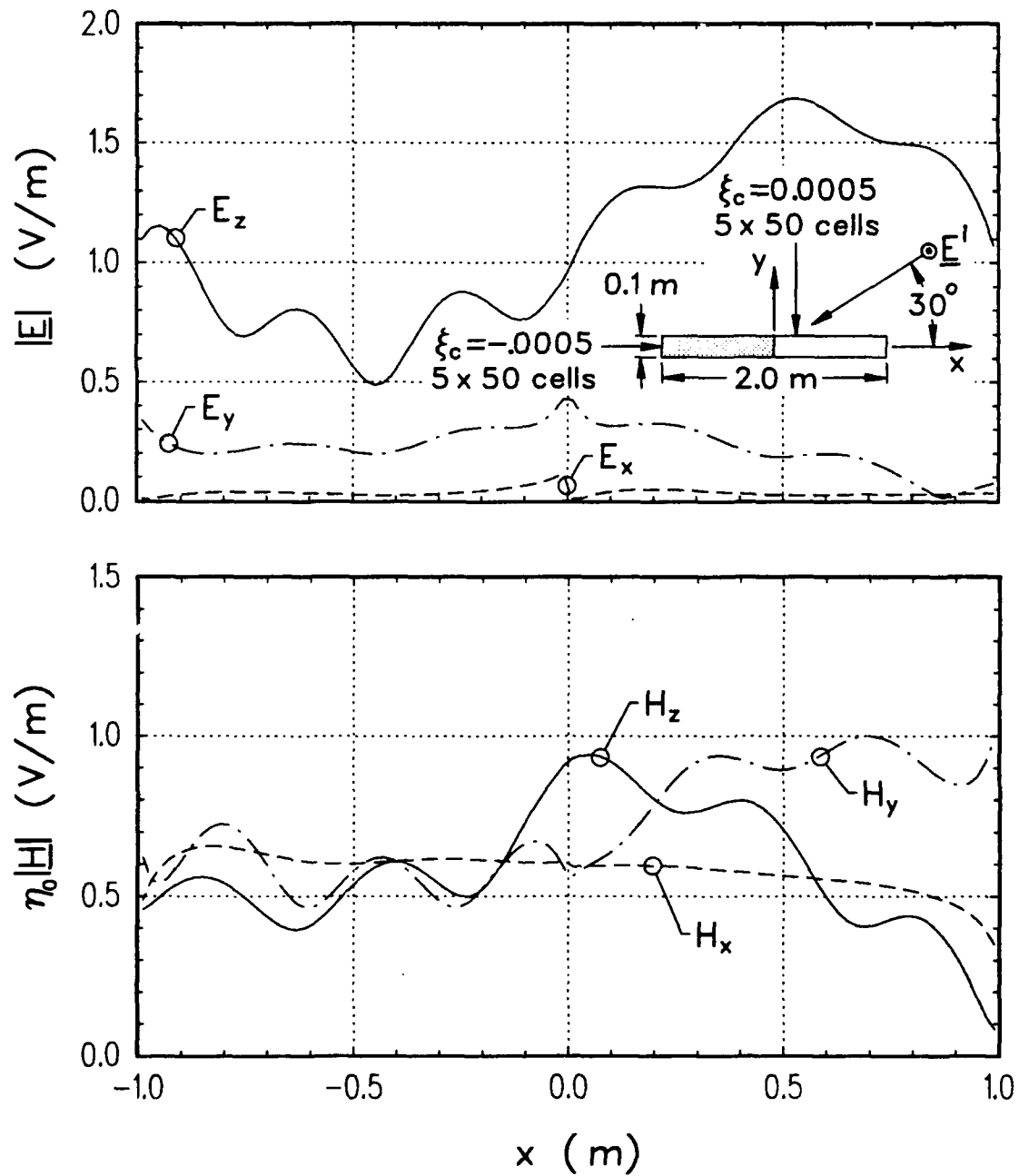


Figure 4.14: Internal fields along $y = 0$ for the inhomogeneous chiral slab shown in Figure 4.13.

chiral materials in Figure 4.14. Figure 4.15 shows the inhomogeneous chiral slab of Figure 4.13 with a TE_Z incident plane wave from 30° off the x -axis. The most significant change from Figure 4.11 is that the field scattered outside the main broadside beam is at least 5 dB higher for both co- and cross-polarized fields. Comparing Figures 4.13 and 4.15, the cross-polarized scattered fields are significantly different, unlike in previous comparisons between the cross-polarized fields for TM_Z and TE_Z incident plane waves. This means that Equation (3.34c), which showed that the cross-polarized bistatic echo widths of circular cylinders for TM_Z and TE_Z incident plane waves are identical, is only true for circular cylinders. However, Figures 4.16 and 4.17 show that the cross-polarized backscattered fields are identical for TM_Z and TE_Z incident plane waves. The numerical results used to generate Figures 4.16 and 4.17 matched within 0.003 dB and 0.01° for magnitude and phase, respectively.

4.5 Half-Plane Numerical Results

This section presents numerical results for TM_Z and TE_Z scattering by two geometries, a chiral slab on a half-plane and a double-wedge covering the tip of a half-plane. All data is at a frequency of 300 MHz. The chiral parameters used in this section obey the limit set in [102] of $|\xi_c| < \sqrt{\epsilon/\mu}$.

Figure 4.18 shows the backscatter echo width pattern for a TM_Z plane wave ($E_z^i = e^{-jk_0(x \cos \phi^i + y \sin \phi^i)}$) incident upon a lossless chiral slab at the tip of a perfectly conducting half-plane. The slab is 1 meter wide and 0.2 meters thick, with parameters of $\epsilon_r = 4.0$, $\mu_r = 1.5$, and $\xi_c = 0.002$ A/V. For comparison, the echo widths of the achiral slab and of the bare half-plane are also shown. Although the half-plane is the dominant scatterer, the presence of the chiral slab does produce a significant change to the echo width. In particular, the chirality produces a cross-polarized component to the echo width which, in the region $\phi^i \leq 120^\circ$, is of comparable magnitude to the co-polarized echo width. This cross-polarized field is a direct result of

Chiral Slab

$$\mu_r = 2, \quad \epsilon_r = 3, \quad \xi_c = 0.0005$$

Freq. = 300 MHz

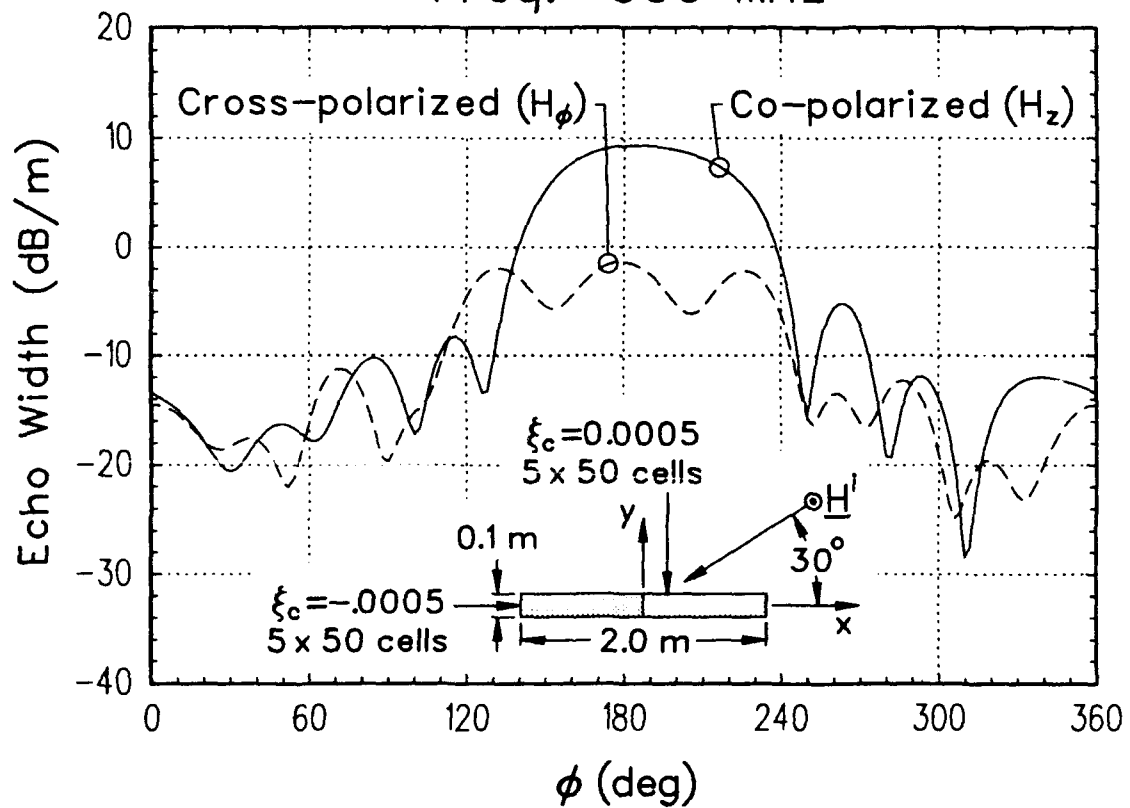


Figure 4.15: The co-polarized and cross-polarized bistatic echo width of a 0.1 m x 2.0 m inhomogeneous chiral slab for a TM_E plane wave incident at 30° off the x-axis.

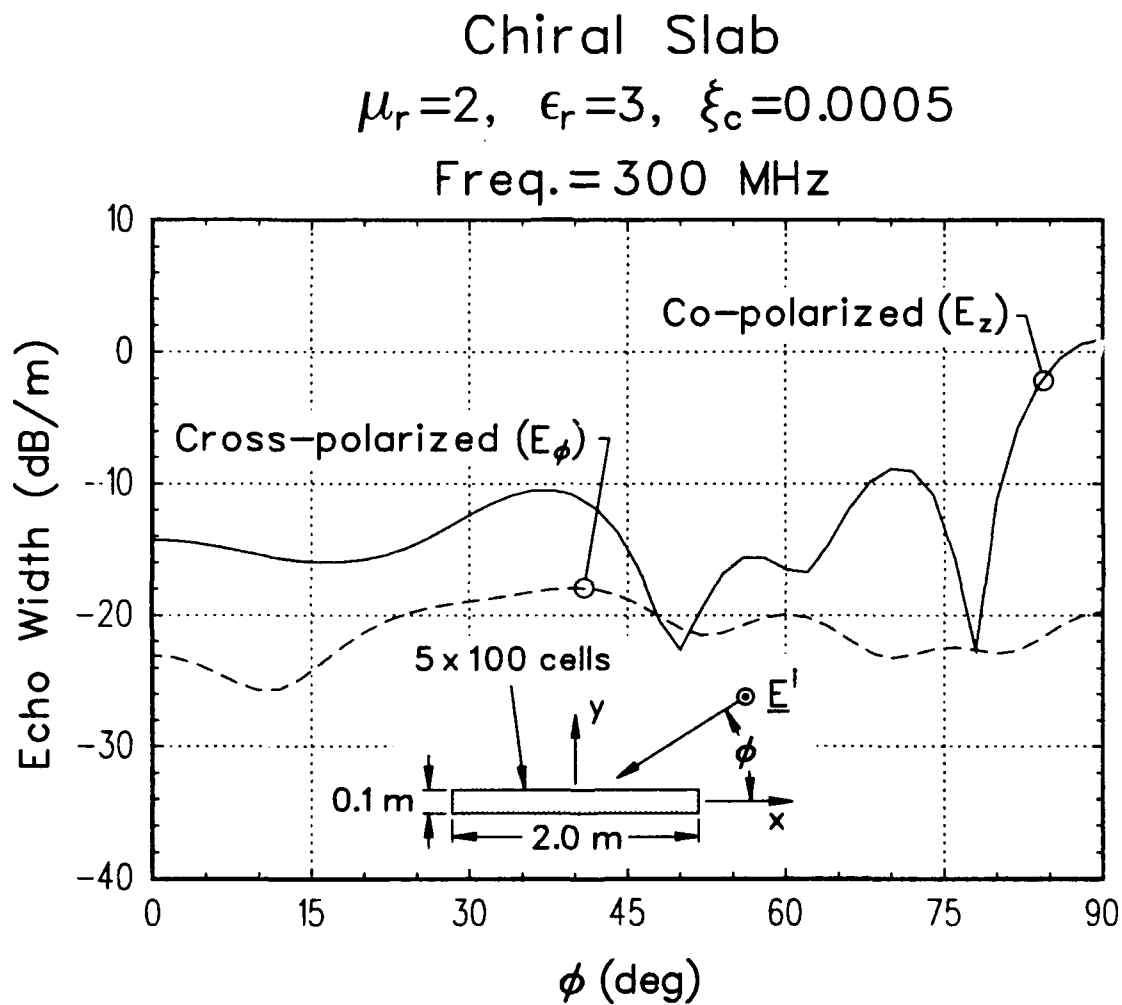


Figure 4.16: The co-polarized and cross-polarized backscatter echo width of a 0.1 m x 2.0 m homogeneous chiral slab for a TM_z plane wave incident at 30° off the x-axis.

Chiral Slab

$$\mu_r = 2, \quad \epsilon_r = 3, \quad \xi_c = 0.0005$$

Freq. = 300 MHz

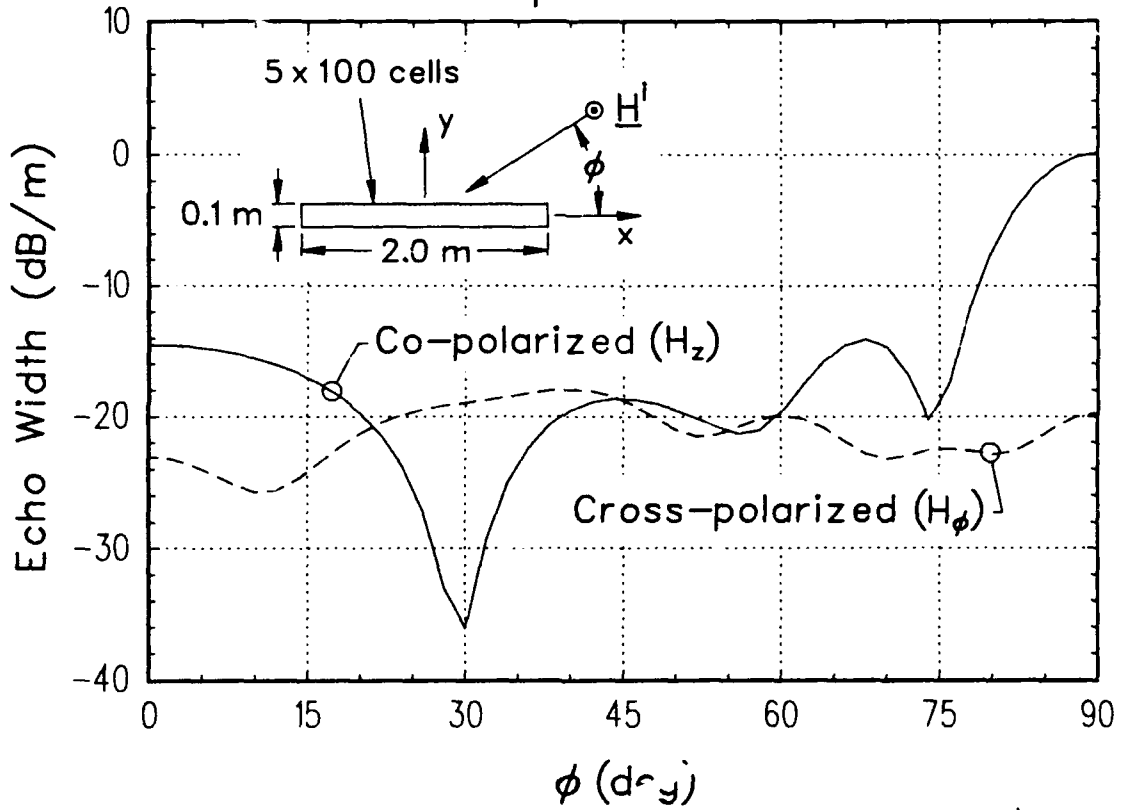


Figure 4.17: The co-polarized and cross-polarized backscatter echo width of a 0.1 m x 2.0 m homogeneous chiral slab for a TE_z plane wave incident at 30° off the x-axis.

Chiral Slab & Half-Plane

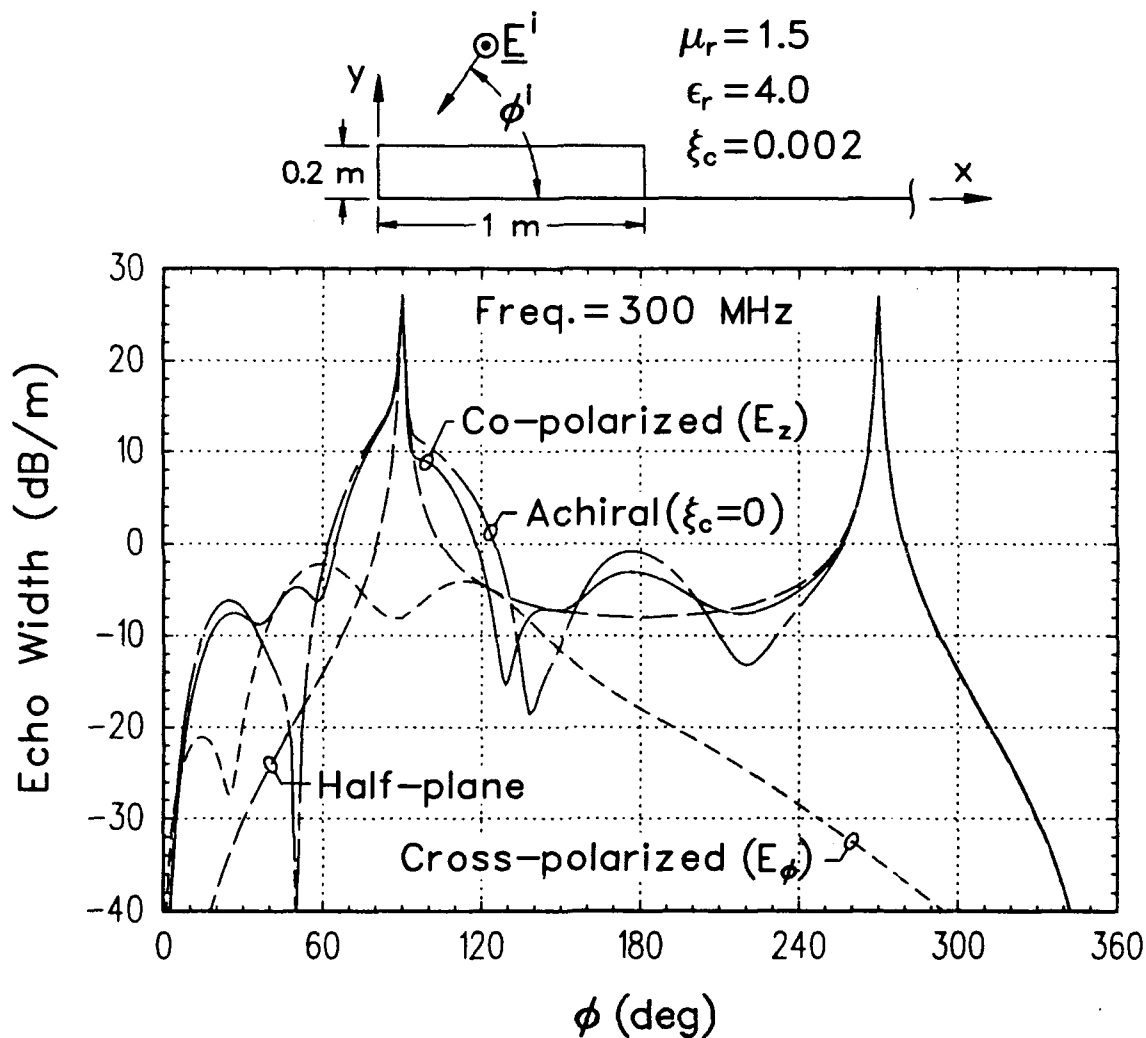


Figure 4.18: The co-polarized and cross-polarized backscatter ($\phi = \phi'$) echo width of a lossless chiral slab at the tip of a perfectly conducting half-plane.

the rotation of polarization which occurs in a chiral medium. The magnitude of the internal fields along the center line ($y = 0.1$ m) of the slab is shown in Figure 4.19 for $\phi' = 60^\circ$. Again, the cross-polarized fields (E_x, E_y, H_z) are a result of the rotation of field polarization in the chiral medium, and are of comparable magnitude to the co-polarized fields (E_z, H_x, H_y).

Figure 4.20 shows the bistatic scattering from a perfectly conducting half-plane with a lossy chiral double-wedge covering the tip. The double-wedge is 2 meters wide and has a maximum thickness of 0.08 meters at the center. The upper graph shows the co-polarized and cross-polarized bistatic echo widths for a TM_z wave incident from 180° ($E_z^i = e^{-jk_0x}$). The bistatic echo width for an identical achiral ($\xi_c = 0$) double-wedge and for the bare half-plane is also shown for comparison. The lower graph displays the same data for a TE_z wave incident from 0° ($H_z^i = e^{jk_0x}$). In each case, the chiral double wedge causes a significant modification to the scattering from the half-plane. For example, for the TM_z case, the chiral wedge reduces the edge on backscatter ($\phi = 180^\circ$) echo width from -8 dB/m to about -60 dB/m, while the achiral value is about -16 dB/m. The chirality also produces a significant cross-polarized component for both the TM_z and TE_z cases. Again, these cross-polarized fields are a direct result of the rotation of polarization in chiral medium.

Chiral Slab & Half-Plane

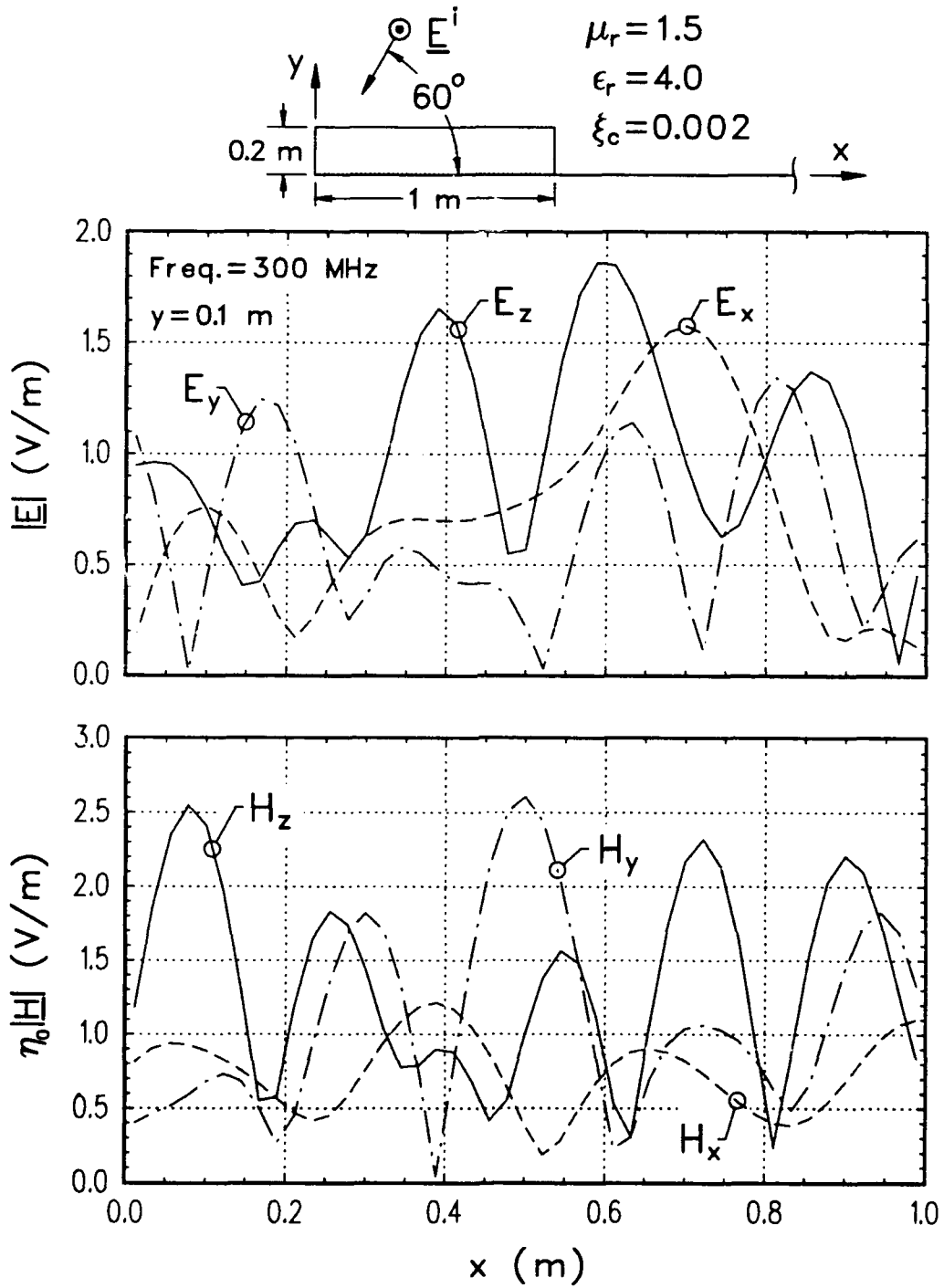


Figure 4.19: Internal fields along $y = 0.1$ meters for the chiral slab and half-plane geometry shown in Figure 4.18 with a TM_z incident wave from 60° .

Chiral Tipped Half-Plane

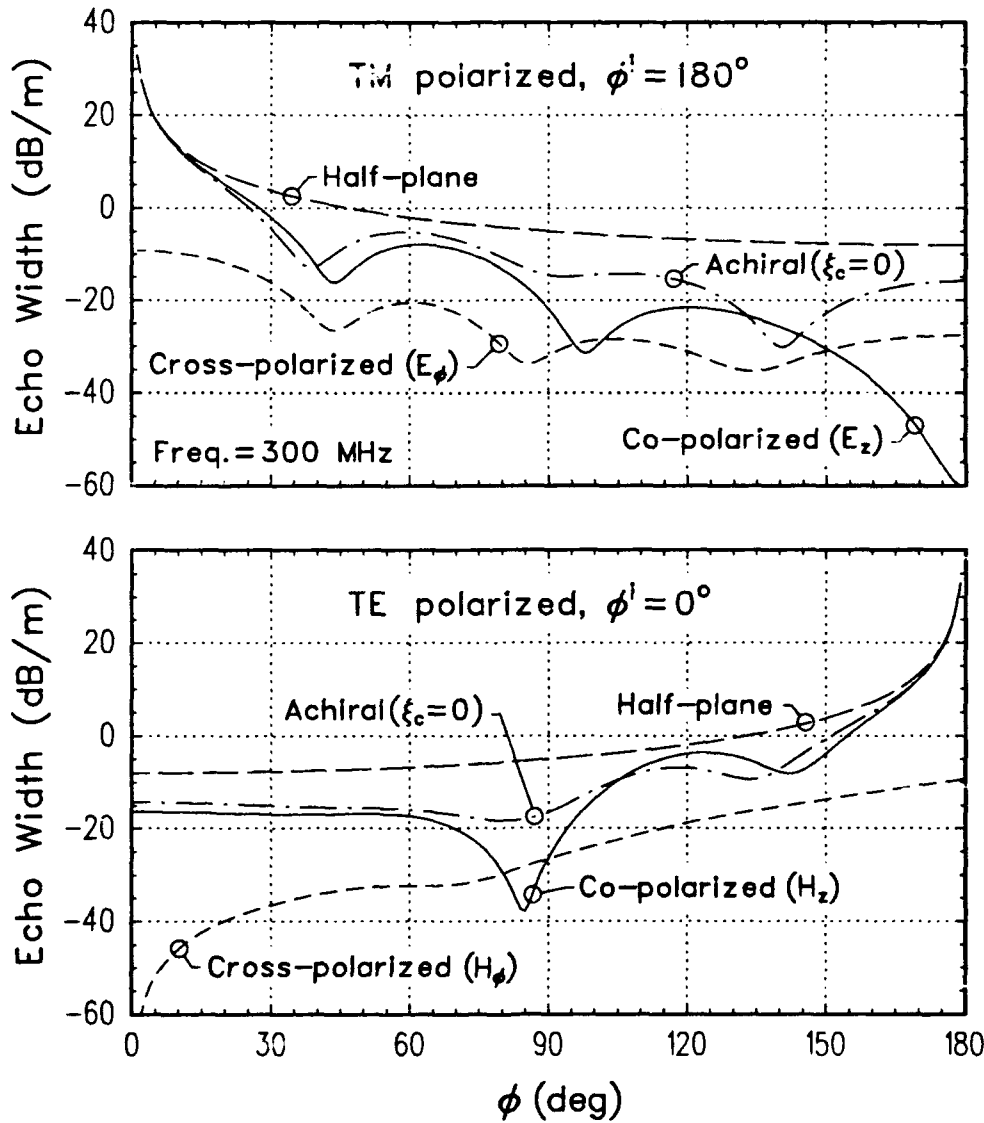
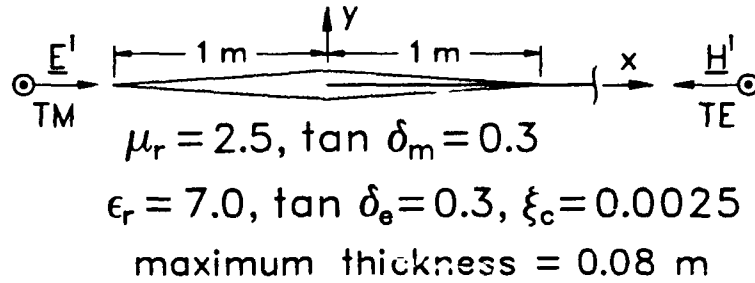


Figure 4.20: The co-polarized and cross-polarized bistatic echo width of a perfectly conducting half-plane with a chiral double-wedge at the tip.

4.6 Summary

This chapter presented a hybrid integral equation method of moments/Green's function solution to the problem of TM_z and TE_z scattering by an inhomogeneous chiral cylinder of arbitrary cross section in free space or in the presence of a perfectly conducting half-plane. The volume equivalence theorem for chiral media was used to formulate a pair of coupled vector integral equations for the equivalent electric and magnetic volume polarization currents representing the chiral cylinder. For chiral cylinders, this pair of vector equations was shown to be equivalent to six coupled scalar equations, which included coupling between the usual TM and TE polarizations. These equations were solved by the method of moments, and numerical data was shown illustrating the convergence and accuracy of the method of moments solution. As in the previous chapter, the chirality of the cylinders caused a significant rotation in the polarization of the scattered fields. The result was that the cross-polarized fields, in the near and far zone, can be as large or larger than the co-polarized fields. In addition, the numerical results showed that the cross-polarized backscatter echo width of at least one noncircular geometry is identical for TM_z and TE_z incident plane waves. An examination of the internal fields of one chiral cylinder showed that the number of cells needed in the method of moments solution increased by a factor of 5. Part of this increase is due to the short wavelength of one of the circular polarizations in chiral media. The remaining increase remains unexplained and may be due to the interaction of the two circular polarizations with different wavelengths.

Chapter 5

A Microstrip Line on a Chiral Substrate

This chapter presents a spectral-domain Galerkin method of moments solution for a microstrip transmission line on a chiral substrate. Most chiral guided wave structures have bifurcated modes [103]–[109], i.e., pairs of modes with the same cutoff frequency. The chiral microstrip line does not have bifurcated modes; thus, the dispersion curves are single valued. However, the longitudinal fields and currents each contain a significant asymmetric component which is not present for an achiral microstrip line. Similarly, the transverse fields and currents both contain a symmetric component which is absent in the achiral case.

The propagation constant and currents for the microstrip line are calculated using the spectral-domain approach [130, 131], which is a Galerkin method of moments solution where the impedance matrix and fields are calculated by numerically evaluating the Fourier transform of a spectral Green's function. This Green's function accounts for the effects of the chiral substrate and the perfectly conducting ground plane. The chiral substrate causes the additional longitudinal asymmetric and transverse symmetric field components, requiring the expansion for the longitudinal and transverse currents to contain both even and odd components. This requirement is satisfied by expanding each current in terms of Chebyshev polynomials weighted

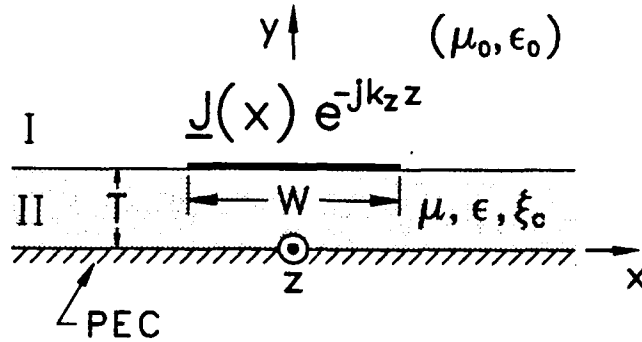


Figure 5.1: Microstrip line on a grounded chiral slab.

by the edge conditions [131]–[135]. A detailed discussion on edge conditions can be found in [136, pp. 385–387].

5.1 Microstrip Field Expansions

The geometry of the problem and the field expansions for each region are presented in this section. The open microstrip line on a grounded chiral slab is shown in Figure 5.1, where the slab (region II) has constitutive parameters (μ, ϵ, ξ_c) and thickness T . The right and left wave numbers, k_R and k_L , and the wave impedance, η_c , are defined in Equations (2.12) and (2.11). The microstrip line is W wide, infinitely thin, and perfectly conducting with a current distribution of $\mathbf{J}(\mathbf{x})e^{-jk_z z}$. Region I ($y > T$) is free space, with parameters (μ_0, ϵ_0) and wave number $k_0 = \omega\sqrt{\mu_0\epsilon_0}$.

5.1.1 Field Expansions in the Free Space Region

First, consider the fields in region I. Since this is a source-free achiral region, these fields may be expanded as the sum of a TM_y field and a TE_y field [115, sec. 3-12]. These fields may be constructed from the magnetic and electric vector potentials

given by

$$\mathbf{A} = \frac{\hat{\mathbf{y}}}{2\pi} e^{jk_y T} \int_{-\infty}^{\infty} \bar{A} e^{-j(k_x x + k_y y + k_z z)} dk_x \quad (5.1a)$$

$$\mathbf{F} = \frac{\hat{\mathbf{y}}}{2\pi} e^{jk_y T} \int_{-\infty}^{\infty} \bar{F} e^{-j(k_x x + k_y y + k_z z)} dk_x \quad (5.1b)$$

where $k_y = -j\sqrt{k_x^2 + k_z^2 - k_0^2}$, satisfying the wave equation and the radiation condition (see Appendix E). The functions \bar{A} and \bar{F} are the Fourier transforms of A_y and F_y with the term $e^{-j(k_y y + k_z z)}$ factored out, and are determined by enforcing the boundary conditions at $y = T$. The TM_y fields are obtained from Equation (5.1a) using $\mathbf{H} = \nabla \times \mathbf{A}$

$$H_x = \frac{j}{2\pi} e^{jk_y T} \int_{-\infty}^{\infty} k_z \bar{A} e^{-j(k_x x + k_y y + k_z z)} dk_x \quad (5.2a)$$

$$H_y = 0 \quad (5.2b)$$

$$H_z = -\frac{j}{2\pi} e^{jk_y T} \int_{-\infty}^{\infty} k_x \bar{A} e^{-j(k_x x + k_y y + k_z z)} dk_x \quad (5.2c)$$

$$E_x = \frac{j}{2\pi} \frac{e^{jk_y T}}{\omega \epsilon_0} \int_{-\infty}^{\infty} k_x k_y \bar{A} e^{-j(k_x x + k_y y + k_z z)} dk_x \quad (5.2d)$$

$$E_y = -\frac{j}{2\pi} \frac{e^{jk_y T}}{\omega \epsilon_0} \int_{-\infty}^{\infty} (k_x^2 + k_z^2) \bar{A} e^{-j(k_x x + k_y y + k_z z)} dk_x \quad (5.2e)$$

$$E_z = \frac{j}{2\pi} \frac{e^{jk_y T}}{\omega \epsilon_0} \int_{-\infty}^{\infty} k_y k_z \bar{A} e^{-j(k_x x + k_y y + k_z z)} dk_x. \quad (5.2f)$$

The TE_y fields are obtained from Equation (5.1b) using $\mathbf{E} = -\nabla \times \mathbf{F}$

$$E_x = -\frac{j}{2\pi} e^{jk_y T} \int_{-\infty}^{\infty} k_z \bar{F} e^{-j(k_x x + k_y y + k_z z)} dk_x \quad (5.3a)$$

$$E_y = 0 \quad (5.3b)$$

$$E_z = \frac{j}{2\pi} e^{jk_y T} \int_{-\infty}^{\infty} k_x \bar{F} e^{-j(k_x x + k_y y + k_z z)} dk_x \quad (5.3c)$$

$$H_x = \frac{j}{2\pi} \frac{e^{jk_y T}}{\omega \mu_0} \int_{-\infty}^{\infty} k_x k_y \tilde{F} e^{-j(k_x x + k_y y + k_z z)} dk_x \quad (5.3d)$$

$$H_y = -\frac{j}{2\pi} \frac{e^{jk_y T}}{\omega \mu_0} \int_{-\infty}^{\infty} (k_x^2 + k_z^2) \tilde{F} e^{-j(k_x x + k_y y + k_z z)} dk_x \quad (5.3e)$$

$$H_z = \frac{j}{2\pi} \frac{e^{jk_y T}}{\omega \mu_0} \int_{-\infty}^{\infty} k_y k_z \tilde{F} e^{-j(k_x x + k_y y + k_z z)} dk_x. \quad (5.3f)$$

5.1.2 Field Expansions in the Chiral Slab

In the chiral slab, the fields are expanded in terms of the right and left circular vector potentials developed in Section 2.3. To satisfy the boundary conditions of zero tangential electric field at $y = 0$, a quasi-TM_y field can be formed by the sum of a RC_y field and a LC_y field. These RC_y and LC_y fields are formed from the vector potentials

$$\mathbf{R}_{y,M} = \frac{\hat{y}}{2\pi} \int_{-\infty}^{\infty} \tilde{Q}_M \cos k_{y,R} y e^{-j(k_x x + k_z z)} dk_x \quad (5.4a)$$

$$\mathbf{L}_{y,M} = -\frac{\hat{y}}{2\pi} \int_{-\infty}^{\infty} \tilde{Q}_M \cos k_{y,L} y e^{-j(k_x x + k_z z)} dk_x \quad (5.4b)$$

where $k_{y,R} = -j\sqrt{k_x^2 + k_z^2 - k_R^2}$ and $k_{y,L} = -j\sqrt{k_x^2 + k_z^2 - k_L^2}$. The resulting field is a TM_y field if $\xi_c = 0$; hence, the name quasi-TM_y. Similarly, a quasi-TE_y field can be formed from the vector potentials

$$\mathbf{R}_{y,E} = \frac{\hat{y}}{2\pi} \int_{-\infty}^{\infty} \tilde{Q}_E \frac{k_R}{k_{y,R}} \sin k_{y,R} y e^{-j(k_x x + k_z z)} dk_x \quad (5.5a)$$

$$\mathbf{L}_{y,E} = \frac{\hat{y}}{2\pi} \int_{-\infty}^{\infty} \tilde{Q}_E \frac{k_L}{k_{y,L}} \sin k_{y,L} y e^{-j(k_x x + k_z z)} dk_x. \quad (5.5b)$$

The functions \tilde{Q}_M and \tilde{Q}_E are determined when enforcing the boundary conditions at $y = T$.

The quasi-TM_y electric fields are calculated by substituting the RC_y and LC_y vector potentials from Equation (5.4) into Equation (2.24) of Section 2.3, producing

$$E_{R,x} = \frac{j}{2\pi} \int_{-\infty}^{\infty} \bar{Q}_M \left(\frac{k_x k_{y,R}}{k_R} \sin k_{y,R} y + k_z \cos k_{y,R} y \right) e^{-j(k_x x + k_z z)} dk_x \quad (5.6a)$$

$$E_{R,y} = \frac{1}{2\pi} \int_{-\infty}^{\infty} \bar{Q}_M \frac{k_x^2 + k_z^2}{k_R} \cos k_{y,R} y e^{-j(k_x x + k_z z)} dk_x \quad (5.6b)$$

$$E_{R,z} = \frac{j}{2\pi} \int_{-\infty}^{\infty} \bar{Q}_M \left(\frac{k_z k_{y,R}}{k_R} \sin k_{y,R} y - k_x \cos k_{y,R} y \right) e^{-j(k_x x + k_z z)} dk_x \quad (5.6c)$$

$$E_{L,x} = \frac{j}{2\pi} \int_{-\infty}^{\infty} \bar{Q}_M \left(\frac{k_x k_{y,L}}{k_L} \sin k_{y,L} y - k_z \cos k_{y,L} y \right) e^{-j(k_x x + k_z z)} dk_x \quad (5.6d)$$

$$E_{L,y} = \frac{1}{2\pi} \int_{-\infty}^{\infty} \bar{Q}_M \frac{k_x^2 + k_z^2}{k_L} \cos k_{y,L} y e^{-j(k_x x + k_z z)} dk_x \quad (5.6e)$$

$$E_{L,z} = \frac{j}{2\pi} \int_{-\infty}^{\infty} \bar{Q}_M \left(\frac{k_z k_{y,L}}{k_L} \sin k_{y,L} y + k_x \cos k_{y,L} y \right) e^{-j(k_x x + k_z z)} dk_x \quad (5.6f)$$

Similarly, the quasi-TE_y electric fields are calculated by substituting the RC_y and LC_y vector potentials from Equation (5.5) into Equation (2.24), producing

$$E_{R,x} = \frac{j}{2\pi} \int_{-\infty}^{\infty} \bar{Q}_E \left(\frac{k_z k_R}{k_{y,R}} \sin k_{y,R} y - k_x \cos k_{y,R} y \right) e^{-j(k_x x + k_z z)} dk_x \quad (5.7a)$$

$$E_{R,y} = \frac{1}{2\pi} \int_{-\infty}^{\infty} \bar{Q}_E \frac{k_x^2 + k_z^2}{k_{y,R}} \sin k_{y,R} y e^{-j(k_x x + k_z z)} dk_x \quad (5.7b)$$

$$E_{R,z} = \frac{j}{2\pi} \int_{-\infty}^{\infty} \bar{Q}_E \left(-\frac{k_x k_R}{k_{y,R}} \sin k_{y,R} y - k_z \cos k_{y,R} y \right) e^{-j(k_x x + k_z z)} dk_x \quad (5.7c)$$

$$E_{L,x} = \frac{j}{2\pi} \int_{-\infty}^{\infty} \bar{Q}_E \left(\frac{k_z k_L}{k_{y,L}} \sin k_{y,L} y + k_x \cos k_{y,L} y \right) e^{-j(k_x x + k_z z)} dk_x \quad (5.7d)$$

$$E_{L,y} = -\frac{1}{2\pi} \int_{-\infty}^{\infty} \bar{Q}_E \frac{k_x^2 + k_z^2}{k_{y,L}} \sin k_{y,L} y e^{-j(k_x x + k_z z)} dk_x \quad (5.7e)$$

$$E_{L,z} = \frac{j}{2\pi} \int_{-\infty}^{\infty} \bar{Q}_E \left(-\frac{k_x k_L}{k_{y,L}} \sin k_{y,L} y + k_z \cos k_{y,L} y \right) e^{-j(k_x x + k_z z)} dk_x. \quad (5.7f)$$

The magnetic fields can now be determined using Equation (2.18) of Section 2.2

$$\begin{pmatrix} \mathbf{H}_R \\ \mathbf{H}_L \end{pmatrix} = \frac{j}{\eta_c} \begin{pmatrix} \mathbf{E}_R \\ -\mathbf{E}_L \end{pmatrix}. \quad (5.8)$$

5.2 Coefficients of the Field Expansions

This section presents the solution for the coefficients in the field expansions. Once these coefficients are known the fields may be calculated in any region. The coefficients are determined by enforcing the boundary conditions at the interface of $y = T$:

$$E_x^I = E_x^{II} \quad (5.9a)$$

$$E_z^I = E_z^{II} \quad (5.9b)$$

$$H_x^I = H_x^{II} - J_x(x) e^{-jk_z z} \quad (5.9c)$$

$$H_z^I = H_z^{II} + J_z(x) e^{-jk_z z} \quad (5.9d)$$

where $J_x(x)$ and $J_z(x)$ are the components of the current $\mathbf{J}(x)$ on the microstrip line. The fields in region I ($E_x^I, E_z^I, H_x^I, H_z^I$) are the sum of the appropriate field components from Equations (5.2) and (5.3). The electric fields in region II (E_x^{II}, E_z^{II}) are the sum of the appropriate field components from Equations (5.6) and (5.7). The magnetic fields in region II (H_x^{II}, H_z^{II}) are determined using the same field components and Equation (5.8).

To solve the boundary condition equations using the spectral-domain approach [130, 131], Equation (5.9) is Fourier transformed from the space domain (x) into the spectral domain (k_x), evaluated at $y = T$, and after some simplification, results in

$$\frac{k_x k_y}{\omega \epsilon_0} \bar{A} - k_z \bar{F} = \bar{Q}_M(k_x C^+ + k_z A^-) + \bar{Q}_E(k_z B^+ - k_x A^-) \quad (5.10a)$$

$$\frac{k_y k_z}{\omega \epsilon_0} \bar{A} + k_x \bar{F} = \bar{Q}_M (k_z C^+ - k_x A^-) + \bar{Q}_E (-k_x B^+ - k_z A^-) \quad (5.10b)$$

$$j k_z \bar{A} + j \frac{k_x k_y}{\omega \mu_0} \bar{F} = \frac{\bar{Q}_M}{\eta_c} (-k_x C^- - k_x A^+) + \frac{\bar{Q}_E}{\eta_c} (-k_z B^- + k_x A^+) - \bar{J}_z \quad (5.10c)$$

$$-j k_x \bar{A} + j \frac{k_y k_z}{\omega \mu_0} \bar{F} = \frac{\bar{Q}_M}{\eta_c} (-k_z C^- + k_x A^+) + \frac{\bar{Q}_E}{\eta_c} (k_x B^- + k_z A^+) + \bar{J}_x \quad (5.10d)$$

where

$$A^\pm = \cos k_{y,R} T \pm \cos k_{y,L} T \quad (5.11a)$$

$$B^\pm = \frac{k_R}{k_{y,R}} \sin k_{y,R} T \pm \frac{k_L}{k_{y,L}} \sin k_{y,L} T \quad (5.11b)$$

$$C^\pm = \frac{k_{y,R}}{k_R} \sin k_{y,R} T \pm \frac{k_{y,L}}{k_L} \sin k_{y,L} T. \quad (5.11c)$$

The quantities \bar{J}_x and \bar{J}_z are the Fourier transforms of the components of $\mathbf{J}(\mathbf{x})$ and are defined by

$$J_{x,z}(\mathbf{x}) = \frac{1}{2\pi} \int_{-\infty}^{\infty} \bar{J}_{x,z}(k_x) e^{-j k_x x} dk_x. \quad (5.12)$$

Equation (5.10) can be rewritten as

$$\frac{k_y}{\omega \epsilon_0} \bar{A} = \bar{Q}_M C^+ - \bar{Q}_E A^- \quad (5.13a)$$

$$-\bar{F} = \bar{Q}_M A^- + \bar{Q}_E B^+ \quad (5.13b)$$

$$-j \frac{k_y}{\omega \mu_0} \bar{F} = \bar{Q}_M \frac{C^-}{\eta_c} - \bar{Q}_E \frac{A^+}{\eta_c} + \frac{k_x \bar{J}_z - k_z \bar{J}_x}{k_x^2 + k_z^2} \quad (5.13c)$$

$$j \bar{A} = -\bar{Q}_M \frac{A^+}{\eta_c} - \bar{Q}_E \frac{B^-}{\eta_c} - \frac{k_z \bar{J}_z + k_x \bar{J}_x}{k_x^2 + k_z^2} \quad (5.13d)$$

where, for example, Equation (5.13a) was obtained multiplying Equation (5.10a) by k_x and Equation (5.10b) by k_z , adding these products, and dividing through by $k_x^2 + k_z^2$. After eliminating \bar{A} and \bar{F} , Equation (5.13) can be written in matrix form as

$$\begin{bmatrix} j \frac{\omega \epsilon_0}{k_y} C^+ + \frac{A^+}{\eta_c} & -j \frac{\omega \epsilon_0}{k_y} A^- + \frac{B^+}{\eta_c} \\ j \frac{k_y}{\omega \mu_0} A^- - \frac{C^-}{\eta_c} & j \frac{k_y}{\omega \mu_0} B^+ + \frac{A^+}{\eta_c} \end{bmatrix} \begin{bmatrix} \bar{Q}_M \\ \bar{Q}_E \end{bmatrix} = \frac{1}{k_x^2 + k_z^2} \begin{bmatrix} -k_z \bar{J}_z - k_x \bar{J}_x \\ k_x \bar{J}_z - k_z \bar{J}_x \end{bmatrix}. \quad (5.14)$$

Equation (5.14) can now be solved for \bar{Q}_M and \bar{Q}_E . In order to find the fields due to the \hat{x} and \hat{z} components of the current, \bar{Q}_M and \bar{Q}_E are written as

$$\bar{Q}_M = \bar{Q}_{M,x} + \bar{Q}_{M,z} \quad (5.15a)$$

$$\bar{Q}_E = \bar{Q}_{E,x} + \bar{Q}_{E,z} \quad (5.15b)$$

where

$$\bar{Q}_{M,x} = \frac{\bar{J}_x}{2\Delta} \left[-k_x \left(j \frac{k_y}{\omega\mu_0} B^+ + \frac{A^+}{\eta_c} \right) - k_z \left(j \frac{\omega\epsilon_0}{k_y} A^- - \frac{B^-}{\eta_c} \right) \right] \quad (5.16a)$$

$$\bar{Q}_{M,z} = \frac{\bar{J}_z}{2\Delta} \left[-k_z \left(j \frac{k_y}{\omega\mu_0} B^+ + \frac{A^+}{\eta_c} \right) + k_x \left(j \frac{\omega\epsilon_0}{k_y} A^- - \frac{B^-}{\eta_c} \right) \right] \quad (5.16b)$$

$$\bar{Q}_{E,x} = \frac{\bar{J}_x}{2\Delta} \left[-k_z \left(j \frac{\omega\epsilon_0}{k_y} C^+ + \frac{A^+}{\eta_c} \right) + k_x \left(j \frac{k_y}{\omega\mu_0} A^- - \frac{C^-}{\eta_c} \right) \right] \quad (5.16c)$$

$$\bar{Q}_{E,z} = \frac{\bar{J}_z}{2\Delta} \left[k_x \left(j \frac{\omega\epsilon_0}{k_y} C^+ + \frac{A^+}{\eta_c} \right) + k_z \left(j \frac{k_y}{\omega\mu_0} A^- - \frac{C^-}{\eta_c} \right) \right] \quad (5.16d)$$

$$(5.16e)$$

and

$$\Delta = (k_x^2 + k_z^2) \left\{ \left[\frac{\epsilon_c}{\mu}(1+S) - \frac{\epsilon_0}{\mu_0}(1-S) \right] + j \left[\frac{k_2 \epsilon_0}{k_y \mu} U + \frac{k_y \epsilon_c}{k_2 \mu_0} V \right] \right\} \quad (5.17a)$$

$$S = \cos k_{y,R} T \cos k_{y,L} T - G^+ \quad (5.17b)$$

$$G^\pm = \frac{1}{2} \left(\frac{k_R}{k_{y,R}} \frac{k_{y,L}}{k_L} \pm \frac{k_{y,R}}{k_R} \frac{k_L}{k_{y,L}} \right) \sin k_{y,R} T \sin k_{y,L} T \quad (5.17c)$$

$$U = \frac{k_{y,R}}{k_R} \sin k_{y,R} T \cos k_{y,L} T + \frac{k_{y,L}}{k_L} \sin k_{y,L} T \cos k_{y,R} T \quad (5.17d)$$

$$V = \frac{k_R}{k_{y,R}} \sin k_{y,R} T \cos k_{y,L} T + \frac{k_L}{k_{y,L}} \sin k_{y,L} T \cos k_{y,R} T \quad (5.17e)$$

with $k_2 = \omega \sqrt{\mu \epsilon_c} = (k_R + k_L)/2$.

5.3 Electric Fields at the Interface

This section uses the results of the previous section to calculate the E_x and E_z fields at the interface, which are used in the method of moments solution for the

propagation constant k_z and the current $\mathbf{J}(\mathbf{x})$ on the microstrip line. These fields are presented below in terms of the even and odd components of the Fourier transforms of these fields generated by $\hat{\mathbf{x}}$ and $\hat{\mathbf{z}}$ polarized traveling wave line sources at the center of the strip ($x = 0, y = T$)

$$\tilde{E}_{x,e}^{J_z} = \frac{1}{\Delta} \left[\left(k_x^2 \frac{k_y}{\omega \mu_0} + k_z^2 \frac{\omega \epsilon_0}{k_y} \right) (1 - S) - \frac{j}{\eta_c} (k_x^2 U + k_z^2 V) \right] \quad (5.18a)$$

$$\tilde{E}_{z,e}^{J_z} = \frac{1}{\Delta} \left[\left(k_x^2 \frac{\omega \epsilon_0}{k_y} + k_z^2 \frac{k_y}{\omega \mu_0} \right) (1 - S) - \frac{j}{\eta_c} (k_x^2 V + k_z^2 U) \right] \quad (5.18b)$$

$$\tilde{E}_{z,o}^{J_z} = \tilde{E}_{x,o}^{J_z} = \frac{k_x k_z}{\Delta} \left[\left(\frac{k_y}{\omega \mu_0} - \frac{\omega \epsilon_0}{k_y} \right) (1 - S) + \frac{j}{\eta_c} (V - U) \right] \quad (5.18c)$$

$$\tilde{E}_{x,o}^{J_z} = -\tilde{E}_{z,o}^{J_z} = j \frac{2k_x k_z}{\eta_c \Delta} G^- \quad (5.18d)$$

$$\tilde{E}_{z,e}^{J_z} = \tilde{E}_{x,e}^{J_z} = j \frac{k_z^2 - k_x^2}{\eta_c \Delta} G^- \quad (5.18e)$$

where G^- , S , U , and V are defined in Equation (5.17). For example, the E_x field generated by the surface current $J_z(\mathbf{x})$ is given by

$$E_x^{J_z}(\mathbf{x}) = \frac{1}{2\pi} \int_{-\infty}^{\infty} \left[\tilde{E}_{x,e}^{J_z}(k_x) + \tilde{E}_{x,o}^{J_z}(k_x) \right] \tilde{J}_z(k_x) e^{-j(k_x x + k_z z)} dk_x \quad (5.19)$$

where $\tilde{E}_{x,e}^{J_z}$ and $\tilde{E}_{x,o}^{J_z}$ are the even and odd components of the Fourier transform of the E_x field due to a $\hat{\mathbf{z}}$ polarized traveling wave line source at $x = 0$ and $y = T$. In a conventional achiral microstrip line $\tilde{E}_{x,o}^{J_z}$, $\tilde{E}_{z,o}^{J_z}$, $\tilde{E}_{z,e}^{J_z}$, and $\tilde{E}_{x,e}^{J_z}$ are zero, causing $J_z(\mathbf{x})$ and $J_x(\mathbf{x})$ to be even and odd functions of x , respectively. However, this is not true for a chiral microstrip line, thereby requiring a set of even and odd expansion functions for each current component.

5.4 Method of Moments Solution

The basis functions and impedance matrix for a Galerkin method of moments solution are presented in this section. The $\hat{\mathbf{x}}$ and $\hat{\mathbf{z}}$ components of the current are expanded as

$$J_x(\mathbf{x}) e^{-jk_z z} = \sum_{n=0}^{N_x} I_{x,n} J_{x,n}(\mathbf{x}) e^{-jk_z z} \quad (5.20a)$$

$$J_z(\mathbf{x})e^{-jk_z z} = \sum_{n=0}^{N_z} I_{z,n} J_{z,n}(\mathbf{x}) e^{-jk_z z} \quad (5.20b)$$

where $I_{x,n}$ and $I_{z,n}$ are the unknown coefficients. The basis functions $J_{x,n}$ and $J_{z,n}$ are Chebyshev polynomials weighted by the edge conditions [131]-[135]

$$J_{x,n}(x) = \frac{4}{\pi W} \frac{U_n(2x/W)}{n+1} \sqrt{1 - (2x/W)^2} \quad (5.21a)$$

$$J_{z,n}(x) = \frac{2}{\pi W} T_n(2x/W) / \sqrt{1 - (2x/W)^2} \quad (5.21b)$$

where $T_n(x)$ and $U_n(x)$ are Chebyshev polynomials of the first and second kinds, respectively. A detailed discussion of edge conditions is presented by Van Bladel [136, pp. 385-387]. From Appendix F, the Fourier transforms of the basis functions are

$$\tilde{J}_{x,n}(k_x) = 2j^n \frac{J_{n+1}(k_x W/2)}{k_x W/2} \quad (5.22a)$$

$$\tilde{J}_{z,n}(k_x) = j^n J_n(k_x W/2) \quad (5.22b)$$

where $J_n(x)$ is an n th-order Bessel function. The first four basis functions for each current component are shown in Figure 5.2, where the functions have been normalized using $x' = x/W$. The primary advantage of these basis functions is that they have closed form Fourier transforms while matching the edge conditions. In addition, although these basis functions are not orthogonal, they are sufficiently orthogonal that the $I_{x,n}$ and $I_{z,n}$ of Equation (5.20) are relatively insensitive to the number of terms used in the expansion. This is shown in Table 5.1 of Section 5.6.

The coefficients $I_{x,n}$ and $I_{z,n}$ are found by using the method of moments to enforce the boundary condition of zero tangential electric fields at the surface of the perfectly conducting microstrip line, i.e.,

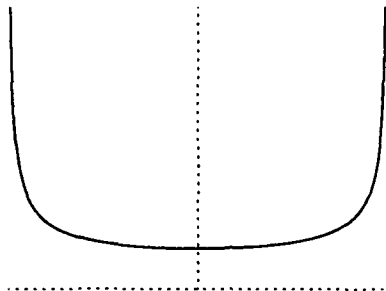
$$E_x^{J_x}(\mathbf{x}) + E_x^{J_z}(\mathbf{x}) = 0 \quad (5.23a)$$

$$E_z^{J_x}(\mathbf{x}) + E_z^{J_z}(\mathbf{x}) = 0 \quad (5.23b)$$

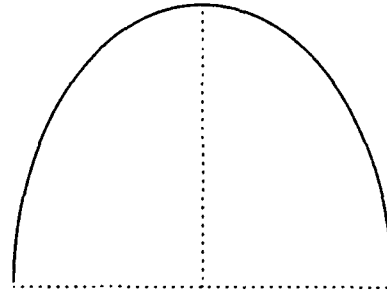
for $|x| < W/2$ and $y = T$. Using Galerkin's method of moments, which uses weight functions equal to the basis functions, Equation (5.23) can be written in block

LONGITUDINAL

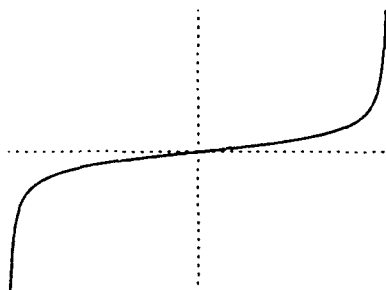
TRANSVERSE



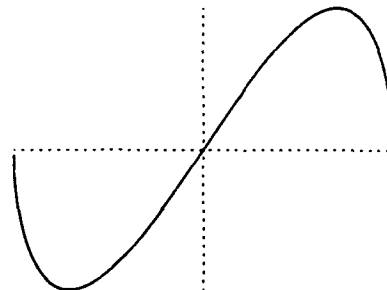
$$1/\sqrt{1-x'^2}$$



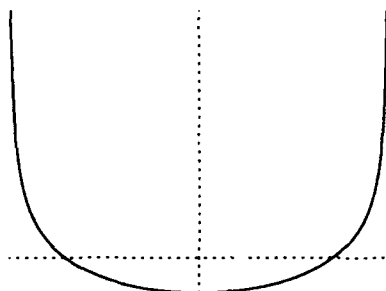
$$\sqrt{1-x'^2}$$



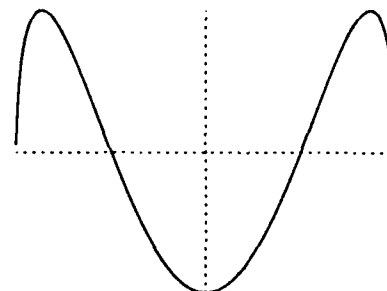
$$x'/\sqrt{1-x'^2}$$



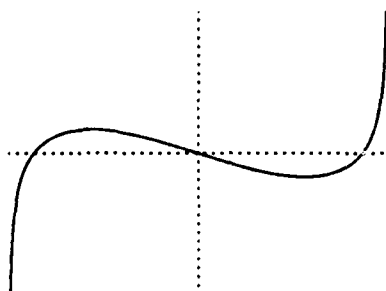
$$x'\sqrt{1-x'^2}$$



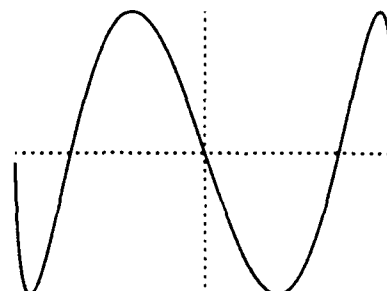
$$(2x'^2 - 1)/\sqrt{1-x'^2}$$



$$(4x'^2 - 1)\sqrt{1-x'^2}$$



$$(4x'^3 - 3x')/\sqrt{1-x'^2}$$



$$(8x'^3 - 4x')\sqrt{1-x'^2}$$

Figure 5.2: First four basis functions for the longitudinal and transverse current components.

matrix form as

$$\begin{bmatrix} Z_{xx} & Z_{xz} \\ Z_{zx} & Z_{zz} \end{bmatrix} \begin{bmatrix} I_x \\ I_z \end{bmatrix} = \begin{bmatrix} 0 \\ 0 \end{bmatrix} \quad (5.24)$$

where $I_x = [I_{x,0} \dots I_{x,N_x}]^T$ and $I_z = [I_{z,0} \dots I_{z,N_z}]^T$. The xz block is given by

$$Z_{xz} = \begin{bmatrix} Z_{xz(0,0)} & \dots & Z_{xz(0,N_z)} \\ \vdots & \ddots & \vdots \\ Z_{xz(N_x,0)} & \dots & Z_{xz(N_x,N_z)} \end{bmatrix} \quad (5.25)$$

where

$$Z_{xz(m,n)} = - \int_{-W/2}^{W/2} E_x^{J_{x,n}}(x) J_{x,m}(x) e^{jk_z^2 x} dx. \quad (5.26)$$

The term $e^{jk_z^2 x}$ occurs in Equation (5.26) because the basis and weighting functions are of the form

$$J_{x,n}(x) e^{-jk_z^2 x} \quad (5.27)$$

and the inner product used for the method of moments solution is [118, sec. 12.2.7]

$$\langle \mathbf{w}(x), \mathbf{g}(x) \rangle = \int_{-W/2}^{W/2} \mathbf{w}^*(x) \cdot \mathbf{g}(x) dx. \quad (5.28)$$

Using Equation (5.19) to calculate $E_x^{J_z}$, Equation (5.26) can be written as

$$Z_{xz(m,n)} = - \frac{e^{j(k_z^* - k_z)z}}{2\pi} \int_{-\infty}^{\infty} \tilde{E}_x^{J_z}(k_x) \tilde{J}_{z,n}(k_x) \tilde{J}_{x,m}(-k_x) dk_x. \quad (5.29a)$$

Impedance elements in the remaining blocks are obtained in a similar fashion and are given by

$$Z_{xx(m,n)} = - \frac{e^{j(k_z^* - k_z)z}}{2\pi} \int_{-\infty}^{\infty} \tilde{E}_x^{J_x}(k_x) \tilde{J}_{x,n}(k_x) \tilde{J}_{x,m}(-k_x) dk_x \quad (5.29b)$$

$$Z_{zx(m,n)} = - \frac{e^{j(k_z^* - k_z)z}}{2\pi} \int_{-\infty}^{\infty} \tilde{E}_z^{J_x}(k_x) \tilde{J}_{z,n}(k_x) \tilde{J}_{z,m}(-k_x) dk_x \quad (5.29c)$$

$$Z_{zz(m,n)} = - \frac{e^{j(k_z^* - k_z)z}}{2\pi} \int_{-\infty}^{\infty} \tilde{E}_z^{J_z}(k_x) \tilde{J}_{z,n}(k_x) \tilde{J}_{z,m}(-k_x) dk_x. \quad (5.29d)$$

The values of k_z for which Equation (5.24) can be solved are the propagation constants of the microstrip line. From linear analysis, Equation (5.24) can only be solved if the impedance matrix is singular, i.e., the determinant is zero. Once the propagation constant k_z is found, the coefficients $I_{x,n}$ and $I_{z,n}$ can be found. One of the most accurate techniques for this problem is singular value decomposition [137, sec. 2.9]. Any matrix, Z , can be factored such that

$$Z = U \Sigma V^T \quad (5.30)$$

where

$$U^T U = V^T V = \begin{bmatrix} 1 & & \\ & \ddots & \\ & & 1 \end{bmatrix} \quad (5.31)$$

and

$$\Sigma = \begin{bmatrix} w_1 & & \\ & \ddots & \\ & & w_n \end{bmatrix}. \quad (5.32)$$

If a matrix is singular, at least one w_i will be zero. Then, the i th column of V is a vector in the null space of Z and is a solution for the vector

$$\begin{bmatrix} I_x \\ I_z \end{bmatrix}. \quad (5.33)$$

In practice, the w_i will be not exactly zero, but it will be numerically small.

5.5 Evaluating the Microstrip Integral Equations

This section is concerned with the efficient numerical evaluation of the electric fields and the elements in the impedance matrix. For example, $E_x^{J_z}$ and Z_{xz} are given by

$$E_x^{J_z}(x) = \frac{1}{2\pi} \int_{-\infty}^{\infty} \tilde{E}_x^{J_z}(k_x) \tilde{J}_z(k_x) e^{-j(k_x x + k_z z)} dk_x \quad (5.34a)$$

$$Z_{xz} = -\frac{e^{j(k_x^* - k_z)z}}{2\pi} \int_{-\infty}^{\infty} \tilde{E}_x^{J_z}(k_x) \tilde{J}_z(k_x) \tilde{J}_z(-k_x) dk_x \quad (5.34b)$$

where the reference to the particular elements of the impedance matrix has been dropped for convenience. As in Equation (5.19), the Fourier transforms for the electric fields and currents can be decomposed into even and odd components:

$$\widetilde{E}_x^{J_z}(k_x) = \widetilde{E}_{x,e}^{J_z}(k_x) + \widetilde{E}_{x,o}^{J_z}(k_x) \quad (5.35a)$$

$$\widetilde{J}_z(k_x) = \widetilde{J}_{z,e}(k_x) + \widetilde{J}_{z,o}(k_x) \quad (5.35b)$$

$$\widetilde{J}_x(-k_x) = \widetilde{J}_{x,e}(k_x) - \widetilde{J}_{x,o}(k_x). \quad (5.35c)$$

Equations (5.35a) and (5.35b) can be combined as

$$\widetilde{E}J_{xz,e}(k_x) = \widetilde{E}_{x,e}^{J_z}(k_x) \widetilde{J}_{z,e}(k_x) + \widetilde{E}_{x,o}^{J_z}(k_x) \widetilde{J}_{z,o}(k_x) \quad (5.36a)$$

$$\widetilde{E}J_{xz,o}(k_x) = \widetilde{E}_{x,e}^{J_z}(k_x) \widetilde{J}_{z,o}(k_x) + \widetilde{E}_{x,o}^{J_z}(k_x) \widetilde{J}_{z,e}(k_x). \quad (5.36b)$$

Then, Equations (5.34a) and (5.34b) can be written as

$$E_x^{J_z}(x) = \frac{1}{\pi} \int_0^{\infty} \widetilde{E}J_{xz,e}(k_x) \cos k_x x e^{-jk_x z} dk_x - \frac{j}{\pi} \int_0^{\infty} \widetilde{E}J_{xz,o}(k_x) \sin k_x x e^{-jk_x z} dk_x \quad (5.37a)$$

$$Z_{xz} = -\frac{e^{j(k_z^* - k_x)z}}{\pi} \int_0^{\infty} \widetilde{E}J_{xz,e}(k_x) \widetilde{J}_{x,e}(k_x) dk_x + \frac{e^{j(k_z^* - k_x)z}}{\pi} \int_0^{\infty} \widetilde{E}J_{xz,o}(k_x) \widetilde{J}_{x,o}(k_x) dk_x. \quad (5.37b)$$

Equations for the remaining electric fields and impedance elements can be written by changing the references to x and z in Equations (5.37a) and (5.37b).

Numerical Integration

Efficient numerical integration of Equations (5.37a) and (5.37b) requires careful examination of the kernels of the integrals. First, consider the region where k_x is small. Surface wave poles exist in the region between k_0 and the maximum of k_R , k_L , where Δ of Equation (5.17a) goes to zero. These singularities can be avoided by

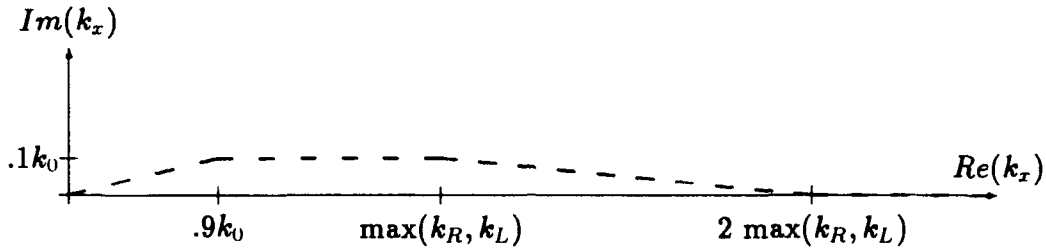


Figure 5.3: Integration contour to avoid surface wave poles.

using the integration contour shown in Figure 5.3. Figure 5.4 shows the integrand of the self-impedance of the Maxwellian ($J_{z,0}$) current distribution for $k_x = 0$ to 1000, a propagation constant of $k_z = 349.3$ ($\lambda_g/\lambda_0 = 0.6$) and several values of ξ_c from 0.0 to 0.005 (the limit set in [102] is $|\xi_c| < \sqrt{\epsilon/\mu} = 0.0053$). The approximate locations of k_0 , k_2 , and $2k_2$ are shown along the $Re(k_x)$ axis for reference, where $k_0 = 209.6$ and $k_2 = 419.2 = \omega\sqrt{\mu\epsilon}$ for a frequency of 10 GHz, $\epsilon_r = 4$, $\mu_r = 1$, $T = 3\text{mm}$, and $W = 3\text{mm}$. The limit of $|\xi_c| < \sqrt{\epsilon/\mu}$ corresponds to $k_{R,L} = k_2(\sqrt{2} \pm 1)$. Due to the wide variation of the integration kernel shown in Figure 5.4, Romberg integration was chosen for the integration contour shown in Figure 5.3.

Next, consider the region where k_x is large. The expressions in Equation (5.18) have the following asymptotic behavior:

$$\tilde{E}_{x,e}^{J_z} \propto k_x \quad (5.38a)$$

$$\tilde{E}_{z,e}^{J_z} \propto 1/k_x \quad (5.38b)$$

$$\tilde{E}_{z,o}^{J_z} = \tilde{E}_{x,o}^{J_z} \propto 1 \quad (5.38c)$$

$$\tilde{E}_{x,o}^{J_z} = -\tilde{E}_{z,o}^{J_z} \propto 1/k_x \quad (5.38d)$$

$$\tilde{E}_{z,e}^{J_z} = \tilde{E}_{x,e}^{J_z} \propto 1. \quad (5.38e)$$

The remaining terms in the integrals of Equation (5.37) are sine, cosine, and Bessel functions. Since the asymptotic form of a Bessel function consists of a cosine function divided by the square root of the argument, all the integrals in Equation (5.37) can

Integrand of Z_{11}

Frequency = 10 GHz

$\epsilon_r = 4, \mu_r = 1, T = 3 \text{ mm}, W = 3 \text{ mm}$

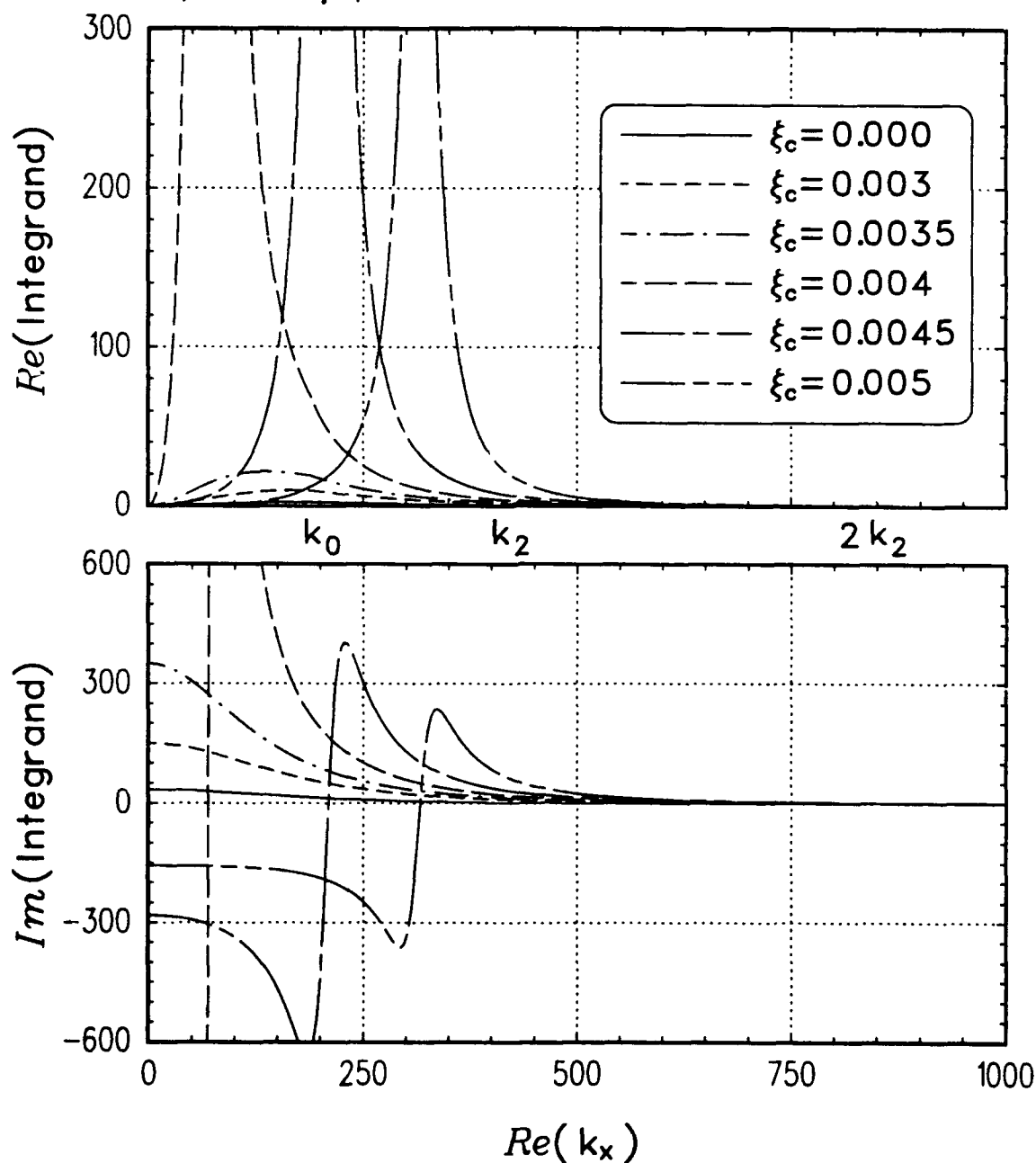


Figure 5.4: Integrand of the self-impedance of a Maxwellian current distribution ($Z_{zz(0,0)}$) for a normalized guide wavelength of 0.6 ($k_z=349.3$) and a range of chirality admittances.

be written for large k_x as

$$\int_0^{\infty} \frac{1}{k_x^P} \cos(\omega_1 k_x + \alpha) \cos(\omega_2 k_x + \beta) dk_x \quad (5.39)$$

where $P = 0.5, 1.5, 2.5$ for electric field calculations and $P = 2, 4$ for impedance calculations. For achiral impedance calculations P is always 2, because $\bar{E}_{x,0}^{J_x}$ is zero for achiral microstrip lines. The closed form of Equation (5.39) is presented in Appendix H in terms of sine, cosine, and Fresnel integrals. Since the expressions of Equation (5.18) approach their asymptotic forms in Equation (5.38) much more rapidly than the Bessel function approaches a cosine function divided by the square root of the argument, the use of these asymptotic forms is limited by the asymptotic form of the Bessel functions.

In the intermediate region between $2\max(k_R, k_L)$ and the start of the asymptotic region, the integrals in Equation (5.37) are similar enough to the asymptotic forms that the number of integration points needed can be predicted from the frequency of the two sinusoids in the integral, i.e., $|\omega_1 + \omega_2|$ and $|\omega_1 - \omega_2|$. An alternative approach for integrating the self-impedance of the Maxwellian current distribution ($Z_{zz(0,0)}$) is presented in Appendix G.

5.6 Numerical Results

This section presents numerical results demonstrating the accuracy of the method of moments solution, and also some effects of chirality on a microstrip transmission line. To simplify comparisons all results are for a substrate of thickness $T = 3$ mm, ϵ_r of 4, and μ_r of 1, with a microstrip line of width $W = 3$ mm. Since the microstrip current can only be found to within a constant, all currents are normalized so that $I_{z,0} = 1$. When plotting currents or fields, the real part is shown as a solid line, and the imaginary part as a dashed line. The initial data will illustrate the accuracy of the method of moments solution by showing that it satisfies the boundary condition of zero tangential electric field on the perfectly conducting strip.

The longitudinal current on a thin achiral microstrip line is essentially the Maxwellian distribution $1/\sqrt{1 - (2x/W)^2}$. The transverse current is an odd function satisfying the edge condition $\sqrt{1 - (2x/W)^2}$, similar to the $J_{x,1}$ expansion function of Equation (5.21a). Figure 5.5 shows the longitudinal (E_z) and transverse (E_x) electric fields at the interface ($y = T$) when these two expansion functions are used in the solution for thin chiral and achiral microstrip lines. Note that this solution produces essentially zero tangential electric field on the strip for the achiral case, but not for the chiral case. This indicates that the method of moments solution for the achiral case is essentially correct. However, the relatively poor field match for the chiral case indicates that it is not correct, and thus more expansion functions are needed. The real asymmetric E_z field component shown in the upper left graph is due to the chirality of the substrate. This field component is unaffected in the solution by even J_z and odd J_x expansion functions, thereby requiring odd J_z and/or even J_x expansion functions for a reasonably physical solution. The imaginary symmetric E_z and real asymmetric E_x field components for both the chiral and achiral cases are virtually identical, indicating that modest chirality produces only a relatively small perturbation in the currents and fields.

A more accurate approximation for the currents is shown in Figure 5.6 using ten longitudinal and ten transverse expansion functions. The left-hand graphs show that the fields nearly satisfy the boundary condition of zero tangential electric field on the microstrip line. The corresponding currents are shown in the right-hand graphs. The even transverse current component, which occurs solely because of the chirality, is significantly larger than the odd transverse current component. The calculated propagation constant for the chiral microstrip line using twenty expansion functions differs only slightly from that of the achiral microstrip line shown in Figure 5.5. The imaginary part of k_z , corresponding to attenuation on the line, is negative and of the order 10^{-8} .

Chiral & Achiral Microstrip Line Two Lowest Achiral Expansion Functions

$\epsilon_r = 4, \mu_r = 1, T = 3 \text{ mm}, W = 3 \text{ mm}$

Frequency = 500 MHz

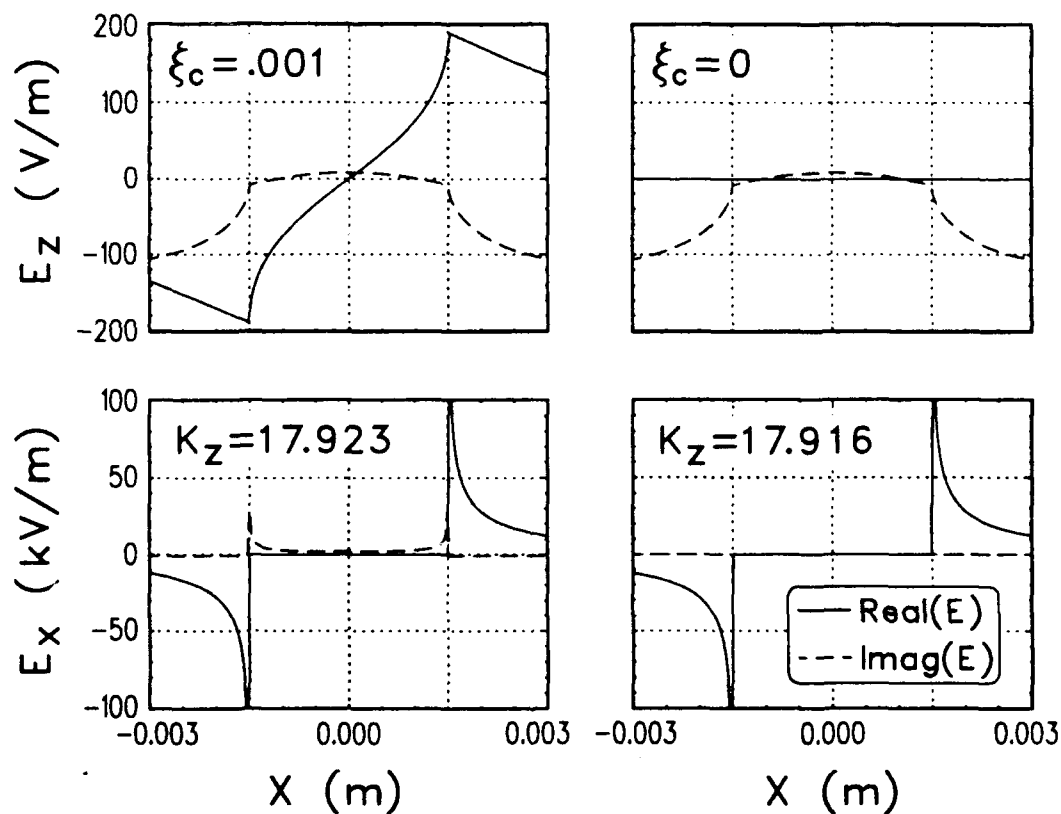


Figure 5.5: E_z and E_x fields at $y = T$ for identical chiral and achiral microstrip lines, solved using the two lowest order expansion functions.

Chiral Microstrip Line

$\epsilon_r = 4$, $\mu_r = 1$, $T = 3$ mm, $W = 3$ mm
 $\xi_c = .001$, Frequency = 500 MHz

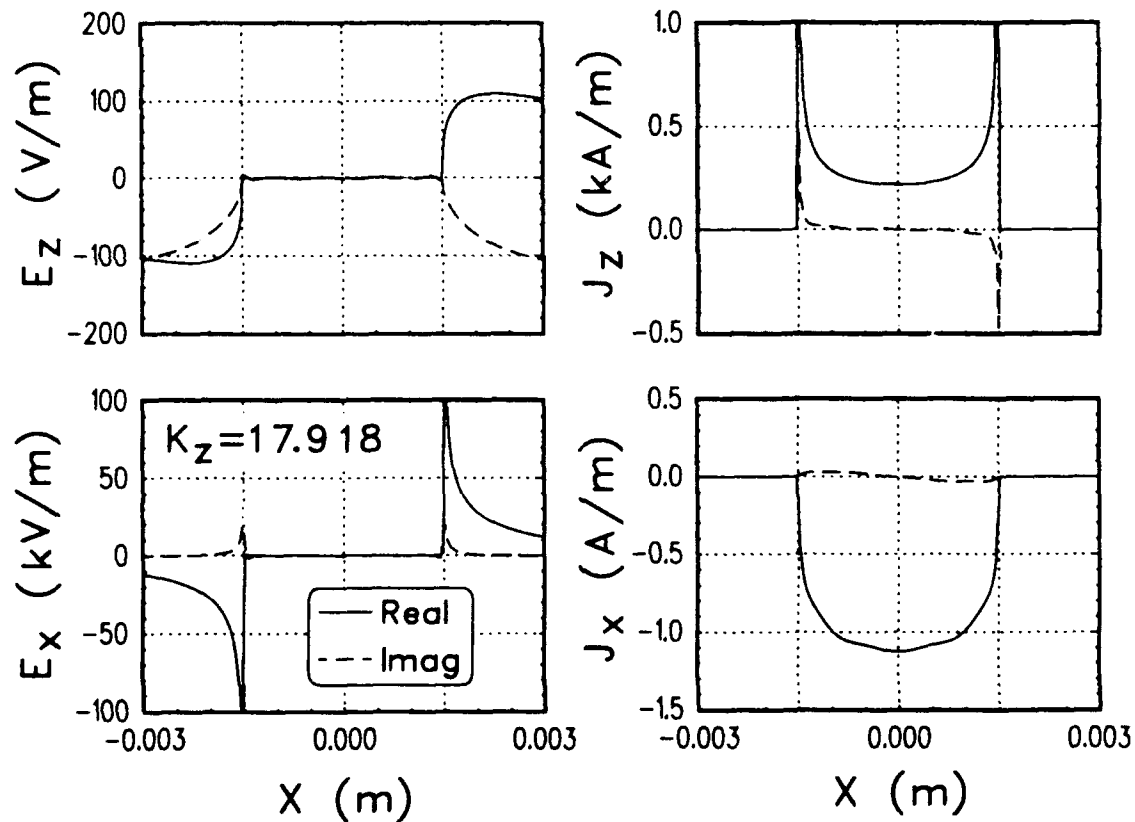


Figure 5.6: Fields and currents at $y = T$ for a chiral microstrip solved using ten J_z modes and ten J_x modes.

The variation of the propagation constant and the current coefficients with respect to the number of basis functions used is shown in Table 5.1 for the geometry and material parameters in Figure 5.6. Accurate calculation of the propagation constant requires very few expansion functions as seen in Table 5.1. However, accurate calculation of the imaginary part of k_z requires an accurate representation of the current on the microstrip line, which is dependent on the width of the microstrip line in wavelengths. For comparison, Figure 5.7 shows the electric fields and currents for the microstrip line examined in Figures 5.5 and 5.6 at 5 GHz.

The dispersion curve shown in Figure 5.8 shows the normalized guide wavelength (λ_g/λ_0) for the fundamental mode of a chiral microstrip line, for a range of chiral parameters. The case $\xi_c = 0$ corresponds to an achiral line. As seen in Figures 5.5 and 5.6, the chirality of the substrate significantly modifies the fields and currents of the microstrip line even for small chiral parameters. However, as Figure 5.8 shows, the propagation constant is not significantly affected unless the chiral parameter is a significant fraction of its maximum value set in [102] of $\xi_{c,max} = \sqrt{\epsilon/\mu}$, which in this case is 0.0053.

Figure 5.9 shows the relationship between substrate thickness and normalized guide wavelength for chiral and achiral microstrip lines at frequencies of 0.5 GHz and 2 GHz. The relationship between microstrip line width and normalized guide wavelength is shown in Figure 5.10 for the same frequencies.

5.7 Summary

This chapter has presented a spectral-domain solution to the problem of propagation on a microstrip transmission line on a chiral substrate. Circular vector potentials were used to expand the fields in the chiral substrate. The primary effect of the chiral substrate is to generate asymmetric longitudinal and symmetric transverse fields. This effect could significantly alter the properties of microwave and higher frequency devices constructed on a chiral substrate.

Table 5.1: Variation of the propagation constant and the current coefficients with respect to the number of basis functions used in the method of moments solution for the geometry and material parameters in Figure 5.6.

k_z	$I_{z,0}$	$I_{z,1}$	$I_{z,1}$	$I_{z,2}$	$I_{z,2}$	$I_{z,3}$	$I_{z,3}$	$I_{z,4}$	$I_{z,4}$
$17.9211 - j1.2(-9)$	1.0								
$17.9452 - j2.8(-8)$	1.0	-0.001355							
$17.9171 + j4.0(-9)$	1.0	-0.002927	-j0.11692						
$17.9181 + j3.0(-8)$	1.0	-0.002948	-j0.11845	-j3.697(-4)					
$17.9178 + j7.0(-9)$	1.0	-0.002958	-j0.11844	-0.01638					
$17.9195 + j1.1(-8)$	1.0	-0.002960	-j0.11845	-0.01935	-0.000613				
$17.9176 + j1.2(-8)$	1.0	-0.002962	-j0.11859	-0.01936	-0.001318	-j0.0524			
$17.9176 + j1.2(-8)$	1.0	-0.002960	-j0.11848	-0.01936	-0.001311	-j0.0518	j1.22(-4)		
$17.9176 + j1.2(-8)$	1.0	-0.002959	-j0.11849	-0.01933	-0.001303	-j0.0518	j1.19(-6)	0.0090	
$17.9180 + j2.6(-8)$	1.0	-0.002960	-j0.11848	-0.01977	-0.001305	-j0.0518	j2.84(-5)	0.0070	-3.8(-4)

Chiral Microstrip Line
 $\epsilon_r = 4$, $\mu_r = 1$, $T = 3$ mm, $W = 3$ mm
 $\xi_c = .001$, Frequency = 5 GHz

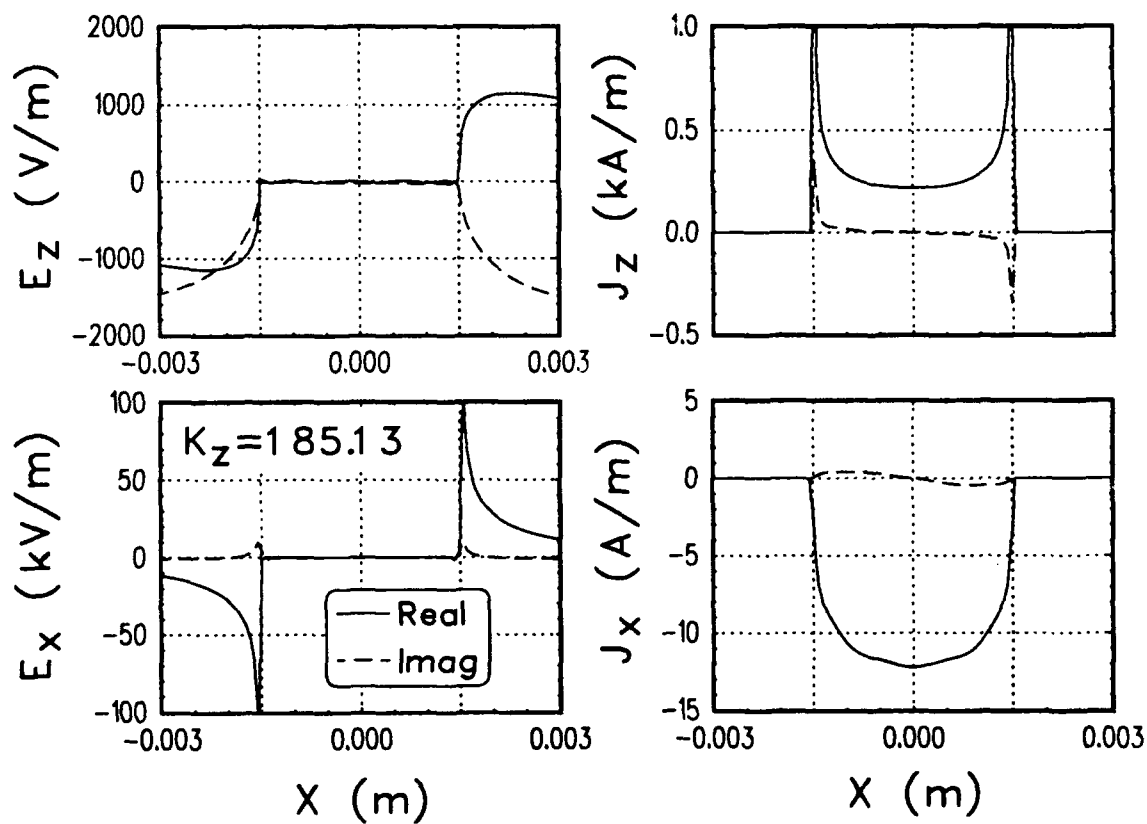


Figure 5.7: Fields and currents at $y = T$ for a chiral microstrip at 5 GHz solved using ten J_z modes and ten J_x modes.

Chiral Microstrip Line

$\epsilon_r = 4$, $\mu_r = 1$, $T = 3$ mm, $W = 3$ mm

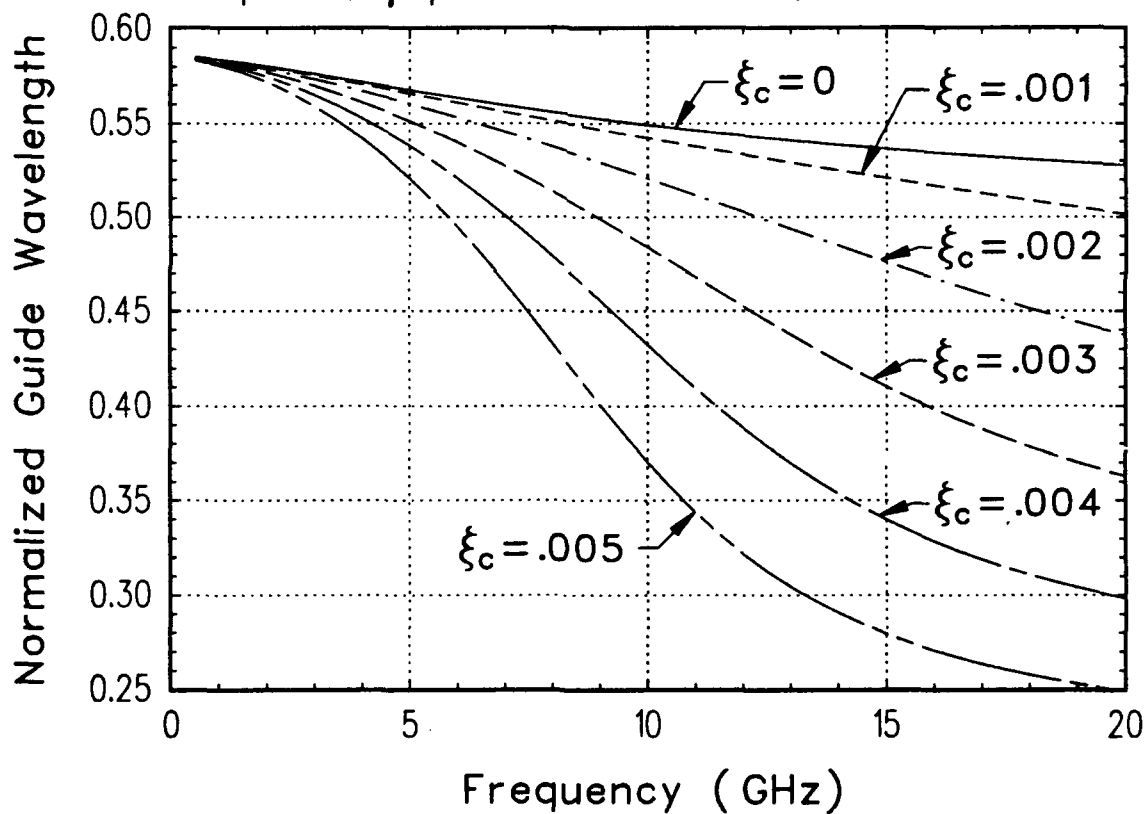


Figure 5.8: Normalized guide wavelength (λ_g/λ_0) versus frequency for the fundamental mode of chiral and achiral microstrip lines, for a range of chiral parameters.

Chiral Microstrip Line

$$\epsilon_r = 4, \mu_r = 1, W = 3 \text{ mm}$$

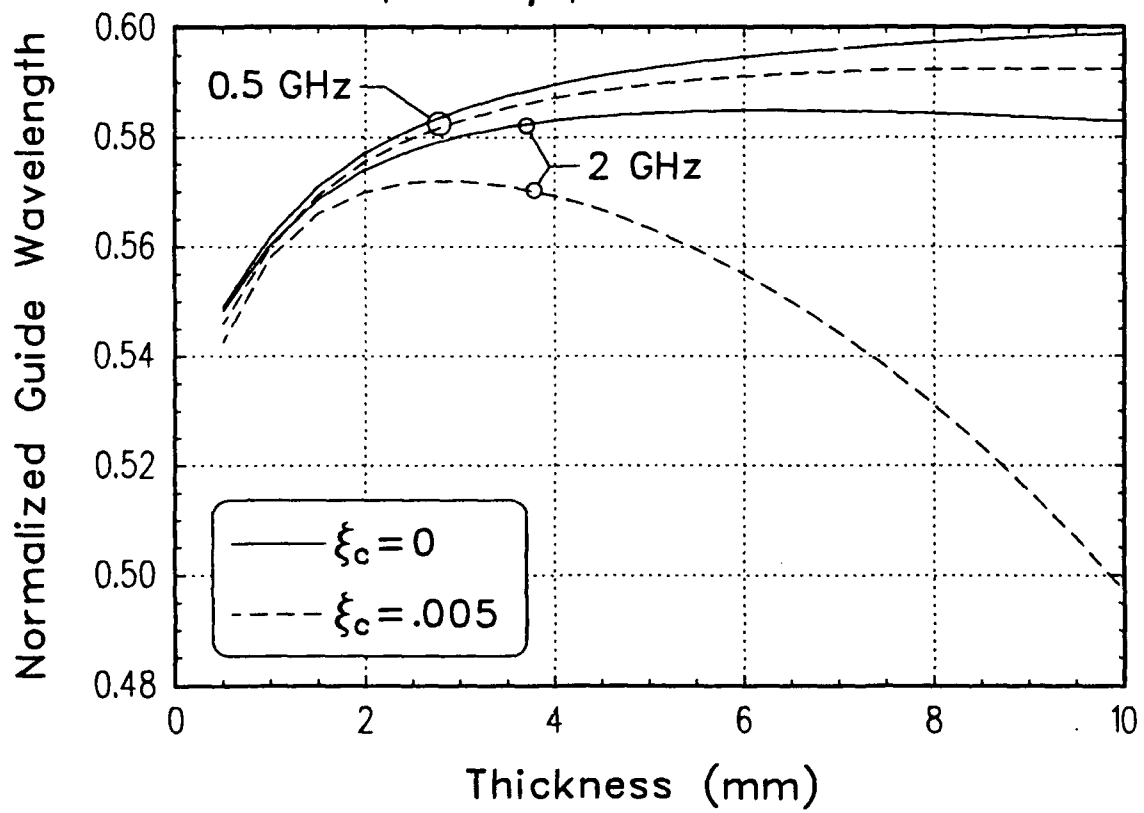


Figure 5.9: Normalized guide wavelength (λ_g/λ_0) versus substrate thickness for the fundamental mode of chiral and achiral microstrip lines at two frequencies.

Chiral Microstrip Line
 $\epsilon_r = 4$, $\mu_r = 1$, $T = 3$ mm

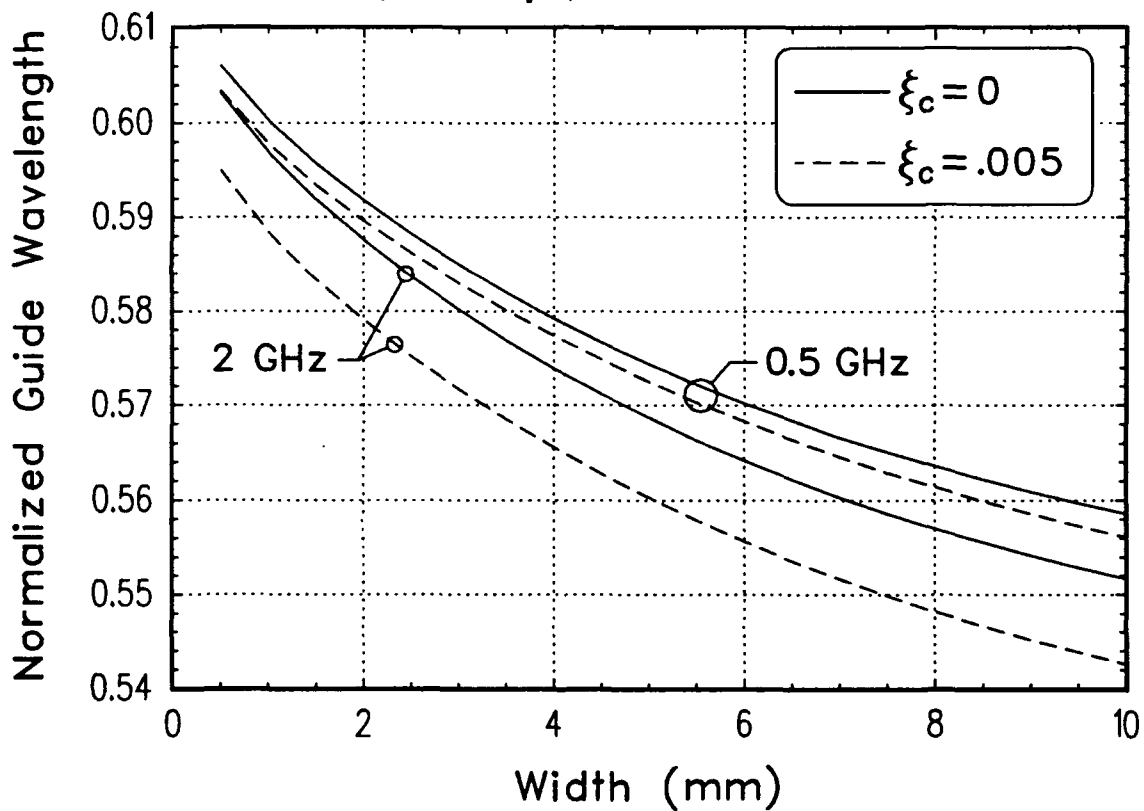


Figure 5.10: Normalized guide wavelength (λ_g/λ_0) versus microstrip line width for the fundamental mode of chiral and achiral microstrip lines at two frequencies.

Chapter 6

Conclusions

In this report, the interaction of objects composed of chiral media with electromagnetic fields was analyzed using eigenfunction and method of moments techniques. The historical basis for the constitutive relationships used for chiral media was discussed in Chapter 1. These constitutive relationships were shown to have a direct relationship to the constitutive relationships for optically active media, which can be derived using quantum mechanics.

Chapter 2 presented one method for solving the wave equation in chiral media. Key parts of this method were then used to develop circular vector potentials, which produce circularly polarized fields useful for field expansions in chiral media. Next, the volume equivalence theorem was developed for chiral media using the same procedure as that used for achiral media, and then was used to develop image theory for chiral media.

An eigenfunction solution for scattering by a multilayer circular chiral cylinder with a center cylinder described by an impedance surface was developed in Chapter 3. The essential difference from achiral eigenfunction solutions was the use of circularly polarized vector wave functions. The formulation was such that the TE_Z solution differed from the TM_Z solution by only a plus/minus sign at one step. Previous work required completely different solutions for TM_Z and TE_Z incident plane waves. An examination of the scattered fields showed that the cross-polarized bistatic echo

width of circular cylinders is identical for TM_Z and TE_Z incident plane waves. The most significant result of this chapter was the effect of chirality on the internal fields. In one case, more J_z than J_ϕ current was induced on a perfectly conducting cylinder coated by two layers of chiral media for a TE_Z incident plane wave, even though the achiral problem would have induced no J_z current on the conducting center cylinder. An examination of the relationship between chirality and scattered fields found that even through the achiral bistatic scattering pattern may have no deep nulls, the co-polarized bistatic pattern for a chiral cylinder can have deep nulls for certain ranges of ξ_c . In one case the backscattered field was entirely cross-polarized for a small range of the chirality admittance.

A pulse-basis point-matching method of moments solution for scattering by an inhomogeneous object composed of chiral media in free-space or in the presence of a perfectly conducting half-plane was presented in Chapter 4. The numerical results showed that the cross-polarized backscatter echo width of at least one noncircular geometry is identical for TM_Z and TE_Z incident plane waves. However, the cross-polarized bistatic echo-width can differ, which is in contrast to the circular cylinders of the previous chapter. An examination of the internal fields of one chiral cylinder showed that the number of cells needed in the method of moments solution increased by a factor of 5. Part of this increase is due to the short wavelength of the circular polarized fields in chiral media. The remaining increase remains unexplained and may be due to the interaction of the two circular polarizations with different wavelengths.

A spectral-domain Galerkin method of moments solution for a microstrip transmission line on a chiral substrate was developed in Chapter 5. The propagation constant of the transmission line showed only a minor change due to the chirality of the media. In contrast, the fields were significantly changed. These fields can be divided into the symmetric and asymmetric field components. The symmetric field components were only slightly affected by the chirality of the media. However,

the asymmetric field components were due in entirety to the chirality of the media. These asymmetric field components would significantly affect the coupling between microstrip lines on a chiral substrate.

Appendix A

Scattering by a Chiral Coated Perfectly Conducting Cylinder

This appendix presents an eigenfunction solution for scattering by a perfectly conducting circular cylinder coated by a single homogeneous layer of chiral media. The development is similar to the more general case of scattering by a multilayer circular chiral cylinder presented in Chapter 3. The geometry of the coated cylinder is shown in Figure A.1, where the constitutive parameters of the chiral coating are (μ, ϵ, ξ_c) with an outer radius of b meters. The right and left wave numbers, k_R and k_L , and the wave impedance, η_c , of the coating are defined by Equations (2.12) and (2.11). The perfectly conducting cylinder has a radius of a meters. The external medium is free space, with parameters (μ_0, ϵ_0) , wave number $k_0 = \omega\sqrt{\mu_0\epsilon_0}$, and characteristic impedance $\eta_0 = \sqrt{\mu_0/\epsilon_0}$.

External and Internal Field Expansions

This section presents the eigenfunction expansions for the fields external and internal to the chiral coated cylinder. The external scattered fields are expanded as in Equation (3.5)

$$\mathbf{E}^S = \sum_{n=-\infty}^{\infty} j^{-n} [a_n \mathbf{N}_n^{(4)}(k_0) + b_n \mathbf{M}_n^{(4)}(k_0)] \quad (\text{A.1a})$$

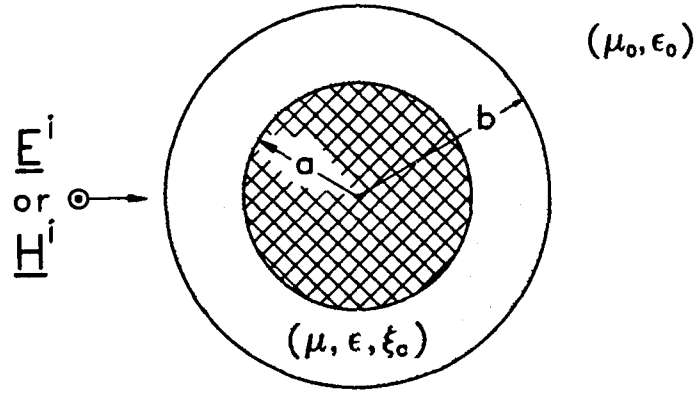


Figure A.1: Geometry of a chiral coated perfectly conducting cylinder.

$$\mathbf{H}^S = \frac{j}{\eta_0} \sum_{n=-\infty}^{\infty} j^{-n} [a_n \mathbf{M}_n^{(1)}(k_0) + b_n \mathbf{N}_n^{(1)}(k_0)] \quad (\text{A.1b})$$

where \mathbf{N}_n and \mathbf{M}_n are defined in Equation (3.2).

Using the right and left circularly polarized vector wave functions [20] from Equation (3.6), the internal fields are expanded as

$$\mathbf{E} = \sum_{n=-\infty}^{\infty} j^{-n} [c_n \mathbf{E}_{R,n}^{(1)} + d_n \mathbf{E}_{L,n}^{(1)} + h_n \mathbf{E}_{R,n}^{(2)} + l_n \mathbf{E}_{L,n}^{(2)}] \quad (\text{A.2a})$$

$$\mathbf{H} = \frac{j}{\eta_0} \sum_{n=-\infty}^{\infty} j^{-n} [c_n \mathbf{E}_{R,n}^{(1)} - d_n \mathbf{E}_{L,n}^{(1)} + h_n \mathbf{E}_{R,n}^{(2)} - l_n \mathbf{E}_{L,n}^{(2)}]. \quad (\text{A.2b})$$

TM_Z Incident Field

This section presents the solution for a TM_Z plane wave normally incident from $\phi = 180^\circ$. As in Equation (3.3), the incident fields are expanded as

$$\mathbf{E}^i = \hat{\mathbf{z}} e^{-jk_0 x} = \sum_{n=-\infty}^{\infty} j^{-n} \mathbf{N}_n^{(1)}(k_0) \quad (\text{A.3a})$$

$$\mathbf{H}^i = -\hat{\mathbf{y}} \frac{1}{\eta_0} e^{-jk_0 x} = \frac{j}{\eta_0} \sum_{n=-\infty}^{\infty} j^{-n} \mathbf{M}_n^{(1)}(k_0). \quad (\text{A.3b})$$

The unknown coefficients are found by enforcing the boundary conditions of continuous tangential electric and magnetic fields at $\rho = b$ and zero tangential electric

fields at $\rho = a$. The scattered field coefficients, a_n and b_n are given by

$$a_n^{TM} = \frac{B_n^{(1)}(L)A_n^{TM} + B_n^{(1)}(R)B_n^{TM} + B_n^{(2)}(L)C_n^{TM} + B_n^{(2)}(R)D_n^{TM}}{\Delta_n^{TM}} \quad (\text{A.4a})$$

$$b_n^{TM} = -\frac{2j\eta_c}{\pi\omega\mu_0 b \Delta_n^{TM}} \cdot [X_n^{(2,2)}U_n^{(1,1)} + X_n^{(1,1)}U_n^{(2,2)} - X_n^{(1,2)}U_n^{(2,1)} - X_n^{(2,1)}U_n^{(1,2)}]. \quad (\text{A.4b})$$

The internal field coefficients c_n , d_n , h_n , and l_n are given by

$$c_n^{TM} = \frac{2j\eta_c}{\pi\omega\mu_0 b} \frac{B_n^{TM}}{\Delta_n^{TM}} \quad (\text{A.5a})$$

$$d_n^{TM} = -\frac{2j\eta_c}{\pi\omega\mu_0 b} \frac{A_n^{TM}}{\Delta_n^{TM}} \quad (\text{A.5b})$$

$$h_n^{TM} = \frac{2j\eta_c}{\pi\omega\mu_0 b} \frac{D_n^{TM}}{\Delta_n^{TM}} \quad (\text{A.5c})$$

$$l_n^{TM} = -\frac{2j\eta_c}{\pi\omega\mu_0 b} \frac{C_n^{TM}}{\Delta_n^{TM}} \quad (\text{A.5d})$$

where

$$\Delta_n^{TM} = -[W_n^{(1)}(L)A_n^{TM} + W_n^{(1)}(R)B_n^{TM} + W_n^{(2)}(L)C_n^{TM} + W_n^{(2)}(R)D_n^{TM}] \quad (\text{A.6})$$

and

$$A_n^{TM} = X_n^{(2,2)}V_n^{(1)}(R) + \frac{2}{\pi k_R a} V_n^{(2)}(L) - X_n^{(2,1)}V_n^{(2)}(R) \quad (\text{A.7a})$$

$$B_n^{TM} = X_n^{(2,2)}V_n^{(1)}(L) + \frac{2}{\pi k_L a} V_n^{(2)}(R) - X_n^{(1,2)}V_n^{(2)}(L) \quad (\text{A.7b})$$

$$C_n^{TM} = X_n^{(1,1)}V_n^{(2)}(R) - \frac{2}{\pi k_R a} V_n^{(1)}(L) - X_n^{(1,2)}V_n^{(1)}(R) \quad (\text{A.7c})$$

$$D_n^{TM} = X_n^{(1,1)}V_n^{(2)}(L) - \frac{2}{\pi k_L a} V_n^{(1)}(R) - X_n^{(2,1)}V_n^{(1)}(L) \quad (\text{A.7d})$$

$$W_n^{(p)}(S) = \frac{\eta_c}{\eta_0} Z_n^{(p)}(k_S b) H_n^{(2)'}(k_0 b) - Z_n^{(p)'}(k_S b) H_n^{(2)}(k_0 b) \quad (\text{A.7e})$$

$$V_n^{(p)}(S) = \frac{\eta_c}{\eta_0} Z_n^{(p)'}(k_S b) H_n^{(2)}(k_0 b) - Z_n^{(p)}(k_S b) H_n^{(2)'}(k_0 b) \quad (\text{A.7f})$$

$$B_n^{(p)}(S) = \frac{\eta_c}{\eta_0} Z_n^{(p)}(k_S b) J_n'(k_0 b) - Z_n^{(p)'}(k_S b) J_n(k_0 b) \quad (\text{A.7g})$$

$$X_n^{(p,q)} = Z_n^{(p)}(k_L a) Z_n^{(q)'}(k_R a) + Z_n^{(p)'}(k_L a) Z_n^{(q)}(k_R a) \quad (\text{A.7h})$$

$$U_n^{(p,q)} = Z_n^{(p)}(k_L b) Z_n^{(q)'}(k_R b) - Z_n^{(p)'}(k_L b) Z_n^{(q)}(k_R b). \quad (\text{A.7i})$$

TE_Z Incident Field

This section presents the solution for a TE_Z plane wave normally incident from $\phi = 180^\circ$. As in Equation (3.4), the incident fields are expanded as

$$\mathbf{E}^i = \hat{\mathbf{y}} j e^{-jk_0 x} = \sum_{n=-\infty}^{\infty} j^{-n} \mathbf{M}_n^{(1)}(k_0) \quad (\text{A.8a})$$

$$\mathbf{H}^i = \hat{\mathbf{z}} \frac{j}{\eta_0} e^{-jk_0 x} = \frac{j}{\eta_0} \sum_{n=-\infty}^{\infty} j^{-n} \mathbf{N}_n^{(1)}(k_0). \quad (\text{A.8b})$$

The unknown coefficients are found by enforcing the boundary conditions of continuous tangential electric and magnetic fields at $\rho = b$ and zero tangential electric fields at $\rho = a$. The scattered field coefficients, a_n and b_n are given by

$$a_n^{TE} = b_n^{TM} \quad (\text{A.9a})$$

$$b_n^{TE} = \frac{A_n^{(1)}(L)A_n^{TE} + A_n^{(1)}(R)B_n^{TE} + A_n^{(2)}(L)C_n^{TE} + A_n^{(2)}(R)D_n^{TE}}{\Delta_n^{TE}} \quad (\text{A.9b})$$

The internal field coefficients $c_n, d_n, h_n,$ and l_n are given by

$$c_n^{TE} = \frac{2j\eta_c}{\pi\omega\mu_0 b} \frac{B_n^{TE}}{\Delta_n^{TE}} \quad (\text{A.10a})$$

$$d_n^{TE} = \frac{2j\eta_c}{\pi\omega\mu_0 b} \frac{A_n^{TE}}{\Delta_n^{TE}} \quad (\text{A.10b})$$

$$h_n^{TE} = \frac{2j\eta_c}{\pi\omega\mu_0 b} \frac{D_n^{TE}}{\Delta_n^{TE}} \quad (\text{A.10c})$$

$$l_n^{TE} = \frac{2j\eta_c}{\pi\omega\mu_0 b} \frac{C_n^{TE}}{\Delta_n^{TE}} \quad (\text{A.10d})$$

where

$$\Delta_n^{TE} = - \left[V_n^{(1)}(L)A_n^{TE} + V_n^{(1)}(R)B_n^{TE} + V_n^{(2)}(L)C_n^{TE} + V_n^{(2)}(R)D_n^{TE} \right] \quad (\text{A.11})$$

and

$$A_n^{TE} = X_n^{(2,2)}W_n^{(1)}(R) - \frac{2W_n^{(2)}(L)}{\pi k_R a} - X_n^{(2,1)}W_n^{(2)}(R) \quad (\text{A.12a})$$

$$B_n^{TE} = X_n^{(2,2)}W_n^{(1)}(L) - \frac{2W_n^{(2)}(R)}{\pi k_L a} - X_n^{(1,2)}W_n^{(2)}(L) \quad (\text{A.12b})$$

$$C_n^{TE} = X_n^{(1,1)}W_n^{(2)}(R) + \frac{2W_n^{(1)}(L)}{\pi k_R a} - X_n^{(1,2)}W_n^{(1)}(R) \quad (\text{A.12c})$$

$$D_n^{TE} = X_n^{(1,1)}W_n^{(2)}(L) + \frac{2W_n^{(1)}(R)}{\pi k_L a} - X_n^{(2,1)}W_n^{(1)}(L) \quad (\text{A.12d})$$

$$A_n^{(p)}(S) = \frac{\eta_c}{\eta_0} Z_n^{(p)'}(k_S b) J_n(k_0 b) - Z_n^{(p)}(k_S b) J_n'(k_0 b). \quad (\text{A.12e})$$

Appendix B

Evaluating the Half-Plane Green's Function Integrals

The Green's function for a \hat{z} polarized line source in the presence of a perfectly conducting half-plane involves the integrals [125, 8.3]

$$S_i(\alpha, \beta) = \int_{\alpha}^{\infty} \frac{e^{-ju^2}}{(u^2 + \beta^2)^{i-1/2}} du, \quad (B.1)$$

for $i = 1, 2$. This appendix presents new and efficient techniques for accurately evaluating these integrals. For a lossless ambient medium α and β are real numbers. The range of α that needs to be explicitly considered can be restricted to $\alpha \geq 0$ using [138]

$$S_i(\alpha, \beta) = S_{i0}(\beta) - S_i(-\alpha, \beta) \quad (B.2)$$

where $i = 1, 2$ and the $S_{i0}(\beta)$ are defined by

$$S_{10}(\beta) = S_1(-\infty, \beta) = -j \frac{\pi}{2} e^{j\beta^2/2} H_0^{(2)} \left(\frac{\beta^2}{2} \right) \quad (B.3a)$$

$$S_{20}(\beta) = S_2(-\infty, \beta) = -j \frac{\pi}{2} e^{j\beta^2/2} \left[H_0^{(2)} \left(\frac{\beta^2}{2} \right) + j H_1^{(2)} \left(\frac{\beta^2}{2} \right) \right]. \quad (B.3b)$$

Figure B.1 shows the real and imaginary parts of the integrand of Equation (B.1) for $i = 1$ and $\beta = 1$. The singularities caused by β can be seen in the lower graph at $u = \pm j$. The branch cut caused by the square root can be seen in both graphs starting at the singularity $u = -j$. Figure B.2 shows the best regions for each

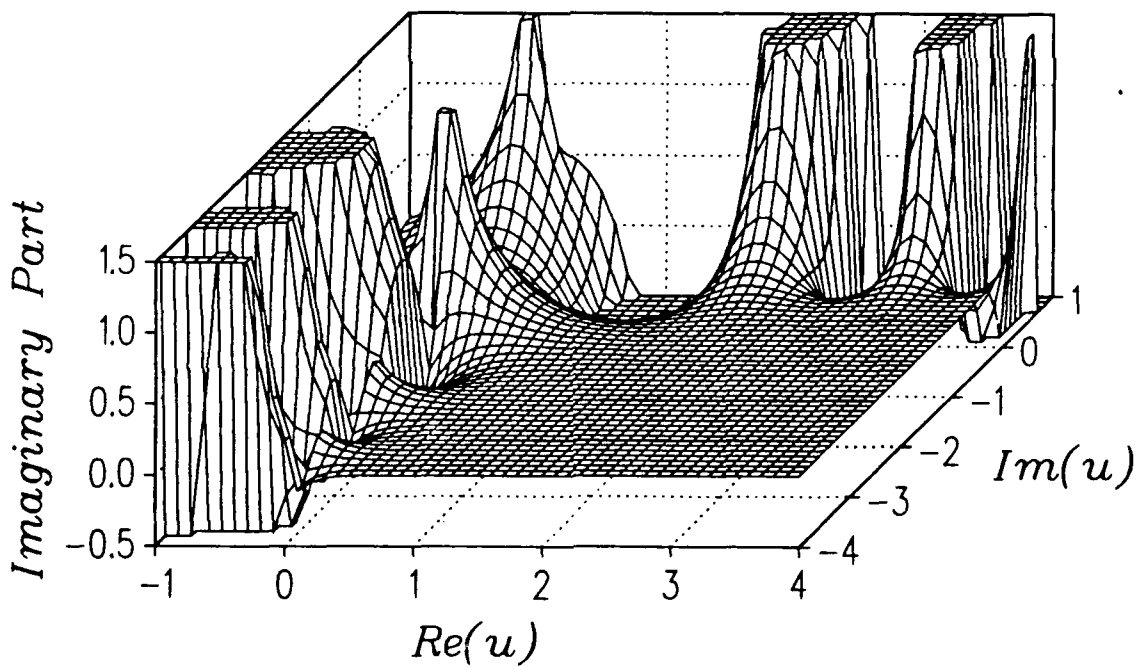
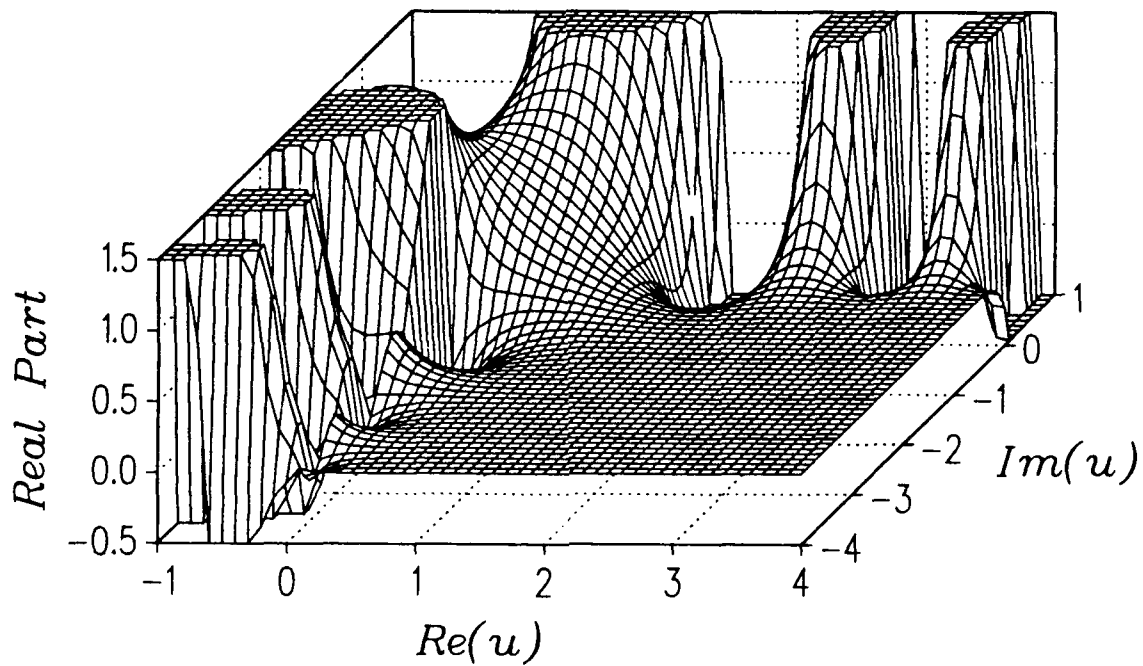


Figure B.1: The real and imaginary parts of the integrand of the half-plane integral for $i = 1$ and $\beta = 1$.

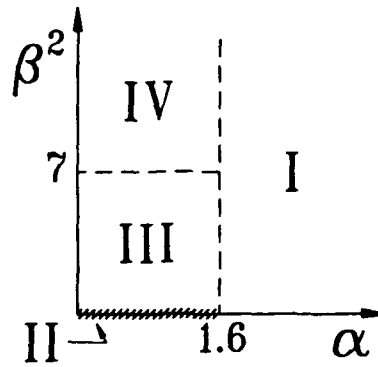


Figure B.2: Regions for each method of evaluating the S_i integrals in the half-plane Green's function for a \hat{z} polarized line source.

method of evaluating the S_i integrals. These methods are presented in the following sections.

Method I: Numerical Integration ($|\alpha| > 1.6$, all β)

This section presents a numerical integration technique for S_1 and S_2 requiring far fewer points than previous approaches [129, 138, 139]. Using the change of variables $u^2 = x$ and $x = \alpha^2 - jt$, where the second change of variables corresponds to changing the integration path for x to the contour $x = \alpha^2$ to $-j\infty + \alpha^2$ to ∞ , Equation (B.1) can be rewritten as

$$S_i(\alpha, \beta) = -j \frac{e^{-j\alpha^2}}{2} \int_0^\infty \frac{e^{-t}}{(\alpha^2 - jt + \beta^2)^{i-1/2} \sqrt{\alpha^2 - jt}} dt \quad (B.4)$$

where the portion of the path at infinity does not contribute to the integral. Figure B.3 shows the resulting contour in the complex u plane. These integrals are now in a form suitable for Gauss-Laguerre Quadrature, which can be written as [140, sec 25.4.45]

$$\int_0^\infty f(x) e^{-x} dx = \sum_{i=1}^N w_i f(x_i) + R_N \quad (B.5)$$

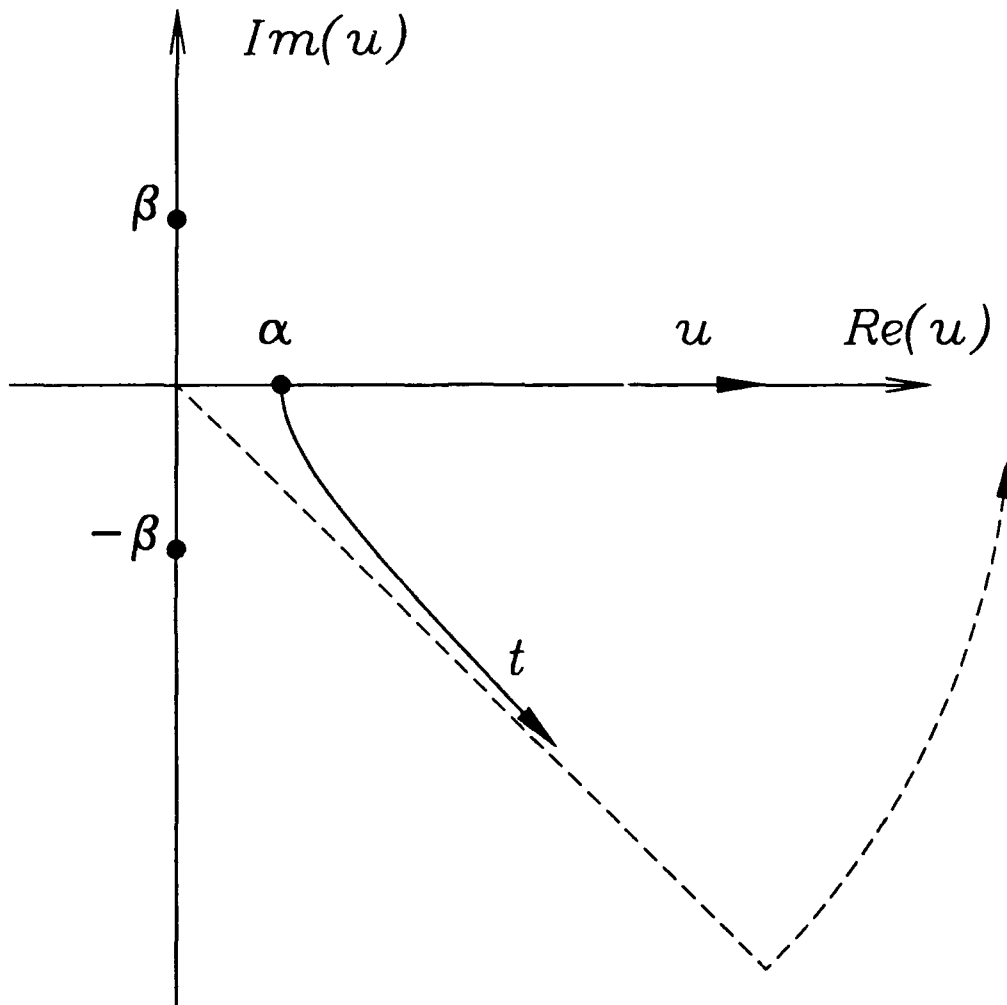


Figure B.3: Integration contour in the complex u plane.

where w_i and x_i are given in [140, table 25.9] for $N = 1, \dots, 10, 12, 15$ and R_N is the remainder. In our case a very conservative upper limit on R_N is given by

$$|R_N| < \begin{cases} \frac{(N!)^2}{2\alpha^{2+4N}} & \text{for } S_1 \\ \frac{(N!)^2(2N+1)}{2\alpha^{4+4N}} & \text{for } S_2. \end{cases} \quad (B.6)$$

Empirically the N required for a relative error of δ in either S_1 or S_2 is approximately given by

$$N \approx -0.1 - \log_{10} \delta (.16 - .03 \log_{10} \delta) - \frac{1}{|\alpha|} \left[1.5 - \frac{2.3}{|\alpha|} + \log_{10} \delta \left\{ 1.6 + \frac{.89}{|\alpha|} + \log_{10} \delta \left(.35 - \frac{1.1}{|\alpha|} \right) \right\} \right] \quad (B.7)$$

for $0 \leq \beta^2 < 2$ and by

$$N \approx .4 - \frac{1}{|\alpha|} \left[1.2 - \frac{.54}{|\alpha|} + \log_{10} \delta \left\{ 2.5 - \frac{1.1}{|\alpha|} + \log_{10} \delta \left(.18 - \frac{0.7}{|\alpha|} \right) \right\} \right] \quad (B.8)$$

for $\beta^2 \geq 2$. These equations were developed for $N = 1, \dots, 10, 12, 15$ and $0.00001 < \delta < 0.01$.

Method II: Exact Integration ($\beta = 0$)

This section presents the special case of $\beta = 0$, where the S_i 's can be exactly integrated

$$S_1(|\alpha|, \beta) = \frac{1}{2} E_1(\alpha^2) \quad (B.9a)$$

$$S_2(|\alpha|, \beta) = \frac{1}{2\alpha^2} e^{-j\alpha^2} - \frac{j}{2} E_1(\alpha^2) \quad (B.9b)$$

where $E_1(z)$ is the exponential integral given by

$$E_1(z) = \int_x^\infty \frac{e^{-ju}}{u} du. \quad (B.10)$$

as defined in [140, sec 5.1].

Method III: Small Argument Approximations ($|\alpha| < 1.6, \beta^2 < 7$)

This section presents efficient small argument approximations for the integrals S_1 and S_2 when α and β are small. In this region the integrals are evaluated using

$$S_i(\alpha, \beta) = \frac{1}{2} S_{i0}(\beta) - \text{sign}(\alpha) \Delta S_i(0, |\alpha|, \beta) \quad (\text{B.11})$$

where $i = 1, 2$, the S_{i0} are defined in Equation (B.3), and the ΔS_i are defined by

$$\Delta S_i(0, \alpha, \beta) = \int_0^\alpha \frac{e^{-ju^2}}{(u^2 + \beta^2)^{i-1/2}} du. \quad (\text{B.12})$$

The ΔS_i can be evaluated using the Taylor series expansion for e^{-ju^2} and integration by parts. For ΔS_1 , where $\beta \neq 0$, this gives

$$\Delta S_1(0, |\alpha|, \beta) = a_1 \ln \left(\left| \frac{\alpha}{\beta} \right| + \sqrt{\left(\frac{\alpha}{\beta} \right)^2 + 1} \right) - j b_2 \frac{|\alpha|}{2} \sqrt{\alpha^2 + \beta^2} \quad (\text{B.13})$$

where a_1 and b_2 are computed using reverse recursion and the relations

$$a_n = 1 + j \frac{2n-1}{2n^2} \beta^2 a_{n+1} \quad (\text{B.14a})$$

$$b_n = a_n - j \frac{n-1}{n^2} \alpha^2 b_{n+1}. \quad (\text{B.14b})$$

The reverse recursion is started at $n = N$, where $a_N = b_N = 1$. Then the relative error, δ , is approximately given by

$$\delta < \frac{4}{N N!} \alpha^{2N-2} \quad (\text{B.15a})$$

$$\delta < \frac{(2N)!}{4^N N!^3} \beta^{2N}. \quad (\text{B.15b})$$

For ΔS_2 , where $\beta \neq 0$, the same technique produces

$$\Delta S_2(0, |\alpha|, \beta) = -j c_1 \ln \left(\left| \frac{\alpha}{\beta} \right| + \sqrt{\left(\frac{\alpha}{\beta} \right)^2 + 1} \right) + \frac{|\alpha|}{\sqrt{\alpha^2 + \beta^2}} \left(j d_1 + \frac{1}{\beta^2} \right) \quad (\text{B.16})$$

where c_1 and d_1 are computed using reverse recursion and the relations

$$c_n = 1 + j \frac{2n+1}{2n(n+1)} \beta^2 c_{n+1} \quad (\text{B.17a})$$

$$d_1 = c_1 + j \frac{1}{4} \alpha^2 d_2 \quad (\text{B.17b})$$

$$d_n = c_n - j \frac{n-1}{n(n+1)} \alpha^2 d_{n+1} \quad \text{for } n > 1. \quad (\text{B.17c})$$

The reverse recursion is started at $n = N$, where $c_N = d_N = 1$. Then the relative error, δ , is approximately given by

$$\delta < \frac{1}{N(N+1)!} \alpha^{2N} \quad (\text{B.18a})$$

$$\delta < \frac{(2N+1)!}{4^N N!^3 (N+1)} \beta^{2N}. \quad (\text{B.18b})$$

Due to the relative size of the terms in Equations (B.13) and (B.16), Equations (B.15a) and (B.18a) provide very accurate estimates on δ for a given α ; however, Equations (B.15b) and (B.18b) give very conservative estimates on δ for a given β . Empirically, the N required for a relative error of δ in S_i is approximately given by

$$N^* \approx \begin{cases} 0.85 - 12.3 \delta^{0.14} + 7.70 \alpha & \text{for } S_1 \\ 2.0 - 12.0 \delta^{0.14} + 7.41 \alpha & \text{for } S_2 \end{cases} \quad (\text{B.19})$$

where N^* is rounded up to $N = 4, 8$, or 13 (i.e. if $N^* = 4.1$, then $N = 8$).

Method IV: Small/Large Argument Approximations

$$(|\alpha| < 1.6, \beta^2 \geq 7)$$

This section presents efficient small/large argument approximations for the integrals S_1 and S_2 when $\alpha < \beta$ and β is large. Again Equation (B.11) is used as in the previous section. Then ΔS_i is evaluated using the binomial expansion for $(u^2 + \beta^2)^{1/2-i}$ and integration by parts. For ΔS_1 this gives

$$\Delta S_1(0, \alpha, \beta) = \frac{1}{|\beta|} \left[e_1 F(\alpha) - \frac{j \alpha}{4 \beta^2} f_2 e^{-j\alpha^2} \right] \quad (\text{B.20})$$

where e_1 and f_2 are computed using reverse recursion and the relations

$$e_n = 1 + j \frac{(2n-1)^2}{4n} \frac{1}{\beta^2} e_{n+1} \quad (\text{B.21a})$$

$$f_n = e_n - \frac{2n-1}{2n} \frac{\alpha^2}{\beta^2} f_{n+1} \quad (\text{B.21b})$$

and $F(\alpha)$ is the Fresnel integral given by

$$F(\alpha) = \int_0^\alpha e^{-ju^2} du. \quad (\text{B.22})$$

The reverse recursion is started at $n = N$, where $e_N = f_N = 1$. Then the relative error, δ , is approximately given by

$$\delta < \frac{(2N)!^2}{4^{2N} N!^3} \frac{1}{\beta^{2N}} \quad (\text{B.23a})$$

$$\delta < \frac{4}{3} \frac{(2N)!}{4^N N!^2} \frac{\alpha^{2N-2}}{\beta^{2N-2}}. \quad (\text{B.23b})$$

For ΔS_2 the same technique produces

$$\Delta S_2(0, \alpha, \beta) = \frac{1}{|\beta|^3} \left[g_1 F(\alpha) - j \frac{3}{4} \frac{\alpha}{\beta^2} h_2 e^{-j\alpha^2} \right] \quad (\text{B.24})$$

where g_1 and h_2 are computed using reverse recursion and the relations

$$g_n = 1 + j \frac{(2n-1)(2n+1)}{4n} \frac{1}{\beta^2} g_{n+1} \quad (\text{B.25a})$$

$$h_n = g_n - \frac{2n+1}{2n} \frac{\alpha^2}{\beta^2} h_{n+1}. \quad (\text{B.25b})$$

The reverse recursion is started at $n = N$, where $g_N = h_N = 1$. Then the relative error, δ , is approximately given by

$$\delta < \frac{(2N+1)(2N)!^2}{4^{2N} N!^3} \frac{1}{\beta^{2N}} \quad (\text{B.26a})$$

$$\delta < \frac{4}{5} \frac{(2N+1)!}{4^N N!^2} \frac{\alpha^{2N-2}}{\beta^{2N-2}} \quad (\text{B.26b})$$

Empirically, the N required for a relative error of δ in S_i is approximately given by

$$N^* \approx \begin{cases} 3.2 - 20.8 \delta^{0.225} + 23.5 \frac{\alpha^2}{\beta^2} & \text{for } S_1 \\ 6.1 - 24.4 \delta^{0.136} + 20.0 \frac{\alpha^2}{\beta^2} & \text{for } S_2 \end{cases} \quad (\text{B.27})$$

where N^* is rounded up to $N = 4, 8,$ or 13 (i.e. if $N^* = 4.1$, then $N = 8$).

In summary, this appendix presented new and efficient techniques for accurately evaluating the integrals needed for the half-plane Green's function of a line source. For a given relative accuracy, these approximations are much faster than the techniques presented in previous work [129, 138, 139].

Appendix C

Chiral Slab and Normal Incident Plane Wave

This appendix presents the solution for a plane wave normally incident on a chiral slab in free space, and in a form simpler than available in [54] and [62]. Consider a right circularly polarized wave normally incident on the chiral slab as shown in Figure C.1. The incident, reflected, internal and transmitted fields are given by

$$\mathbf{E}^i = (\hat{\mathbf{x}} - j\hat{\mathbf{z}}) e^{jk_0 y} \quad (\text{C.1a})$$

$$\mathbf{E}^r = R (\hat{\mathbf{x}} - j\hat{\mathbf{z}}) e^{-jk_0 y} \quad (\text{C.1b})$$

$$\mathbf{E}^{i1} = T_{int} (\hat{\mathbf{x}} - j\hat{\mathbf{z}}) e^{jk_R y} \quad (\text{C.1c})$$

$$\mathbf{E}^{r1} = R_{int} (\hat{\mathbf{x}} - j\hat{\mathbf{z}}) e^{-jk_L y} \quad (\text{C.1d})$$

$$\mathbf{E}^t = T (\hat{\mathbf{x}} - j\hat{\mathbf{z}}) e^{jk_2 y} \quad (\text{C.1e})$$

where $k_0 = \omega \sqrt{\mu_0 \epsilon_0}$, $k_2 = \omega \sqrt{\mu_2 \epsilon_2}$, $k_{R,L} = k_c \pm k_\xi$, $k_c = \omega \sqrt{\mu \epsilon_c}$, $k_\xi = \omega \mu \xi_c$, and $\epsilon_c = \epsilon + \mu \xi_c^2$. Simple matching of fields at the boundaries produces

$$T_{int} = T \frac{\eta_2 + \eta_c}{2\eta_2} \quad (\text{C.2a})$$

$$R_{int} = T \frac{\eta_2 - \eta_c}{2\eta_2} \quad (\text{C.2b})$$

$$T = \frac{\eta_2}{e^{jk_\xi l}} \left(\frac{e^{jk_0 l} + R e^{-jk_0 l}}{\eta_2 \cos k_c l + j\eta_c \sin k_c l} \right) \quad (\text{C.2c})$$

$$R = \frac{\eta_{eff} - \eta_0}{\eta_{eff} + \eta_0} e^{j2k_0 l} \quad (\text{C.2d})$$

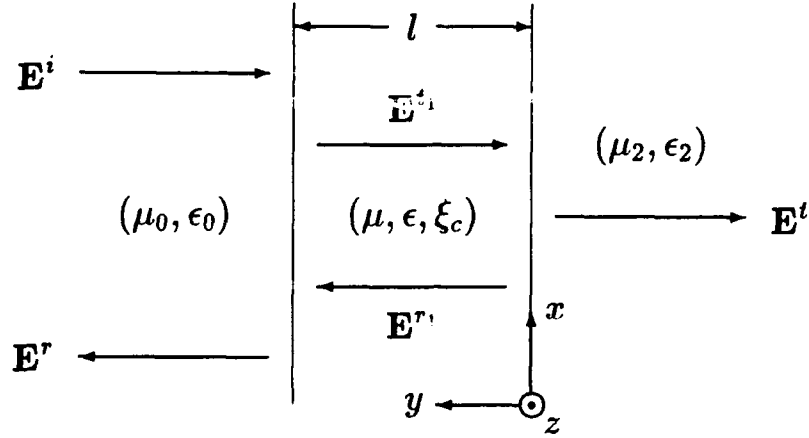


Figure C.1: Geometry for an infinite chiral slab

$$\eta_{eff} = \eta_c \frac{\eta_2 + j\eta_c \tan k_c l}{\eta_c + j\eta_2 \tan k_c l} \quad (C.2e)$$

where $\eta_0 = \sqrt{\mu_0/\epsilon_0}$, $\eta_c = \sqrt{\mu/\epsilon_c}$, $\eta_2 = \sqrt{\mu_2/\epsilon_2}$, and l is the thickness of the slab. For the case of a left circularly polarized wave, replace k_ξ by $-k_\xi$ in the above equations. If medium 2 is a perfect conductor, $\eta_{eff} = j\eta_c \tan k_c l$. For a linearly polarized plane wave the solution is simply the sum of the right and left circularly polarized solutions.

Appendix D

Fields of Circular Vector Potentials

This appendix presents the fields produced by the circular vector potentials developed in Section 2.3. For the \hat{x} right circular vector potential

$$\mathbf{R} = \hat{x} (a \sin k_{y,R} y + b \cos k_{y,R} y) e^{-j(k_x x + k_z z)} \quad (D.1)$$

the field components are

$$E_x = \frac{k_z^2 + k_{y,R}^2}{k_R} (a \sin k_{y,R} y + b \cos k_{y,R} y) e^{-j(k_x x + k_z z)} \quad (D.2a)$$

$$E_y = -j \left[\left(a k_z - b \frac{k_x k_{y,R}}{k_R} \right) \sin k_{y,R} y + \left(b k_z + a \frac{k_x k_{y,R}}{k_R} \right) \cos k_{y,R} y \right] e^{-j(k_x x + k_z z)} \quad (D.2b)$$

$$E_z = - \left[\left(a \frac{k_x k_z}{k_R} - b k_{y,R} \right) \sin k_{y,R} y + \left(b \frac{k_x k_z}{k_R} + a k_{y,R} \right) \cos k_{y,R} y \right] e^{-j(k_x x + k_z z)} \quad (D.2c)$$

For the \hat{x} left circular vector potential

$$\mathbf{L} = \hat{x} (a \sin k_{y,L} y + b \cos k_{y,L} y) e^{-j(k_x x + k_z z)} \quad (D.3)$$

the field components are

$$E_x = - \frac{k_z^2 + k_{y,L}^2}{k_L} (a \sin k_{y,L} y + b \cos k_{y,L} y) e^{-j(k_x x + k_z z)} \quad (D.4a)$$

$$E_y = -j \left[(ak_z + b \frac{k_x k_{y,L}}{k_L}) \sin k_{y,L} y + (bk_z - a \frac{k_x k_{y,L}}{k_L}) \cos k_{y,L} y \right] e^{-j(k_x x + k_z z)} \quad (D.4b)$$

$$E_z = \left[(a \frac{k_x k_z}{k_L} + bk_{y,L}) \sin k_{y,L} y + (b \frac{k_x k_z}{k_L} - ak_{y,L}) \cos k_{y,L} y \right] e^{-j(k_x x + k_z z)}. \quad (D.4c)$$

For the \hat{y} right circular vector potential

$$\mathbf{R} = \hat{y} (a \sin k_{y,R} y + b \cos k_{y,R} y) e^{-j(k_x x + k_z z)} \quad (D.5)$$

the field components are

$$E_x = j \left[(ak_z + b \frac{k_x k_{y,R}}{k_R}) \sin k_{y,R} y + (bk_z - a \frac{k_x k_{y,R}}{k_R}) \cos k_{y,R} y \right] e^{-j(k_x x + k_z z)} \quad (D.6a)$$

$$E_y = \frac{k_x^2 + k_z^2}{k_R} (a \sin k_{y,R} y + b \cos k_{y,R} y) e^{-j(k_x x + k_z z)} \quad (D.6b)$$

$$E_z = -j \left[(ak_x - b \frac{k_{y,R} k_z}{k_R}) \sin k_{y,R} y + (bk_x + a \frac{k_{y,R} k_z}{k_R}) \cos k_{y,R} y \right] e^{-j(k_x x + k_z z)}. \quad (D.6c)$$

For the \hat{y} left circular vector potential

$$\mathbf{L} = \hat{y} (a \sin k_{y,L} y + b \cos k_{y,L} y) e^{-j(k_x x + k_z z)} \quad (D.7)$$

the field components are

$$E_x = j \left[(ak_z - b \frac{k_x k_{y,L}}{k_L}) \sin k_{y,L} y + (bk_z + a \frac{k_x k_{y,L}}{k_L}) \cos k_{y,L} y \right] e^{-j(k_x x + k_z z)} \quad (D.8a)$$

$$E_y = -\frac{k_x^2 + k_z^2}{k_L} (a \sin k_{y,L} y + b \cos k_{y,L} y) e^{-j(k_x x + k_z z)} \quad (D.8b)$$

$$E_z = -j \left[(ak_x + b \frac{k_{y,L} k_z}{k_L}) \sin k_{y,L} y + (bk_x - a \frac{k_{y,L} k_z}{k_L}) \cos k_{y,L} y \right] e^{-j(k_x x + k_z z)}. \quad (D.8c)$$

For the \hat{z} right circular vector potential

$$\mathbf{R} = \hat{z} (a \sin k_{y,R} y + b \cos k_{y,R} y) e^{-j(k_x x + k_z z)} \quad (D.9)$$

the field components are

$$E_x = - \left[\left(a \frac{k_x k_z}{k_R} + b k_{y,R} \right) \sin k_{y,R} y + \left(b \frac{k_x k_z}{k_R} - a k_{y,R} \right) \cos k_{y,R} y \right] e^{-j(k_x x + k_z z)} \quad (D.10a)$$

$$E_y = j \left[\left(a k_x + b \frac{k_{y,R} k_z}{k_R} \right) \sin k_{y,R} y + \left(b k_x - a \frac{k_{y,R} k_z}{k_R} \right) \cos k_{y,R} y \right] e^{-j(k_x x + k_z z)} \quad (D.10b)$$

$$E_z = \frac{k_x^2 + k_{y,R}^2}{k_R} (a \sin k_{y,R} y + b \cos k_{y,R} y) e^{-j(k_x x + k_z z)}. \quad (D.10c)$$

For the \hat{z} left circular vector potential

$$\mathbf{L} = \hat{z} (a \sin k_{y,L} y + b \cos k_{y,L} y) e^{-j(k_x x + k_z z)} \quad (D.11)$$

the field components are

$$E_x = \left[\left(a \frac{k_x k_z}{k_L} - b k_{y,L} \right) \sin k_{y,L} y + \left(b \frac{k_x k_z}{k_L} + a k_{y,L} \right) \cos k_{y,L} y \right] e^{-j(k_x x + k_z z)} \quad (D.12a)$$

$$E_y = j \left[\left(a k_x - b \frac{k_{y,L} k_z}{k_L} \right) \sin k_{y,L} y + \left(b k_x + a \frac{k_{y,L} k_z}{k_L} \right) \cos k_{y,L} y \right] e^{-j(k_x x + k_z z)} \quad (D.12b)$$

$$E_z = - \frac{k_x^2 + k_{y,L}^2}{k_L} (a \sin k_{y,L} y + b \cos k_{y,L} y) e^{-j(k_x x + k_z z)}. \quad (D.12c)$$

Appendix E

Spectral Domain Fields in a Half Space

This appendix examines the wave numbers of a spectral domain field in a half space of $y > 0$. Assume a spectral domain field given by

$$\psi = \int_{-\infty}^{\infty} \bar{\psi}(k_x) e^{-j(k_x x + k_y y + k_z z)} dk_x \quad (E.1)$$

where

$$k_0^2 = k_x^2 + k_y^2 + k_z^2. \quad (E.2)$$

For $+z$ propagation, with $k_z = \beta_z - j\alpha_z$,

$$e^{-jk_z z} = e^{-\alpha_z z} e^{-j\beta_z z} \quad (E.3)$$

which requires that both α_z and β_z be greater than zero. The fields must decay as $y \rightarrow \infty$, therefore $\alpha_y > 0$, using $k_y = \beta_y - j\alpha_y$ and

$$e^{-jk_y y} = e^{-\alpha_y y} e^{-j\beta_y y}. \quad (E.4)$$

Take k_0 and k_x to be real, then from Equation (E.2)

$$k_0^2 = k_x^2 + \beta_y^2 - \alpha_y^2 + \beta_x^2 - \alpha_x^2 \quad (E.5a)$$

$$0 = -j2\alpha_y\beta_y - j2\alpha_x\beta_x. \quad (E.5b)$$

From Equation (E.5b)

$$\beta_y = -\frac{\alpha_z \beta_z}{\alpha_y} \quad (E.6)$$

therefore

$$\beta_y < 0 \quad (E.7)$$

and

$$k_y = \begin{cases} -\sqrt{k_0^2 - k_x^2 - k_z^2} & \text{for } k_x^2 + k_z^2 < k_0^2 \\ -j\sqrt{k_x^2 + k_z^2 - k_0^2} & \text{for } k_x^2 + k_z^2 > k_0^2. \end{cases} \quad (E.8)$$

Appendix F

Fourier Transforms for Microstrip Problems

This appendix presents some of the Fourier transforms used in microstrip problems and how they are obtained. The Fourier transform

$$\int_{-\infty}^{\infty} J_n(ax) e^{-jbx} dx = \begin{cases} (-j)^n \frac{2 T_n(b/a)}{\sqrt{a^2 - b^2}} & \text{for } |b| < a \\ 0 & \text{for } |b| > a \end{cases} \quad (F.1)$$

where T_n is a Chebyshev polynomial of the first kind, can be obtained directly from [141, sec. 6.671.8-10].

The Chebyshev polynomials of the first and second kinds have the following properties

$$T_n(\cos \theta) = \cos n\theta \quad (F.2a)$$

$$U_{n-1}(\cos \theta) = \frac{\sin n\theta}{\sin \theta} \quad (F.2b)$$

$$\frac{d}{d\theta} [\sin \theta U_{n-1}(\cos \theta)] = n T_n(\cos \theta). \quad (F.2c)$$

As a consequence of Equation (F.2c)

$$\frac{d}{dx} (\sqrt{1-x^2} U_{n-1}(x)) = -n \frac{T_n(x)}{\sqrt{1-x^2}}. \quad (F.3)$$

Starting with

$$J_n(at) \xrightarrow{\mathcal{F}} (-j)^n \frac{2 T_n(\omega/a)}{\sqrt{a^2 - \omega^2}} \quad \text{for } |\omega| < a \quad (F.4)$$

use Equation (F.2c) to get

$$J_n(at) \xleftrightarrow{\mathcal{F}} (-j)^n \frac{-2}{na} \frac{d}{d\omega} \left[\sqrt{a^2 - \omega^2} U_{n-1}(\omega/a) \right] \quad \text{for } |\omega| < a. \quad (F.5)$$

The derivative property for Fourier transforms is

$$(-jt)f(t) \xleftrightarrow{\mathcal{F}} \frac{d}{d\omega} F(\omega). \quad (F.6)$$

Comparing Equation (F.5) and (F.6) the following relationship can be obtained

$$\frac{j}{t} J_n(at) \xleftrightarrow{\mathcal{F}} (-j)^n \frac{-2}{na} \frac{d}{d\omega} \left[\sqrt{a^2 - \omega^2} U_{n-1}(\omega/a) \right] \quad \text{for } |\omega| < a. \quad (F.7)$$

which can be written as

$$\int_{-\infty}^{\infty} \frac{J_n(ax)}{x} e^{-jbx} dx = \begin{cases} (-j)^{n-1} \frac{2}{na} \sqrt{a^2 - b^2} U_{n-1}(b/a) & \text{for } |b| < a \\ 0 & \text{for } |b| > a \end{cases} \quad (F.8)$$

Edge Modes

Edge modes on microstrip lines can be represented by

$$\frac{\sqrt{a - \omega}}{\sqrt{a + \omega}} = \frac{1}{\sqrt{a^2 - \omega^2}} - \frac{\omega}{\sqrt{a^2 - \omega^2}} \quad (F.9a)$$

$$\frac{\sqrt{a + \omega}}{\sqrt{a - \omega}} = \frac{1}{\sqrt{a^2 - \omega^2}} + \frac{\omega}{\sqrt{a^2 - \omega^2}}. \quad (F.9b)$$

From Equation (F.4), the Fourier transforms of these edge mode functions are given by

$$\frac{1}{2} [J_0(at) - jaJ_1(at)] \xleftrightarrow{\mathcal{F}} \begin{cases} \frac{\sqrt{a-\omega}}{\sqrt{a+\omega}} & \text{for } |\omega| < a \\ 0 & \text{for } |\omega| > a \end{cases} \quad (F.10a)$$

$$\frac{1}{2} [J_0(at) + jaJ_1(at)] \xleftrightarrow{\mathcal{F}} \begin{cases} \frac{\sqrt{a+\omega}}{\sqrt{a-\omega}} & \text{for } |\omega| < a \\ 0 & \text{for } |\omega| > a. \end{cases} \quad (F.10b)$$

Fourier transforms for these and more complicated edge mode type functions can also be calculated using Equations 3.384.1 of [141].

Appendix G

Numerical Integration for the Self-Impedance of the Dominant Microstrip Current

This appendix presents a technique which can be applied to the integration of the self-impedance of the Maxwellian current distribution on a microstrip line. This is the $Z_{zz(0,0)}$ term of Section 5.4 and can be written as

$$Z_{zz(0,0)} = \int_0^{\infty} \frac{f(k_x)}{k_x^2} \cos^2 \left(\frac{k_x W}{2} - \frac{\pi}{4} \right) dx \quad (G.1)$$

where $f(k_x)$ approaches a constant for large k_x .

Consider the integral

$$I = \int_0^{\infty} f(x) dx \quad (G.2)$$

where $f(x) \propto x^{-a}$ for $a > 1$ and large x . The integral can be written as

$$I = I_0(X) + I_1(X) + I_{\infty}(X) \quad (G.3)$$

where

$$I_0(X) = \int_0^X f(x) dx \quad (G.4a)$$

$$I_1(X) = \int_X^{X+\Delta} f(x) dx \quad (G.4b)$$

$$I_{\infty}(X) = \int_{X+\Delta}^{\infty} f(x)dx. \quad (G.4c)$$

Next, define a constant c such that

$$I_1(X) = c \int_X^{X+\Delta} x^{-a} dx \quad (G.5)$$

then

$$c = \frac{I_1(X)}{(a-1)[X^{1-a} - (X+\Delta)^{1-a}]} \quad (G.6)$$

For large x

$$I_{\infty}(X) \approx c \int_{X+\Delta}^{\infty} x^{-a} dx \quad (G.7a)$$

$$\approx \frac{I_1(X)}{(1 + \Delta/X)^{a-1} - 1} \quad (G.7b)$$

This technique is used by integrating to a point X_0 , integrating the additional distance Δ , and using Equation (G.7b) to estimate $I_{\infty}(X_0)$ and repeating for $X_1 = X_0 + \Delta$. By comparing $I_{\infty}(X_0)$ and $I_{\infty}(X_1)$ an estimate of the error can be obtained.

For the microstrip impedance problem, Δ would be chosen as the length of one or more cycles of the sinusoid, in this case $\Delta = n \times \frac{2\pi}{\beta}$ and the first X would be chosen to be near a null. For this special case of $a = 2$, $I_{\infty}(X)$ is given by

$$I_{\infty}(X) = I_1(X) \frac{X}{\Delta} \quad (G.8)$$

Appendix H

Generalized Sine and Cosine Integrals

This appendix presents generalized sine and cosine integrals which are extensions of the sine and cosine integrals

$$Si(z) = \int_0^z \frac{\sin t}{t} dt \quad (\text{H.1a})$$

$$Ci(z) = -\int_z^\infty \frac{\cos t}{t} dt \quad (\text{H.1b})$$

$$si(z) = -\int_z^\infty \frac{\sin t}{t} dt \quad (\text{H.1c})$$

$$= Si(z) - \frac{\pi}{2} \quad (\text{H.1d})$$

and the Fresnel integrals

$$S(z) = \int_0^z \sin \frac{\pi}{2} t^2 dt = \frac{1}{\sqrt{2\pi}} \int_0^{\frac{\pi}{2} z^2} \frac{\sin s}{\sqrt{s}} ds \quad (\text{H.2a})$$

$$C(z) = \int_0^z \cos \frac{\pi}{2} t^2 dt = \frac{1}{\sqrt{2\pi}} \int_0^{\frac{\pi}{2} z^2} \frac{\cos s}{\sqrt{s}} ds \quad (\text{H.2b})$$

as defined in [140, sec. 5.2, 7.3].

The first extension is for higher powers in the denominator

$$si(z, P) = - \int_z^{\infty} \frac{\sin t}{t^P} dt = \frac{1}{P-1} \left[\frac{\sin z}{t^{P-1}} + Ci(z, P-1) \right] \quad (\text{H.3a})$$

$$Ci(z, P) = - \int_z^{\infty} \frac{\cos t}{t^P} dt = \frac{1}{P-1} \left[\frac{\cos z}{t^{P-1}} - si(z, P-1) \right] \quad (\text{H.3b})$$

where $si(z, 1) = si(z)$ and $Ci(z, 1) = Ci(z)$.

The second extension is to double cosine and sine functions

$$CCi(z, P, \omega_1, \alpha, \omega_2, \beta) = - \int_z^{\infty} \frac{1}{t^P} \cos(\omega_1 t + \alpha) \cos(\omega_2 t + \beta) dt \quad (\text{H.4a})$$

$$CSi(z, P, \omega_1, \alpha, \omega_2, \beta) = - \int_z^{\infty} \frac{1}{t^P} \cos(\omega_1 t + \alpha) \sin(\omega_2 t + \beta) dt. \quad (\text{H.4b})$$

Each of these functions can be written as the sum of four terms

$$CCi(z, P, \omega_1, \alpha, \omega_2, \beta) = CCi_1 + CCi_2 + CCi_3 + CCi_4 \quad (\text{H.5a})$$

$$CSi(z, P, \omega_1, \alpha, \omega_2, \beta) = CSi_1 + CSi_2 + CSi_3 + CSi_4 \quad (\text{H.5b})$$

where

$$CCi_1 = \frac{\cos(\alpha - \beta)}{2} |\omega_1 - \omega_2|^{P-1} Ci(|\omega_1 - \omega_2|z, P) \quad (\text{H.6a})$$

$$CCi_2 = \frac{\cos(\alpha + \beta)}{2} |\omega_1 + \omega_2|^{P-1} Ci(|\omega_1 + \omega_2|z, P) \quad (\text{H.6b})$$

$$CCi_3 = - \frac{\sin(\alpha - \beta)}{2} |\omega_1 - \omega_2|^{P-1} si(|\omega_1 - \omega_2|z, P) \quad (\text{H.6c})$$

$$CCi_4 = - \frac{\sin(\alpha + \beta)}{2} |\omega_1 + \omega_2|^{P-1} si(|\omega_1 + \omega_2|z, P) \quad (\text{H.6d})$$

$$CSi_1 = - \frac{\cos(\alpha - \beta)}{2} |\omega_1 - \omega_2|^{P-1} si(|\omega_1 - \omega_2|z, P) \quad (\text{H.6e})$$

$$CSi_2 = \frac{\cos(\alpha + \beta)}{2} |\omega_1 + \omega_2|^{P-1} si(|\omega_1 + \omega_2|z, P) \quad (\text{H.6f})$$

$$CSi_3 = - \frac{\sin(\alpha - \beta)}{2} |\omega_1 - \omega_2|^{P-1} Ci(|\omega_1 - \omega_2|z, P) \quad (\text{H.6g})$$

$$CSi_4 = \frac{\sin(\alpha + \beta)}{2} |\omega_1 + \omega_2|^{P-1} Ci(|\omega_1 + \omega_2|z, P) \quad (\text{H.6h})$$

with adjustments for special cases:

$\omega_1 - \omega_2 < 0$: change sign on CCi_3 and CSi_1

$\omega_1 + \omega_2 < 0$: change sign on CCi_4 and CSi_2

$\omega_1 - \omega_2 = 0$: $CCi_3 = 0$, $CSi_1 = 0$, and

$$CCi_1 = -\frac{\cos(\alpha - \beta)}{2} \frac{z^{1-P}}{P-1} \quad (\text{H.7a})$$

$$CSi_3 = \frac{\sin(\alpha - \beta)}{2} \frac{z^{1-P}}{P-1} \quad (\text{H.7b})$$

$\omega_1 + \omega_2 = 0$: $CCi_4 = 0$, $CSi_2 = 0$, and

$$CCi_2 = -\frac{\cos(\alpha + \beta)}{2} \frac{z^{1-P}}{P-1} \quad (\text{H.8a})$$

$$CSi_4 = -\frac{\sin(\alpha + \beta)}{2} \frac{z^{1-P}}{P-1} \quad (\text{H.8b})$$

Appendix I

Evaluation of the Microstrip Impedance Elements in the Spatial Domain

This appendix presents spatial domain equations and sample numerical results used to verify elements of the method of moments impedance matrix presented in Chapter 5. Since the spatial-domain Green's function for a microstrip line does not exist in closed form, a substrate with material parameters (μ_0, ϵ_0) is necessary to evaluate the impedance matrix in the spatial domain for simple tests. The resulting problem can be decomposed into the self-impedance of a strip in free space, and the mutual impedance of the strip and its image. The geometry of the equivalent problem is shown in Figure I.1.

The first test involves numerical integration of the self-impedance of J_z current modes. The self-impedance of a J_z current mode in free space is given by

$$Z_{zz,s} = \frac{k_0^2 - k_z^2}{4\omega\epsilon} \int_{-W/2}^{W/2} \int_{-W/2}^{W/2} H_0^{(2)}(k_t|x - x'|) J_z(x') dx' W_z(x) dx \quad (I.1)$$

and the mutual impedance of the current mode and its image is given by

$$Z_{zz,i} = -\frac{k_0^2 - k_z^2}{4\omega\epsilon} \int_{-W/2}^{W/2} \int_{-W/2}^{W/2} H_0^{(2)}(k_t\sqrt{(x - x')^2 + 4t^2}) J_z(x') dx' W_z(x) dx \quad (I.2)$$

using Equation (J.15b) and the Z_{zz} equivalent of Equation (5.26).

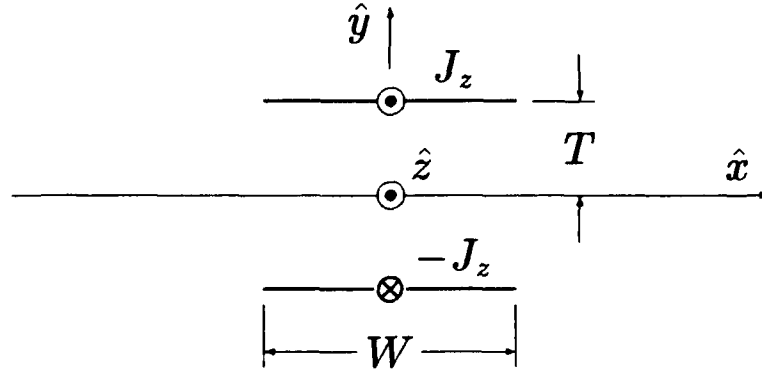


Figure I.1: Equivalent geometry for self-impedance of J_z microstrip current mode.

For $W = 0.1$, $T = 0.1$, $k_0 = 10.479$ (500 MHz), $k_z = 10k_0$, and $J_z(x') = W_z(x) = 1/W$, numerical integration of Equation (I.1) plus Equation (I.2) using Gaussian Quadrature with 280 and 288 points¹ results in a value of $Z_{zz} = -j17663$, which differs from the spectral domain value of $Z_{zz} = -j17596$ by 0.4 percent. For $J_z(x) = W_z(x) = 1/(\pi\sqrt{W^2/4 - x^2})$, the same numerical integration results in a value of $Z_{zz} = -j18849$, which differs from the spectral domain value of $Z_{zz} = -j19012$ by 0.9 percent.

The second test involves closed form integration of the self-impedance of J_x current modes using the small argument approximations for Hankel functions. The \hat{x} -component of the electric field at the surface of the strip shown in Figure I.1 due to a J_x surface current is given by

$$E_x(J_x) = \frac{-1}{4\omega\epsilon} e^{-jk_z z} \int_{-W/2}^{W/2} \left[k_z^2 H_0^{(2)}(k_t \rho) + \frac{k_t}{\rho} H_1^{(2)}(k_t \rho) \right] J_x(x') dx' \quad (I.3)$$

using Equation (J.13a), $y = y'$, and letting $T \rightarrow \infty$ so that the image current does not contribute to the electric field at the strip. For $k_z = 0$ and $J_x(x') = 1/W$, then

¹The logarithmic singularity of the Hankel function is avoided by using a different number of points for the each of the double integrals.

Equation (I.3) reduces to

$$E_x(J_x) = \frac{-k_0}{4\omega\epsilon W} \int_{-W/2}^{W/2} \frac{1}{|x-x'|} H_1^{(2)}(k_0|x-x'|) dx'. \quad (I.4)$$

Using the small argument approximation for the Hankel function and integrating, Equation (I.4) is approximately given by

$$E_x(J_x) \approx -\frac{\omega\mu_0}{8} - \frac{j}{2\pi\omega\epsilon W} \left[\frac{1}{x-W/2} - \frac{1}{x+W/2} \right]. \quad (I.5)$$

For point-matching with $k_z = 0$, the self-impedance of a J_x current mode is approximately given by

$$Z_{xx,s} = -E_x(J_x)|_{x=0} \approx \frac{\omega\mu_0}{8} - \frac{j2}{\pi\omega\epsilon W^2}. \quad (I.6)$$

For a frequency of 500 MHz, $W = 0.06$, and $T \rightarrow \infty$, Equation (I.6) gives a result of $Z_{xx,s} = 493.5 - j6358$, compared to $Z_{xx,s} = 465 - j5449$ using spectral domain integration.

For a weighting function in the shape of a triangle given by

$$W_x(x) = \begin{cases} \frac{1}{W^2}(W/2 - x) & \text{for } 0 < x < W/2 \\ \frac{1}{W^2}(W/2 + x) & \text{for } -W/2 < x < 0 \end{cases} \quad (I.7)$$

the self-impedance of a J_x current mode is given by

$$Z_{xx,s} \approx \frac{\omega\mu_0}{8} - \frac{j4}{\pi\omega\epsilon W^2} \ln 2. \quad (I.8)$$

For a frequency of 500 MHz, $W = 0.06$, and $T \rightarrow \infty$, Equation (I.8) gives a result of $Z_{xx,s} = 493.5 - j8813$, compared to $Z_{xx,s} = 490 - j7976$ using spectral domain integration. For $T = 0.1$, the mutual impedance of the image can be calculated by numerically double integrating Equation (J.13a) multiplied by the weighting function, resulting in $Z_{xx,i} = 101.4 + j528.2$, compared to $Z_{xx,i} = 102 + j529$ using spectral domain integration by subtracting the impedances for $T \rightarrow \infty$ and $T = 0.1$.

For $k_z \neq 0$ and $J_r(x') = 1/W$, Equation (I.3) reduces to

$$E_r(J_r) = \frac{-1}{4\omega\epsilon W} \left[k_z^2 \int_{-W/2}^{W/2} H_0^{(2)}(k_t|x-x'|) dx' + k_t \int_{-W/2}^{W/2} \frac{1}{|x-x'|} H_1^{(2)}(k_0|x-x'|) dx' \right]. \quad (I.9)$$

Using the small argument approximations for the Hankel functions and integrating Equation (I.9) with the triangular weighting function given in Equation (I.7), the self-impedance is approximately given by

$$Z_{xx,s} \approx \frac{1}{4\pi\omega\epsilon W} \left[k_z^2 \left(W - j\frac{2}{\pi}W \left[-\frac{11}{6} + \frac{1}{3}\ln 2 + \ln \frac{\gamma k_t}{2}W \right] \right) + k_t \left(k_t \frac{W}{2} - j\frac{16}{\pi k_t W} \ln 2 \right) \right] \quad (I.10)$$

where $\gamma = 1.781$.

For a frequency of 500 MHz, $W = 0.06$, $T \rightarrow \infty$, and $k_z = 0.1k_0$; Equation (I.10) gives a result of $Z_{xx,s} = 498.4 - j8817$, compared to $Z_{xx,s} = 495 - j7969$ using spectral domain integration. For $T = 0.1$, the mutual impedance of the image can be calculated by numerically double integrating Equation (J.13a) multiplied by the weighting function, resulting in $Z_{xx,i} = 94.4 + j530.2$, compared to $Z_{xx,i} = 95 + j530$ using spectral domain integration by subtracting the impedances for $T \rightarrow \infty$ and $T = 0.1$. Changing the parameters to $W = 0.03$ and $k_z = 0.5k_0$; the results are $Z_{xx,s} = 616.9 - j35330$ using Equation (I.10) and $Z_{xx,s} = 616 - j33952$ using spectral domain integration. The mutual impedance of the image for $T = 0.1$ was $Z_{xx,i} = -89.2 + j560.3$ numerically and $Z_{xx,i} = -89 + j560$ by spectral domain integration.

The integrals of the small argument approximations of the Hankel functions used in this Appendix are summarized in Appendix L.

Appendix J

Two-Dimensional Traveling Wave Electric Currents

This appendix presents the fields of a two-dimensional traveling wave electric current given by

$$\mathbf{J}(\mathbf{r}') = \mathbf{J}(\boldsymbol{\rho}') e^{-jk_z z'} \quad (\text{J.1})$$

in a two-dimensional region, R . The vector potential of an arbitrary current in a volume V with a wave number k is calculated using

$$\mathbf{A}(\mathbf{r}) = \frac{1}{4\pi} \int_V \mathbf{J}(\mathbf{r}') \frac{e^{-jk r}}{r} dV' \quad (\text{J.2})$$

where $r = |\mathbf{r} - \mathbf{r}'|$. Since the region is independent of z , the z integration of Equation (J.2) can be done using

$$\frac{1}{\pi} \int_{-\infty}^{\infty} \frac{e^{-jk\sqrt{\rho^2 + (z-z')^2}}}{\sqrt{\rho^2 + (z-z')^2}} e^{-jk_z z'} dz' = -j e^{-jk_z z} H_0^{(2)}(k_t \rho) \quad (\text{J.3})$$

from Appendix K, where

$$r = \sqrt{\rho^2 + (z - z')^2} \quad (\text{J.4a})$$

$$\rho = \sqrt{(x - x')^2 + (y - y')^2} \quad (\text{J.4b})$$

$$k_t = \sqrt{k^2 - k_z^2}. \quad (\text{J.4c})$$

The resulting equation for the vector potential of an arbitrary traveling wave electric current in a z -independent region is given by

$$\mathbf{A}(\boldsymbol{\rho}) = -\frac{j}{4} e^{-jk_z z} \int_R H_0^{(2)}(k_t \rho) \mathbf{J}(\boldsymbol{\rho}') dR'. \quad (\text{J.5})$$

The z -independent component of the current can be written in rectangular coordinates as

$$\mathbf{J}(\boldsymbol{\rho}') = \hat{\mathbf{x}} J_x(\boldsymbol{\rho}') + \hat{\mathbf{y}} J_y(\boldsymbol{\rho}') + \hat{\mathbf{z}} J_z(\boldsymbol{\rho}') \quad (\text{J.6})$$

where each component produces a vector potential of the same polarization, i.e.,

$$\hat{\mathbf{x}} J_x(\boldsymbol{\rho}') \rightarrow \hat{\mathbf{x}} A_x(\boldsymbol{\rho}) \quad (\text{J.7a})$$

$$\hat{\mathbf{y}} J_y(\boldsymbol{\rho}') \rightarrow \hat{\mathbf{y}} A_y(\boldsymbol{\rho}) \quad (\text{J.7b})$$

$$\hat{\mathbf{z}} J_z(\boldsymbol{\rho}') \rightarrow \hat{\mathbf{z}} A_z(\boldsymbol{\rho}). \quad (\text{J.7c})$$

The electric and magnetic fields are calculated from the individual vector potentials using $\mathbf{H} = \nabla \times \mathbf{A}$ and $\mathbf{E} = -j\omega\mu\mathbf{A} + \frac{1}{j\omega\epsilon} \nabla(\nabla \cdot \mathbf{A})$.

The fields of a $\hat{\mathbf{x}}$ polarized traveling wave current are

$$\mathbf{H} = -jk_z A_x \hat{\mathbf{y}} - \frac{\partial A_x}{\partial y} \hat{\mathbf{z}} \quad (\text{J.8a})$$

$$\mathbf{E} = \frac{-j}{\omega\epsilon} \left[\left(A_x k^2 + \frac{\partial^2 A_x}{\partial x^2} \right) \hat{\mathbf{x}} + \frac{\partial^2 A_x}{\partial x \partial y} \hat{\mathbf{y}} - jk_z \frac{\partial A_x}{\partial x} \hat{\mathbf{z}} \right] \quad (\text{J.8b})$$

where the explicit dependent on $\boldsymbol{\rho}$ has been dropped for clarity. Similarly, the fields of a $\hat{\mathbf{y}}$ polarized traveling wave current are

$$\mathbf{H} = jk_z A_y \hat{\mathbf{x}} + \frac{\partial A_y}{\partial x} \hat{\mathbf{z}} \quad (\text{J.9a})$$

$$\mathbf{E} = \frac{-j}{\omega\epsilon} \left[\frac{\partial^2 A_y}{\partial x \partial y} \hat{\mathbf{x}} + \left(A_y k^2 + \frac{\partial^2 A_y}{\partial y^2} \right) \hat{\mathbf{y}} - jk_z \frac{\partial A_y}{\partial y} \hat{\mathbf{z}} \right] \quad (\text{J.9b})$$

and the fields of a $\hat{\mathbf{z}}$ polarized traveling wave current are

$$\mathbf{H} = \frac{\partial A_z}{\partial y} \hat{\mathbf{x}} - \frac{\partial A_z}{\partial x} \hat{\mathbf{y}} \quad (\text{J.10a})$$

$$\mathbf{E} = \frac{-j}{\omega\epsilon} \left[-jk_z \frac{\partial A_z}{\partial x} \hat{\mathbf{x}} - jk_z \frac{\partial A_z}{\partial y} \hat{\mathbf{y}} \right] + (k^2 - k_z^2) A_z \hat{\mathbf{z}}. \quad (\text{J.10b})$$

The partial derivatives in Equations (J.8)-(J.10) reduce to the derivatives of $H_0^{(2)}(k_t \rho)$ given below:

$$\frac{\partial}{\partial x} H_0^{(2)}(k_t \rho) = -k_t \frac{x - x'}{\rho} H_1^{(2)}(k_t \rho) \quad (\text{J.11a})$$

$$\frac{\partial}{\partial y} H_0^{(2)}(k_t \rho) = -k_t \frac{y - y'}{\rho} H_1^{(2)}(k_t \rho) \quad (\text{J.11b})$$

$$\frac{\partial^2}{\partial x \partial y} H_0^{(2)}(k_t \rho) = k_t \frac{(x - x')(y - y')}{\rho^2} \left[\frac{2}{\rho} H_1^{(2)}(k_t \rho) - k_t H_0^{(2)}(k_t \rho) \right] \quad (\text{J.11c})$$

$$\begin{aligned} \frac{\partial^2}{\partial x^2} H_0^{(2)}(k_t \rho) &= k_t \frac{(x - x')^2 - (y - y')^2}{\rho^3} H_1^{(2)}(k_t \rho) \\ &\quad - k_t^2 \frac{(x - x')^2}{\rho^2} H_0^{(2)}(k_t \rho) \end{aligned} \quad (\text{J.11d})$$

$$\begin{aligned} \frac{\partial^2}{\partial y^2} H_0^{(2)}(k_t \rho) &= k_t \frac{(y - y')^2 - (x - x')^2}{\rho^3} H_1^{(2)}(k_t \rho) \\ &\quad - k_t^2 \frac{(y - y')^2}{\rho^2} H_0^{(2)}(k_t \rho). \end{aligned} \quad (\text{J.11e})$$

For example, the \hat{x} and \hat{z} components of the electric field produced by the traveling wave electric current

$$\mathbf{J}(\rho') = \hat{x} J_x(\rho') e^{-jk_z z'} \quad (\text{J.12})$$

in a region R are given by

$$\begin{aligned} E_x(J_x) &= \frac{-1}{4\omega\epsilon} e^{-jk_z z} \int_R \left[\left(k^2 - k_t^2 \frac{(x - x')^2}{\rho^2} \right) H_0^{(2)}(k_t \rho) \right. \\ &\quad \left. + k_t \frac{(x - x')^2 - (y - y')^2}{\rho^3} H_1^{(2)}(k_t \rho) \right] J_x(\rho') dR' \end{aligned} \quad (\text{J.13a})$$

$$E_z(J_x) = \frac{-jk_z k_t}{4\omega\epsilon} e^{-jk_z z} \int_R \frac{x - x'}{\rho} H_1^{(2)}(k_t \rho) J_x(\rho') dR'. \quad (\text{J.13b})$$

The \hat{x} and \hat{z} components of the electric field produced by the traveling wave electric current

$$\mathbf{J}(\rho') = \hat{z} J_z(\rho') e^{-jk_z z'} \quad (\text{J.14})$$

in a region R are given by

$$E_x(J_z) = -\frac{jk_z k_t}{4\omega\epsilon} e^{-jk_z z} \int_R \frac{x - x'}{\rho} H_1^{(2)}(k\rho) J_x(\rho') dR' \quad (\text{J.15a})$$

$$E_z(J_z) = -\frac{k^2 - k_z^2}{4\omega\epsilon} e^{-jk_z z} \int_R H_0^{(2)}(k_t\rho) J_z(\rho') dR'. \quad (\text{J.15b})$$

Appendix K

Spherical Wave Spectrum of a Cylindrical Traveling Wave

This appendix develops a spherical wave spectrum of a cylindrical traveling wave starting with the cylindrical wave spectrum of a spherical wave given by

$$\frac{e^{-jk\sqrt{\rho^2+(z-z')^2}}}{\sqrt{\rho^2+(z-z')^2}} = \frac{1}{2j} \int_{-\infty}^{\infty} H_0^{(2)}(\rho\sqrt{k^2-\omega^2}) e^{j\omega(z-z')} d\omega \quad (K.1)$$

which can be developed using Equations (5-136), (5-137), and (5-138) of [115, p. 244] and is given in abbreviated form in Equation (5-139) and in Equation (6.614.4) of [141]. Let

$$f(z) = \frac{e^{-jk\sqrt{\rho^2+(z-z')^2}}}{\sqrt{\rho^2+(z-z')^2}} \quad (K.2)$$

and

$$F(\omega) = \frac{\pi}{j} H_0^{(2)}(\rho\sqrt{k^2-\omega^2}) e^{-j\omega z'} \quad (K.3)$$

Now, using the Fourier transforms

$$f(z) = \frac{1}{2\pi} \int_{-\infty}^{\infty} F(\omega) e^{j\omega z} d\omega \quad (K.4a)$$

$$F(\omega) = \int_{-\infty}^{\infty} f(z) e^{-j\omega z} dz \quad (K.4b)$$

the final relationship is obtained:

$$\frac{\pi}{j} H_0^{(2)}(\rho\sqrt{k^2-\omega^2}) e^{-j\omega z'} = \int_{-\infty}^{\infty} \frac{e^{-jk\sqrt{\rho^2+(z-z')^2}}}{\sqrt{\rho^2+(z-z')^2}} e^{-j\omega z} dz \quad (K.5)$$

Equation (10) of [139] incorporates a similar result with $\gamma = -j\omega$.

Appendix L

Small Argument Approximations for Integrals of Hankel Functions

This appendix presents small argument approximations for several integrals of Hankel functions multiplied by other functions, using

$$H_0^{(2)}(z) \approx 1 - j \frac{2}{\pi} \ln \frac{\gamma}{2} z \quad (\text{L.1a})$$

$$H_1^{(2)}(z) \approx \frac{z}{2} + j \frac{2}{\pi z} \quad (\text{L.1b})$$

where $\gamma = 1.781$.

$$\int_{-a}^a H_0^{(2)}(k|x-x'|) dx' \approx 2a - j \frac{2}{\pi} \left[(a-x) \ln \frac{\gamma k}{2} |z-a| + (a+x) \ln \frac{\gamma k}{2} |x+a| - 2a \right] \quad (\text{L.2})$$

$$\int_{-a}^a \frac{1}{|x-x'|} H_1^{(2)}(k|x-x'|) dx' \approx ka + j \frac{2}{\pi k} \left[\frac{1}{x-a} - \frac{1}{x+a} \right] \quad (\text{L.3})$$

$$\int_{-a}^a \int_{-a}^a H_0^{(2)}(k|x-x'|) dx' w(x) dx \approx 2a - j \frac{4a}{\pi} \left(-\frac{11}{6} + \frac{1}{3} \ln 2 + \ln \gamma ka \right) \quad (\text{L.4})$$

$$\int_{-a}^a \int_{-a}^a \frac{1}{|x-x'|} H_1^{(2)}(k|x-x'|) dx' w(x) dx \approx ka - j \frac{8}{\pi ka} \ln 2 \quad (\text{L.5})$$

where

$$w(x) = \begin{cases} \frac{1}{a^2}(a-x) & \text{for } 0 < x < a \\ \frac{1}{a^2}(a+x) & \text{for } -a < x < 0. \end{cases} \quad (L.6)$$

Appendix M

Limitations of the Reciprocity Theorem in Two-Dimensions

This appendix examines the limitations of the reciprocity theorem in two-dimensions and shows a practical example where the reciprocity theorem is not valid [142]. First, we will derive the reciprocity theorem following the classical approach [115, sec. 3-8].

Consider two time-harmonic sources a and b with electric and magnetic current densities $(\mathbf{J}^a, \mathbf{M}^a)$ and $(\mathbf{J}^b, \mathbf{M}^b)$, respectively, radiating in a region containing a linear isotropic inhomogeneous medium (μ, ϵ) . Source a or b radiating alone in the region produces the fields $(\mathbf{E}^a, \mathbf{H}^a)$ or $(\mathbf{E}^b, \mathbf{H}^b)$, where the fields are related by

$$\nabla \times \mathbf{H}^a = j\omega\epsilon\mathbf{E}^a + \mathbf{J}^a \quad (\text{M.1a})$$

$$-\nabla \times \mathbf{E}^a = j\omega\mu\mathbf{H}^a + \mathbf{M}^a \quad (\text{M.1b})$$

or

$$\nabla \times \mathbf{H}^b = j\omega\epsilon\mathbf{E}^b + \mathbf{J}^b \quad (\text{M.2a})$$

$$-\nabla \times \mathbf{E}^b = j\omega\mu\mathbf{H}^b + \mathbf{M}^b \quad (\text{M.2b})$$

respectively.

Equations (M.1) and (M.2) are combined using the vector identity

$$\nabla \cdot (\mathbf{A} \times \mathbf{B}) = \mathbf{B} \cdot \nabla \times \mathbf{A} - \mathbf{A} \cdot \nabla \times \mathbf{B} \quad (\text{M.3})$$

resulting in

$$\begin{aligned}\nabla \cdot (\mathbf{E}^b \times \mathbf{H}^a) &= \mathbf{H}^a \cdot \nabla \times \mathbf{E}^b - \mathbf{E}^b \cdot \nabla \times \mathbf{H}^a \\ &= -j\omega\mu\mathbf{H}^a \cdot \mathbf{H}^b - \mathbf{H}^a \cdot \mathbf{M}^b - j\omega\epsilon\mathbf{E}^b \cdot \mathbf{E}^a - \mathbf{E}^b \cdot \mathbf{J}^a\end{aligned}\quad (\text{M.4})$$

and

$$\begin{aligned}\nabla \cdot (\mathbf{E}^a \times \mathbf{H}^b) &= \mathbf{H}^b \cdot \nabla \times \mathbf{E}^a - \mathbf{E}^a \cdot \nabla \times \mathbf{H}^b \\ &= -j\omega\mu\mathbf{H}^b \cdot \mathbf{H}^a - \mathbf{H}^b \cdot \mathbf{M}^a - j\omega\epsilon\mathbf{E}^a \cdot \mathbf{E}^b - \mathbf{E}^a \cdot \mathbf{J}^b\end{aligned}\quad (\text{M.5})$$

Subtracting Equation (M.5) from (M.4) yields

$$\nabla \cdot (\mathbf{E}^b \times \mathbf{H}^a - \mathbf{E}^a \times \mathbf{H}^b) = \mathbf{H}^b \cdot \mathbf{M}^a - \mathbf{H}^a \cdot \mathbf{M}^b + \mathbf{E}^a \cdot \mathbf{J}^b - \mathbf{E}^b \cdot \mathbf{J}^a \quad (\text{M.6})$$

which is the point form of the Lorentz reciprocity theorem.

Applying the divergence theorem to Equation (M.6) yields

$$\begin{aligned}\oiint_S (\mathbf{E}^b \times \mathbf{H}^a - \mathbf{E}^a \times \mathbf{H}^b) \cdot d\mathbf{S} &= \\ &= \iiint_V (\mathbf{H}^b \cdot \mathbf{M}^a - \mathbf{H}^a \cdot \mathbf{M}^b + \mathbf{E}^a \cdot \mathbf{J}^b - \mathbf{E}^b \cdot \mathbf{J}^a) dv\end{aligned}\quad (\text{M.7})$$

where S is a closed surface over the volume V and $d\mathbf{S}$ is the outward normal at S . This is the general form of the Lorentz reciprocity theorem [131, pg. 49].

The sources a and b are confined to volumes V_a and V_b , enclosed by surfaces S_a and S_b , respectively, as shown in Figure M.1, where volume V_0 is the source-free region, enclosed by the surface $\Sigma + S_a + S_b$. Since $(\mathbf{J}^a, \mathbf{M}^a)$ and $(\mathbf{J}^b, \mathbf{M}^b)$ are zero in V_0 , the right-hand side of Equation (M.7) is zero for $V = V_0$, resulting in the Lorentz reciprocity theorem for a source-free region

$$\oiint_{\Sigma+S_a+S_b} (\mathbf{E}^b \times \mathbf{H}^a - \mathbf{E}^a \times \mathbf{H}^b) \cdot d\mathbf{S} = 0. \quad (\text{M.8})$$

For sources of finite extent in all three-dimensions, the surface Σ is taken to be a sphere of radius $r \rightarrow \infty$. Then the radiation condition

$$\oiint_{\Sigma_{r \rightarrow \infty}} (\mathbf{E}^b \times \mathbf{H}^a - \mathbf{E}^a \times \mathbf{H}^b) \cdot d\mathbf{S} = 0 \quad (\text{M.9})$$

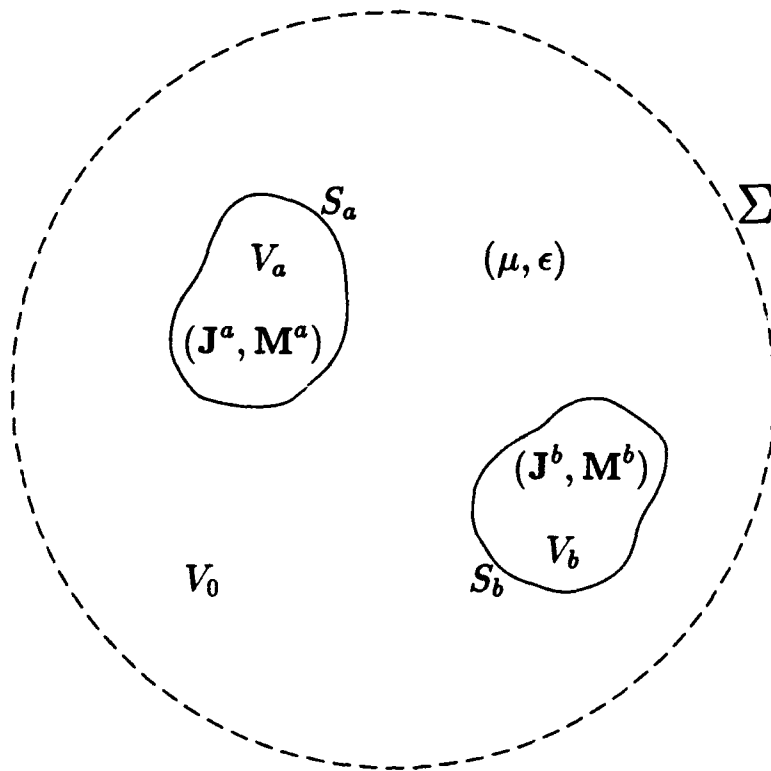


Figure M.1: Sources a and b in a region enclosed by the surface Σ .

is used to reduce Equation (M.8) to

$$\oiint_{S_a} (\mathbf{E}^b \times \mathbf{H}^a - \mathbf{E}^a \times \mathbf{H}^b) \cdot d\mathbf{S} = - \oiint_{S_b} (\mathbf{E}^b \times \mathbf{H}^a - \mathbf{E}^a \times \mathbf{H}^b) \cdot d\mathbf{S} \quad (\text{M.10})$$

which is often written as

$$\iiint_{V_a} (\mathbf{E}^b \cdot \mathbf{J}^a - \mathbf{H}^b \cdot \mathbf{M}^a) dv = \iiint_{V_b} (\mathbf{E}^a \cdot \mathbf{J}^b - \mathbf{H}^a \cdot \mathbf{M}^b) dv \quad (\text{M.11})$$

using Equation (M.7).

However, for sources of finite radial extent in two-dimensions, the source-free volume V_0 is a cylinder with two axial voids and the surface Σ is the outer surface of this volume and can be decomposed into three surfaces:

$$\Sigma = \Sigma_{\rho \rightarrow \infty} + \Sigma_{z \rightarrow \infty} + \Sigma_{z \rightarrow -\infty} \quad (\text{M.12})$$

The radiation condition only applies for the surface $\Sigma_{\rho \rightarrow \infty}$, so the reciprocity theorems of Equations (M.10) and (M.11) are not valid for general sources of finite radial extent.

Next, we will consider under which conditions the surfaces $\Sigma_{z \rightarrow \infty}$ and $\Sigma_{z \rightarrow -\infty}$ do not contribute to Equation (M.8). This contribution is given by

$$\iint_{\Sigma_{z \rightarrow \infty}} (\mathbf{E}^b \times \mathbf{H}^a - \mathbf{E}^a \times \mathbf{H}^b) \cdot d\mathbf{S} + \iint_{\Sigma_{z \rightarrow -\infty}} (\mathbf{E}^b \times \mathbf{H}^a - \mathbf{E}^a \times \mathbf{H}^b) \cdot d\mathbf{S}. \quad (\text{M.13})$$

The most common fields in two-dimensions can be described as traveling wave fields where the only z variation of the fields is $e^{-jk_z z}$. The two limiting cases are TE_z and TM_z fields, where $k_z = 0$, and TEM fields, where $k_z = k = \omega\sqrt{\mu\epsilon}$. Since the regions of interest are source-free, i.e., the surfaces $\Sigma_{z \rightarrow \infty}$ and $\Sigma_{z \rightarrow -\infty}$, the fields can be represented as the sum of the fields generated by the magnetic and electric vector potentials [115, sec. 3-12] given by

$$\mathbf{A} = \hat{\mathbf{z}}\Psi(x, y)e^{-jk_z z} \quad (\text{M.14a})$$

$$\mathbf{F} = \hat{\mathbf{z}}\Phi(x, y)e^{-jk_z z}. \quad (\text{M.14b})$$

The resulting fields are given by

$$\begin{aligned} \mathbf{E} &= -\nabla \times \mathbf{F} - j\omega\mu\mathbf{A} + \frac{\nabla(\nabla \cdot \mathbf{A})}{j\omega\epsilon} \\ &= \left\{ \left(-\hat{x} \frac{\partial\Phi}{\partial y} + \hat{y} \frac{\partial\Phi}{\partial x} \right) \right. \\ &\quad \left. + \frac{1}{j\omega\epsilon} \left[-jk_z \hat{x} \frac{\partial\Psi}{\partial x} - jk_z \hat{y} \frac{\partial\Psi}{\partial y} + \hat{z} (k^2 - k_z^2) \Psi \right] \right\} e^{-jk_z z} \quad (\text{M.15a}) \end{aligned}$$

$$\begin{aligned} \mathbf{H} &= \nabla \times \mathbf{A} - j\omega\epsilon\mathbf{F} + \frac{\nabla(\nabla \cdot \mathbf{F})}{j\omega\mu} \\ &= \left\{ \left(\hat{x} \frac{\partial\Psi}{\partial y} - \hat{y} \frac{\partial\Psi}{\partial x} \right) \right. \\ &\quad \left. + \frac{1}{j\omega\mu} \left[-jk_z \hat{x} \frac{\partial\Phi}{\partial x} - jk_z \hat{y} \frac{\partial\Phi}{\partial y} + \hat{z} (k^2 - k_z^2) \Phi \right] \right\} e^{-jk_z z}. \quad (\text{M.15b}) \end{aligned}$$

First, individually consider the surface integrals of Equation (M.13) point-wise

$$(\mathbf{E}^b \times \mathbf{H}^a - \mathbf{E}^a \times \mathbf{H}^b) \cdot \hat{z} \quad (\text{M.16})$$

where \hat{z} is from $d\mathbf{S} = \hat{z} dx dy$. Using Equation (M.15), the first term can be expanded in rectangular coordinates as

$$\begin{aligned} (\mathbf{E}^b \times \mathbf{H}^a) \cdot \hat{z} &= \left\{ \left(-\frac{\partial\Phi^b}{\partial y} - \frac{k_z^b}{\omega\epsilon} \frac{\partial\Psi^b}{\partial x} \right) \hat{x} + \left(\frac{\partial\Phi^b}{\partial x} - \frac{k_z^b}{\omega\epsilon} \frac{\partial\Psi^b}{\partial y} \right) \hat{y} \right\} e^{-jk_z^b z} \times \\ &\quad \left\{ \left(\frac{\partial\Psi^a}{\partial y} - \frac{k_z^a}{\omega\mu} \frac{\partial\Phi^a}{\partial x} \right) \hat{x} - \left(\frac{\partial\Psi^a}{\partial x} + \frac{k_z^a}{\omega\mu} \frac{\partial\Phi^a}{\partial y} \right) \hat{y} \right\} e^{-jk_z^a z} \quad (\text{M.17}) \end{aligned}$$

$$\begin{aligned} &= \left\{ \left(\frac{\partial\Phi^b}{\partial y} \frac{\partial\Psi^a}{\partial x} - \frac{\partial\Phi^b}{\partial x} \frac{\partial\Psi^a}{\partial y} \right) \right. \\ &\quad + \frac{k_z^a}{\omega\mu} \left(\frac{\partial\Phi^b}{\partial y} \frac{\partial\Phi^a}{\partial y} + \frac{\partial\Phi^b}{\partial x} \frac{\partial\Phi^a}{\partial x} \right) \\ &\quad + \frac{k_z^b}{\omega\epsilon} \left(\frac{\partial\Psi^b}{\partial x} \frac{\partial\Psi^a}{\partial x} + \frac{\partial\Psi^b}{\partial y} \frac{\partial\Psi^a}{\partial y} \right) \\ &\quad \left. + \frac{k_z^a k_z^b}{k^2} \left(\frac{\partial\Psi^b}{\partial x} \frac{\partial\Phi^a}{\partial y} - \frac{\partial\Psi^b}{\partial y} \frac{\partial\Phi^a}{\partial x} \right) \right\} e^{-j(k_z^a + k_z^b)z}. \quad (\text{M.18}) \end{aligned}$$

The second term may be obtained in a similar fashion. Then Equation (M.16) reduces to

$$\begin{aligned} (\mathbf{E}^b \times \mathbf{H}^a - \mathbf{E}^a \times \mathbf{H}^b) \cdot \hat{\mathbf{z}} = e^{-j(k_x^b + k_x^a)z} \left\{ \right. \\ \left. \left(1 - \frac{k_z^a k_z^b}{k^2} \right) \left[\left(\frac{\partial \Phi^b}{\partial y} \frac{\partial \Psi^a}{\partial x} - \frac{\partial \Phi^b}{\partial x} \frac{\partial \Psi^a}{\partial y} \right) - \left(\frac{\partial \Psi^b}{\partial x} \frac{\partial \Phi^a}{\partial y} - \frac{\partial \Psi^b}{\partial y} \frac{\partial \Phi^a}{\partial x} \right) \right] \right. \\ \left. + (k_z^a - k_z^b) \left[\frac{1}{\omega \mu} \left(\frac{\partial \Phi^b}{\partial y} \frac{\partial \Phi^a}{\partial y} + \frac{\partial \Phi^b}{\partial x} \frac{\partial \Phi^a}{\partial x} \right) - \frac{1}{\omega \epsilon} \left(\frac{\partial \Psi^b}{\partial x} \frac{\partial \Psi^a}{\partial x} + \frac{\partial \Psi^b}{\partial y} \frac{\partial \Psi^a}{\partial y} \right) \right] \right\}. \quad (\text{M.19}) \end{aligned}$$

Equation (M.19) is zero for TEM fields, where $k_z = k$. Using Equation (M.19), Equation (M.13) is zero for traveling wave fields where $k_z^a = -k_z^b$, and as a special case, TE_z and TM_z fields where $k_z^a = k_z^b = 0$. Under limited special cases, Equation (M.19) may be zero for general traveling waves.

Microstrip Transmission Line

The method of moments solution of a microstrip transmission line is one case where the limitations of the reciprocity theorem are important. This problem consists of finding the electric field of a traveling wave current when calculating the method of moments impedance matrix. This is one case where the Galerkin method of moments impedance matrix is not symmetric. To avoid the complexity of the microstrip Green's function, consider the mutual impedance between the currents $\hat{\mathbf{x}}J_x(x)e^{-jk_z z}$ and $\hat{\mathbf{z}}J_z(x)e^{-jk_z z}$ in free space using Equations (J.13b) and (J.15a)

$$Z_{xz} = - \int_{-W/2}^{W/2} \left[-\frac{jk_z k_t}{4\omega\epsilon} \int_{-W/2}^{W/2} \frac{x-x'}{|x-x'|} H_1^{(2)}(k|x-x'|) J_z(x') dx' \right] J_x(x) dx \quad (\text{M.20a})$$

$$Z_{zx} = - \int_{-W/2}^{W/2} \left[-\frac{jk_z k_t}{4\omega\epsilon} \int_{-W/2}^{W/2} \frac{x'-x}{|x'-x|} H_1^{(2)}(k|x-x'|) J_x(x) dx \right] J_z(x') dx' \quad (\text{M.20b})$$

where $k_t = \sqrt{k^2 - k_z^2}$. In this special case $Z_{xz} = -Z_{zx}$. Clearly, for a microstrip line the relationship would be more complicated, but definitely $Z_{xz} \neq Z_{zx}$, except in limited special cases.

Bibliography

- [1] D. L. Jaggard, A. R. Mickelson, and C. H. Papas, "On Electromagnetic Waves in Chiral Media," *Appl. Phys.*, vol. 18, pp. 211-216, 1979.
- [2] J. Applequist, "Optical Activity: Biot's Bequest," *Amer. Scientist*, vol. 75, pp. 59-68, Jan.-Feb. 1987.
- [3] E. U. Condon, "Theories of Optical Rotatory Power," *Revs. Modern Phys.*, vol. 9, pp. 432-457, Oct. 1937.
- [4] J. A. Kong, *Theory of Electromagnetic Waves*. New York: Wiley, 1975.
- [5] J. A. Kong, *Electromagnetic Wave Theory*. New York: Wiley, 1986.
- [6] E. J. Post, *Formal Structure of Electromagnetics*. Amsterdam: North-Holland, 1962.
- [7] H. Unz, "Electromagnetic Radiation in Drifting Tellegen Anisotropic Medium," *IEEE Trans. Antennas Propagat.*, vol. AP-11, pp. 573-578, Sept. 1963.
- [8] D. K. Cheng and J.-A. Kong, "Covariant Descriptions of Bianisotropic Media," *Proc. IEEE*, vol. 56, pp. 248-251, Mar. 1968.
- [9] T. H. O'Dell, *The Electrodynamics of Magneto-Electric Media*. Amsterdam: North-Holland, 1970.
- [10] B. R. Chawla and H. Unz, *Electromagnetic Waves in Moving Magneto-Plasmas*. Lawrence: University Press of Kansas, 1971.
- [11] J. A. Kong, "Image Theory for Bianisotropic Media," *IEEE Trans. Antennas Propagat.*, vol. AP-19, pp. 451-452, May 1971.
- [12] J. A. Kong, "Theorems of Bianisotropic Media," *Proc. IEEE*, vol. 60, pp. 1036-1046, Sept. 1972.
- [13] C. M. Krowne, "Electromagnetic Theorems for Complex Anisotropic Media," *IEEE Trans. Antennas Propagat.*, vol. AP-32, pp. 1224-1230, Nov. 1984.

- [14] K. Suchy, C. Altman, and A. Schatzberg, "Orthogonal Mapping of Time-Harmonic Electromagnetic Fields in Inhomogeneous (Bi)Anisotropic Media," *Radio Science*, vol. 20, pp. 149-160, Mar.-Apr. 1985.
- [15] W. Weiglhofer, "Scalarisation of Maxwell's Equations in General Inhomogeneous Bianisotropic Media," *Proc. IEE*, vol. 134, Pt. H, pp. 357-360, Aug. 1987.
- [16] T. A. Maldonado and T. K. Gaylord, "Accurate Method to Determine the Eigenstates of Polarization in Gyrotropic Media," *Appl. Opt.*, vol. 28, pp. 2075-2086, 1989.
- [17] A. Lakhtakia, V. V. Varadan, and V. K. Varadan, "Time-Harmonic and Time-Dependent Dyadic Green's Functions for some Uniaxial Gyroelectromagnetic Media," *Appl. Opt.*, vol. 28, pp. 1049-1052, Mar. 15, 1989.
- [18] A. Lakhtakia, "Polarizability Dyadics of Small Bianisotropic Spheres," *J. Phys. France*, vol. 51, pp. 2235-2242, Oct. 1990.
- [19] I. N. Bronshtein and K. A. Semendyayev, *Handbook of Mathematics*. New York: Van Nostrand Reinhold, 1985.
- [20] C. F. Bohren, "Scattering of Electromagnetic Waves by an Optically Active Cylinder," *J. Colloid Interface Sci.*, vol. 66, pp. 105-109, Aug. 1978.
- [21] W. Kauzmann, *Quantum Chemistry*. New York: Academic Press, 1957.
- [22] E. U. Condon, W. Altar, and H. Eyring, "One-Electron Rotatory Power," *J. Chem. Phys.*, vol. 5, pp. 753-775, Oct. 1937.
- [23] W. Moffitt and A. Moscowitz, "Optical Activity in Absorbing Media," *J. Chem. Phys.*, vol. 30, pp. 648-660, Mar. 1959.
- [24] J. G. Kirkwood, "On the Theory of Optical Rotatory Power," *J. Chem. Phys.*, vol. 5, pp. 479-491, June 1937.
- [25] W. J. Kauzmann, J. E. Walter, and H. Eyring, "Theories of Optical Rotatory Power," *Chem. Revs.*, vol. 26, pp. 339-407, 1940.
- [26] H. Eyring, J. Walter, and G. E. Kimball, *Quantum Chemistry*. New York: Wiley, 1944.
- [27] I. Tinoco, Jr. and W. G. Hammerle, "The Influence of an External Electric Field on the Optical Activity of Fluids," *J. Phys. Chem.*, vol. 60, pp. 1619-1623, Dec. 1956.
- [28] A. Sommerfeld, *Optics*. New York: Academic Press, 1964.

- [29] D. J. Caldwell and H. Eyring, *The Theory of Optical Activity*. New York: Wiley, 1971.
- [30] A. S. Schneider, "Circular Dichroism and Optical Rotatory Dispersion of Scattering Suspensions," *Chem. Phys. Lett.*, vol. 8, pp. 604-608, Mar. 1971.
- [31] E. Fredericq and C. Houssier, *Electric Dichroism and Electric Birefringence*. Oxford: Clarendon Press, 1973.
- [32] E. B. Priestley, *Introduction to Liquid Crystals*. New York: Plenum, 1974, p. 203.
- [33] M. Orchin, F. Kaplan, R. S. Macomber, R. M. Wilson, and H. Zimmer, *The Vocabulary of Organic Chemistry*. New York: Wiley, 1980, p. 125.
- [34] L. S. Corley and O. Vogl, "Optically Active Polychloral," *Polymer Bull.*, vol. 3, pp. 211-217, 1980.
- [35] W. J. Harris and O. Vogl, "Synthesis of Optically Active Polymers," *Polymer Preprints*, vol. 22, pp. 309-310, Aug. 1981.
- [36] A. Lakhtakia, "Polarizability dyadics of small chiral ellipsoids," *Chem. Phys. Lett.*, vol. 174, pp. 583-586, Nov. 1990.
- [37] K. F. Lindman, "Über die durch ein aktives Raumgitter erzeugte Rotationspolarisation der elektromagnetischen Wellen," *Ann. d. Phys.*, vol. 69, pp. 270-284, 1922.
- [38] K. F. Lindman, "Über eine durch ein isotropes System von spiralförmigen Resonatoren erzeugte Rotationspolarisation der elektromagnetischen Wellen," *Ann. d. Phys.*, vol. 63, pp. 621-644, 1920.
- [39] M. H. Winkler, "An Experimental Investigation of Some Models for Optical Activity," *J. Phys. Chem.*, vol. 60, pp. 1656-1659, Dec. 1956.
- [40] I. Tinoco, Jr. and M. P. Freeman, "The Optical Activity of Oriented Copper Helices. I. Experimental," *J. Phys. Chem.*, vol. 61, pp. 1196-1200, Sept. 1957.
- [41] D. J. Gordon, "Mie Scattering by Optically Active Particles," *Biochemistry*, vol. 11, no. 3, pp. 413-420, 1972.
- [42] C. F. Bohren, "Light Scattering by an Optically Active Sphere," *Chem. Phys. Lett.*, vol. 29, pp. 458-462, Dec. 1974.
- [43] C. F. Bohren and D. R. Huffman, *Absorption and Scattering of Light by Small Particles*. New York: Wiley, 1983.

- [44] C. F. Bohren, "Scattering of Electromagnetic Waves by an Optically Active Spherical Shell," *J. Chem. Phys.*, vol. 62, pp. 1566-1571, Feb. 1975.
- [45] C. F. Bohren, "Circular Dichroism and Optical Rotatory Dispersion Spectra of Arbitrarily Shaped Optically Active Particles," *J. Theor. Biol.*, vol. 65, pp. 755-767, Apr. 1977.
- [46] C. F. Bohren, "Angular Dependence of the Scattering Contribution to Circular Dichroism," *Chem. Phys. Lett.*, vol. 40, pp. 391-396, June 1976.
- [47] N. Engheta and A. R. Mickelson, "Transition Radiation Caused by a Chiral Plate," *IEEE Trans. Antennas Propagat.*, vol. AP-30, pp. 1213-1216, Nov. 1982.
- [48] N. Engheta and S. Bassiri, "Čerenkov Radiation in Chiral Media," *J. Appl. Phys.*, vol. 68, pp. 4393-4398, Nov. 1, 1990.
- [49] X. Sun and D. L. Jaggard, "Accelerated Particle Radiation in Chiral Media," *J. Appl. Phys.*, vol. 69, pp. 34-38, Jan. 1, 1991.
- [50] M. P. Silverman, "Specular Light Scattering from a Chiral Medium: Unambiguous Test of Gyrotropic Constitutive Relations," *Lettere al Nuovo Cimento*, vol. 43, pp. 378-382, Aug. 1985.
- [51] M. P. Silverman, "Reflection and Refraction at the Surface of a Chiral Medium: Comparison of Gyrotropic Constitutive Relations Invariant or Noninvariant Under a Duality Transformation," *J. Opt. Soc. Amer. A*, vol. 3, pp. 830-837, June 1986.
- [52] A. Lakhtakia, V. V. Varadan, and V. K. Varadan, "A Parametric Study of Microwave Reflection Characteristics of a Planar Achiral-Chiral Interface," *IEEE Trans. Electromag. Compat.*, vol. EMC-28, pp. 90-95, May 1986.
- [53] A. Lakhtakia, V. K. Varadan, and V. V. Varadan, "Excitation of a planar achiral/chiral interface by near fields," *J. Wave-Mater. Interact.*, vol. 3, pp. 231-241, July 1988.
- [54] S. Bassiri, C. H. Papas, and N. Engheta, "Electromagnetic Wave Propagation Through a Dielectric-Chiral Interface and Through a Chiral Slab," *J. Opt. Soc. Amer. A*, vol. 5, pp. 1450-1459, Sept. 1988.
- [55] A. Lakhtakia, V. K. Varadan, and V. V. Varadan, "Reflection of Elastic Plane Waves at a Planar Achiral-Chiral Interface," *J. Acoustical Soc. Amer.*, vol. 87, pp. 2314-2318, June 1990.

- [56] A. Lakhtakia, V. V. Varadan, and V. K. Varadan, "Reflection of Plane Waves at Planar Achiral-Chiral Interfaces: Independence of the Reflected Polarization State from the Incident Polarization State," *J. Opt. Soc. Amer. A*, vol. 7, pp. 1654-1656, Sept. 1990.
- [57] A. Lakhtakia, "On Extending the Brewster Law at Planar Interfaces," *Optik*, vol. 84, no. 5, pp. 160-162, 1990.
- [58] A. J. Viitanen, I. V. Lindell, and A. H. Sihvola, "Eigensolutions for the Reflection Problem of the Interface of Two Chiral Half-Spaces," *J. Opt. Soc. Amer. A*, vol. 7, pp. 683-692, Apr. 1990.
- [59] A. Lakhtakia, V. V. Varadan, and V. K. Varadan, "What Happens to Plane Waves at the Planar Interface of Mirror-Conjugated Chiral Media," *J. Opt. Soc. Amer. A*, vol. 6, pp. 23-26, Jan. 1989.
- [60] A. Lakhtakia, V. V. Varadan, and V. K. Varadan, "Scattering by Periodic Achiral-Chiral Interfaces," *J. Opt. Soc. Amer. A*, vol. 6, pp. 1675-1681, Nov. 1989. correction May 1990, page 951.
- [61] T. Guire, V. V. Varadan, and V. K. Varadan, "Influence of Chirality on the Reflection of EM Waves by Planar Dielectric Slabs," *IEEE Trans. Electromag. Compat.*, vol. 32, pp. 300-303, Nov. 1990.
- [62] V. K. Varadan, V. V. Varadan, and A. Lakhtakia, "On the Possibility of Designing Anti-Reflection Coating Using Chiral Composites," *J. Wave-Mater. Interact.*, vol. 2, pp. 71-81, Jan. 1987.
- [63] D. L. Jaggard and N. Engheta, "ChirosorbTM as an Invisible Medium," *Electronics Letters*, vol. 25, pp. 173-174, Feb. 1989.
- [64] D. L. Jaggard, N. Engheta, and J. Liu, "Chiroshield: A Salisbury/Dallenbach Shield Alternative," *Electronics Letters*, vol. 26, pp. 1332-1333, Aug. 1990.
- [65] H. Cory and I. Rosenhouse, "Electromagnetic Wave Propagation Along a Chiral Slab," *Proc. IEE*, vol. 138, Pt. H, pp. 51-54, Feb. 1991.
- [66] V. V. Varadan, A. Lakhtakia, and V. K. Varadan, "Reflection and Transmission Characteristics of a Structurally Chiral Slab: Intrinsic Anisotropy and Form Chirality," *Optik*, vol. 80, no. 1, pp. 27-32, 1988.
- [67] A. Lakhtakia, V. K. Varadan, and V. V. Varadan, "Scattering and Absorption Characteristics of Lossy Dielectric, Chiral, Nonspherical Objects," *Appl. Opt.*, vol. 24, pp. 4146-4154, Dec. 1985.
- [68] P. L. E. Uslenghi, "Scattering by an Impedance Sphere Coated with a Chiral Layer," *Electromagnetics*, vol. 10, pp. 201-211, Jan.-June 1990.

- [69] A. Lakhtakia, V. K. Varadan, and V. V. Varadan, "Eigenmodes of a Chiral Sphere with a Perfectly Conducting Coating," *J. Phys. D*, vol. 22, pp. 825-828, June 14, 1989.
- [70] M. S. Kluskens and E. H. Newman, "Scattering by a Multilayer Chiral Cylinder," *IEEE Trans. Antennas Propagat.*, vol. AP-39, pp. 91-96, Jan. 1991.
- [71] M. S. Kluskens and E. H. Newman, "Scattering by an Arbitrary Cross Section Chiral Cylinder," June 1989 IEEE Antennas and Propagation/URSI Symposium, San Jose, CA.
- [72] M. S. Kluskens and E. H. Newman, "Scattering by a Chiral Cylinder of Arbitrary Cross Section," *IEEE Trans. Antennas Propagat.*, vol. AP-38, pp. 1448-1455, Sept. 1990.
- [73] M. S. Kluskens and E. H. Newman, "Scattering by a Chiral Cylinder of Arbitrary Cross Section in the Presence of a Half-Plane," in *PIER Book on Chirality* (J. A. Kong, ed.), New York: Elsevier, 1991.
- [74] R. Rojas, "Integral Equations for the Scattering by Three Dimensional Inhomogeneous Chiral Bodies," in *PIER Book on Chirality* (J. A. Kong, ed.), New York: Elsevier, 1991.
- [75] A. Lakhtakia, "On a Fourth-Order Wave Equation for EM Propagation in Chiral Media," *Appl. Phys. B*, vol. 36, pp. 163-165, 1985.
- [76] A. Lakhtakia, V. K. Varadan, and V. V. Varadan, "On the Influence of Chirality on the Scattering Response of a Chiral Scatter," *IEEE Trans. Electromag. Compat.*, vol. EMC-29, pp. 70-72, Feb. 1987.
- [77] V. K. Varadan, A. Lakhtakia, and V. V. Varadan, "A Comment on the Solutions of the Equation $\nabla \times a = ka$," *J. Phys. A*, vol. 20, pp. 2649-2650, 1987.
- [78] V. K. Varadan, A. Lakhtakia, and V. V. Varadan, "Radiated Potentials and Fields in Isotropic Chiral Media," *J. Phys. A*, vol. 20, pp. 4697-4702, 1987.
- [79] V. V. Varadan, A. Lakhtakia, and V. K. Varadan, "On the Equivalence of Sources and Duality of Fields in Isotropic Chiral Media," *J. Phys. A*, vol. 20, pp. 6259-6264, 1987.
- [80] A. Lakhtakia, V. V. Varadan, and V. K. Varadan, "Field Equations, Huygens's Principle, Integral Equations, and Theorems for Radiation and Scattering of Electromagnetic Waves in Isotropic Chiral Media," *J. Opt. Soc. Amer. A*, vol. 5, pp. 175-184, Feb. 1988.

- [81] W. S. Weiglhofer, "Isotropic Chiral Media and Scalar Hertz Potentials," *J. Phys. A*, vol. 21, pp. 2249-2251, 1988.
- [82] A. Lakhtakia, V. K. Varadan, and V. V. Varadan, "Influence of Impedance Mismatch Between a Chiral Scatterer," *J. Mod. Opt.*, vol. 36, pp. 1385-1392, Oct. 1989.
- [83] V. V. Varadan, Y. Ma, and V. K. Varadan, "Effects of Chiral Microstructure on EM Wave Propagation in Discrete Random Media," *Radio Science*, vol. 24, pp. 785-792, Nov.-Dec. 1989.
- [84] N. Engheta, M. W. Kowarz, and D. L. Jaggard, "Effect of Chirality on the Doppler Shift and Aberration of Light Waves," *J. Appl. Phys.*, vol. 66, pp. 2274-2277, Sept. 15, 1989.
- [85] J. C. Monzon, "Radiation and Scattering in Homogeneous General Biisotropic Regions," *IEEE Trans. Antennas Propagat.*, vol. AP-38, pp. 227-235, Feb. 1990.
- [86] A. Lakhtakia, V. K. Varadan, and V. V. Varadan, "Dilute Random Distribution of Small Chiral Spheres," *Appl. Opt.*, vol. 29, pp. 3627-3632, Sept. 1990.
- [87] W. S. Weiglhofer, "Electromagnetic Field Representation in (Inhomogeneous) Isotropic Chiral," *Electromagnetics*, vol. 10, pp. 271-278, Oct. 1990.
- [88] S. Bassiri, N. Engheta, and C. H. Papas, "Dyadic Green's Function and Dipole Radiation in Chiral Media," *Alta Freq.*, vol. LV, pp. 83-88, Mar.-Apr. 1986.
- [89] A. Lakhtakia, V. K. Varadan, and V. V. Varadan, "Regarding the Sources of Radiation Fields in an Isotropic Chiral Media," *J. Wave-Mater. Interact.*, vol. 2, pp. 183-189, July/Oct. 1987.
- [90] N. Engheta and S. Bassiri, "One- and Two-Dimensional Dyadic Green's Functions in Chiral Media," *IEEE Trans. Antennas Propagat.*, vol. AP-37, pp. 512-515, Apr. 1989.
- [91] A. Lakhtakia, V. V. Varadan, and V. K. Varadan, "Radiation by a Straight Thin-Wire Antenna Embedded in an Isotropic Chiral Media," *IEEE Trans. Electromag. Compat.*, vol. EMC-30, pp. 84-87, Feb. 1988.
- [92] D. L. Jaggard, X. Sun, and N. Engheta, "Canonical Sources and Duality in Chiral Media," *IEEE Trans. Antennas Propagat.*, vol. AP-36, pp. 1007-1013, July 1988.
- [93] N. Engheta and M. W. Kowarz, "Antenna Radiation in the Presence of a Chiral Sphere," *J. Appl. Phys.*, vol. 67, pp. 639-647, Jan. 15, 1990.

- [94] A. Lakhtakia, V. K. Varadan, and V. V. Varadan, "Radiation by a Point Electric Dipole Embedded in a Chiral Sphere," *J. Phys. D*, vol. 23, pp. 481-485, May 14, 1990.
- [95] A. Lakhtakia, V. K. Varadan, and V. V. Varadan, "Surface Integral Equations for Scattering by PEC Scatterers in Isotropic Chiral Media," *Int. J. Engng Sci.*, vol. 29, no. 2, pp. 179-185, 1991.
- [96] V. K. Varadan, A. Lakhtakia, and V. V. Varadan, "Scattering by Beaded Helices: Anisotropy and Chirality," *J. Wave-Mater. Interact.*, vol. 2, pp. 153-160, Apr. 1987.
- [97] V. V. Varadan, A. Lakhtakia, and V. K. Varadan, "Equivalent Dipole Moments of Helical Arrangements of Small, Isotropic, Point-polarizable Scatterers: Application to Chiral Polymer Design," *J. Appl. Phys.*, vol. 63, pp. 280-284, Jan. 1988.
- [98] T. Guire, M. Umari, V. V. Varadan, and V. K. Varadan, "Microwave Measurements on Chiral Composites," June 1988 URSI Radio Science Meeting, Syracuse, NY.
- [99] M. H. Umari, V. V. Varadan, and V. K. Varadan, "Rotation and Dichroism Associated with Microwave Propagation in Chiral Composite Samples," *submitted*, 1990.
- [100] A. H. Sihvola and I. V. Lindell, "Chiral Maxwell-Garnett Mixing Formula," *Electronics Letters*, vol. 26, pp. 118-119, Jan. 1990.
- [101] A. Lakhtakia, V. K. Varadan, and V. V. Varadan, "Effective Properties of a Sparse Random Distribution of Non-interacting Small Chiral Spheres in a Chiral Host Medium," *J. Phys. D*, vol. 24, pp. 1-6, Jan. 14, 1991.
- [102] N. Engheta and D. L. Jaggard, "Electromagnetic Chirality and Its Applications," *IEEE Antennas and Propagation Society Newsletter*, vol. 30, pp. 6-12, Oct. 1988.
- [103] V. K. Varadan, A. Lakhtakia, and V. V. Varadan, "Propagation in a parallel-plate waveguide wholly filled with a chiral medium," *J. Wave-Mater. Interact.*, vol. 3, pp. 267-272, July 1988.
- [104] C. Eftimiu and L. W. Pearson, "Guided Electromagnetic Waves in Chiral Media," *Radio Science*, vol. 24, pp. 351-359, May-June 1989.
- [105] N. Engheta and P. Pelet, "Modes in Chiro-waveguides," *Optics Letters*, vol. 14, pp. 593-595, June 1989.

- [106] P. Pelet and N. Engheta, "The Theory of Chirowaveguides," *IEEE Trans. Antennas Propagat.*, vol. AP-38, pp. 90-98, Jan. 1990.
- [107] P. Pelet and N. Engheta, "Coupled-mode Theory for Chirowaveguides," *J. Appl. Phys.*, vol. 67, pp. 2742-2745, Mar. 15, 1990.
- [108] J. A. M. Svedin, "Propagation Analysis of Chirowaveguides Using the Finite-Element Method," *IEEE Trans. Microwave Theory Tech.*, vol. 38, pp. 1488-1496, Oct. 1990.
- [109] N. Engheta and P. Pelet, "Mode Orthogonality in Chirowaveguides," *IEEE Trans. Microwave Theory Tech.*, vol. 38, pp. 1631-1634, Nov. 1990.
- [110] D. L. Jaggard, N. Engheta, M. W. Kowarz, P. Pelet, J. C. Liu, and Y. Kim, "Periodic Chiral Structures," *IEEE Trans. Antennas Propagat.*, vol. AP-37, pp. 1447-1452, Nov. 1989.
- [111] M. W. Kowarz and N. Engheta, "Spherical Chirolenses," *Optics Letters*, vol. 15, pp. 299-301, Mar. 1990.
- [112] N. Engheta, "Theory of Chiro-Strip Antennas," June 1988 URSI Radio Science Meeting, Syracuse, NY.
- [113] N. Engheta, "Chiral Substrate in Microstrip Antennas: Chirostrip Antennas," July 1989 PIERS: Progress In Electromagnetic Research Symposium, Boston, MA.
- [114] J. A. Stratton, *Electromagnetic Theory*. New York: McGraw-Hill, 1941.
- [115] R. F. Harrington, *Time-Harmonic Electromagnetic Fields*. New York: McGraw-Hill, 1961.
- [116] D. R. Rhodes, "On the Theory of Scattering by Dielectric Bodies," Report 475-1, Antenna Lab., The Ohio State University, Columbus, July 1953.
- [117] M. H. Cohen, "Application of the Reaction Concept to Scattering Problems," *IRE Trans. Antennas Propagat.*, vol. AP-3, pp. 193-199, Oct. 1955.
- [118] C. A. Balanis, *Advanced Engineering Electromagnetics*. New York: Wiley, 1989.
- [119] M. S. Kluskens and E. H. Newman, "Image Theory for Chiral Bodies," *IEEE Trans. Antennas Propagat.*, vol. AP-39, pp. 676-677, May 1991.
- [120] J. H. Richmond, "Efficient Recursive Solutions for Plane and Cylindrical Multilayers," Report 1968-1, Antenna Lab., The Ohio State University, Columbus, Aug. 10, 1965.

- [121] H. W. Bussey and J. H. Richmond, "Scattering by a Lossy Dielectric Circular Cylindrical Multilayer, Numerical Values," *IEEE Trans. Antennas Propagat.*, vol. AP-23, pp. 723-725, Sept. 1975.
- [122] T. B. A. Senior, "Approximate Boundary Conditions," *IEEE Trans. Antennas Propagat.*, vol. AP-29, pp. 826-829, Sept. 1981.
- [123] R. F. Harrington, *Field Computation by Moment Method*. New York: Macmillan, 1968.
- [124] R. F. Harrington, "Matrix Methods for Field Problems," *Proc. IEEE*, vol. 55, pp. 136-149, Feb. 1967.
- [125] J. J. Bowman, T. B. A. Senior, and P. L. E. Uslenghi, *Electromagnetic and Acoustic Scattering by Simple Shapes*. New York: Hemisphere, 1987.
- [126] C. T. Tai, *Dyadic Green's Functions in Electromagnetic Theory*. Scranton, PA: Intext, 1971.
- [127] J. H. Richmond, "Scattering by a Dielectric Cylinder of Arbitrary Cross Section Shape," *IEEE Trans. Antennas Propagat.*, vol. AP-13, pp. 334-341, May 1965.
- [128] J. H. Richmond, "TE-Wave Scattering by a Dielectric Cylinder of Arbitrary Cross-Section Shape," *IEEE Trans. Antennas Propagat.*, vol. AP-14, pp. 460-464, July 1966.
- [129] E. H. Newman, "TM and TE Scattering by a Dielectric/Ferrite Cylinder in the Presence of a Half-Plane," *IEEE Trans. Antennas Propagat.*, vol. AP-34, pp. 804-813, June 1986.
- [130] T. Itoh and R. Mittra, "Spectral-Domain Approach for Calculating the Dispersion Characteristics of Microstrip Lines," *IEEE Trans. Microwave Theory Tech.*, vol. 21, pp. 496-499, July 1973.
- [131] R. E. Collin, *Field Theory of Guided Waves*. New York: IEEE Press, 1991.
- [132] T. Kitazawa and Y. Hayashi, "Propagation Characteristics of Striplines with Multilayered Anisotropic Media," *IEEE Trans. Microwave Theory Tech.*, vol. 31, pp. 429-433, June 1983.
- [133] M. Kobayashi and T. Iijima, "Frequency-Dependent Characteristics of Current Distributions on Microstrip," *IEEE Trans. Microwave Theory Tech.*, vol. 37, pp. 799-801, Apr. 1989.

- [134] F. Medina, M. Horno, and H. Baudrand, "Generalized Spectral Analysis of Planar Lines on Layered Media Including Uniaxial and Biaxial Dielectric Substrates," *IEEE Trans. Microwave Theory Tech.*, vol. 37, pp. 504-511, Mar. 1989.
- [135] Y. Yuan and D. P. Nyquist, "Full-Wave Perturbation Theory Based upon Electric Field Integral Equations for Coupled Microstrip Transmission Lines," *IEEE Trans. Microwave Theory Tech.*, vol. 38, pp. 1576-1584, Nov. 1990.
- [136] J. Van Bladel, *Electromagnetic Fields*. New York: McGraw-Hill, 1964.
- [137] W. H. Press, B. P. Flannery, S. A. Teukolsky, and W. T. Vetterling, *Numerical Recipes*. New York: Cambridge University Press, 1986.
- [138] E. H. Newman, "TM Scattering by a Dielectric Cylinder in the Presence of a Half-Plane," *IEEE Trans. Antennas Propagat.*, vol. AP-33, pp. 773-782, July 1985.
- [139] E. H. Newman, "The Fields of a Traveling Wave Line Source in the Vicinity of a Half-Plane," *IEEE Trans. Antennas Propagat.*, vol. AP-35, pp. 866-870, July 1987.
- [140] M. Abramowitz and I. A. Stegun, *Handbook of Mathematical Functions*. Washington, D. C.: NBS, 1964.
- [141] I. S. Gradshteyn and I. M. Ryzhik, *Table of Integrals, Series, and Products*. Orlando, Florida: Academic Press, 1980.
- [142] E. H. Newman, "A Note on the Reciprocity Theorem for Traveling Wave Currents," 1987. unpublished.